

AD-A273 368

1

A STUDY OF DIFFUSIVITY IN THE BCC SOLID  
SOLUTION OF Nb-Al AND  
Nb-Ti-Al SYSTEM

S DTIC  
ELECTE  
NOV 30 1993  
A

BY

JOSE GUADALUPE LUIS RUIZ APARICIO

This document has been approved  
for public release and sale; its  
distribution is unlimited

A THESIS PRESENTED TO THE GRADUATE SCHOOL  
OF THE UNIVERSITY OF FLORIDA  
IN PARTIAL FULFILLMENT OF THE REQUIREMENTS  
FOR THE DEGREE OF MASTER OF SCIENCE

UNIVERSITY OF FLORIDA

1990

93 11 29 078

93 5 26 049

93-29193

To Laurita



Accesion For	
NTIS CRA&I	<input checked="" type="checkbox"/>
DTIC TAB	<input type="checkbox"/>
Unannounced	<input type="checkbox"/>
Justification _____	
By _____	
Distribution / _____	
Availability Codes	
Dist	Avail and/or Special
A-1	

DTEG QUALITY INSPECTED 5

To my Parents  
Luis y Reyna

and my brothers

Jorge  
Joel  
Cristina  
Marisela  
Mauricio  
Arturo  
Hugo

## ACKNOWLEDGEMENTS

The author is profoundly grateful to Dr. Fereshteh Ebrahimi, supervisory committee chairperson, for her advise, support, and patience for the achievement of this research. Her guidance and inspiration throughout this work will be always appreciated. The author wishes to thank Dr. Robert T. DeHoff, member of the supervisory committee, for his invaluable contributions during the elaboration of this work, and Dr. Ellis D. Verink Jr., member of the supervisory committee, for his continuous encouragement for the realization of this investigation.

I would like to express my deepest appreciation to the National University of Mexico, especially to Dr. Francisco Barnez de Castro, Chairman of the Chemistry School, Dr. Alejandro Pissanty Baruch and members of the Scholarship Subcommittee of the Chemistry School, and to the members of the Scholarship Committee (DGAPA), for giving me the opportunity to perform my graduate studies abroad.

I am also very grateful to the faculty of the Department of Materials Science and Engineering who always were ready to help me throughout the course of my studies. I am obliged to Wayne Acree for helping me during the evaluation of the samples using electron microprobe for this research. Last, but not least, I wish to thank to my friends and classmates during these last two years, especially Dr. Yoeng Seo Kim, Jesus Castillo, Lixion Lu, Joe and Arindam De. It was fun guys!

The financial support from the DARPA Composites Program (contract # N00014-88-J1100) is gratefully appreciated.

## TABLE OF CONTENTS

	Page
ACKNOWLEDGMENTS.....	iv
LIST OF TABLES.....	viii
LIST OF FIGURES.....	ix
ABSTRACT.....	xix
 <b>CHAPTER</b>	
1 INTRODUCTION.....	1
2 LITERATURE REVIEW.....	5
2.1 Nb-Al-Ti System.....	5
2.1.1 Phase Diagram.....	5
2.1.2 Diffusivity.....	12
2.1.3 Oxidation.....	34
2.2 Diffusion Theory and Mechanism.....	40
2.2.1 Binary Diffusion.....	40
2.2.1.1 Fick's Laws of Diffusion.....	41
a) D Constant, steady- and no-steady states.....	42
b) The Boltzmann-Matano method.....	43
2.2.1.3 Binary Diffusion by a Vacancy MechanismThe Kirkendall Effect and Darken Analysis.....	46
2.2.2 Ternary Diffusion.....	56
2.2.2.1 The Diffusivity Matrix.....	56
2.2.2.2 Experimental Determination of [D <sub>ij</sub> ]. The Infinite Diffusion Couple.....	60
2.2.2.3 Diffusion Penetration Tendencies and Composition Path Patterns.....	66
2.2.2.4 Zero Flux Plane.....	72

	Page
3 MATERIALS AND EXPERIMENTAL PROCEDURE.....	73
3.1 Materials.....	73
3.2 Alloy Preparation.....	76
3.3 Preparation of Diffusion Couples.....	79
3.4 Interdiffusion Heat Treatments.....	86
3.5 Analytical Microscopy.....	87
3.6 Calculation Method.....	89
4 DIFFUSIVITY EVALUATION IN THE BINARY Nb-Al SYSTEM.....	90
4.1 Diffusion Couple Preparation.....	90
a) As Arc-Melt Structure.....	91
b) Homogenized Structure.....	95
c) Diffusion Bonding.....	108
4.2 Diffusivity Analysis.....	112
4.2.1 Post Diffusion Microstructural Analysis of Binary Diffusion Couples.....	114
4.2.2 Measurement of Concentration Profiles.....	114
4.2.3 Concentration Profile Analysis.....	118
4.2.4 Calculation of the Interdiffusion Coefficient.....	122
a) Determination of the Matano Interface.....	122
b) Evaluation of $J_i(x)$ .....	134
c) Evaluation of the Concentration Gradient .....	137
d) Evaluation of Diffusivity, Activation Energy and Frequency Factor.....	140
4.2.5 Calculation of Intrinsic Diffusivities.....	154
4.3 Discussion.....	162
4.4 Summary.....	167
5 DIFFUSIVITY ANALYSIS IN THE TERNARY Nb-Ti-Al SYSTEM .....	170
5.1 Microstructural Analysis.....	172
5.2 Composition Profiles.....	184
5.2.1 The $\beta_1/X$ Couples: Effect of Ti content.....	193
5.2.2 Effect of Concentration Gradient.....	193
5.2.3 Critical Points.....	204
5.2.5 Temperature Effect.....	208
5.3 Penetration Depth.....	208
5.4 Composition Paths.....	218

5.4.1	The Nb-rich Corner.....	218
		Page
5.4.2	The Constant Nb:Ti Ratio Zone.....	221
5.4.3	The Ti-Rich Corner.....	221
5.5	Kirkendall Shifts.....	228
5.5	Crossover Displacements.....	230
5.6	Discussion.....	231
5.7	Summary.....	236
6	CONCLUSIONS.....	238
APPENDIX A	PROBLEMS ASSOCIATED WITH THE MEASUREMENT OF COMPOSITION PROFILES BY MICROPROBE ANALYSIS.....	240
REFERENCES.....	247	
BIOGRAPHICAL SKETCH <sup>3</sup> .....	253	

## LIST OF TABLES

Table	Page
2.1 Self-diffusion coefficients of Ti as measured by Trace diffusivity [21] and calculated by [20].....	17
2.2 Frequency factors Do and activation energies Q for Ti and Nb diffusion in Ti and Ti-Nb alloys (From Ref. [24]).....	21
2.3 The pre-exponential constants for diffusion of Aluminum in alpha Ti according to [40] and references therein.....	30
2.4 The pre-exponential constants for diffusion of Aluminum in beta Ti according to [40] and references therein.....	31
3.1 Ingot analysis of pure materials.....	75
3.2 Alloy compositions.....	77
3.3 Comparison of chemical analysis results for binary alloy $\gamma_0$ (Nb-4.5Al).....	78
3.4 List of diffusion couples .....	85
4.1 Interstitial content of alloys (ppm).....	116
4.2 Temperature and concentration dependencies of the interdiffusion coefficient in the system Nb-Al system.....	151
4.3 Activation energy and frequency factor values for interdiffusion in b.c.c. Nb-Al alloy a different Al composition.....	153
4.4 Intrinsic diffusivity of Al in (bcc) Nb.....	155
4.5 Composition-dependent activation energy and frequency factor values for intrinsic diffusion of Al.....	161
4.6 Solute diffusion in Nb-X system (From Ref. [77]).....	166
4.7 Interdiffusivity data for the phases in the Nb-Al system.....	168
5.1 Depth of penetration in ternary diffusion couples of system (B.C.C.) Nb-Ti-Al.....	215
5.2 Kirkendall shift measurements.....	229
5.3 Penetration ratios observed in the ternary couples of this study.....	232

## LIST OF FIGURES

Figure		Page
2.1	The Ti-Nb phase diagram [9].....	6
2.2	The Al-Nb phase diagram [10].....	7
2.3	The Ti-Al phase diagram [11].....	8
2.4	The Nb-Ti-Al Liquidus Projection [12].....	10
2.5	Isothermal section at 1200 °C in the Nb-Ti-Al ternary system [12].....	11
2.6	Temperature dependence of the diffusion of Ti <sup>44</sup> and V <sup>48</sup> in titanium [18].....	14
2.7	Computer fit of the experimental data for the diffusion of Ti <sup>44</sup> in titanium to the proposed by Kidson [19]. (From [18]).....	16
2.8	Measured diffusion coefficients of Ti (circles) and Nb (triangles) in different Ti-Nb alloys as a function of temperature [24].....	19
2.9	Diffusion coefficients of Ti (circles) and Nb (triangles) as a function of composition for 3 different temperatures [24].....	20
2.10	Self-diffusion in b.c.c. metals. Plot of the self-diffusion coefficient against the reduced reciprocal temperature [28].....	23
2.11	Concentration dependence of coefficient of mutual diffusion in Ti-Nb system: 1-1400°, 2- 1300°, 3- 1200°, 4- 1100°, 5- 1000 °C. From [30].....	24
2.12	Concentration dependence of activation energy and pre-exponential factor of mutual diffusion in the Ti-Nb system [30].....	25
2.13	Interdiffusion coefficients vs at% for the diffusion of Al in $\alpha$ -Ti. The present data obtained at 900° and 635 °C are compared with results published by 1) [38], and 2) [39]. (From Ref. [36]).....	29

Figure	Page
2.14 The diffusivities of oxygen and Al in $\alpha$ -Ti. The numbers in the plot correspond to the series numbers in Table 2.3 [40].....	32
2.15 The diffusivities of O, Al, and V in $\beta$ -Ti. The numbers in the plot correspond to the series numbers in Tables 2.4 [40].....	33
2.16 Diffusion coefficient as a function of reciprocal temperature of unalloyed Nb, and apparent diffusion coefficient for 2 Nb-Ti alloys [43].....	35
2.17 Parabolic rate constant vs Temperature for oxidation resistance materials [46].....	38
2.18 Typical composition profile of an annealed diffusion couple. The Matano interface is positioned to make the hatched areas on (cross hatched area), and the tangent values employed to calculate the intertdiffusion coefficient at a composition $c = 0.2c_0$ .....	45
2.19 Atomic jumps in a b.c.c. crystal considered in the model calculation made by [59]. a) Type A: jumps to the nearest-neighbour position, b) Type B: jumps to the second nearest-neighbor position, c) Type C: jumps to the third nearest-neighbour position.....	48
2.20 Potential barriers for the cited types of individual jumps starting at $r= 0$ and ending at $r= 1$ . The maximum value of each curve corresponds to the migration energy for the particular hopping event[59].....	49
2.21 Migration energy for self-diffusion in dependence on the binding energy of the crystal in comparison with the experimental data refered therein. The line drawn presents the calculated relation by [59].....	51
2.22 The Lattice Reference Frame.....	55
2.23 Composition Paths in a ternary system isotherm.....	59
2.24 Evaluation of Matano integrals and slopes at a given composition for evaluation of diffusion coefficients in ternary systems.....	62
2.25 a) The direct coefficient of diffusion for Cu, $D_{11}^3$ in units $10^{-12} \text{ cm}^2/\text{sec}$ , at $725^\circ\text{C}$ . Filled circles indicate intersections of diffusion paths, and open squares indicate extreme points in the composition profile [65].....	64

Figure	Page
2.25 Continue b) The direct coefficient of diffusion for Ag D <sub>22</sub> <sup>3</sup> in units 10 <sup>-12</sup> cm <sup>2</sup> /sec, at 725 °C. Filled circles indicate intersections of diffusion paths, and open squares indicate extreme points in the composition profile [65].....	64
2.26 a) Model for a ternary diffusion couple with independent concentration penetration tendencies; b) total concentration curve; c) computation of Kirkendall shift; d) prediction of Kirkendall shift; e) atom-fraction penetration profiles for the unrelaxed lattice; and f) computed composition path [69].....	68
2.27 a) Model for a ternary diffusion couple with concentration dependent penetration tendencies; b) total concentration curve; c) computation of Kirkendall shift; d) prediction of Kirkendall shift; e) atom-fraction penetration profiles for the unrelaxed lattice; and f) computed composition path. Note the ondulation in component B (e) and the displacement of the crossover point on the path (f). [69].....	71
3.1 A flow chart showing the experimental procedure for the preparation and analysis of the diffusion couples.....	74
3.2 Furnace assembly used for all heat treatments in this research.....	80
3.3 Experimental set-up for hot-pressing bonding of diffusion couples.....	84
4.1 Optical micrograph showing the dendritic microstructure in a Nb-4.5Al alloy after arc-melted. Note the big columnar grains.....	92
4.2 A typical experimental composition profile for aluminum obtained by microprobe analysis showing the microsegregation present in an arc-melted Nb-4.5Al specimen.....	93
4.3 a) BSE micrograph, and b) a typical experimental composition profile for Al obtained by microprobe analysis showing microsegregation through a dendrite in an arc-melted Nb-4.5Al specimen.....	94
4.4 BSE micrograph of the levitated and copper-chilled quenched Nb-7.1Al alloy after homogenization at 1400°C for 2 hours and furnace cooling. Presence of particles Nb <sub>3</sub> Al in the matrix ( $\beta$ phase) is observed.....	96

Figure	Page
4.5      BSE micrograph showing the two-phase structure obtained in a Nb-4.5Al alloy after annealing at 1400°C for 8.5 hrs.....	98
4.6      a) Secondary Electron micrograph, and b) EDX spectrum obtained from the matrix ( $\beta$ phase) of a Nb-4.5Al alloy after annealing at 1400°C for 8.5 hours.....	99
4.6      (Continued) c) EDX spectrum obtained from a precipitate formed inside a grain of a Nb-4.5Al alloy after annealing at 1400°C for 8.5 hours.....	100
4.7      a) Secondary Electron micrograph, and b) EDX spectrum obtained from a precipitate formed at the grain boundary of a Nb-4.5Al alloy after annealing at 1400°C for 8.5 hours.....	101
4.8      Auger analysis of a precipitate located inside a grain of Nb-4.5Al alloy annealed at 1400°C for 8.5 hours.....	102
4.9      Standard Auger spectrum obtained from pure alumina [73].....	104
4.10     Auger spectrum obtained from the matrix ( $\beta$ phase) of a Nb-4.5Al alloy after annealing at 1400 °C for 8.5 hours.....	105
4.11     Optical micrographs showing the microstructure of a Nb-4.5Al alloy after two different homogenization treatments: a) 1400 °C for 8.5 hours, b) 1400 °C for 6 hours.....	106
4.12     A low magnification BSE micrograph of a Nb-4.5Al alloy after being heat treated at 1400°C for 6 hours. Note how the amount of alumina precipitation lessen from top (sample surface) to bottom (sample middle section).....	107
4.13     BSE micrograph of a Nb-4.5Al sample as-homogenized condition. Alumina presence in the $\beta$ -phase matrix is very scarce.....	109
4.14     a) Secondary Electron micrograph, and b) Al composition profile of $\beta$ -phase matrix close to an alumina particle...	110
4.15     A low magnification BSE micrograph of a diffusion couple with zirconia markers: a) Before diffusion treatment, and b) after diffusion treatment at 1400°C for 4 hours.....	111
4.16     a) BSE micrograph of diffusion couple interface with Yttria markers before diffusion treatment, and b) the aluminum concentration profile across the boundary.....	113

Figure	Page
4.17 Backscattered electron micrographs showing the resultant microstructures of a Nb/Nb-4.5Al diffusion couple after diffusion treatment. a) Near interface. b) Away from interface.....	115
4.18 A typical experimental composition profile for aluminum obtained by microprobe analysis of a diffusion couple Nb/Nb-4.5Al after annealing at 1450 °C for 4.5 hours. Note the sudden drop in the Al composition profile in the Nb side of the couple.....	117
4.19 a) Secondary electron micrograph, and b) a typical experimental composition profile for Al obtained by microprobe analysis of a Nb/Nb-4.5Al diffusion couple after annealing at 1350 °C for 5.5 hours.....	119
4.20 Schematic representation of the modified cubic spline intervals employed for curve fitting.....	121
4.21 A typical composition profile for aluminum after incorrect spline cubic fitting. Note the discontinuities along the curve.....	123
4.22 Fitting of experimental composition profiles by the spline cubic method for the Nb/Nb-4.5Al couple heat treated at 1350 °C: a) Experimental curve,b) Fitted profile.....	124
4.23 Fitting of experimental composition profiles by the spline cubic method for the Nb/Nb-4.5Al couple heat treated at 1400 °C: a) Experimental curve, b) Fitted profile.....	126
4.24 Fitting of experimental composition profiles by the spline cubic method for the Nb/Nb-4.5Al couple heat treated at 1450 °C: a) Experimental curve, b) Fitted profile.....	128
4.25 Fitting of experimental composition profiles by the spline cubic method for the Nb/Nb-4.5Al couples heat treated at 1500 °C: a) Experimental curve, b) Fitted profile.....	130
4.26 Fitting of experimental composition profiles by the spline cubic method for Nb/Nb-4.5Al couple heat treated at 1550°C: a) Experimental curve, b) Fitted profile.....	132
4.27 a) Typical calculated interdiffusion flux profiles for binary diffusion couples Nb/Nb-4.5Al interdiffused at 1350 °C.....	135
4.28 b) Typical calculated interdiffusion flux profiles for binary diffusion couples Nb/Nb-4.5Al interdiffused at 1550 °C.....	136

Figure	Page
4.29 Typical calculated composition gradient and interdiffusion coefficient profiles illustrating false peaks due to a bad designation of parabolic regions during the fitting procedure for binary diffusion couples Nb/Nb-4.5Al interdiffused at 1550 °C. a) Derivative, b) Coefficient of Interdiffusion.....	138
4.30 a) Composition gradient, and b) interdiffusion coefficient profiles for Nb/Nb-4.5Al diffusion couple heat treated at 1350 °C.....	141
4.31 a) Composition gradient, and b) interdiffusion coefficient profiles for Nb/Nb-4.5Al diffusion couple heat treated at 1400 °C.....	143
4.32 a) Composition gradient, and b) interdiffusion coefficient profiles for Nb/Nb-4.5Al diffusion couple heat treated at 1450 °C.....	145
4.33 a) Composition gradient, and b) interdiffusion coefficient profiles for Nb/Nb-4.5Al diffusion couple heat treated at 1500 °C.....	147
4.34 a) Composition gradient, and b) interdiffusion coefficient profiles for Nb/Nb-4.5Al diffusion couple heat treated at 1550 °C.....	149
4.35 Dependency of the interdiffusion coefficient on the Al composition at several temperatures.....	152
4.36 The temperature dependency of the intrinsic diffusion coefficient of Al in Nb at the aluminum concentration of 3.0 at%.....	156
4.37 The temperature dependency of the intrinsic diffusion coefficient of Al in Nb at the aluminum concentration of 2.5 at%.....	157
4.38 The temperature dependency of the intrinsic diffusion coefficient of Al in Nb at the aluminum concentration of 2.0 at%.....	158
4.39 The temperature dependency of the intrinsic diffusion coefficient of Al in Nb at the aluminum concentration of 1.5 at%.....	159
4.40 The temperature dependency of the intrinsic diffusion coefficient of Al in Nb at the aluminum concentration of 1.0 at%.....	160
4.41 Comparison between this work and Ref. [6] for the temperature dependence of the diffusion coefficient of Al in Nb.....	163

Figure	Page
5.1 Schematic representation of the ternary diffusion couples employed in this research.....	171
5.2 Micrographs showing the duplex structure ( $\alpha+\beta$ ) of the as-received Ti: a) Optical micrograph, as-etched condition; b) BSE image.....	174
5.3 BSE micrograph of $\beta_1$ alloy (Nb-42.5Ti-15Al) after homogenization at 1400 °C for 6 hours.....	175
5.4 Optical micrograph of the bonded interface in diffusion couple #12 ( $\beta_1/Ti$ ) after bonding at 700 °C for 2 hours showing the duplex structure $\alpha+\beta$ of the Ti side of the couple.....	176
5.5 a) BSE micrograph of interface in diffusion couple #12 ( $\beta_1/Ti$ ) before diffusion treatment; b) the three composition profiles across the boundary.....	177
5.6 Optical micrograph of the Ti side next to the bonded interface in diffusion couple #12 ( $\beta_1/Ti$ ) after diffusion treatment at 1200 °C for 6 hours. Note the duplex ( $\alpha+\beta$ ) zone with the acicular morphology next to the interface.....	179
5.7 Optical micrograph showing precipitation of $\alpha$ phase at the interface and grain boundaries of the ternary $\beta_1$ (Nb-42.5Ti-15Al) side of the couple after bonding at 900 °C for 2 hours.....	180
5.8 BSE micrographs showing precipitation of $\alpha$ phase in the ternary side of the couples along the interface: a) diffusion couple #9 ( $\beta_1/\beta_3$ ); and b) diffusion couple #11 ( $\beta_2/\beta_3$ ).....	181
5.9 BSE micrograph of bonded interface in diffusion couple #10 ( $\beta_2/\beta_3$ ) after bonding at 900 °C for 2 hours showing the presence of second phase ( $\alpha$ )on both sides of the interface.....	182
5.10 BSE micrograph of the interface in diffusion couple #6 ( $\beta_1/Nb$ ) after diffusion treatment at 1400 °C for 6 hours. Microprobe analysis contamination over the precipitation-free structure is detailed.....	183

Figure	Page
5.11 BSE micrograph of the $\beta_2$ side away of the interface of diffusion couple #10 ( $\beta_2/\beta_3$ ) after diffusion treatment at 1200 °C for 6 hours, and subsequent treatment at 920 °C for 2 hours. Reprecipitation of the second phase is observed.....	185
5.12 Penetration curves of the 3 components in the couple #6 ( $\beta_1/\text{Nb}$ ), heat treated at 1400 °C for 6 hours.....	186
5.13 Penetration curves of the 3 components in the couple #7 ( $\beta_1/\beta_3$ ), heat treated at 1400 °C for 6 hours.....	187
5.14 Penetration curves of the 3 components in the couple #8 ( $\beta_1/\text{Nb}$ ) heat treated at 1200 °C for 6 hours.....	188
5.15 Penetration curves of the 3 components in the couple #9 ( $\beta_1/\beta_3$ ), heat treated at 1200 °C for 6 hours.....	189
5.16 Penetration curves of the 3 components in the couple #10 ( $\beta_2/\beta_3$ ), heat treated at 1200 °C for 6 hours.....	190
5.17 Penetration curves of the 3 components in the couple #11 ( $\beta_2/\beta_0$ ), heat treated at 1200 °C for 6 hours.....	191
5.18 Penetration curves of the 3 components in the couple #12 ( $\beta_1/\text{Ti}$ ), heat treated at 1200 °C for 6 hours.....	192
5.19 Penetration curves of Al in three different diffusion couples heat treated at 1200 °C for 6 hours.....	194
5.20 Penetration curves of Nb in three different diffusion couples heat treated at 1200 °C for 6 hours.....	195
5.21 Penetration curves of Ti in three different diffusion couples heat treated at 1200 °C for 6 hours.....	196
5.22 Composition profiles of Al in diffusion couples #9 and #10 after heat treatment at 1200 °C for 6 hours.....	197
5.23 Composition profiles of Nb in diffusion couples #9 and #10 after heat treatment at 1200 °C for 6 hours.....	198
5.24 Composition profiles of Ti in diffusion couples #9 and #10 after heat treatment at 1200 °C for 6 hours.....	199
5.25 Composition profiles of the 3 components at constant Al concentration (couple #9 $\beta_1/\beta_3$ ) after heat treatment at 1200 °C for 6 hours.....	200
5.26 Comparison of penetration depth of Al in couples involving alloy $\beta_2$ (#10 ( $\beta_3/\beta_2$ ) and #11 ( $\beta_0/\beta_2$ )).....	201
5.27 Comparison of penetration depth of Nb in couples involving alloy $\beta_2$ (#10 ( $\beta_3/\beta_2$ ) and #11 ( $\beta_0/\beta_2$ )).....	202

Figure	Page
5.28 Comparison of penetration depth of Ti in couples involving alloy $\beta_2$ (#10 ( $\beta_3/\beta_2$ ) and #11 ( $\beta_0/\beta_2$ )).....	203
5.29 Critical point observed in the Al composition profile after diffusion treatment of couple #11( $\beta_0/\beta_2$ ) at 1200 °C for 6 hours.....	205
5.30 Critical point observed in the Nb composition profile after diffusion treatment of couples #7 ( $\beta_0/\beta_2$ ), #9 ( $\beta_3/\beta_1$ ) and #10 ( $\beta_3/\beta_2$ ) at 1200 °C for 6 hours.....	206
5.31 Critical point observed in the Ti composition profile after diffusion treatment of couple #9 $\beta_3/\beta_1$ at 1200 °C for 6 hours.....	207
5.32 Composition profile for Al after interdiffusion treatment at 1200 °C (#8 ) and 1400 °C (#6) for 6 hours.....	209
5.33 Composition profile for Nb after interdiffusion treatment at 1200 °C (#8) and 1400 °C (#6) for 6 hours.....	210
5.34 Composition profile for Ti after interdiffusion treatment at 1200 °C (#8) and 1400 °C (#6) for 6 hours.....	211
5.35 Composition profile for Al after interdiffusion treatment at 1200 °C (#7) and 1400 °C (#9) for 6 hours.....	212
5.36 Composition profile for Ti after interdiffusion treatment at 1200 °C (#7 ) and 1400 °C (#9) for 6 hours.....	213
5.37 Composition profile for Ti after interdiffusion treatment at 1200 °C (#7) and 1400 °C (#9) for 6 hours.....	214
5.38 Composition path for diffusion couple #8 ( $\beta_1/Nb$ ), and schematic representation of the crossover displacement. Δ Middle point composition ○ Matano plane composition.....	219
5.39 Composition path for diffusion couple #6 ( $\beta_1/Nb$ ). and schematic representation of the crossover displacement. Δ Middle point composition. ○ Matano plane composition.....	220
5.40 Composition path for diffusion couple #11( $\beta_0/\beta_2$ ).and schematic representation of the crossover displacement. Δ Middle point composition ○ Matano plane composition.....	222

**Abstract of Thesis Presented to the Graduate School of  
the University of Florida in Partial Fulfillment of  
the Requirements for the Degree of Master of Science.**

**EVALUATION OF THE DIFFUSIVITY OF ALUMINUM IN  
NIOBIUM BASED ALLOYS**  
BY  
**J. G. LUIS RUIZ APARICIO**

DECEMBER 1990

Chairperson: Dr. Fereshteh Ebrahimi

Major Department: Materials Science and Engineering

Niobium alloys with improved resistance to oxidation are needed for use as structural alloys. The feasibility of forming protective alumina scales in Nb-Al-X alloys by the selective oxidation of aluminum has been demonstrated and also has been shown that a low aluminum diffusivity is the major factor limiting the selective oxidation of aluminum. Additions of certain elements such as titanium are thought to have a beneficial action on accelerating this diffusivity but information on the effect of alloying additions is limited.

In this thesis, diffusion studies in the binary Nb-Al system by the Matano-Boltzmann method, and diffusion analyses in the ternary Nb-Al-Ti system through concepts such as Kirkendall shift, crossover displacements, penetration tendencies and composition paths, were conducted to evaluate the diffusivity of Al and the effect of Ti on Nb-based alloys.

Nb-Al, Nb-Ti, Nb-Al-Ti (b.c.c.) solid solutions were prepared by arc-melting and were homogenized in a high vacuum furnace before the fabrication of diffusion couples. Bonding of the diffusion couples

was obtained by hot pressing in a temperature range of 700° to 1000 °C for two hours. A fine dispersion of yttria chopped fibers was used as markers. The diffusion treatment temperatures were varied from 1350° to 1550 °C and 1200 °C to 1400 °C for the binary and ternary studies respectively. Microprobe analysis was employed for the evaluation of composition profiles in all the diffusion couples.

The interdiffusion coefficient for the  $\beta$  solid solution of Nb-Al system varied linearly with Al concentration in the range of 1-3 at% and it followed a linear Arrhenius behavior as a function of temperature in the range of 1350 °C-1550°C. The average activation energy for diffusivity of Al in Nb was calculated to be 78.4 Kcal/mole with a frequency factor of  $4.5 \times 10^{-2}$  cm<sup>2</sup>/sec. These values are smaller than those reported in the literature for a higher temperature range. This discrepancy is attributed to the differences in the evaluation method and the temperature range. The influence of divacancy mechanism, which is known to operate at higher temperatures in Nb, may account for the higher diffusion rate and activation energy.

The composition path and penetration tendencies in the Nb-Ti-Al system suggest that Ti is the fastest element in the  $\beta$  solid solution. Qualitatively the penetration tendencies correlate with the melting point of the alloys. The results of Kirkendall shift measurement were found to be in agreement with the calculated crossover displacement. The results obtained in this study suggest that the addition of Ti to the binary alloy increases the general diffusivity of the system.

## CHAPTER 1 INTRODUCTION

During the last decade, the necessity of both higher performance requirements and new applications for spacecrafts has renewed the interest in the development of advanced aerospace materials. The aerospace industry has set the reduction of aircraft weight, extension of flying ranges, increment of payloads and shortening of take-off requirements among its permanent objectives. The accomplishment of these goals demands the development of materials with improved physical and mechanical properties such as strength to density ratio, fatigue resistance, high temperature rupture strength, creep resistance, high temperature corrosion resistance and fracture toughness. Currently, it is thought that aircraft engines work at half of their potential horsepower due to limitations such as strength and melting point of the existing high-temperature Ni-based superalloys, which are the major structural material used in military aircraft turbine engines. State-of-the-art superalloys are limited in temperature capability to 1100 °C. However, there is an immediate need for a metallic material capable of withstanding temperatures up to 1400 °C.

Because of their special properties at high temperature, refractory alloys were considered in the development of aerospace materials in the early '60's, when aircraft and aerospace nuclear

propulsion were developed. Among these refractory metals, the lower density niobium alloys were investigated for turbine applications. Their long-term, high-temperature strength, ductility, and creep resistance are well retained at high temperatures, comparable to those obtained in nickel-base superalloys, but their poor oxidation resistance in environments rich in atmospheric gas species [1, 2] and the arrival of superalloys properly cooled halted their development [3]. At present, niobium alloys are used in non-critical sections of aircraft engines, like exhaust nozzle components, where their high melting temperature are needed.

A recent approach to solving the problem of poor oxidation of many high temperature structural materials is the addition of aluminum as an alloying element. Alumina  $\text{Al}_2\text{O}_3$  is a stable oxide that usually shows a good adherence to the metallic alloys. There are two main problems associated with the oxidation behavior of the aluminum containing high temperatures alloys. In the case of alloys such as Fe-Cr-Al, the fast diffusion of cations through the alumina scale leads to the occurrence of the oxidation process at gas/oxide interface and consequently voids are formed at oxide/metal interface, which results in oxide spallation and poor adherence of the oxide to the alloy. In the case of Nb alloys it has been suggested [4] that the slow diffusivity of aluminum prevents the continuous formation of alumina and transition oxides are rapidly formed and hence undesirable high oxidation rates are achieved. Oxidation studies on Nb-Al alloys [5] have indicated that a minimum aluminum content of 50 at% is required to obtain a continuous alumina scale.

The addition of alloying elements such as Ti, Mo and V has been shown to reduce the oxidation rate of Nb alloys.

Although the poor oxidation resistance of the Al containing Nb alloys has been related to the low diffusivity of Al, there have been very limited studies [6] in which the diffusivity of Al in Nb has been measured indirectly. The purpose of this research was to evaluate the diffusivity of aluminum in binary Nb-Al and ternary Nb-Al-Ti solid solution alloys. The experimental approach used in this study is based on the diffusion couple technique [7] with post-diffusion treatment evaluation of composition profiles by electron microprobe analysis (EPMA). Optical and scanning electron microscopy (SEM) methods were employed for the evaluation of the microstructure. The alloys were prepared by arc-melting of high purity metals. The diffusivity measurements were conducted in the temperature range of 1350 °C to 1550 °C for the binary case and 1200 °C to 1400 °C for the ternary one.

The first part of this thesis approaches briefly the theory of diffusion from both a phenomenological and an atomistic point of view. In addition, a mathematical analysis of the theory is presented as it provides the basis for the Fortran-77 source code [8] used for the evaluation of the coefficient of diffusion of Al in the binary system. The basis for the experimental techniques employed through this work, as well as a review of the previous work done in the binary Nb-Al system and the ternary Nb-Al-Ti system are also presented in this chapter. Chapter 3 simply describes the materials used and the experimental procedures followed throughout this research. The results for the binary Nb-Al system and for the

ternary Nb-Al-Ti system are presented and discussed in Chapters 4 and 5, respectively. Results in Chapter 4 include a discussion about the experimental difficulties found during the preparation of the binary alloy Nb-Al used in the binary couples. The discussion of the ternary diffusion results in Chapter 5 is based on a phenomenological approach of basic concepts such as composition paths, Kirkendall displacements and penetration tendencies. A summary of results for binary and ternary diffusion is given at the end of the respective chapters, with the final conclusions of this research presented in Chapter 6.

## CHAPTER 2 LITERATURE REVIEW

This chapter is divided into three sections. First the literature concerning the Nb-Ti-Al system is reviewed. The subjects prevalent to this section include phase stability, diffusivity and oxidation in ternary and the constitutive binary systems. The second part of this review concentrates on the mathematical formalism and mechanisms of diffusion in binary and ternary systems consisting of single phase crystalline materials.

### 2.1 Nb-Ti-Al system

#### 2.1.1 Phase diagram

This section is devoted to establish the limits of both temperature and composition for the b.c.c.  $\beta$  phase in the Nb-Al-Ti ternary phase diagram.

The binary diagrams composing this ternary system are presented in Figures 2.1-2.3. The Nb-Ti system, Figure 2.1, features an isomorphous-type, complete solubility of both components in a b.c.c. phase at temperatures above 882 °C at the Ti side [9]. This phase field extends to room temperature as Nb content increases.

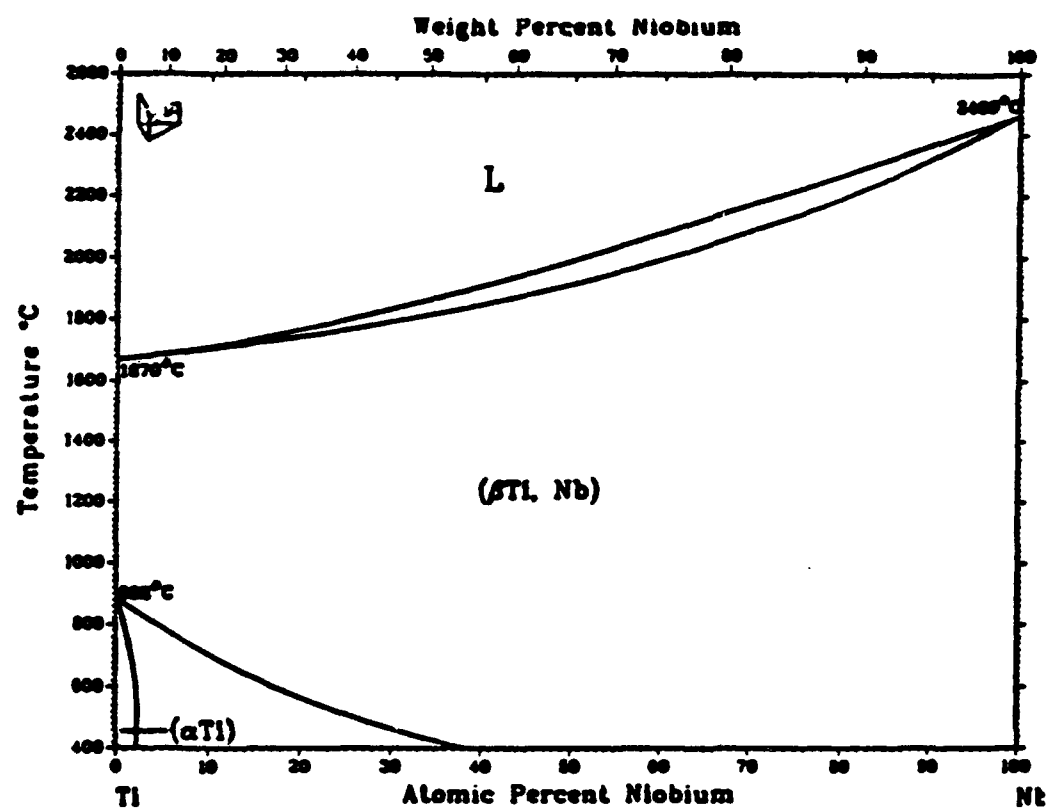


Figure 2.1 The Ti-Nb phase diagram [9].

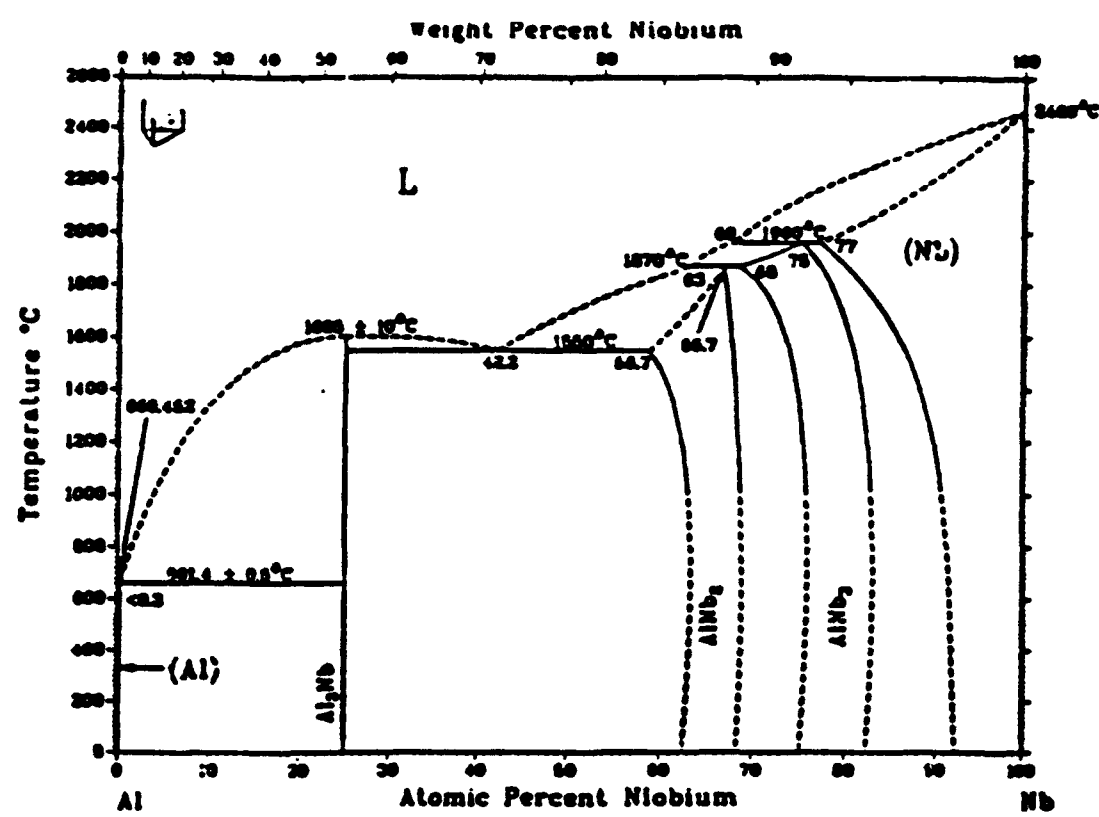


Figure 2.2 The Al-Nb phase diagram [10].

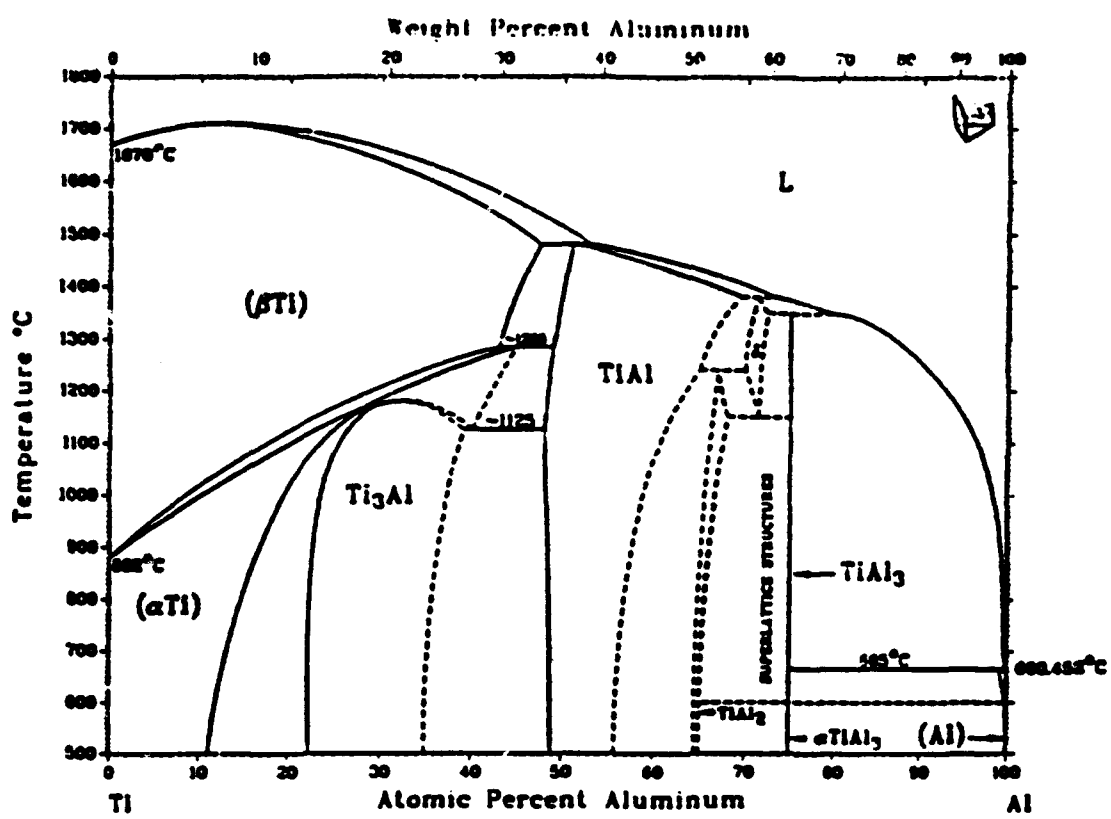


Figure 2.3 The Ti-Al phase diagram [11].

The other phase present is the h.c.p.  $\alpha$ -Ti phase, which is stable at high Ti contents and temperatures below 882 °C.

Nb-Al and Ti-Al systems exhibit intermetallic compound formation, namely:  $\alpha_2$ -Ti<sub>3</sub>Al (DO<sub>19</sub>),  $\gamma$ -TiAl (Ll<sub>0</sub>), and  $\eta$ -TiAl<sub>3</sub> (DO<sub>22</sub>) in the Ti-Al system, and  $\delta$ -Nb<sub>3</sub>Al (A15),  $\sigma$ -Nb<sub>2</sub>Al (D<sub>8B</sub>), and  $\eta$ -NbAl<sub>3</sub> (DO<sub>22</sub>) in the Nb-Al system, in addition to the terminal solid solutions. The solubility of Al in Nb at room temperature is not very well established. The phase diagram [10] suggests a solubility limit of 7.5 at%. Maximum solubility of Al in b.c.c. Nb is 23 at% which is reached at 1960 °C. The  $\beta$  phase in the Ti-Al [11] phase diagram is stable only at elevated temperatures. The solubility of Al in  $\beta$ -Ti increases with temperature, reaching a 48.5 at% maximum solubility at 1475 °C.

The ternary Nb-Al-Ti system has been the subject of several investigations during the last decade as a result of the recent activity on development of alloys for high temperature applications. It is a rather complicated system featuring several transition equilibria. Perepezko *et. al.* [12] and Kaltenbach *et. al.* [13] recently have performed a systematic evaluation of this system including mappings of liquidus projections and determination of isothermal sections of the system at 1200 °C. Both studies show excellent agreement with each other and studies made by Benderzky *et al.* [14] and Jewet *et. al.* [15]. Examples of liquidus projections and the isothermal section at 1200 °C are given in Figures 2.4 and 2.5. The liquidus surface features several four-phase equilibria (I-IV) with the subscripts 1, 2,... indicating the temperature sequence (1 higher than 2). In accordance with [12], the binary invariant reactions are represented

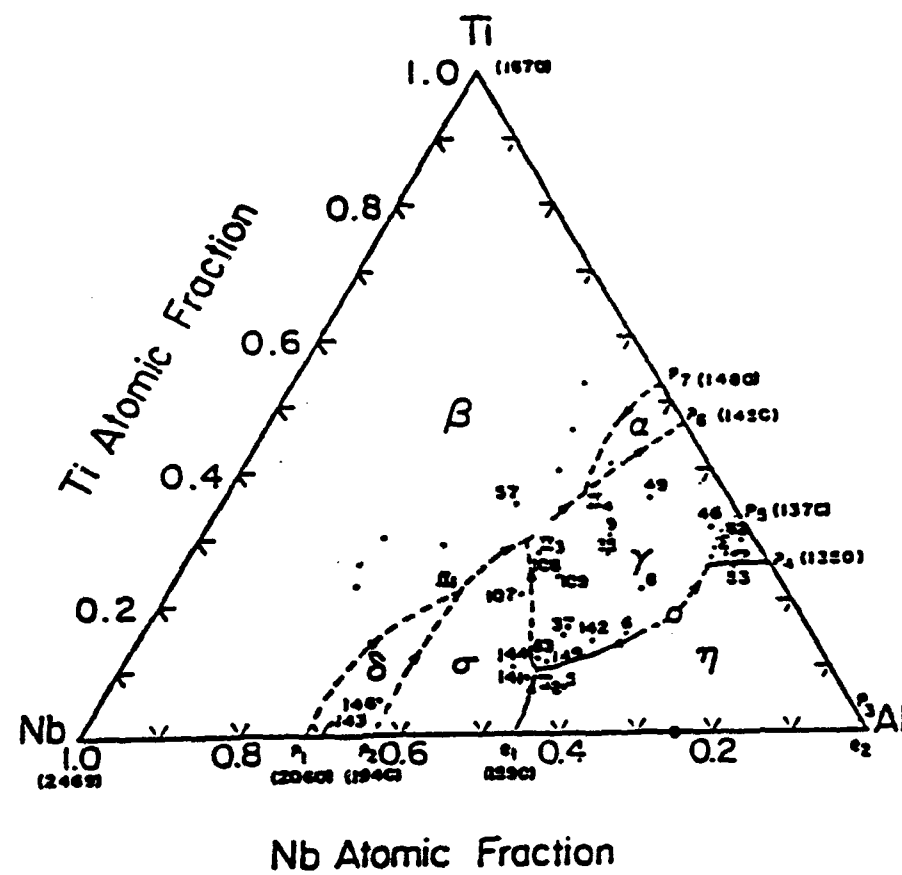
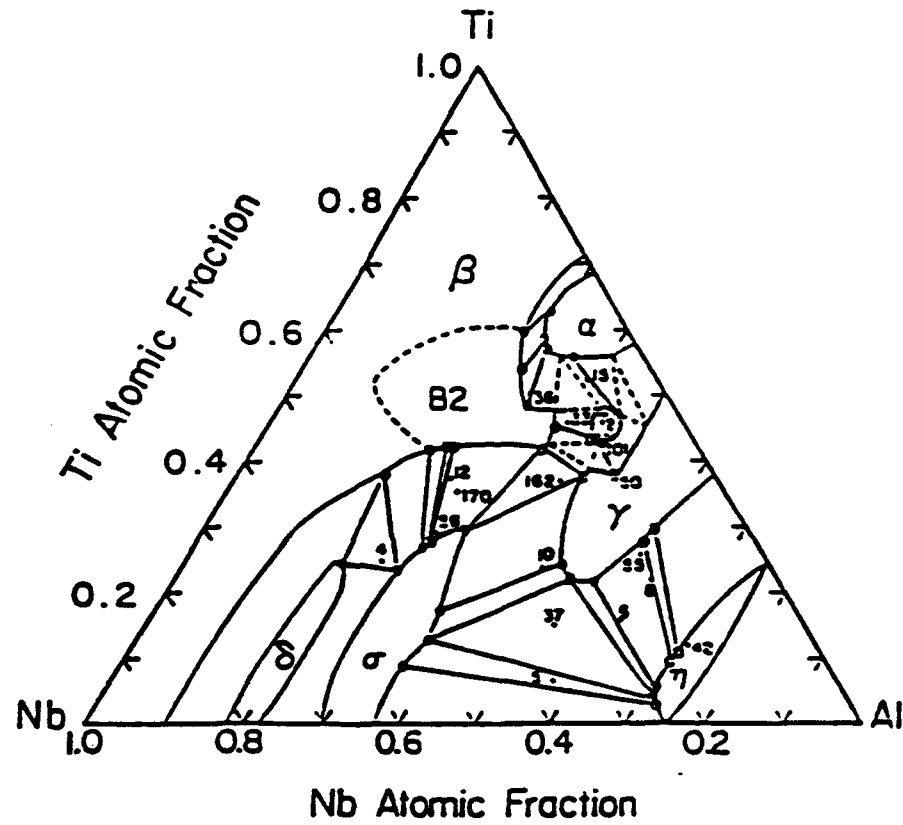


Figure 2.4 The Nb-Ti-Al Liquidus Projection [12].



**Figure 2.5** Isothermal section at 1200 °C in the Nb-Ti-Al ternary system [12].

as  $\pi$  (peritectic) and  $e_i$  (eutectic). There is only one saddle point in the system which is indicated by an open circle in Figure 2.4. The arrows inscribed upon the lines show the directions of the slopes for the univariant equilibria (liquidus valleys) toward lower temperatures.

It is observed that the liquidus valleys decrease in temperature from the high temperature peritectic points in the Nb-Al side swinging clockwise towards the Al corner of the triangle. The  $\beta$ -phase surface exhibits the highest melting points and it covers a big range of the total area of the liquidus projection surface. The large solubility of Al in  $\beta$  phase decreases with temperature. This can be observed by contrasting the extension of the  $\beta$ -phase field of the liquidus projections with their respective isotherm at 1200 °C. In accordance with these projections, the solubility limit for Al in the b.c.c. solid solution depends on both the temperature and the Nb (or Ti) content. As the temperature is raised and the Ti content increased, Al becomes more soluble.

### 2.1.2 Diffusivity

In general, 'normal' diffusion in metals is characterized by the following properties [16]:

- 1)  $D_0$  and  $Q$  are temperature independent over a wide range of temperatures,
- 2)  $D_0$  lies in a range of 0.05 to 5 cm<sup>2</sup>/sec,
- 3)  $Q$  (cal/mole) is approximately equal to 34·T<sub>m</sub> (melting temperature, K),

4) The diffusion value for substitutional impurities is within an order of magnitude of the self-diffusion rate of the host atoms.

In accordance with diffusivity investigations, there are a number of b.c.c. metals which show anomalous diffusion behaviors. They do not present "normal" diffusion. For these metals the Arrhenius plot presents a curvature that is more pronounced than that seen in f.c.c. metals, for which is a result of divacancies contributions [17]. As mentioned earlier, the Ti-Nb system exhibits a complete solubility in b.c.c. phase at elevated temperatures. Ti, among others, is one of these b.c.c. metals with anomalous behavior [18]. Murdock *et. al.* [18] found that  $\ln D$  vs  $1/T$  plots for diffusion of  $Ti^{44}$  in Ti were fitted best by a line of continuous curvature (Figure 2.6), which indicated an increase in  $Q$  and  $D_0$  with the temperature. They proposed the model that Kidson [19] used for the diffusivity of Zr (b.c.c.) to explain their results. In accordance with this model, there are two competing volume diffusion mechanisms operating in the two temperature regions: intrinsic and extrinsic. He [19] attributed the low-temperature 'extrinsic' region to the presence of a temperature-independent concentration of vacancies due to the presence of impurities, like oxygen atoms, which cause the concentration of this type of vacancies to be much greater than the concentration of 'intrinsic' or thermal vacancies at low temperature. The total curve can be obtained by the sum of 2 exponential terms representing each of these contribution. The resulting equation obtained by Murdock *et. al.* [20] for the Ti case is:

$$D_{Ti\ 44} = 3.58 \times 10^{-4} \exp(-31,200/RT) + 1.09 \exp(-60,000/RT) \text{ cm}^2/\text{sec} \quad \dots \quad (2.1)$$

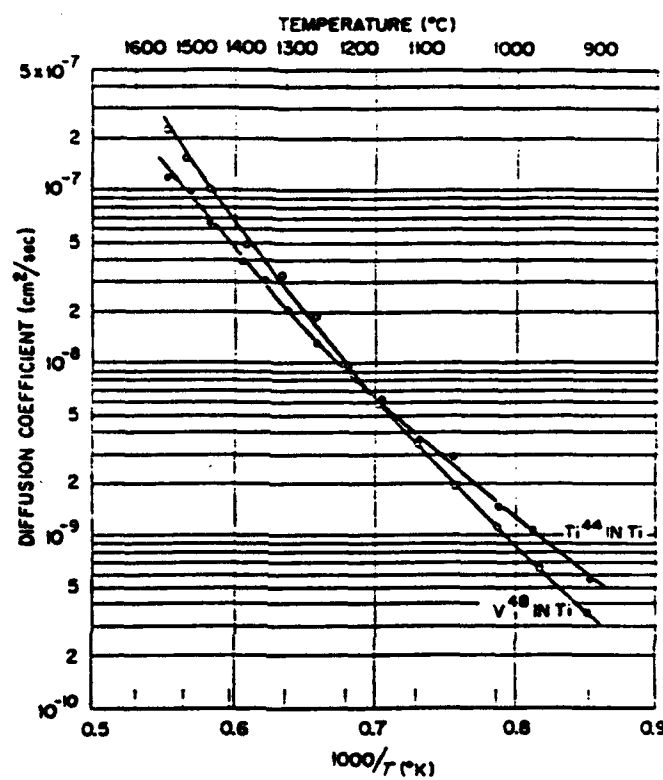


Figure 2.6

Temperature dependence of the diffusion of  $\text{Ti}^{44}$  and  $\text{V}^{48}$  in titanium [18].

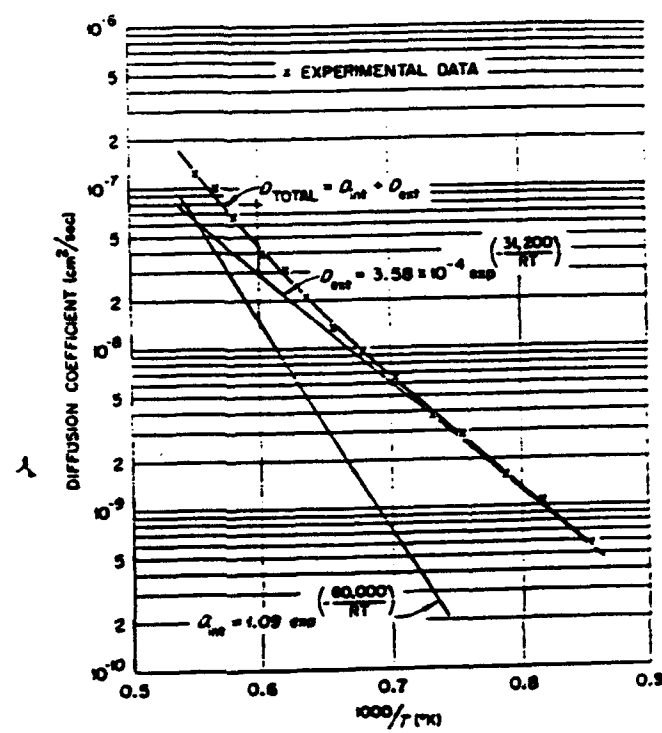


Figure 2.7

Computer fit of the experimental data for the diffusion of  $\text{Ti}^{44}$  in titanium to the proposed by Kidson [19]. (From [18]).

Table 2.1 Self-Diffusion coefficients of Ti as measured by trace diffusivity [21] and calculated by [20]

Jump Model	$T = 1460^{\circ}\text{C}$ $D \times 10^{12} (\text{m}^2/\text{sec})$	$T = 1530^{\circ}\text{C}$ $D \times 10^{12} (\text{m}^2/\text{sec})$
Tetrahedral Sites	1.9	3.1
Octahedral Sites	2.5	3.9
NNN Position	9.1	10.8
NN Position	5.4	8.9
Tracer Diffusivities	7.9	12.9

the Arrhenius plot which they assumed was caused by a divacancy effect at high temperatures and was fitted by the expression:

$$D = (3.7 \pm 0.3) \exp(-4.54 \text{ eV}/kT) + \\ (8 \pm 3) \times 10^{-3} \exp(-3.62 \text{ eV}/kT) \text{ cm}^2/\text{s} \quad \dots \dots \dots \quad (2.2)$$

Pontau and Lazarous [24] experimentally evaluated the diffusivity of Ti and Nb in b.c.c. Ti-Nb alloys at different concentrations, which were chosen to avoid the  $\alpha/\beta$  transition and to obtain the metastable  $\omega$  phase [25]. This  $\omega$  phase as discussed earlier is thought to enhance diffusion in other b.c.c. materials like Ti and Zr [20, 26]. They [24] determined simultaneously the diffusion coefficients for Ti and Nb radioactive tracers over the temperature range of 950°-1511 °C using lathe-sectioning techniques. Their results are presented in Figures 2.8 and 2.9 and Table 2.2. They found no evidence of anomalous behavior in the diffusivity behavior, except for low values of  $D_0$  and  $Q$  compared to those reported by [27]. Their Arrhenius plots were moderately curved, but due to lack of enough points an accurate two exponential fit to their data could not be performed. They did not find any evidence that supported the enhancement of diffusion at low temperatures by the presence of  $\omega$ -phase nor via dislocations, and concluded that an operating normal relaxed vacancy-divacancy mechanism was consistent with their results.

Newmann and Tolle [28] recently analyzed the published data in self-diffusion of b.c.c. metals by assuming a two-defect model and various one-defect models. They found that Nb self-diffusion data could be fitted accurately by the 2-exponential model proposed by Eizinger *et. al.* [23]. They pointed out that oxygen contents up to 800 p.p.m. have no influence on the diffusion coefficient. In accordance

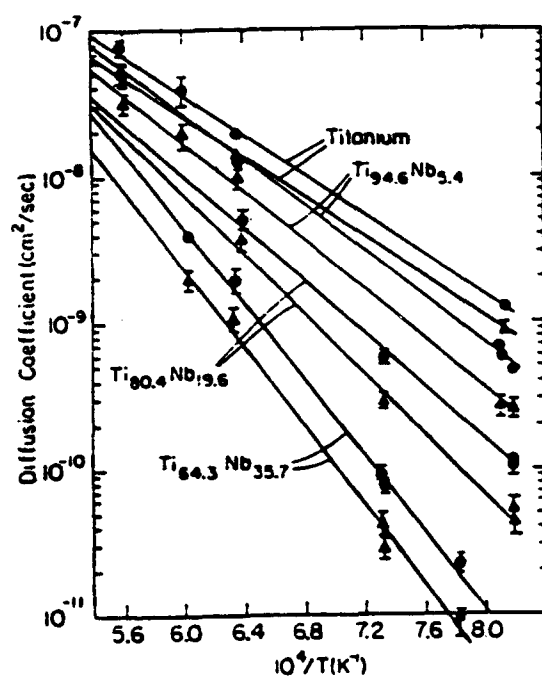


Figure 2.8 Measured diffusion coefficients of Ti (circles) and Nb (triangles) in different Ti-Nb alloys as a function of temperature [24].

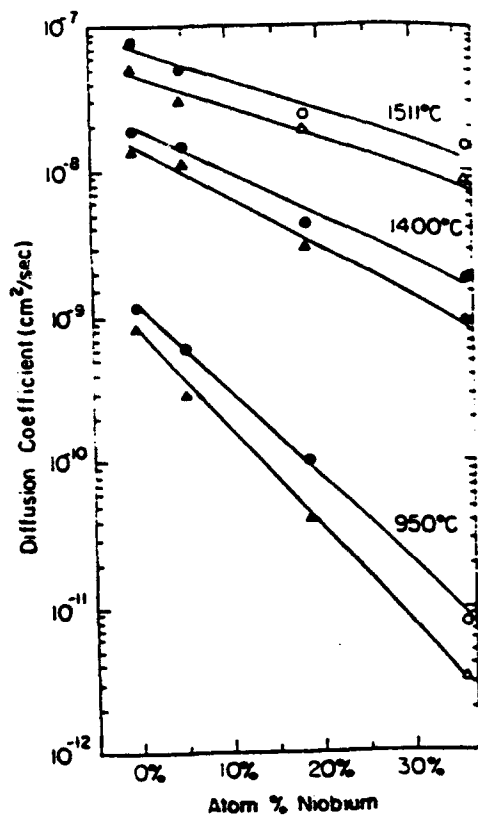


Figure 2.9

Diffusion coefficients of Ti (circles) and Nb (triangles) as a function of composition for 3 different temperatures [24].

Table 2.2 Frequency factors  $D_0$  and activation energies Q for Ti and Nb diffusion in Ti and Ti-Nb alloys (From Ref. [24])

Composition	Tracer	$D_0$ (cm <sup>2</sup> /sec)	Q (kcal/mole)
Ti	Ti	$(4.54 \pm 0.77) \times 10^{-4}$	$31.30 \pm 0.43$
	Nb	$(2.91 \pm 0.42) \times 10^{-4}$	$31.03 \pm 0.43$
$Ti_{31.6}Nb_{31.4}$	Ti	$(1.27 \pm 0.23) \times 10^{-3}$	$35.61 \pm 0.58$
	Nb	$(1.79 \pm 0.44) \times 10^{-3}$	$38.22 \pm 0.90$
$Ti_{16.4}Nb_{19.6}$	Ti	$(3.15 \pm 1.38) \times 10^{-3}$	$41.96 \pm 1.24$
	Nb	$(1.18 \pm 0.14) \times 10^{-2}$	$47.33 \pm 1.61$
$Ti_{64.3}Nb_{33.7}$	Ti	$(2.51 \pm 1.03) \times 10^{-1}$	$59.02 \pm 1.03$
	Nb	$(2.98 \pm 1.17) \times 10^{-1}$	$61.73 \pm 1.45$

with their analysis, b.c.c. metals can be divided in three groups: Group IVb (Ti, Zr, Hf) where the metals show an abnormally high diffusivity at low temperatures, Group V and VI (refractory metals) which show a more or less normal behavior, and Group I (alkaline metals) which fall in between the previous two. This classification is better observed in the normalized plot in Figure 2.10. They concluded that one-defect mechanism is improbable for both refractory and alkaline b.c.c. metals, but they could not discuss either the nature of the diffusion mechanisms that operate at high temperature.

Hu An *et. al.* [29] measured the interdiffusivity of the Nb-Ti system at low temperatures ( $300^{\circ}$ - $350^{\circ}$ C) using X-ray diffraction techniques in compositionally modulated structures with an initial content of 50 at% Ti and 50 at% Nb. They determined a value lower than  $10^{-20}$  cm<sup>2</sup>/sec for the interdiffusion of the system, which is in agreement with the diffusivity results obtained at high temperature by Ugaste and Zaykin [30] using tracer technique. Ugaste and Zaykin [30] also investigated the concentration dependence of the interdiffusion coefficient in this system. Figure 2.11 shows a comparison of their results with those from other authors which prove to be completely inconsistent. Figure 2.12 also gives the concentration dependence of the activation energy Q and the pre-exponential factor D<sub>0</sub>. Despite the inconsistency in concentration dependence of D values, the Q values seem to be consistent with the values given in Table 2.2. In general, D increases strongly with the Ti concentration, which is consistent with the concentration dependence of the solidus temperature. Consistently, the activation energy

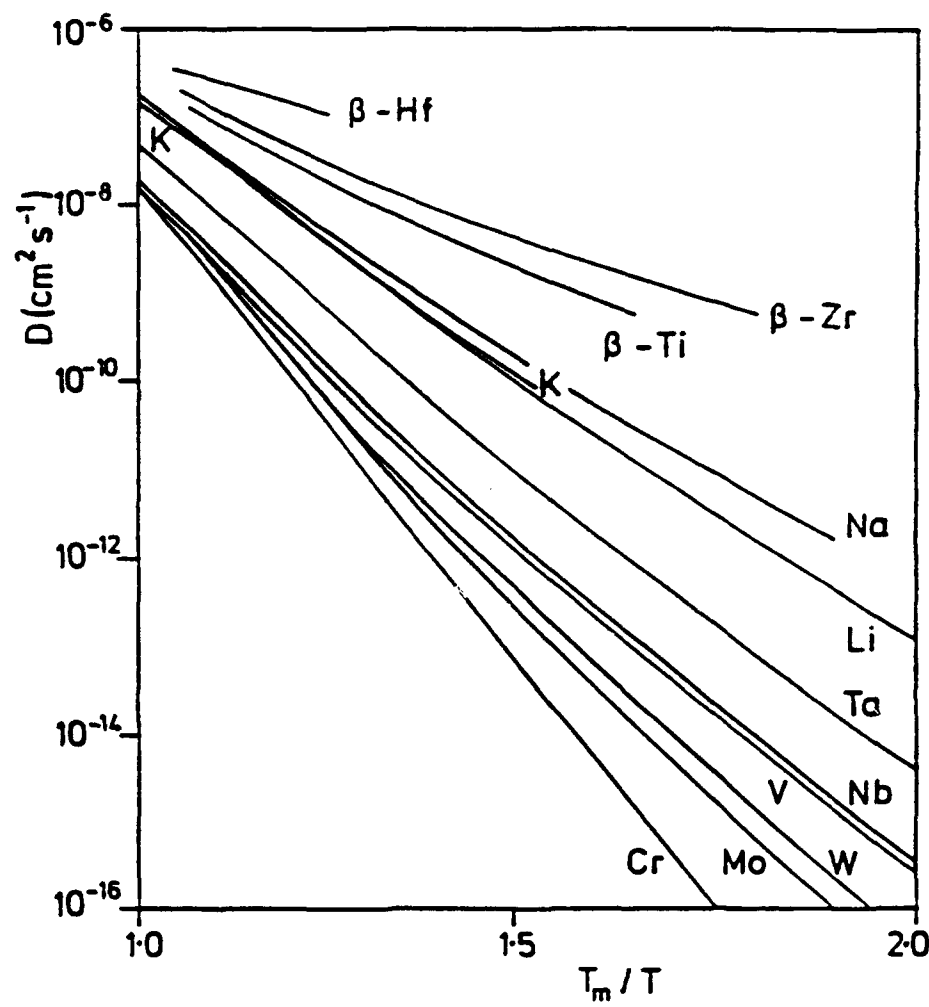


Figure 2.10      Self-diffusion in b.c.c. metals. Plot of the self-diffusion coefficient against the reduced reciprocal temperature [28].

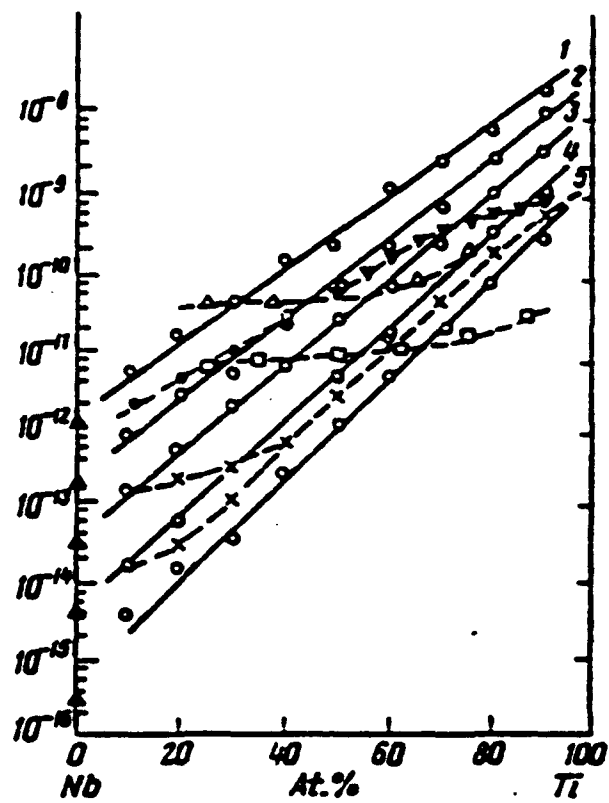


Figure 2.11 Concentration dependence of coefficient of mutual diffusion in Ti-Nb system:  
1-1400°, 2- 1300°, 3- 1200°, 4- 1100°,  
5- 1000 °C. From [30].

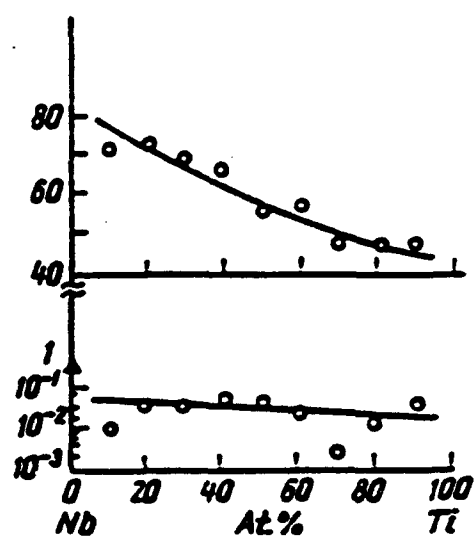


Figure 2.12 Concentration dependence of activation energy and pre-exponential factor of mutual diffusion in the Ti-Nb system [30].

increases with the Nb content.

The only information available on the diffusivity of Al in Nb is the back-calculated diffusivity from the evaporation rates of aluminum from dilute Nb-Al alloys conducted by Nikolaev and Bodrov [6]. In accordance with their experiments, the aluminum diffusivity follows an Arrhenius behavior that can be expressed as:

$$D_{Al} = 450 +/- 10 \exp[-(102730 +/- 7000)/RT] \text{ cm}^2/\text{sec} \dots\dots (2.3)$$

They evaluated the thermodynamic and kinetic characteristics of the evaporation of aluminum present in niobium as an impurity ( $10^{-2}$ - $10^{-3}$  at%) by atomic absorption spectroscopy in an argon atmosphere. Their proposed method to measure the diffusivity of impurities in the solid phase is based on measuring the rate of decay of the atomic absorption by plotting the kinetic curves for the evaporation process. They found that at a given temperature the concentration of aluminum vapor over the sample stays close to the equilibrium value for a short period of time (30 seconds), followed by a steep fall of the vapor pressure curve due to a depletion of aluminum from the surface of the sample. After measuring the absorption of aluminum vapors from pure aluminum and alloys containing a known amount of it, they calculated the Al activity coefficient and its temperature dependence. From these experiments they were able to determine the kinetics of the evaporation process, that is, the motion of the atoms in the solid phase. During the first part of the process the transport of the aluminum atoms from the surface of the sample is achieved by evaporation. The subsequent decay of the absorption curve denoted a rate limitation on the availability of aluminum atoms caused by the diffusion of the aluminum in the niobium. They

implied that the diffusion step of the evaporation process obeyed the expression [31]:

$$N^s(t)/N_0^s = \exp[-y^2] \operatorname{erfc}(y) \quad (2.4)$$

where  $N^s(t)$  and  $N_0^s$  are the aluminum concentrations at the surface of the sample at the time of the measurement and at the beginning of the experiment respectively, and

$$y^2 = \beta^2 t D^s \quad (2.5)$$

where  $D^s$  is the diffusion coefficient to be calculated and  $\beta$  is an experimental constant. In accordance with their research this method offers speed of operation, continuous observation of the diffusion process, and application to the solid state diffusion of alloy components at the impurity concentration level ( $<10^{-2}$  at.%). However, the method is not direct and is based on many assumptions.

Raissanen *et. al.* [32] investigated the diffusivity of Al in polycrystalline ion-implanted  $\alpha$ -Ti in the temperature range of 600 °C to 950 °C using ion-beam techniques. They found the following expression for the coefficient of diffusion:

$$D (\text{cm}^2/\text{sec}) = 7.4 \times 10^{-7} \exp[-1.62 (\text{eV})/kT] \quad \dots \dots \dots (2.6)$$

Pokoev *et. al.* [33] also investigated the Al diffusivity in  $\alpha$ -Ti using x-ray diffraction techniques at 700-850 °C in a vapor deposited Al layer on Ti foil. They found that the temperature dependence of the diffusion coefficient is given by the following equation:

$$D (\text{cm}^2/\text{sec}) = 9.7 \times 10^{-5} \exp[27,500 (\text{cal}/\text{mole})/RT] \quad (2.7)$$

Chaplanov *et. al.* [34] conducted annealings on Ti-Al films at 200-500 °C temperature range. Below 300 °C interdiffusion occurred with subsequent formation of Ti-Al solid solutions. However, above this

temperature intermetallic phases such as  $TiAl_3$ ,  $TiAl$  were formed. The formation of a  $TiAl_3$  has been reported elsewhere [35-37]. Zhao *et. al.* [35] studied the reaction kinetics of Ti films on Al substrate at 450-550 °C, and found that the formation of a  $TiAl_3$  layer always occurs at the Ti/Al interface. Rao and Houska [36] studied the inverse case, i. e. Al film-Ti substrate, and found the same  $TiAl_3$  layer formed. However, when the film was initially heated up to 900 °C, there was a release of Al into  $\alpha$ -Ti in the first stages, but longer annealing times eventually led to the decomposition of the  $TiAl_3$  layer with a substantial release of Al into the substrate. According with their results, the variation of the coefficient of diffusion with composition was less than one order of magnitude when the composition changed from 0 to 20 at% (Figure 2.13) [38, 39]. Because of the limited solubility, they could not calculate accurately the coefficient of diffusion for the  $TiAl_3$  phase, but it was estimated that it tended to be one order of magnitude smaller than the diffusion in the  $\alpha$ -Ti (Al) phase at 900 °C.

Liu and Welch [40] made a survey of the diffusion data for aluminum in both  $\alpha$ - and  $\beta$ -Ti. Tables 2.3 and 2.4 show the pre-exponential and activation energy of aluminum diffusion in  $\alpha$ - and  $\beta$ -Ti, respectively, and Figures 2.14 and 2.15 present the Arrhenius plots coefficient of diffusion. The Al diffusion data in  $\alpha$ -Ti show poor agreement as they are scattered. As to the diffusivity data for  $\beta$ -Ti phase, again the differences in the reported values for Al are considerable, and no clear explanation is offered about it.

The diffusion of interstitial elements in Nb-Ti and Ti-Al alloys has been extensively studied. Vasileva *et. al.* [41], for example,

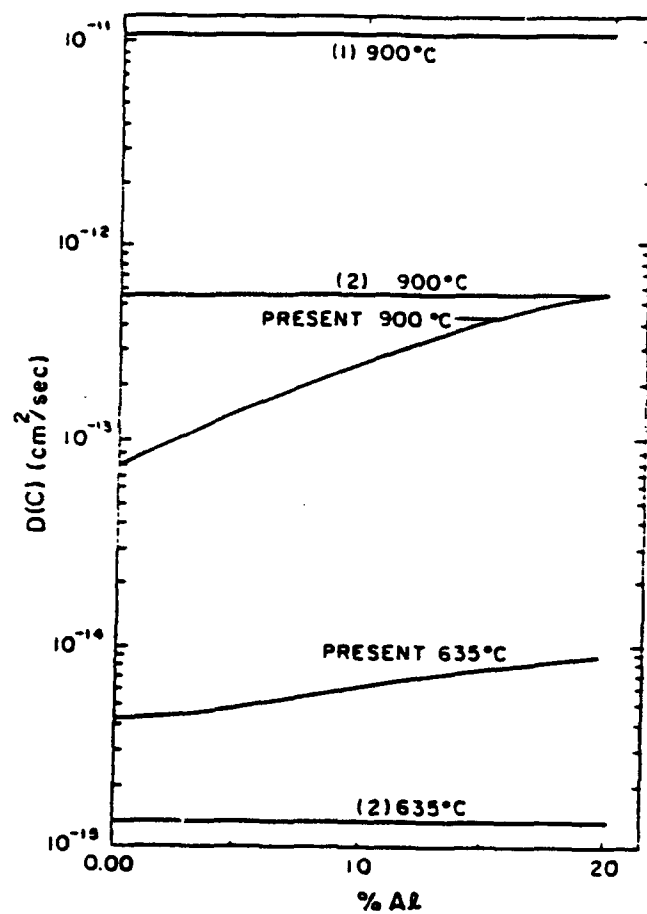


Figure 2.13 Interdiffusion coefficients vs at% for the diffusion of Al in  $\alpha$ -Ti. The present data obtained at  $900^\circ$  and  $635^\circ\text{C}$  are compared with results published by 1) [38], and 2) [39]. (From Ref. [36]).

Table 2.3 The pre-exponential constants for diffusion of Aluminum in alpha Ti according to [40] and References therein.

Ser. No.	Temp. (K)	$D_0$ ( $\text{m}^2/\text{sec}$ )	$Q$ (kJ/mole)	Alloy	Method	Ref.
1	1107 to 1173	$1.60 \times 10^{-7}$	99.2	Ti-10 at. pct Al	conc. grad.	44
2	833 to 921	$9.59 \times 10^{-10}$	92.5*	Ti	conc. grad., EMA*	45
3	973 to 1173	$1.58 \times 10^{-10}$	77.0	Ti-2Al	conc. grad.	46
4	973 to 1173	$8.70 \times 10^{-17}$	70.7	Ti-4.1Al	conc. grad.	46

(a) derived from the diffusion data

(b) electron microprobe analysis

Table 2.4 The pre-exponential constants for diffusion of Aluminum in beta Ti according to [40] and References therein.

Ser. No.	Temp. (K)	$D_0$ (m <sup>2</sup> /sec)	$Q$ (kJ/mole)	Alloy	Method	Ref.
1	1256 to 1323	$1.4 \times 10^{-9}$	$91.7 \pm 15$	Ti-2 at. pct Al	conc. grad.	44
2	1256 to 1323	$9.0 \times 10^{-9}$	$107 \pm 20$	Ti-12 at. pct Al	conc. grad.	44
3	1373 to 1523	$1.09 \times 10^{-9}$	172	Ti-2.2 Al	conc. grad.	46
4	1373 to 1523	$2.90 \times 10^{-9}$	180	Ti-4.55 Al	conc. grad.	46

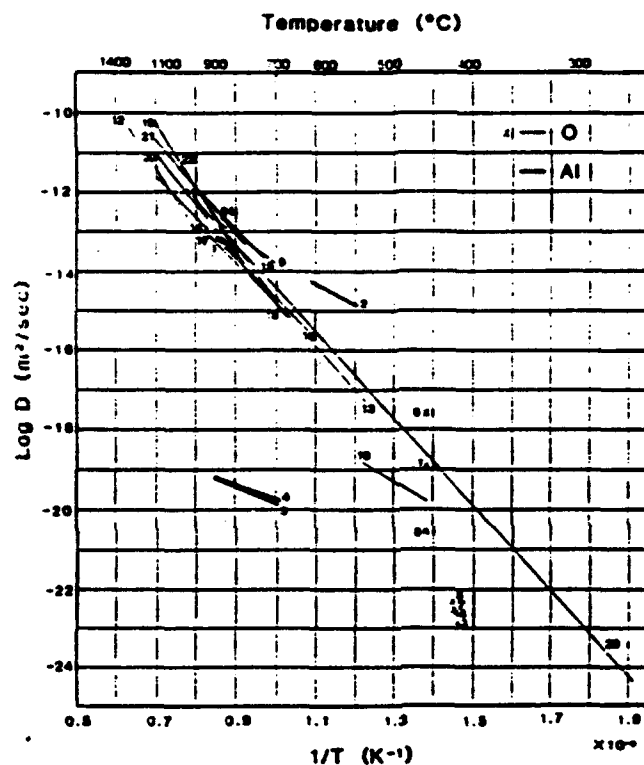


Figure 2.14 The diffusivities of oxygen and Al in  $\alpha$ -Ti. The numbers in the plot correspond to the series numbers in Table 2.3 [40].

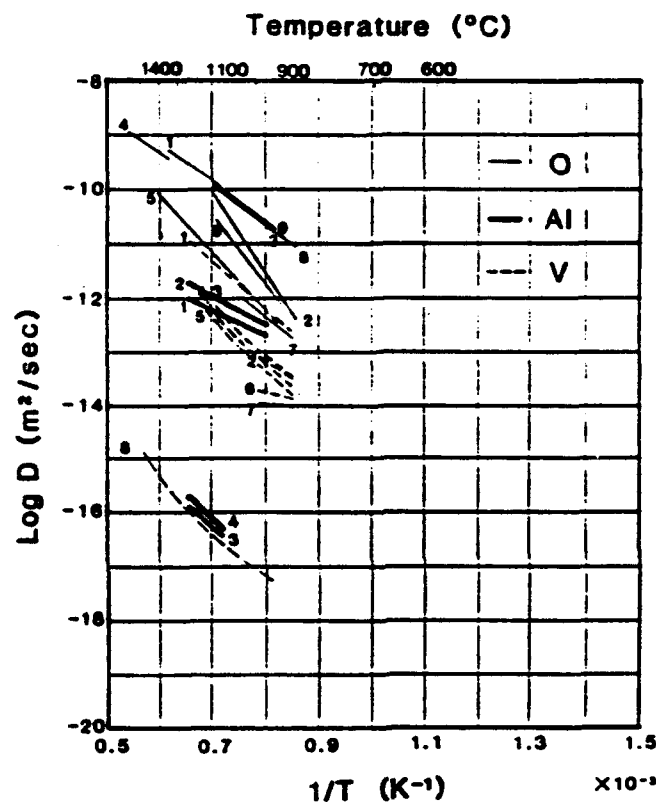


Figure 2.15      The diffusivities of O, Al, and V in  $\beta$ -Ti.  
The numbers in the plot correspond to  
the series numbers in Tables 2.4 [40].

determined the activation energies for N diffusion at 600-800 °C in Nb (21.2 kcal/mole), and Nb-10 at%Ti (26-26.2 kcal/mole). Lauf [42] studied the effect of additions of substitutional solutes to Nb in the oxygen diffusivity. He found that additions up to 5 % of Ti resulted in a decrease of the O diffusivity in as much as one order of magnitude. It was suggested that this was caused by trapping of oxygen by substitutional solute atoms, with a substitutional/oxygen binding energy of 0.6-0.8 eV for the Ti case.

Regarding another interstitial element, Cannelli and Cantelli [43] have conducted extensive research on the presence of hydrogen in Nb-Ti alloys. They determined the diffusivity of this interstitial element by means of the Gorsky effect [44]. In their research they found that substitutional Ti acted as a trapping center for H and lowered its mobility, as shown by Figure 2.16.

### **2.1.3 Oxidation**

Niobium has a high melting point and a good strength at high temperatures but oxidizes very easily at temperatures above 650 °C. The main oxidation product is  $\text{Nb}_2\text{O}_5$  which exhibits paralinear kinetics, i. e., the oxidation rate of Nb for short times follows a parabolic behavior and becomes linear at longer exposure times. The reason for this transition is due to the cracking of the  $\text{Nb}_2\text{O}_5$  scale under the developed compressive growth stresses. An extensive study [45] on the effect of doping on the cracking behavior of  $\text{Nb}_2\text{O}_5$  has led to the conclusion that Nb alloys capable of producing a surface oxide other than  $\text{Nb}_2\text{O}_5$  to separate the alloy from the

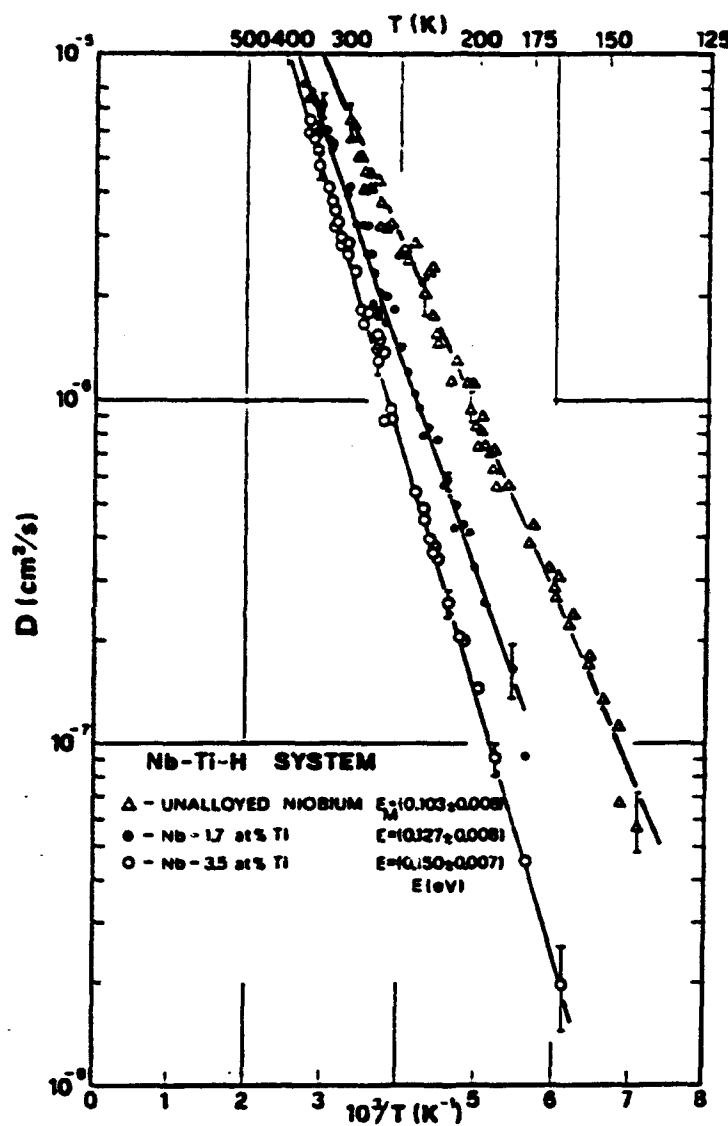


Figure 2.16

Diffusion coefficient as a function of reciprocal temperature of unalloyed Nb, and apparent diffusion coefficient for 2 Nb-Ti alloys [43].

corrosive environment are required. The most effective alloying additions, that is, those that produced the lowest oxidation rates, were found to be aluminum, chromium and iron.

Svedberg [5] studied the effect of alloying to improve the oxidation resistance of Nb-based alloys. He has reported that the lowest oxidation rate was observed for NbAl<sub>3</sub>, which forms a protective continuous layer of alumina Al<sub>2</sub>O<sub>3</sub> by the selective oxidation of Al. Any other Nb-Al alloy with an Al content less than 75 atomic % was not able to form alumina scales at 1200 °C. Although the reason for this behavior is still not clear, it is known that the formation of a protective layer generally requires that the oxide of the added element to be more stable than any other oxide of the major component of the alloy. Since alumina is very stable and diffusivity of oxygen through its film is rather slow, aluminum is preferred as an alloying element to improve oxidation resistance.

Generally, the parabolic rate constant of a material is a common estimation of the maximum temperature of its useful resistance to oxidation. In accordance with Wagner's Diffusion-controlled theory of oxidation [46], when the cations are the more mobile species across the oxide scale on the substrate surface, the parabolic rate constant can be expressed as:

$$(m/A) = k'' t \quad \dots \dots \dots (2.8)$$

where A is the area over which reaction occurs. In this case, k'' is also referred to as a 'scaling constant', and was derived considering measurements of the mass increase of the specimen m as the reaction parameter to follow the oxidation reaction. Usually, a weight gain of approximately 20 mg/cm<sup>2</sup> in 1000 hours exposure time,

corresponding to a parabolic rate constant value of  $1 \times 10^{-10} \text{ g}^2\text{cm}^{-4}/\text{s}$ , is a useful limit to measure oxidation resistance. In accordance with Figure 2.17, alloys forming alumina scales in NiAl compound will be useful up to 1400 °C. When  $\text{Al}_2\text{O}_3$  is formed in Nb, the maximum useful temperature for such alloy will be also 1400 °C, and not 1500 °C according with the  $\text{Nb}_2\text{O}_5$  melting point. The reason for this decrease is the formation of a eutectoid between mixed oxides of Al and Nb which would lead to very fast rates of oxidation. Thus, Nb-Al alloys may be used at temperatures up to 1400 °C for extended periods of time when they are protected by alumina scales. The main problem of applying the protective layer method is that the selective oxidation of aluminum can take place not only by forming a protective, continuous surface film at slow oxidation rates, but also by an undesirable rapid internal alumina precipitation. According to Meier and Perkins [4], the problem that complicates the transition from external to internal oxidation is the formation of transient oxides of the substrate material during the oxidation process. When transient oxides such as  $\text{Nb}_2\text{O}_5$  form, the alumina nuclei formed at the alloy surface will be continuously removed into the growing transient oxide, avoiding the formation of such protective film [47]. Therefore, the formation of transient oxides such as  $\text{Nb}_2\text{O}_5$  must be suppressed so that an alumina film could be developed. Following the analysis by Wagner [48] for the case where these transients oxides are avoided, they estimated that the transition from external to internal oxidation in Nb-Al alloys occurs at a minimum content of Al in the alloy, which is function of factors such as diffusivity of Al and O, alloying additions, and oxidation temperature, as established by

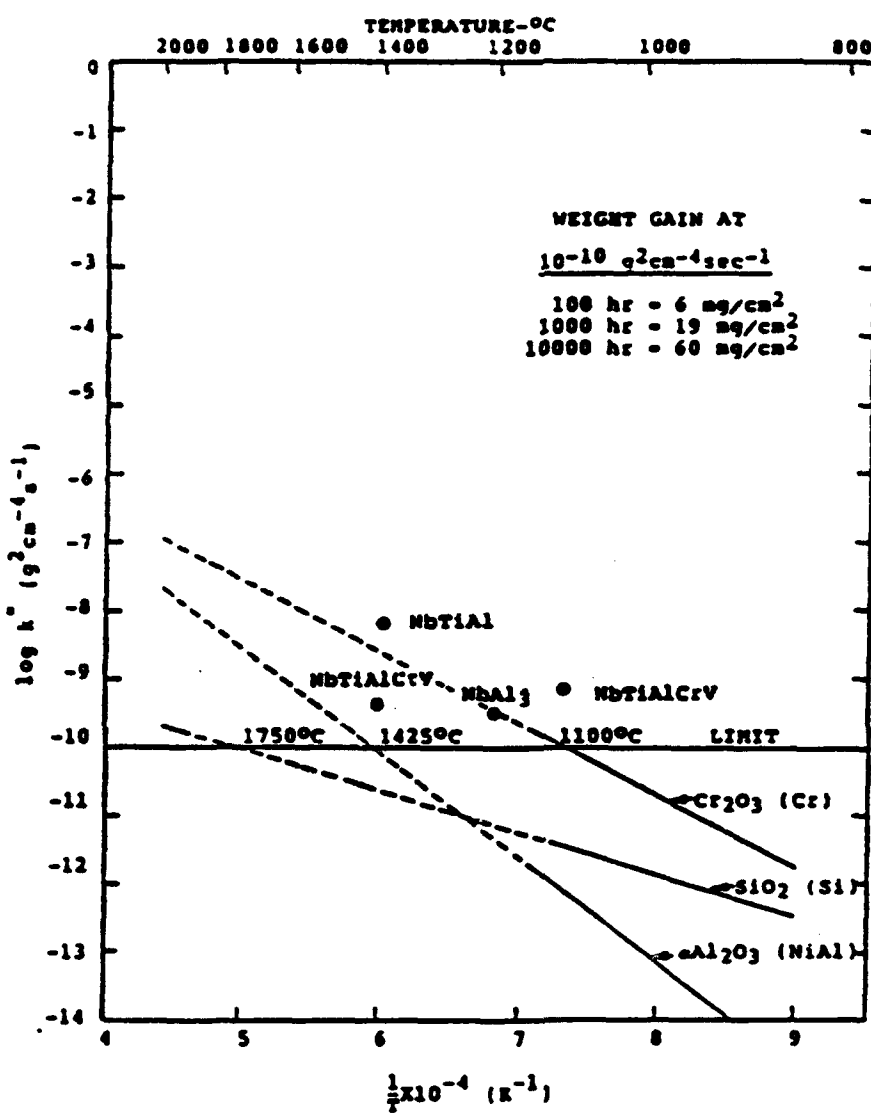


Figure 2.17 Parabolic rate constant vs Temperature for oxidation resistance materials [46].

the following equation:

$$N_{Al}^o > [(\pi g^*/3) \cdot N_0^{(s)} \cdot (D_0 V_m) / (D_{Al} V_{ox})]^{1/2} \quad \dots \dots \dots \quad (2.9)$$

which encourage the formation of the alumina at lower aluminum compositions in the alloy by an increase in the aluminum diffusivity and a decrease in the solubility and diffusivity of oxygen. Estimations made by Perkins and Meier [4] indicated that it is very difficult to form a protective alumina film on binary Nb-Al alloys at low enough aluminum content to consider them still Nb-base. In accordance with observations from other authors [49], the interdiffusion coefficient of b.c.c. Nb-Al alloys has been found to increase considerably with aluminum content, and the value reported by Bodrov and Nikolaev (section 2.1.2) is probably an underestimate. It has been suggested [50] that the probability of formation of an alumina external layer would be enhanced by accelerating the diffusivity of aluminum by means of the use of other alloying elements. In accordance with some authors [4], an increase in the diffusivity of aluminum of about 2-3 orders of magnitude is possible if an extended b.c.c. solid solution existed. The elements that increase the solubility of aluminum in b.c.c. Nb are titanium, iron, chromium and vanadium.

The solubility of oxygen in the Nb-based alloys can be suppressed by the additions of alloying elements by the gettering effect of these elements. As mentioned in the previous section, Ti is one of these elements which, in addition, forms an oxide that has a desired stability between  $Al_2O_3$  and Nb oxides. As explained by Lauf *et. al.* [51], the addition of 1-5% of solutes such as Ta, Ti, V, or Zr to Nb-based alloys decreases the O diffusivity significantly.

The topics of internal and external oxidation of alloy solutes have been studied extensively [50, 52, 53]. It is clear from these investigations that oxidation protection can be obtained by means of complex mechanisms that involve the diffusivity of O into the metal substrate to form oxide particles or films that require a solute to diffuse out such substrate. Titanium would appear to be a probably effective addition for increasing  $D_{Al}$  and decreasing  $D_O$  and  $N_O$  in Nb-based alloys. Additions of 20% Ti should nearly double the solubility of aluminum in niobium at 1400 °C as it forms a continuous b.c.c. solid solution with niobium which can dissolve 42-48 at.% of aluminum at 1400 °C [4].

## 2.2 Diffusion Theory and Mechanism

### 2.2.1 Binary Diffusion

When two different components are placed in contact and allowed to interact at a moderate temperature, thermodynamics predicts that a variety of compositions and phases may form. Under adequate experimental circumstances the interaction between the two components, so-called *Diffusion*, eventually would lead to the reproduction of all the phases between the end compositions. Diffusion is defined as the movement of atoms in a solution as a consequence of an initial chemical potential gradient, usually expressed as a composition gradient, which the thermodynamically unstable system try to eliminate by going to its lower energy state (equilibrium). When the interaction between the two components is conducted in single phase, the matter will flow in a manner that will

decrease the concentration gradient with the net flow of matter ceasing when no chemical potential gradient exists anymore , that is, when homogeneity in the system is reached. Specifically in solids, the diffusion is conducted by either a vacancy mechanism (substitutional solid solutions) or interstitial displacement of solute atoms (interstitial solid solution) depending on the size difference between the solute and solvent atoms making up the solution. Next, a brief analysis of the fundamentals of the theory of diffusion for the diffusivity, mostly in substitutional solid solutions, is presented.

#### 2.2.1.1 Fick's Laws of Diffusion

Adolph Fick [54] proposed in 1885 an equation that fitted the fact that the flow of matter of component  $i, J_i$ , across a given plane goes to zero as the system reaches equilibrium, i.e., the concentration gradient vanishes:

$$J_i = - D_i [\partial c_i / \partial x] \quad (i=1,2) \quad \dots \dots \dots \quad (2.10)$$

where  $c_i$  is the concentration of component  $i$ , and  $x$  is the distance taken parallel to the concentration gradient of such component. The proportional factor in equation 2.10 is known as the coefficient of diffusion (or simply diffusivity). Originally  $D$  was conceived as a constant at a fixed temperature, which later on was proved to be true only for gas solutions.

Equation 2.10 is valid only when the considered system is under steady state conditions (no concentration changes in a point with time). To take into account the variation of composition with

time, Fick's first law is inserted into an equation describing a local conservation of mass. The Fick's second law can be expressed as:

$$\frac{dc_i}{dt} = \operatorname{div} J_i = -\operatorname{div} [ -D \nabla c_k ] \quad \dots \quad (2.11)$$

This equation has the properties of a continuity equation and stems only from the conservation of matter. There are two classical solutions to Fick's second law, which are discussed here.

a) D constant, steady- and non-steady states

If D is independent of position equation 2.11 can be expressed as

$$\frac{dc_i}{dt} = D \nabla [\nabla c_k] = D \nabla^2 c_k \quad \dots \quad (2.12)$$

where  $\nabla^2$  is the Laplacian

$$\nabla^2 = \frac{\partial^2}{\partial x^2, \partial y^2, \partial z^2} \quad \dots \quad (2.13)$$

if a steady state exists,  $\frac{\partial c}{\partial t}$  equals zero. Assuming the simplest case (unidirectional diffusion) equation 2.12 reduces to  $D \cdot (\frac{\partial c}{\partial t}) = 0$ . This case does not occur very often. When the diffusivity is not a function of composition (or position for that matter) but non-steady state is acting, equation 2.11 is expressed as:

$$\frac{dc}{dt} = D \frac{\partial^2 c}{\partial x^2} \quad \dots \quad (2.14)$$

A solution to this equation will express the concentration of a component *i* as a function of position and time,  $c(x,t)$ , under the adequate initial and boundary conditions. In the case of semi-infinite solids:

$$c(x,t) = c'/2 [1 + \operatorname{erf}(x/2\sqrt{Dt})] \quad \dots \quad (2.15)$$

where  $c'$ =initial solute concentration of the richer side in component *i*

$$\operatorname{erf} = \text{error function} = (2/\sqrt{\pi}) \int_0^z \exp(-u^2) du$$

b) The Boltzmann-Matano Method

The coefficient of diffusion varies with composition in real experiments. The dependence of  $D$  on composition forces the Fick's second law to be written as:

$$\delta \partial c_i / \delta \partial t = - \partial [D_i(\partial c_i / \partial x)] / \partial x \quad \dots \quad (2.16)$$

This is an inhomogeneous differential equation, which its solution is extremely difficult in the best case. The most common solution employed in metallurgical studies on diffusion is the so-called Boltzmann-Matano analysis, which allows  $D$  to be calculated from a concentration profile plot. This method is based on a solution of Fick's second law proposed by Boltzmann [55] in 1884 and was proposed for the first time by Matano [56] in 1933. After a diffusion couple has been prepared and annealed at a fixed temperature during a time  $t$  the experimental concentration-penetration curve  $c(x,t)$  is experimentally determined (e.g. microprobe analysis). The resultant curve should not be necessarily symmetric and in that case an error function solution can not be applied. A solution to equation 2.16 may be obtained by applying the so-called lamda substitution  $\lambda$  [57]:

$$\lambda = x / \sqrt{t} \quad \dots \quad (2.17)$$

which can convert the partial differential equation 2.16 into a total differential equation relating  $c$  and the variable  $\lambda$ . This transformation results in:

$$[-\lambda/2] dc = d[D dc/d\lambda] \quad \dots \quad (2.18)$$

Equation 2.18 is constituted only by total derivatives since  $c$  is only function of  $\lambda$ . Integrating 2.18:

$$-\int_{c_-}^c \lambda/2 \, dc = \int_{c_-}^c d[D \, dc/d\lambda] = [D \, dc/d\lambda] \Big|_{c_-}^c \quad \dots \quad (2.19)$$

where  $c_-$ =original composition (constant)

$c$ = variable composition at point  $\lambda$  (or  $xt^{-1/2}$ )

$$= D(c) \, dc/d\lambda - D(c_-) \, dc/d\lambda \quad \dots \quad (2.20)$$

$$\text{Arranging 2.19: } D(c) = [-\int_{c_-}^c \lambda/2 \, dc] [d\lambda/dc] \quad \dots \quad (2.21)$$

Differentiating equation 2.17 at a fixed time gives:

$$d\lambda = dx/t^{1/2} \quad \dots \quad (2.22)$$

Substituting in 2.21 yields:

$$D(c) = -1/2t (dx/dc)_c \int_{c_-}^c x \, dc \quad \dots \quad (2.23)$$

This solution requires a proper evaluation of the  $x=0$  point corresponding to the original interface, which may be evaluated by applying a conservation of mass condition. A procedure to locate the original interface from the composition profile considers Figure 2.18.

The total area under the curve is given by:

$$\int_{c_-}^c c(x) \, dx \quad \dots \quad (2.24)$$

The plane at which  $x=0$ , so-called Matano interface, is determined by finding the value of  $x$  in the diffusion zone ( $x_0$ ) such that

$$\int_{c_-}^c c_- \, dx = \int_{c_-}^c c_+ \, dx = \int_{c_-}^c c(x) \, dx \quad \dots \quad (2.25)$$

Graphically, the Matano interface is the line that makes the two hatched areas in Figure 2.18 equal. This figure also presents a sketch of the area under the curve ( $\int x \, dc$ ) and the inverse of the slope  $dx/dc$  as a function of composition (position). Note that the Matano

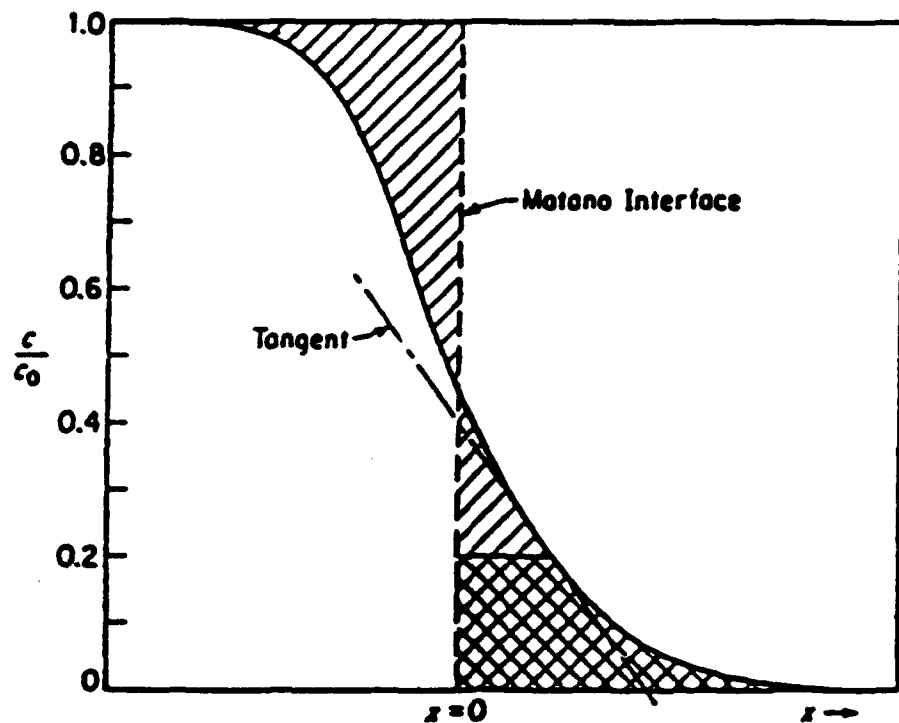


Figure 2.18

Typical composition profile of an annealed diffusion couple. The Matano interface is positioned to make the hatched areas equal (cross hatched area), and the tangent values employed to calculate the interdiffusion coefficient at a composition  $c = 0.2 \cdot c_0$ .

interface is characterized by a maximum at the area under the curve and a minimum in the inverse of the slope. The error in the calculated  $D$  is largest at the ends of the curve where  $c_-/c_+$  approaches zero or one as in those regions the integral is small and  $dx/dc$  large. As mentioned before, the Matano-Boltzmann method is widely employed in metallurgical diffusion studies as it is very useful for determining  $D$  over a range of compositions in alloys. Among its advantages are the wide availability and development of both electron analysis techniques and computers, which make this procedure highly automated. However, one detriment in the procedure is that equation 2.23 assumes that the atomic volume of the alloy is independent of composition, which is a seldom case.

#### 2.2.1.4 Binary Diffusion by a Vacancy Mechanism, The Kirkendall Effect and Darken Analysis

Two mechanisms have been proposed to explain diffusion in substitutional solid solutions. The first is the cooperative movement of atoms. Zener's ring or direct interchange, described later in this section, are examples of this mechanism. However, energetic considerations and the fact that the Kirkendall effect occurs, ruled out these mechanisms as possible ways for substitutional diffusion to occur. The second kind of mechanism implies the movement of a single atom at a time, and the example is the universally accepted mechanism of vacancy diffusion. In this case, the atom of an adjacent site simply jumps into the vacancy, but for that to happen, a small displacement of the neighboring atoms is required, which constitutes

one of the energy terms required for diffusion encountered in the expression:

$$D = \alpha a^2 Z v \exp^{-(\Delta G_m + \Delta G_f)/RT} \quad \dots \quad (2.26)$$

where  $Z$  = coordination number

$a$  = lattice parameter

$\alpha$  = crystallographic geometric factor

$v$  = vibration frequency of a solute atom in an interstitial site

$\Delta G_m$  = free energy per mole needed for solute atoms to jump between interstitial sites.

$\Delta G_f$  = free energy term per mole associated with the formation of vacancies.

The pre-exponential factor is fairly constant with the temperature and can be joined in a single term called frequency factor  $D_0$ .

Knowledge of the operating mechanisms of diffusion in b.c.c. materials is not as extended as that for f.c.c. metals. Self-diffusion and impurity diffusion in b.c.c. metals occurs via vacancies. In a b.c.c. lattice the barrier for the jump of one atom into a neighbor vacant site is more complex than it is in f.c.c. structures because of the saddle point barrier with double maxima in energy that the hopping atom must overcome [58]. Fritzsch *et. al.* [59] studied the diffusion via vacancies as the dominant mechanism in b.c.c. metals by calculating the parameters of a given interaction, such as the influence of lattice constant and binding energy, between the atoms and the lattice. They considered three types of jumps as exemplified in Figure 2.19, and calculated their potential curves (Figure 2.20), which show that the jump to the next nearest neighbor type A is favored due to the smaller distortion in the hopping event. They

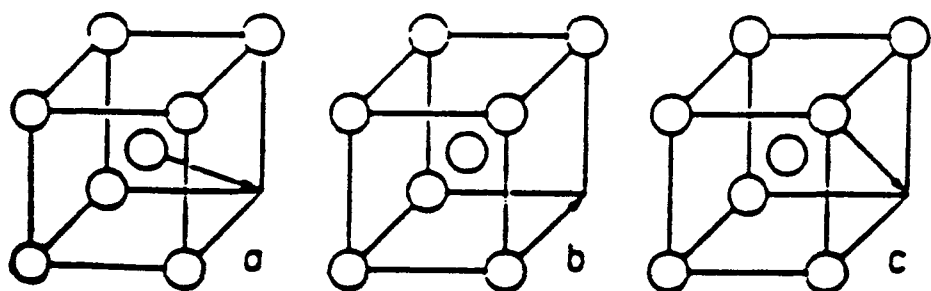


Figure 2.19

Atomic jumps in a b.c.c. crystal considered in the model calculation made by [59]. a) Type A: jumps to the nearest-neighbour position, b) Type B: jumps to the second nearest-neighbor position, c) Type C: jumps to the third nearest-neighbour position.

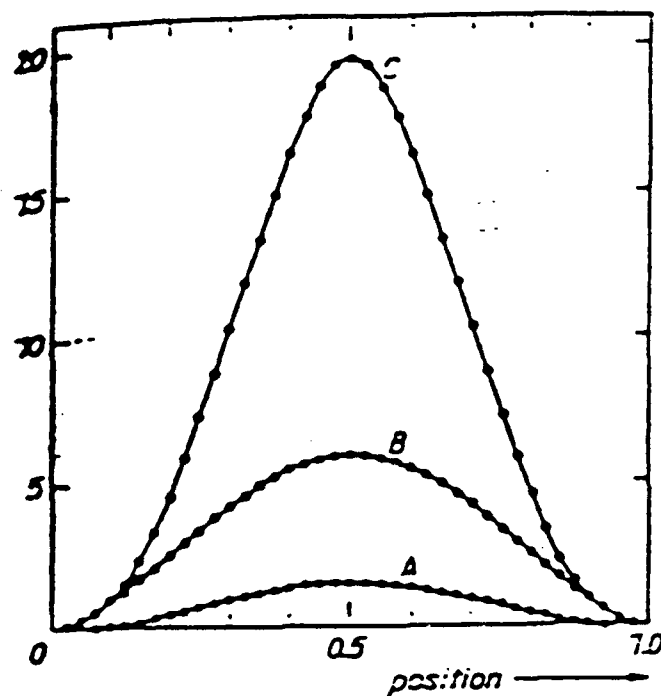


Figure 2.20 Potential barriers for the cited types of individual jumps starting at  $r=0$  and ending at  $r=1$ . The maximum value of each curve corresponds to the migration energy for the particular hopping event [59].

found a strong proportionality between migration energy and the binding energy of the crystal for the self-diffusion case (Figure 2.21), which is in good agreement with published experimental data. As to the impurity diffusion case, it was concluded that the bigger the impurity atom, the higher would be the migration energy, which also agrees with experimental data presented by Tiwari *et. al.* [60]. The binding energy found by [59] has only a small effect in this migration energy.

Regarding with the solution to the diffusion equations presented before, it should be pointed out that the Matano-Boltzmann solution gives only one diffusion coefficient,  $D$ , that completely describes the process. In this kind of experiment, the coordinate system employed is fixed relative to the ends of the specimen, and it is observed that the diffusivity gives rise to the movement of one part of the diffusion couple relative to the other. Therefore, any movement of lattice planes relative to the ends of the couple is recorded as a flux and affects  $D$  (equation 2.10), even though such translation does not correspond to any jumping of atoms from one site to another. Since the process takes place in a chemical concentration gradient the resultant  $D$  represents the chemical diffusion coefficient, also called the interdiffusion coefficient. For the complete description of the diffusion behavior of binary substitutional solid solutions, however, at least five different diffusion coefficients are needed for each concentration, namely:

$D$ = interdiffusion coefficient

$D_{A,B}$ = intrinsic diffusion coefficients of A and B components

$D^*_{A,B}$ = tracer diffusion coefficients of A and B components

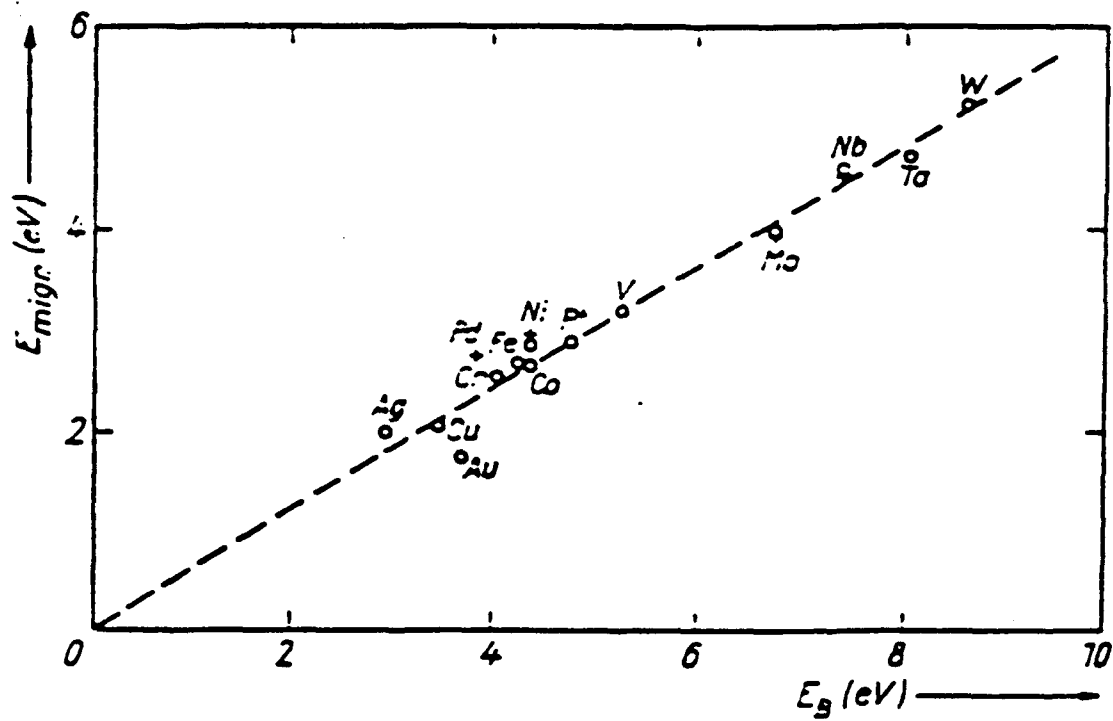


Figure 2.21 Migration energy for self-diffusion in dependence on the binding energy of the crystal in comparison with the experimental data referred therein. The line drawn presents the calculated relation by [59].

The tracer diffusion coefficients arises from the fact that studies showed that the self diffusion coefficients [61] are in general different for the two elements. In self-diffusivity studies one studies the diffusion of a radioactive isotope solute in a matrix of the same (non-radioactive) metal. Except for a small mass difference, the two atomic species are identical. This mass difference permits to calculate the jump frequency of the isotope and a self-diffusion coefficient, which for b.c.c. metals is given by:

$$D_{b.c.c.} = a^2/8\tau \quad \dots \quad (2.27)$$

where  $\tau$  is the dwell time of an atom in a lattice position. Thus, a relationship between the chemical diffusion coefficient and the self-diffusion coefficients must be found. Such relation was brought about in 1947, when Kirkendall and Smigelskas [7] conducted diffusion experiments on diffusion couples formed by a rectangular bar of 70-30 brass plated with 0.1 inch of copper. The original feature of their work was the incorporation of Mo wires in the interface of the two materials as markers (Mo is insoluble in either Cu or Zn). After annealing, a thin slice of the couple was cut and metallographically prepared to measure the distance between markers. The experiment was repeated at different annealing times. In all cases was found that the markers distance decreased an amount proportional to the square root of the annealing time, even after subtracting the small volume change in adding Cu to brass. The only way to explain this markers shift was that each of the two atomic forms moved with different velocities, i. e., that the flux of Zn atoms outwards across the markers plane be much larger than the flux of Cu atoms inwards.

across the same plane. Later work in different systems prove the generality of this concept.

The Kirkendall effect can be taken as a confirmation of the vacancy mechanism of diffusion in cubic materials (f.c.c. and b.c.c.). As mentioned earlier, another possible diffusion mechanism in substitutional solid solutions of b.c.c. metals is the ring mechanism proposed by Zener [62]. Here, the energy needed for diffusion is smaller due to a more open structure; however, experiments on many diffusion couples composed of a number of different b.c.c. metals showed that a Kirkendall effect occurred. Interchange mechanisms such as the ring one require that the rate at which atoms of *A* move must equal the rate at which *B* atoms move in the other direction. Consequently, no Kirkendall effect would be observed.

Kirkendall's experiment showed that the atoms of two species in a diffusion couple move at different rates. Thus in accordance with this concept, the interdiffusion coefficient previously defined should be used only to describe the flow of components relative to some component averaged convective velocity and basically is the same for components *A* and *B*. Kirkendall experiment showed that using the right reference frame for the motion of the atoms, one can get a different result for the diffusion behavior of each of the components and talk about a behavior which is intrinsic to each of the components.

In 1948, Darken [63] published an excellent phenomenological analysis of diffusion of alloys based on such experiment. He contended that the markers motion was due to an imbalance of flows

of the two components, and that each component had a flow of rate of his own, bringing along the definition of intrinsic diffusion coefficients. Consider Figure 2.22 and define  $v_L$  to be the local velocity of the lattice during interdiffusion. In the Kirkendall experiment, after some annealing time, the markers plane will move in the positive direction. If markers are placed in all the couple, those in the diffusion zone will move in a different extension. In the corners there will not be movement and  $v_L = 0$ , whereas in the middle (interface)  $v_L$  will be maximum. From his analysis, Darken derived two equations. The first one:

$$v_L = [-D_B + D_A] (\partial X_A / \partial x) \quad \dots \quad (2.38)$$

permits to obtain the Kirkendall velocity at any point. For example, at the corners of a semi-infinite diffusion couple,  $dX_A/dx$  equals zero, and then  $v_L = 0$ , whereas at the interface the local gradient will be maximum and  $v_L$  will be maximum too. The value  $v_L$  can be measured experimentally by measuring the velocity of the markers and the local concentration gradient by microprobe analysis. The other Darken's equation can be expressed as:

$$D = X_B D_A + X_A D_B \quad \dots \quad (2.39)$$

Again,  $D$  can be determined experimentally by the Boltzmann-Matano method. To obtain  $D_A$  and  $D_B$  at a given composition one needs to determine the markers velocity and the interdiffusion at the position in the couple where the markers reside. From the composition profile obtained, for instance, by microprobe analysis the variables  $X_A$ ,  $X_B$ , and  $dX_A/dx$  can be determined at that point. Then by solving simultaneously equation 2.38 and 2.39, the intrinsic diffusion coefficients can be calculated:

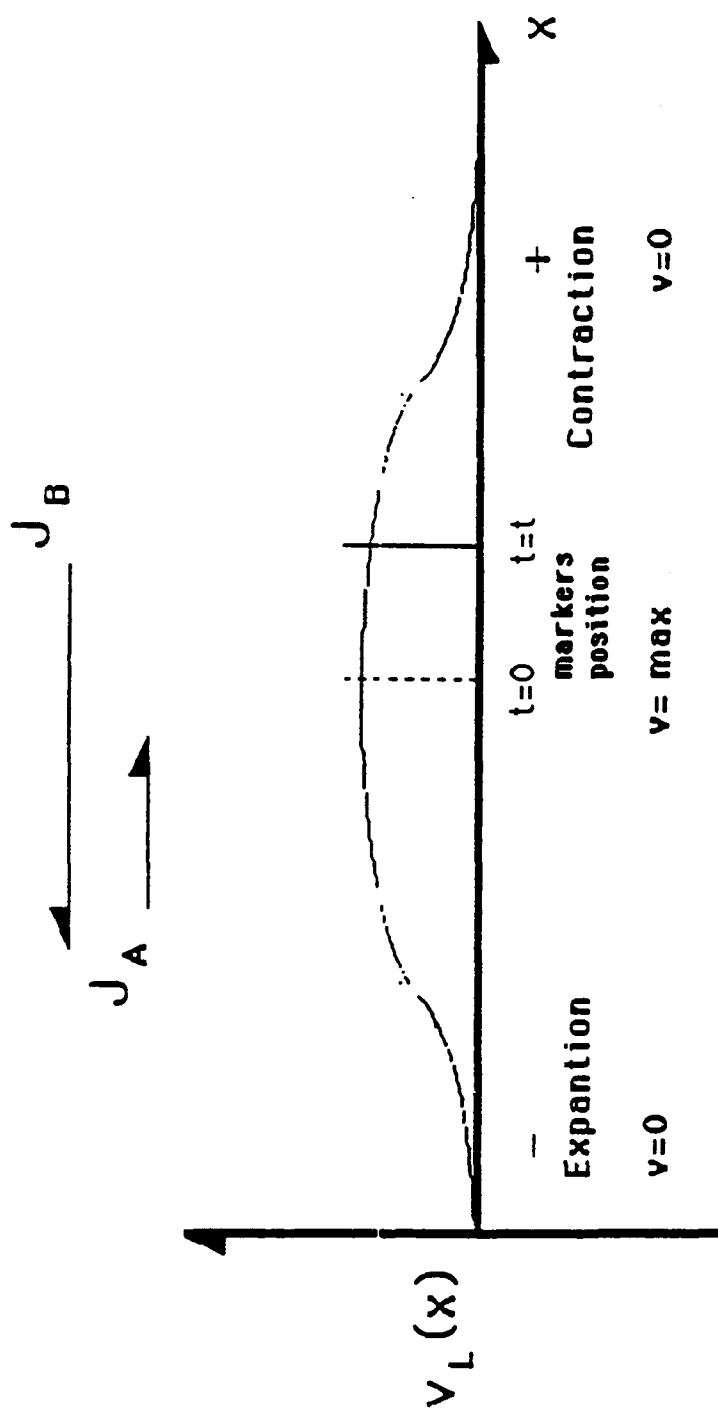


Figure 2.22 The Lattice Reference Frame.

$$\begin{aligned} D_A &= D + X_A v_L [\partial X_A / \partial x] \\ D_B &= D + X_B v_L [\partial X_B / \partial x] \end{aligned} \quad \dots \quad (2.40)$$

### 2.2.2 Ternary Diffusion

The analysis of a diffusion process in multicomponent systems (ternary or higher order) is rather complicated. Even in the most common case (temperature and pressure constant, no external force fields) the appearance of diffusion flux of any component is able to cause diffusion redistribution of all the other components. As to the effort needed, in general the amount of experimental work required increases approximately as the square of the multiplicity of the system. In order to alleviate the complexity of the analysis, "the experimental approach of ternary systems must be accompanied by an exhaustive theoretical investigation of all aspects of the problem" [64]. In this section a brief review of the formal elements of the ternary diffusion theory in single phase substitutional systems is presented. For the sake of simplicity during the analysis possible effects such as volume changes of mixing, lateral dimensional changes and pore formation will be neglected.

#### 2.2.2.1 The Diffusivity Matrix

At present the most common method to define the total set of mutual diffusion coefficients in multicomponent systems is that of Matano-Kirkaldy [64]. A brief explanation of its fundaments follows.

As in the binary case, the flux equations may be written in terms of either the chemical potential gradient (cal/mole) or the concentration gradient (mole/cm<sup>3</sup>) in the Kirkendall (lattice fixed) frame of reference. Generally, the flow equation (Fick's First Law) for this case is:

$$J_i = \sum_{j=2}^c [D_{ij}] \nabla c_j \quad \dots \dots \dots \quad (2.41)$$

where  $[D_{ij}]$  is known as the matrix of diffusivities. Note that  $j$  runs from 2 to  $c$  in this equation. In a ternary system there are two independent composition variables. Therefore, a diffusion couple experiment requires the determination of two independent composition profiles to characterize a couple. Since to a good approximation:

$$c_1 + c_2 + c_3 = c \text{ (moles/cm}^3\text{)} = \text{constant} \quad \dots \dots \dots \quad (2.42)$$

and its derivative:

$$\nabla c_1 + \nabla c_2 + \nabla c_3 = 0 \quad \dots \dots \dots \quad (2.43)$$

then, the dependent variable:

$$\nabla c_3 = -(\nabla c_1 + \nabla c_2) \quad \dots \dots \dots \quad (2.44)$$

Regarding with the index  $i$  in the equation 2.41, it runs only over two components because the 3 fluxes are not independents:

$$J_1 + J_2 + J_3 = 0 \quad \dots \dots \dots \quad (2.45)$$

From Gibb's phase rule, ternary systems offer an extra degree of freedom as compared to binary couples. This fact means that the sequence of compositions (so-called composition path) in ternary systems may be different from couple to couple in the same system. Such composition path is time invariant for semi-infinite couples and is represented by a continuous curve on the Gibbs triangle ternary

phase diagram representation that connects the endpoint compositions of the alloys making up the diffusion couple (Figure 2.23).

When the dependent variable is component 3, equation 2.41 can be expressed as:

$$\begin{aligned} J_1 &= - D_{11}^3 \frac{\partial c_1}{\partial x} - D_{12}^3 \frac{\partial c_2}{\partial x} \\ J_2 &= - D_{21}^3 \frac{\partial c_1}{\partial x} - D_{22}^3 \frac{\partial c_2}{\partial x} \end{aligned} \quad \dots \quad (2.46)$$

One problem associated with the definition of the diffusion coefficient in a ternary system, however, is that it depends upon the choices made for the dependent flux and concentration gradient; so, the same equation 2.41 can be rewritten as (using short nomenclature):

$$\begin{aligned} J_1 &= - D_{11}^2 \nabla c_1 - D_{13}^2 \nabla c_3 \\ J_2 &= - D_{21}^2 \nabla c_1 - D_{23}^2 \nabla c_3 \end{aligned} \quad \dots \quad (2.47)$$

when component 2 is the dependent variable. Substituting 2.44 in 2.47:

$$\begin{aligned} J_1 &= - D_{11}^2 \nabla c_1 - D_{13}^2 (-\nabla c_1 - \nabla c_2) \\ J_2 &= - D_{21}^2 \nabla c_1 - D_{23}^2 (-\nabla c_1 - \nabla c_2) \end{aligned}$$

then,

$$\begin{aligned} J_1 &= - [D_{11}^2 - D_{13}^2] \nabla c_1 - D_{13}^2 (-\nabla c_1 - \nabla c_2) \\ J_2 &= - [D_{21}^2 - D_{23}^2] \nabla c_1 - D_{23}^2 (-\nabla c_1 - \nabla c_2) \end{aligned} \quad \dots \quad (2.48)$$

comparing with 2.46:

$$\begin{aligned} D_{11}^3 &= [D_{11}^2 - D_{13}^2] \\ D_{12}^3 &= - D_{13}^2 \\ D_{21}^3 &= [D_{21}^2 - D_{23}^2] \\ D_{22}^3 &= - D_{23}^2 \end{aligned} \quad \dots \quad (2.49)$$

These relationships among the coefficients of diffusion lack physical

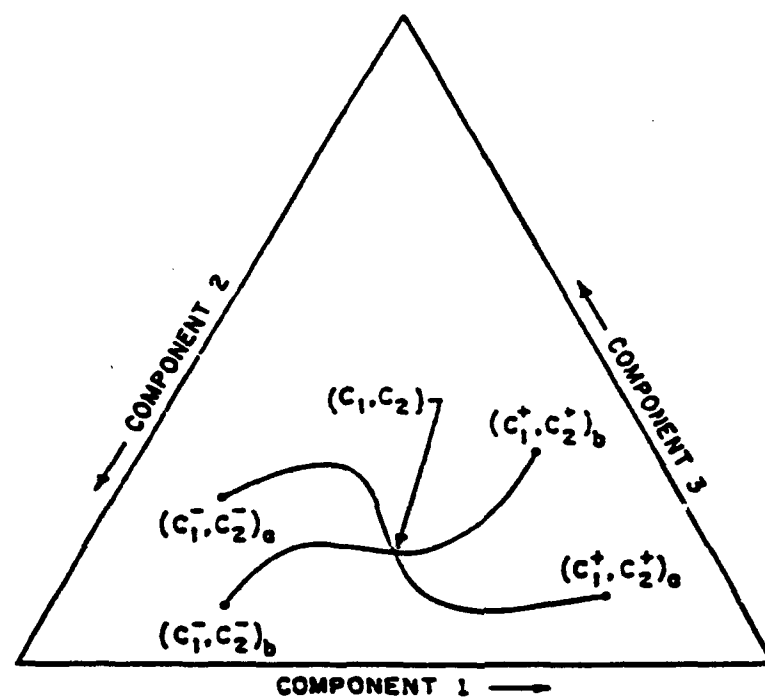


Figure 2.23 Composition Paths in a ternary system isotherm.

meaning, and a result such as  $D_{11} > D_{22}$  may not necessarily imply that component 1 moves faster than component 2 in the system.

In equation 2.46, the on-diagonal element ( $i=j$ ), known also as the mutual diffusion coefficients, reflect how the gradient of component  $i$  influences the flux of the same component. The so-called off diagonal terms (or indirect coefficients) report how the gradient of the other components affect the flux of the component  $i$ . Frequently, the off-diagonal terms are much smaller than the on-diagonal terms.

### 2.2.2.2 Experimental Determination of $|D_{ij}|$ . The infinite Diffusion couple.

As in the binary case, the infinite diffusion couple is one of the most useful techniques to obtain solid-state ternary diffusion data because the associate boundary conditions leads to a particular rather simply integrals of the diffusion equation. For instance, applying local conservation of mass on equation 2.46 it is possible to derive the equivalent of Fick's Second Law:

$$\begin{aligned}\frac{\partial c_1}{\partial t} &= \partial(D_{11}^3 \frac{\partial c_1}{\partial x})/\partial x + \partial(D_{12}^3 \frac{\partial c_2}{\partial x})/\partial x \\ \frac{\partial c_2}{\partial t} &= \partial(D_{21}^3 \frac{\partial c_1}{\partial x})/\partial x + \partial(D_{22}^3 \frac{\partial c_2}{\partial x})/\partial x\end{aligned}\quad \dots\dots\dots (2.50)$$

subject to the boundary and initial conditions:

$$c_i(\pm x, 0) = c_i(\pm \infty, t) = c_i \pm \quad \dots\dots\dots (2.51)$$

As in the binary system, in this case it is possible to make the lamda-substitution (equation 2.17), and convert the partial differential

equation 2.50 into a total differential equation, which after the Matano-Boltzmann solution yields:

$$-\frac{(1/2_t) \int_{c_1}^{c_1(\lambda)} \lambda dc_1}{c_1} = D_{11}^3 \frac{dc_1/d\lambda}{c_1(\lambda)} + D_{12}^3 \frac{dc_2/d\lambda}{c_2(\lambda)} \quad \dots \quad (2.52a)$$

similarly,

$$-\frac{(1/2_t) \int_{c_2}^{c_2(\lambda)} \lambda dc_1}{c_2} = D_{21}^3 \frac{dc_1/d\lambda}{c_1(\lambda)} + D_{22}^3 \frac{dc_2/d\lambda}{c_2(\lambda)} \quad \dots \quad (2.52b)$$

The left side of equations 2.52 can be empirically evaluated with the composition profile of each component (Matano Integral). This is graphically illustrated in Figure 2.24. Then for a particular composition, the information needed to evaluate equation 2.52 is  $\int \lambda dc$ , obtained by a numerical technique, and the slope of the curve at that composition point, which can be readily obtained. Thus, at any composition there are two simultaneous linear equations with a set of 4 unknowns:  $D_{11}, D_{12}, D_{21}, D_{22}$ . To make the system determinate, therefore, it is necessary to produce another independent diffusion couple and perform the same analysis on its composition profile.

Consider Figure 2.23. If the diffusion couples have been chosen so that their compositions paths on the ternary isotherm cross at coordinates  $(c_1, c_2)$ , we see that there are 4 equations and 4 unknowns soluble only at that concentration  $(c_1, c_2)$  which is common to both couples; the values of the set of form  $D_{ij}$ 's, being functions only of compositions but not the gradients, will be the same for that composition that appears in both couples. Thus, the bottom line is that the matrix  $[D_{ij}]$  can be determined by the Matano-like analysis in two diffusion couples at their crossing points, over which no

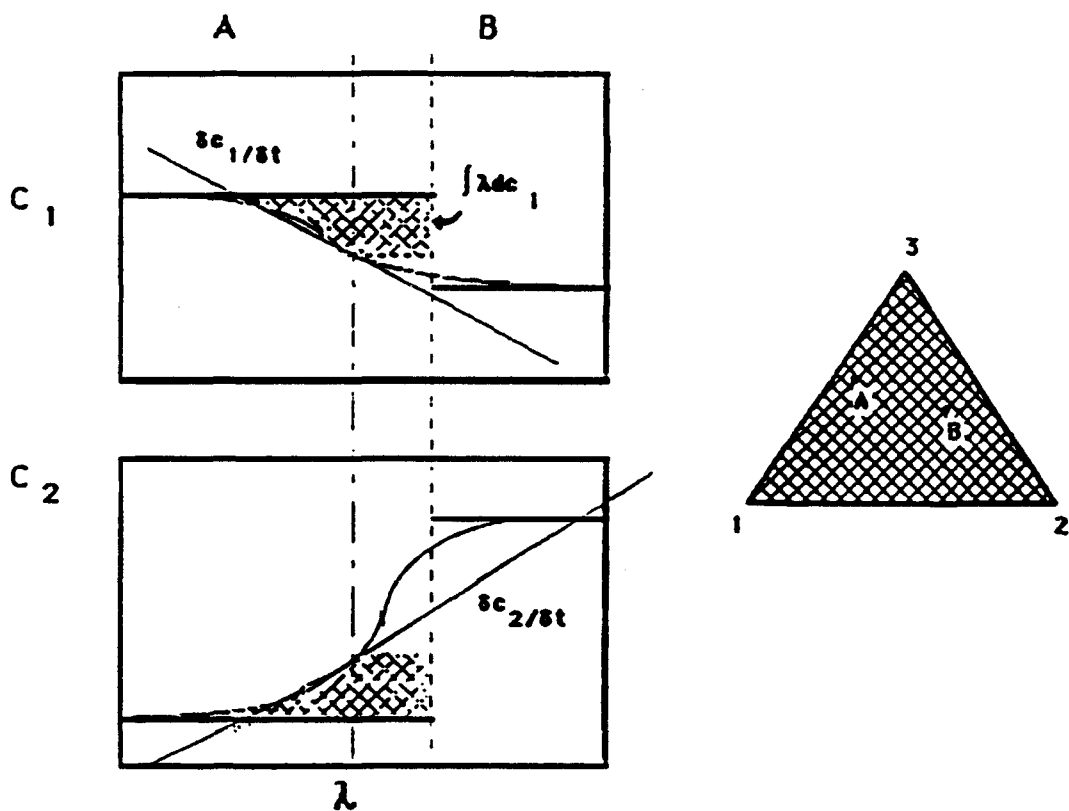


Figure 2.24 Evaluation of Matano integrals and slopes at a given composition for evaluation of diffusion coefficients in ternary systems.

control exists. One problem associated is that the crossing point composition is usually one end of the composition path which makes no easy the evaluation of the integral and slope, diminishing the precision of the result. Then, the general strategy employed in experimental studies generates a whole collection of diffusion couples that survey the ternary region to be studied. After determining the resultant composition profiles and their corresponding composition paths, the integrals and derivatives are evaluated at all crossing points that happen to develop between pairs of couples. It should be pointed out that a given couple could have a lot of intersections with other couples. The results of this kind of study are usually reported as a counter map of each of the diffusion coefficients:  $D_{11}$ ,  $D_{12}$ ,  $D_{21}$ ,  $D_{22}$  as a function of composition on the Gibbs triangle (Figure 2.25) [65]. These values are far from the real physical meaning, so that if  $D_{11} > D_{12}$  that does not mean necessarily that component 1 moves faster than component 2. The interdiffusion studies in Cu-Ag-Au system by Ziebold and Oglivie are a typical application of these strategy [65].

The amount of experimental work required to survey the 2-dimensional surface of the Gibbs' triangle for each  $D_{ij}$  can be reduced drastically by the use of special procedures and theoretical knowledge about the diffusivities. Special procedures for evaluating the 3 independent mutual coefficients have been described by [66-68].

Some important experimental tendencies in typical ternary studies indicate that the maximum in  $D$  occurs usually close to the corresponding value of the minimum melting point. Another

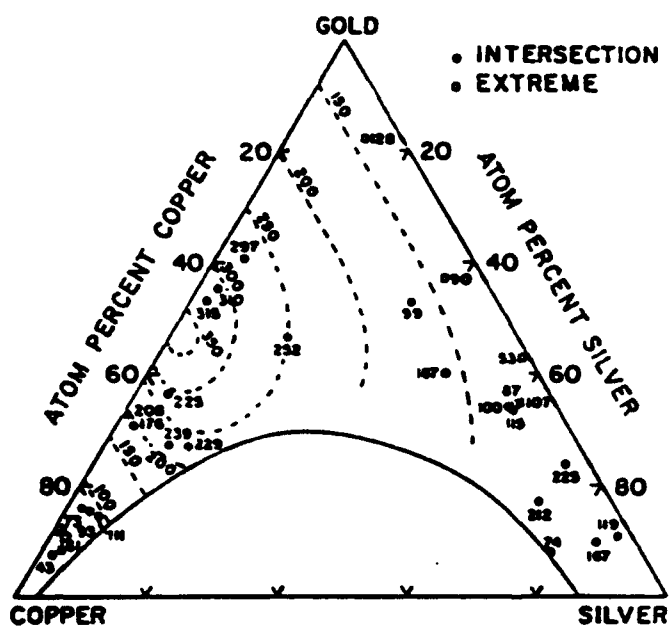


Figure 2.25

a) The direct coefficient of diffusion for Cu D<sub>11</sub><sup>3</sup> in units 10<sup>-12</sup> cm<sup>2</sup>/sec at 725 °C. Filled circles indicate intersections of diffusion paths, and open squares indicate extreme points in the composition profile [65].

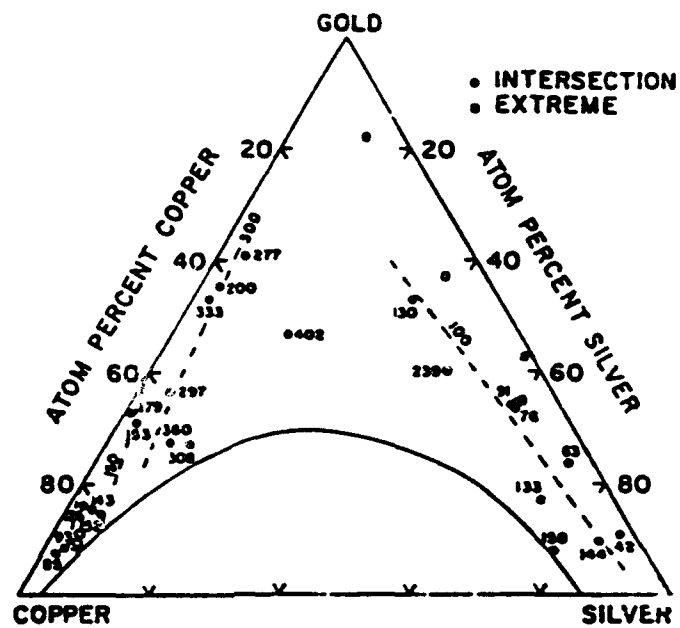


Figure 2.25

(Continue) b) The direct coefficient of diffusion for Ag  $D_{22}^3$  in units  $10^{-12} \text{ cm}^2/\text{sec}$  at  $725^\circ\text{C}$ . Filled circles indicate intersections of diffusion paths, and open squares indicate extreme points in the composition profile [65].

interesting observation is that to calculate  $D_{ij}$  from extreme values (maximum or minimum) in the composition profiles, we do not need a crossing point since the  $\nabla c_{ij}$  equals to zero at that particular concentration reducing the equations 2.46 to a system of 2 equations and 2 unknowns:

$$\begin{aligned} J_1 &= - D_{11}^3 \partial c_1 / \partial x - D_{12}^3 \partial c_2 / \partial x = - D_{11}^3 \partial c_1 / \partial x \\ &\dots\dots\dots (2.53) \\ J_2 &= - D_{21}^3 \partial c_1 / \partial x - D_{22}^3 \partial c_2 / \partial x = - D_{21}^3 \partial c_1 / \partial x \end{aligned}$$

#### 2.2.2.4 Diffusion Penetration Tendencies and Composition Path Patterns

In 1974, DeHoff *et. al.* [69] published a new viewpoint on the analysis of the diffusion behavior in ternary systems where  $[D_{ij}]$  is replaced by the relative penetration tendencies of the 3 species. Through this approach, the calculation of a complete pattern of composition paths and Kirkendall shifts on the Gibbs triangle for the relative penetration tendencies of the components is relatively simple.

During their analysis, they made 3 assumptions. First, the interpenetrations of the species occur on a rigid lattice so that appreciable excess and deficit of atoms can occur on one side and the other. To do this, the normal continuous feedback of vacancies was changed for a one-step feedback that permitted the readjustment of the lattice. This was recognized as physically unreal, but essential for the calculation of the Kirkendall shift for the system. The third element of the approach was approximating the concentration-

penetration curves for each component as straight line with the rigid lattice as the coordinate system. In this case, when the depth of penetration of an element depended on composition, the concentration-penetration curve was approximated by two straight line segments.

Consider a diffusion couple made up by alloys A-50at%B (*P* side) and B-50at%C (*Q* side) in a single ternary system *A-B-C* whose relative penetration depths are independent of composition and already known:  $A \geq B \geq C$ . Figure 2.26a shows the linear composition profiles (in atoms/cm<sup>3</sup>) for this couple in a rigid lattice before and after the diffusion treatment. In accordance with the relative depths of penetration, component *A* draws deeply from the *P* side of the couple and penetrates deeply in the *Q* side of the couple. Regardless of its mobility, component *B* does not move since no concentration gradient for it is present. Component *C* slightly penetrates into the *P* side and draws from a shallow depth on the *Q* side. The total concentration of atoms in the unshifted lattice (Figure 2.26b), obtained by adding the number of atoms of the 3 species point by point, clearly shows a deficiency of atoms/cm<sup>3</sup> in the *P* side and an excess of them in the *Q* side. Since  $c_0$  is considered to be independent of composition, it is necessary to generate a number of vacancies proportional to the area  $A_1$  in the right side, which in turn will increase the thickness of the *Q* side and decrease the *P* side of the couple. This unbalance will produce a Kirkendall shift (translation of the original weld interface) toward the left side of the couple, shown as  $x_k$  in Figure 2.26c. Since all the positions in the diffusion zone are shifted by this process, the original coordinate system  $x_0$  (rigid

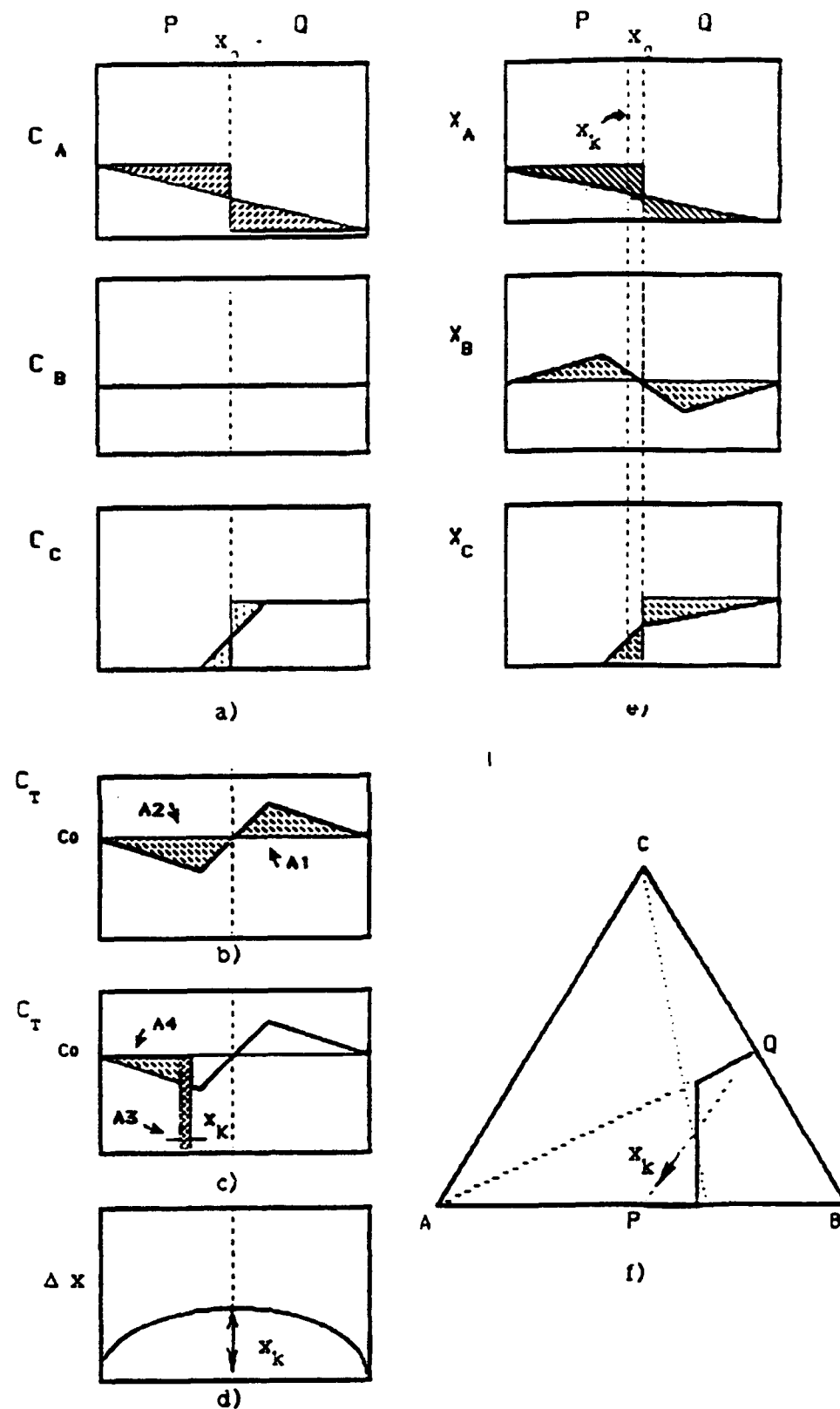


Figure 2.26 a) Model for a ternary diffusion couple with independent concentration penetration tendencies; b) total concentration curve; c) computation of Kirkendall shift; d) prediction of Kirkendall shift; e) atom-fraction penetration profiles for the unrelaxed lattice; and f) computed composition path [69].

lattice) is transformed to a new coordinate system  $x$  which is all moved to the left. The magnitude of this change, however, is different in different positions. For example, at  $x_1$  this magnitude is proportional to the volume change accumulated to the left of this point by the annihilation of vacancies (area  $A_3$ ), which must be equal to the volume occupied by these vacant sites prior to their annihilation (area  $A_4$ ). By equating these two areas at each point of the affected lattice, it is possible estimate the magnitude of the lattice displacement of the original system,  $\Delta x$ . Note that the Kirkendall shift is maximum at the weld interface (Figure 2.26d).

The atomic fractions of  $X_A$ ,  $X_B$ , and  $X_C$  are shown in Figure 2.26e. They are derived at any point of the unshifted system by dividing the corresponding  $c_i$  by the respective  $c_t$ . This curves would be the experimental result given by the microprobe analysis. Observe how the profile corresponding to the component  $B$  varies up and down as it crosses the diffusion zone suggesting a movement of atoms  $B$  from the right side of the couple in a possible uphill diffusion way. However, as mentioned earlier there is not effective flow of atoms  $B$  at all because of the absence of a  $B$  concentration gradient, and the variation of its composition is due only to the imbalance in the distribution of  $A$  and  $C$  atoms. Finally Figure 2.26f shows a plot of the composition path and Kirkendall shift that would be observed for this kind of system. There are some interesting observations that should be noted in this plot. For example, the two ends of the path point directly toward the corner of the fastest component  $A$ , and the central part of the path tends to point toward the corner of the slowest component  $C$ . This causes a considerable

deviation of the composition path from the straight line joining the endpoint compositions (concentration tie-line) with the path curve crossing at half way of this tie-line. The intersecting point is called the cross over-point and is important in the determination of the Kirkendall shift.

When the mobility of the atomic species in the couple varies with composition, the depths of penetration and draw for each component are different on the 2 sides of the couple. This case is illustrated in Figure 2.27 [69]. The only difference with the previous case is that the penetration and draw depths are larger in the left side of the couple (richest in the fastest component A) and more shallow in the other side. The determination of the concentration at the welded interface is given by the fact that the triangular areas on both sides of the couple must be equal for each component (conservation of atoms). A similar analysis to that given above would explain the plots for this case. Nevertheless, some interesting deviations in the composition path for this case must be mentioned. One is the displacement of the crossover point toward the *P* side of the couple. An important characteristic of the crossover point is that its composition correspond to that of the original weld interface. The other difference is that the penetration curves are skewed, which causes an enlargement and a shortening in the the length of the segments at the end of the composition path in the *P* and *Q* side, respectively.

This approach was successfully applied by the authors to generate simple penetration tendency models that reproduce

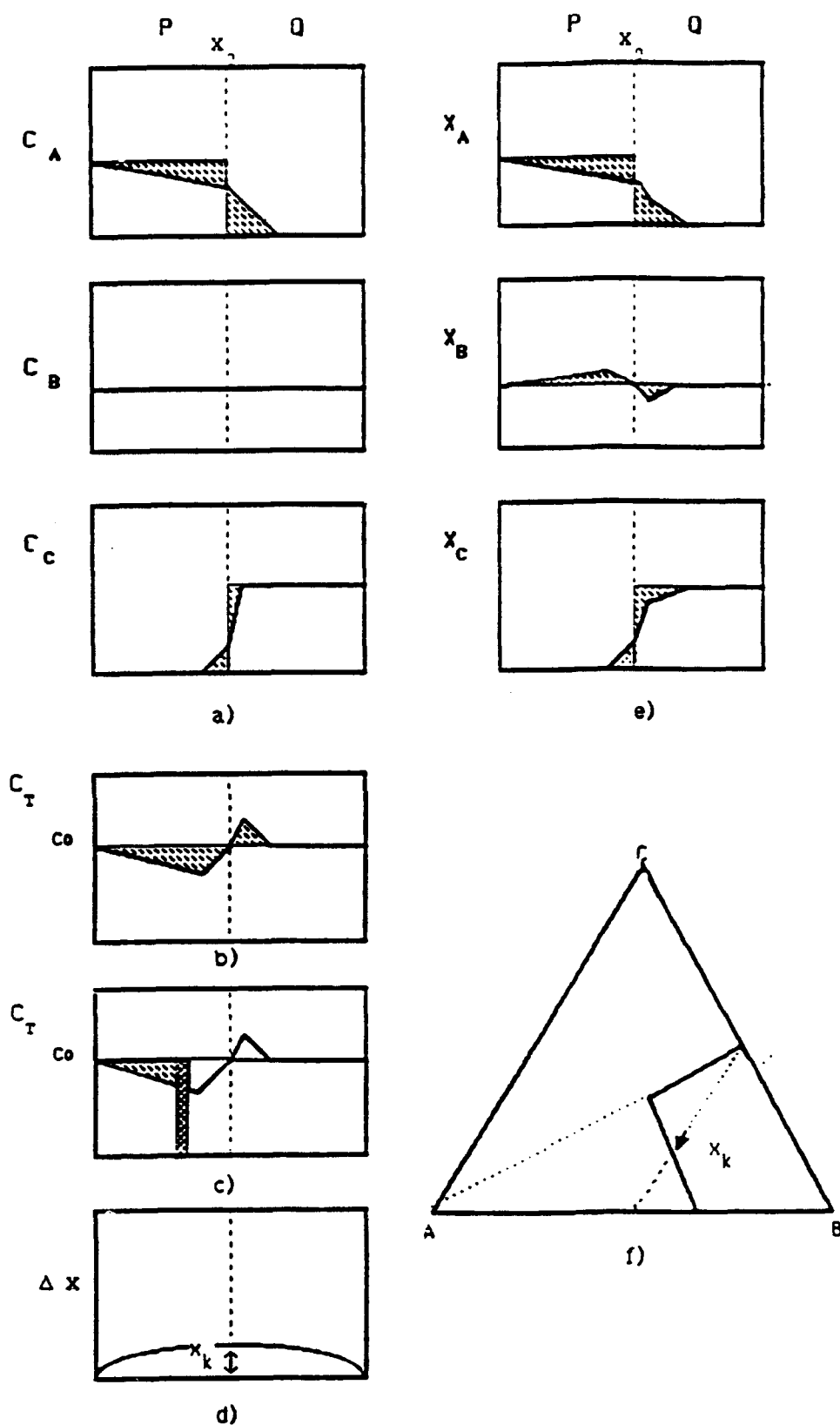


**Figure 2.27** a) Model for a ternary diffusion couple with concentration dependent penetration tendencies; b) total concentration curve; c) computation of Kirkendall shift; d) prediction of Kirkendall shift; e) atom-fraction penetration profiles for the unrelaxed lattice; and f) computed composition path. Note the undulation in component B (e) and the displacement of the crossover point on the path (f). [69]

experimental composition paths and Kirkendall shift patterns in different ternary systems, such as Cu-Ag-Au, Cu-Ni-Zn and Cu-Ni-Zn.

#### 2.2.2.3 Zero Flux Plane

In 1979, Dayananda and Kim [70] described a different way to calculate interdiffusion fluxes in binary and multicomponent systems directly from composition profiles of isothermal diffusion couples by an analysis directly derivable from the continuity equation without the need for a prior knowledge of interdiffusion coefficients, the only assumption being constant molar volume. A major outcome of their interdiffusivity studies on the Cu-Ni-Zn system was the identification of 'zero flux plane' for each component within the diffusion zone of the diffusion couples. They defined a 'zero flux plane' as the plane where the interdiffusion flux of a component goes to zero and on either side of the plane occurs a change or reversal in the direction of the interdiffusion flux of the component.

## CHAPTER 3

### MATERIALS AND EXPERIMENTAL PROCEDURES

In this chapter a description of materials and experimental techniques employed throughout this research is given. A flow chart that represents the experimental procedure for preparation and analysis of diffusion couples is given in Figure 3.1. The experimental procedure consists of alloy preparation by arc-melting, homogenization, diffusion couple preparation, interdiffusion heat treatment, analytical analysis using microprobe, and computerized analysis of the composition profiles. These steps are explained in the following sections.

#### 3.1 Materials

The alloys used in this study were prepared by arc-melting of high purity materials (99.99% Nb and Ti, 99.999% Al). The pure metals were in the form of a 5-mm-thick niobium sheet obtained from Teledyne-Wah-Chang, a 6.35-mm-diameter titanium rod from Aesar, and a 38-mm-diameter aluminum rod from United Mineral Corporation. Table 3.1 gives the ingot analysis of the pure metals.

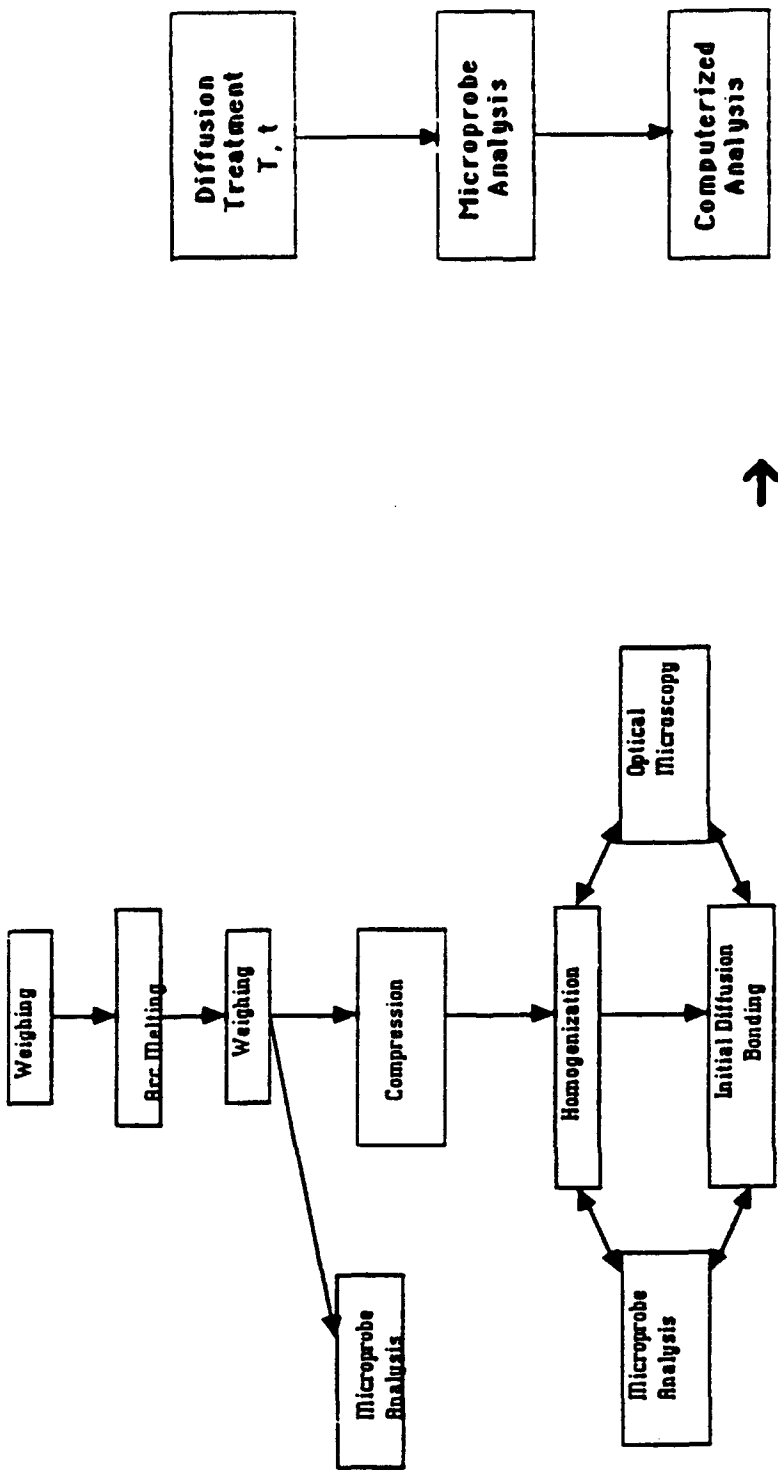


Figure 3.1- A flow chart showing the experimental procedure for the preparation and analysis of the diffusion couples.

Figure 3.1-

**Table 3.1 Ingot Analysis of Pure Materials**

Element	O ppm	N ppm	C ppm	H ppm	Ti	Al	Nb
Nb	100	55	<30	<5	<40 ppm	<20 ppm	balance
Al	<50	<5	92	<5	<50 ppm	balance	<100 ppm
Ti	217	6	30	33	balance	0.6 w%	0.1 w%

### 3.2 Alloy Preparation

The binary and ternary alloys were prepared by arc melting weighed amounts of pure metals on a water-cooled-jacket copper stage under an oxygen-gettered argon atmosphere. Before melting, a vacuum of 100 mtorr in the chamber was attained and then argon, previously dried in a gettering furnace was allowed into the system up to a pressure of -15 KPa. The purging operation was repeated at least 4 times before proceeding to melt. The specimens were melted under an Ar pressure of -35 KPa. Each specimen was melted at least 4 times to assure compositional homogeneity of the buttons. The buttons were weighed after each melting operation so that Al losses could be monitored. Weight losses were detected only in buttons of the binary Nb-Al alloy and accounted for approximately 25% of the initial Al weight. In order to obtain the desired composition in the alloy, an excess of pure Al, equivalent to these losses, was added to the samples before melting.

After metallography preparation, the alloys were analyzed by microprobe analysis, whose results proved that the Al-loss estimation was correct. The resultant compositions from the microprobe analysis are shown in Table 3.2. In order to check their accuracy, some of the alloys were sent out for wet chemical analysis. Table 3.3 compares the results obtained by both techniques for the binary alloy. A good agreement of results is observed.

Table 3.2. Alloy compositions

	Nb	Al	Ti			
Alloy Designation	at %	wt %	at %	wt %	at %	wt %
$\beta_0$	96.5	98.65	4.5	1.35	--	--
$\beta_1$	42.5	61.8	15	6.33	42.5	31.86
$\beta_2$	47.75	64.81	4.5	1.77	47.75	33.42
$\beta_3$	50	65.98	--	--	50	34.02
$\beta_4$	35	53.73	15	6.69	50	53.73

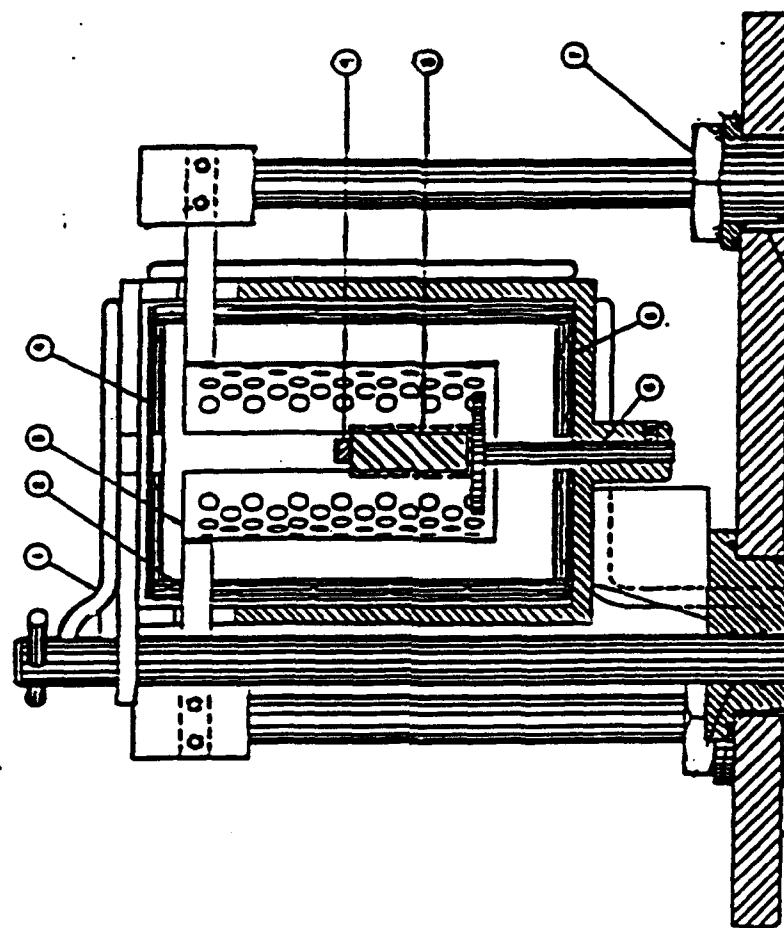
Table 3.3 Comparison of chemical analysis results for binary alloy  
 $\beta_0$  (Nb-4.5Al)  
 (atomic %)

Element	% Calculated from Al losses	% Microprobe Analysis	% Wet Chemical Analysis(*)
Al	4.38	4.31	4.26
Nb	95.42	95.69	>95

(\*) Teledyne Wah Chang, Albany

### 3.3 Preparation of Diffusion Couples

The arc melted buttons in the form of spherical cap-like shape of approximately 3 gram weight and 8 mm height, were studied using optical and electron microscopy. Microprobe analysis showed macrosegregation and significant microsegregation in the microstructure. Therefore, a homogenization of the alloys was required. The buttons were plastically deformed to a disk-like shape, 5-mm thick, at room temperature using a press. The new shape permitted to obtain flat surfaces and the plastic deformation expedited the subsequent homogenization through breaking down of the dendrite arms. All the heat treatments performed in this research, i.e. the homogenization and the diffusion annealings, were done in a Minivac Furnace Series 2400 Vacuum Bell Jar , which is an ultra-high temperature vertical cold wall vacuum furnace capable of temperatures up to 2000 °C. A schematic representation of the furnace assembly employed for all the heat treatments is illustrated in Figure 3.2 The pumping system, consisting of mechanical and diffusion pumps and furnished with ionization gauges, is able to produce a  $10^{-6}$  torr vacuum in the bell jar. To prevent any penetration of oxygen into the alloys during heat treatments, the samples were wrapped in tantalum foil (100  $\mu\text{m}$  thick). The binary Nb-Al alloy ( $\beta_0$ ) proved to be also an excellent oxygen getter. Before heating up the samples, a vacuum of 1E-5 was obtained in the bell jar. The conditions for the homogenization treatment depended on the chemical composition of the samples. In the case of binary alloy  $\beta_0$ , the treatment was done at 1400 °C for 6 hours. For all other



ITEM	DESCRIPTION
1	Cover & tube assembly
2	Shield, heat
3	Element, heater
4	Shield, heat, top
5	Shield, heat bottom
6	Hearth
7	Electrode
8	Alumina stage
9	Sample, Ta-wrapped

Figure 3.2 Furnace assembly used for all heat treatments in this research.

alloys, the homogenization was conducted at the same temperature but for only 4 hours. The lower time is due to the presence of titanium which reduces the melting point, and subsequently increases the rate of diffusivity and the homogenization process. The system was heated up to 950 °C for 30 minutes, and then brought to the homogenization temperature of 1400 °C in 5 minutes. After annealing, the samples were cooled down in the furnace. Optical microscopy and backscattered electron analysis were performed on the heat treated samples to ensure that the microsegregation was removed and specimens were homogenized. Since an environmentally affected zone, which is depleted in Al and has high oxygen content, develops in the vicinity of the surface of the homogenized specimens, the surface layer was removed and rectangular specimens of ( $1 \times 1 \times 0.5 \text{ cm}^3$ ) were cut from the homogenized buttons. Samples were prepared metallographically for the subsequent diffusion bonding using a fixture that permitted to obtain parallel surface.

As mentioned in section 2.3, one of the simplest techniques to assemble solid state diffusion couples is the window-frame technique [71]. In this method, the two members of the couple are polished flat and mechanically clamped together. In some cases, like in this study, a short heat treatment at a temperature below the interdiffusion heat temperature is used to facilitate the diffusion bonding. The use of suitable markers to delineate the original bonded interface is important. Their size should be small enough to avoid interfering with the diffusion bonding process but big enough to be detected by the SEM. They also should be chemically inert with the components

of the couple to avoid their decomposition during the heat treatments. For this research, yttria ( $\text{Y}_2\text{O}_3$ ) particles, 1  $\mu\text{m}$  in size, were employed.

The diffusion couples for this investigation were prepared using a Centorr Series 600 Hot-Press Furnace. The steel chamber has a workable space of 76 mm diameter x 127 mm high and is water cooled by a flow of 5 GPM at 50 psi and 20 °C. This system uses an induction coil as a heater element to achieve temperatures up to 1500 °C in vacuum and neutral atmospheres. It is equipped with a mechanical pump that permits to achieve a vacuum in the order of 1E-2 torr. For inert gas operations, inlet valves, relief valves and a combination pressure-vacuum gauge are provided. To operate with argon or any other inert gas atmosphere, the chamber can be evacuated by means of the pumping system and then backfilled with the desired inert gas. The specimens to form the diffusion couple were compressed together by means of a hydraulic press with a steel ram, 25.4 mm in diameter, coming down from the top of the chamber. The temperature measurements were carried out by a fast-respond optical pyrometer with adjusted chromatic compensation and a precision of  $\pm 10$  °C.

Two kinds of diffusion couples were built for this research. For the binary diffusion study a two-part couple was used, whereas for the ternary diffusion case a sandwich-like couple was made. Small drops of a dilute solution of the fine chopped yttria particles in acetone were deposited as markers over the polished surface of the specimens. The couple was compressed together inside a graphite die. The 3-piece die consists of a stage where the sample to be

compressed rests, a ram through which the load is applied, and a case to hold the whole system. Before setting the sample in the graphite die, a very thin film of boron nitride, a very stable material at the employed bonding temperatures, was sprayed over the faces in contact with the specimen so that the diffusivity of the carbon into the sample was prevented. In addition, a 100- $\mu\text{m}$ -thick tantalum foil was placed between the boron nitride layer and the sample. The whole system was then set into the induction coil in the chamber, as shown in Figure 3.3. As in the arc melting operation, the chamber was purged 5 times with gettered Ar before heating up the system to the bonding temperature.

The diffusion couples investigated in this research are listed in Table 3.3. The bonding temperature was  $1030 \pm 10^\circ\text{C}$  for the binary diffusion system Nb(p)/ $\beta$ O and  $930 \pm 10^\circ\text{C}$  for the couples including ternary alloys, except the couple made with pure Ti. Once at the bonding temperature, a stress of approximately 2 MPa was applied to the system and held for the length of the diffusion bonding. After cooling down, the bonded diffusion couple was cut into two parts. A section perpendicular to the bonded interface was metallographically prepared for examining the quality of the bonded interface. The characterization of the bonded interface prior to the interdiffusion was done using optical microscopy, scanning electron microscopy and microprobe analysis. A solution of Kroll's reagent (10 ml HF, 30 ml H<sub>2</sub>NO<sub>3</sub>, 50 ml H<sub>2</sub>O) was used as an etchant for revealing the microstructure of the ternary Nb-Al-Ti alloys.

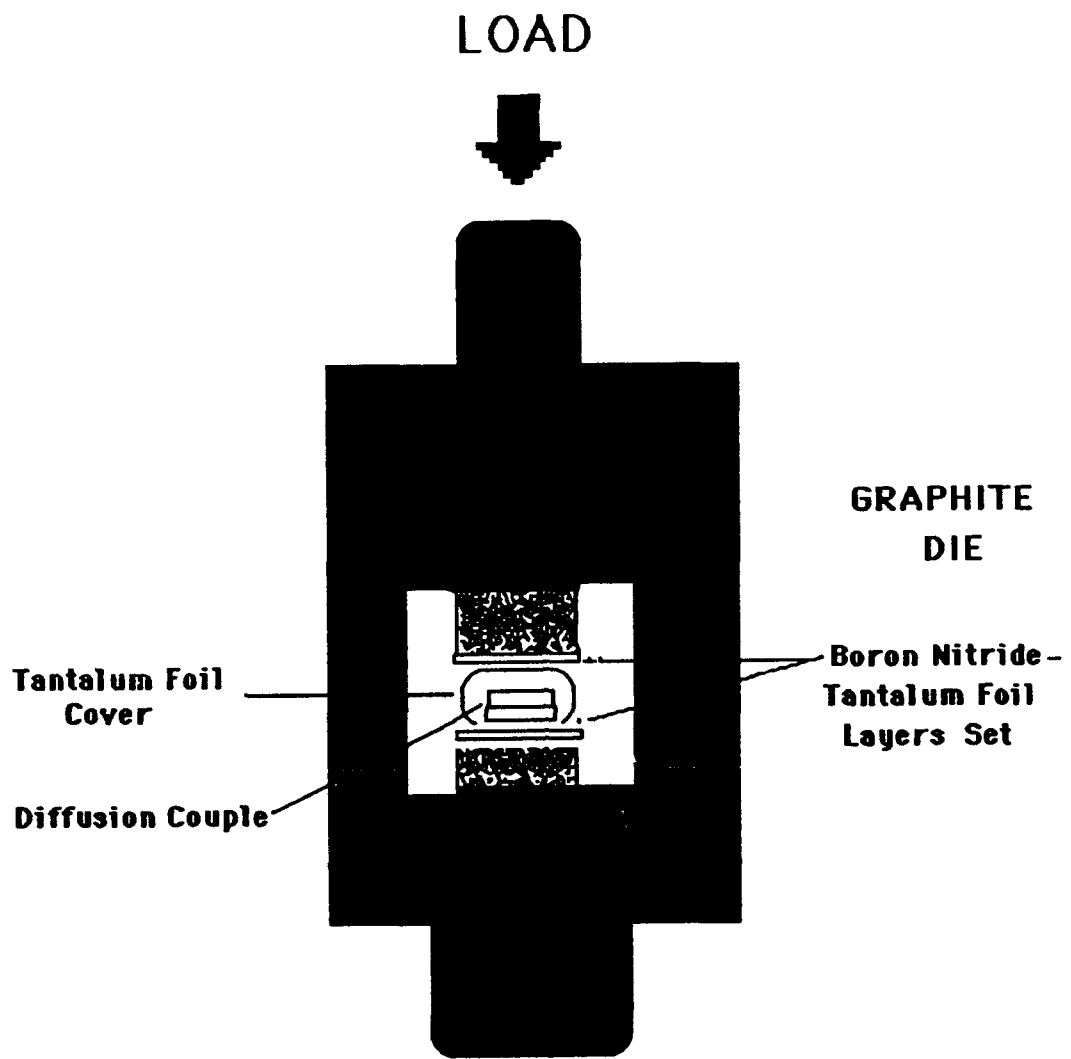


Figure 3.3

Experimental set-up for hot-pressing bonding of diffusion couples.

Table 3.4. List of diffusion couples

Couple #	System	Designation	Diffusion Treatment	Characteristic of Alloy Components
1	Binary	Nb(p)/ $\beta$ 0	1350°C, 21 hr.	Binary Nb-4.5Al
2	Binary	Nb(p)/ $\beta$ 0	1400°, 8.0	Binary Nb-4.5Al
3	Binary	Nb(p)/ $\beta$ 0	1450°, 4.5	Binary Nb-4.5Al
4	Binary	Nb(p)/ $\beta$ 0	1500°, 5.5	Binary Nb-4.5Al
5	Binary	Nb(p)/ $\beta$ 0	1550°, 4.5	Binary Nb-4.5Al
6	Ternary	Nb(p)/ $\beta$ 1/Nb(p)	1400°, 6.0	Disimilar compositions
7	Ternary	$\beta$ 3/ $\beta$ 1/ $\beta$ 3	1400°, 6.0	Constant Nb:Ti Ratio
8	Ternary	Nb(p)/ $\beta$ 1/Nb(p)	1200°, 6.0	Disimilar compositions
9	Ternary	$\beta$ 3/ $\beta$ 1/ $\beta$ 3	1200°, 6.0	Constant Nb:Ti Ratio
10	Ternary	$\beta$ 3/ $\beta$ 2/ $\beta$ 3	1200°, 6.0	Constant Nb:Ti Ratio
11	Ternary	$\beta$ 2/ $\beta$ 0/ $\beta$ 2	1200°, 6.0	Similar Al concentration
12	Ternary	$\beta$ 1/Ti <sub>(p)</sub> / $\beta$ 1	1200°, 6.0	Disimilar compositions

### 3.4 Interdiffusion Heat Treatments

The diffusion couples were wrapped in tantalum foil, put upon the alumina stage in the vacuum furnace, as shown in Figure 3.2, and were surrounded by the Nb-Al binary alloy as a getter. A vacuum of 1E-5 torr was set in the bell jar before heating up to the interdiffusion temperature. Again, similar to the homogenization process, a short heating time ( $\approx$ 5 minutes) from 950 °C to the treatment temperature was registered. A close control of temperature ( $\pm 5$  °C) was achieved by using a type C (W-5%Re) thermocouple. Since the vacuum bell jar furnace lacks a quenching capability, the samples were cooled inside the furnace. The cooling rate, however, was fast enough to avoid further diffusion upon cooling. For example, it took less than 90 seconds to go from 1550° to 950 °C, which is a negligible time compared to the duration of the interdiffusion treatments employed in this research.

To evaluate the diffusivity of aluminum in the binary Nb-Al alloys, the couples (#1 to #5) were annealed for various lenght of time in the temperature range of 1350°-1550 °C. The duration of the heat treatment was limited by a lower bound sufficient to produce a diffusivity zone of at least 25  $\mu\text{m}$  at the lowest treatment temperature, and an upper bound to avoid alumina formation in the binary Nb-Al alloy at higher temperatures. Table 3.4 provides the details regarding the binary interdiffusion treatments conducted.

With respect to the ternary system, diffusion treatments of the sandwich-like diffusion couples were conducted at two different temperatures (1200° and 1400 °C). First, diffusion couples #6 and #7

were treated at 1400 °C. Since the resultant penetration zone was very large, the treatment temperature was decreased to 1200 °C. The interdiffusion time for the ternary alloys was held constant (6 hours) in order to compare the penetration tendencies in these couples.

### 3.5 Analytical Microscopy

The diffusion couples used in this study as well as the materials employed during their construction were chemically analyzed and structurally characterized by Microprobe Analysis (EPMA), and Scanning Electron Microscopy (SEM) (Backscattering Electron BSE and Secondary Electron SE modes), respectively. These analyses were performed in the diffusion couples before and after the diffusion treatment in order to check the extent of diffusion and possible phase transformation during the bonding process, and to obtain the respective concentration profiles for the diffusivity analysis. Concentration profiles were obtained using a JEOL Superprobe 733 electron microprobe. This system is equipped with a tungsten filament electron gun and four wavelength dispersive spectrometers (WDS). A 15-kV, 1- $\mu$ m electron beam with a current of 100 nanoamp was employed in this research. The quantitative interpretation of the x-ray signal is obtained after applying the ZAF technique, which is based on standard element intensities and corrects the measured intensities for experimental effects such as atomic number Z, absorption A and fluorescence F [72]. The compositions of Nb, Al, and Ti were calculated by monitoring and measuring the intensities of AlK $\alpha$  ( $E=1.487$  keV,  $\lambda=8.339$  Å), TiK $\alpha$  ( $E=$

4.511 keV,  $\lambda = 2.749 \text{ \AA}$ ), and NbL $\alpha$  ( $E \approx 2.166 \text{ keV}$ ,  $\lambda = 5.724 \text{ \AA}$ ) x-ray signals. The Nb- and Ti- x-ray radiations were detected using a system of PET crystal/Xe gas filled detector. The PET crystal has a Bragg's equation's characteristic  $2d$  value of 8.742  $\text{\AA}$  and is usually used for relatively long wavelength radiations. On the other hand, the Al x-ray signals were detected using a TAP (Thalium Acid Phthalate) analyzing crystal with a characteristic  $2d$  value of 25.757  $\text{\AA}$ , and a PT10-gas-flow (90% Ar-10% CH<sub>4</sub>) proportional counter. This system is commonly used for detecting the x-ray energies of light elements. The x-ray counting process during the microprobe analysis was statistically controlled. A composition standard deviation of 0.1 at% Al, and a 200-second maximum counting time were set to obtain all the composition profiles in this investigation. The concentration profiles were determined by a point-to-point counting technique. For the binary diffusion case the measurements were done using 1  $\mu\text{m}$  steps. Larger steps (5-10  $\mu\text{m}$ ) were required for those ternary diffusion couples (1400 °C treatments) which showed large penetration zones.

Microstructural analysis of the samples were performed in a SEM Jeol model 103. BSE analysis was conducted in samples where chemical composition issues were wanted, whereas SE mode was used when the morphology of the structure was being analyzed. This microscope has the capability to detect elements with Z>5 for qualitative analysis.

### 3.6 Calculation Method

The composition profile data obtained from the binary diffusion couples were then introduced to a Fortran-77 source code [8] that includes several subroutines. The first of them was used to fit a smooth composition curve to the experimental composition profiles. Then, a different subprogram determined the position where the Matano Interface was located in the fitted curve, and finally, the last subroutine calculated the concentration gradient, the interdiffusion flux, and the coefficients of interdiffusion on the basis of the fitted concentration curve and the Matano plane location. Each of the subprograms makes use of routines from the International Mathematics and Statistics Library (IMSL). For the fitting of experimental data, a modified cubic spline routine (ICSVKU) was employed. The modifications to such routine include the introduction in each side of the concentration profile of a linear zone, which spline cubic equations can not account for, and a parabolic zone, which smooths the connection between the linear and cubic curves. Details regarding the problems arising by the set up of these zones are provided in Chapter 4. The other two subroutines use a routine (QDAG) to do numerical integration only. Regarding the ternary diffusion results, the software described above was applied only to determine the Matano interface location for individual elements. This Fortran-77 program was run in the VAX System at the University of Florida.

## CHAPTER 4

### DIFFUSIVITY EVALUATION IN THE BINARY Nb-Al SYSTEM

This chapter presents the results and their discussion of the binary diffusivity of Al in b.c.c. Nb. The chapter is divided into four sections. The first one discusses the procedure performed for the preparation of the diffusion couples used in this part of the study. Then the results obtained for the evaluation of the binary diffusivity are presented. The third section discusses these results, and a summary of the findings is presented at the end of the chapter.

#### 4.1 Diffusion Couple Preparation

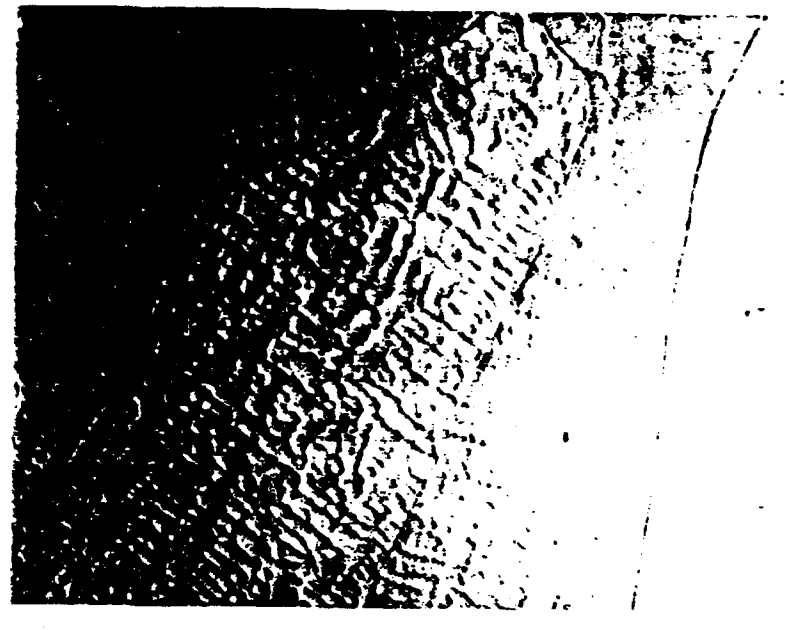
This study is based on the evaluation of diffusivity by using the traditional method of the diffusion couple whose fabrication began by preparing buttons of Nb-4.5 at% Al alloy by arc-melting of high purity materials (Al, Nb). In order to eliminate macro- and microsegregation from the arc-melted button, it was deformed plastically by compression and then annealed at 1400 °C. Once homogenized, the specimen was prepared metallographically to be bonded by the window-frame technique to a previously prepared pure Nb sample. This section discusses the experimental details involved in the preparation of the diffusion couples.

a. As Arc-Melt Structure

The dendritic microstructure of the as arc-melted Nb-Al alloy is shown in Figure 4.1. An oriented columnar grain structure permits to assert the direction of solidification (from bottom to top). The average width of grains in the center of the samples was estimated to be  $300 \mu\text{m}$ . To have such large grains to start with is helpful for bulk diffusion studies as it decreases the possible contribution of grain boundary diffusivity.

The levels of both macro- and micro-segregation of the Al in the arc-melted button were evaluated using microprobe analysis. The macro-segregation of aluminum was measured using a large beam of  $20 \mu\text{m}$  in diameter, which was scanned over the sample from top to bottom using  $200 \mu\text{m}$  steps. Figure 4.2 shows the resultant profile. A second type of analysis was conducted to evaluate the interdendritic microsegregation of aluminum. This information was used to predict the annealing time needed to eliminate the microsegregation of Al at the annealing temperature. Figure 4.3 depicts an example of the composition profile obtained from dendritic arms. In accordance with above analyses, the aluminum concentration in the sample after the arc-melting procedure was generally around 5.5 atomic percent in the Al-rich dendritic zones.

The interdendritic spacing was measured in the middle of the sample over a structure similar to the one shown in Figure 4.3a. The average interdendritic spacing was found to be  $20 \mu\text{m}$  ( $\lambda = 10 \mu\text{m}$ ). The homogenization time at  $1400^\circ\text{C}$  was estimated using the data regarding the interdendritic spacing, and the Al concentration



— 100  $\mu\text{m}$

Figure 4.1      Optical micrograph showing the dendritic microstructure in a Nb-4.5Al alloy after arc-melted. Note the big columnar grains.

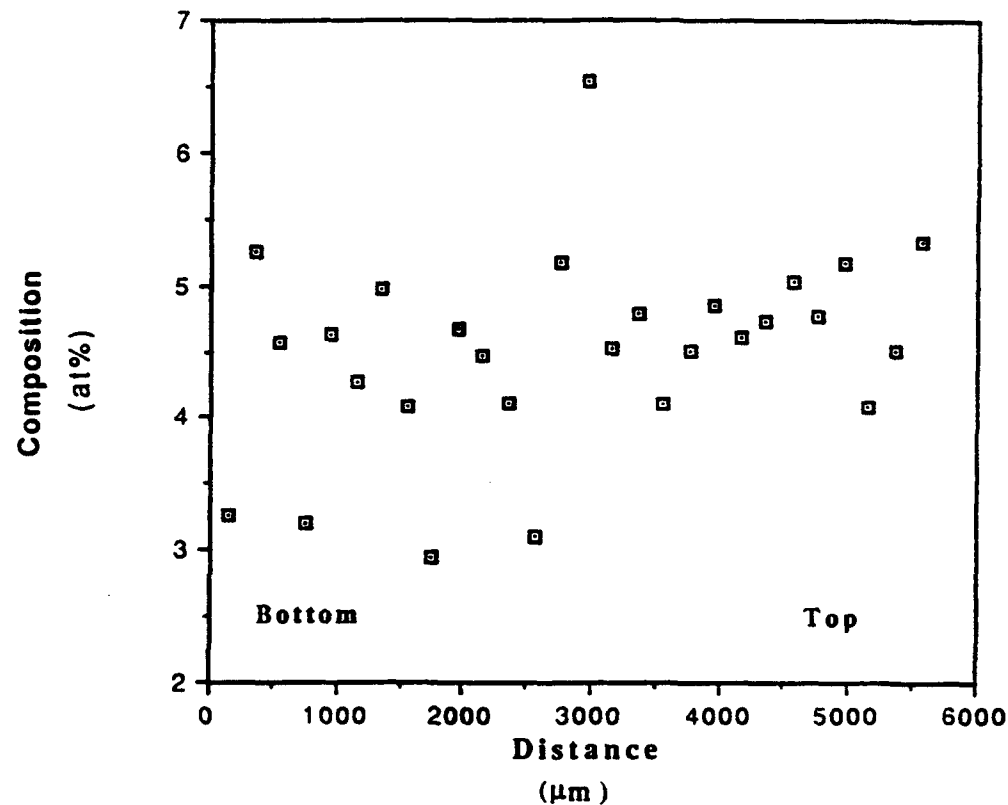


Figure 4.2 A typical experimental composition profile for aluminum obtained by microprobe analysis showing the microsegregation present in an arc-melted Nb-4.5Al specimen.

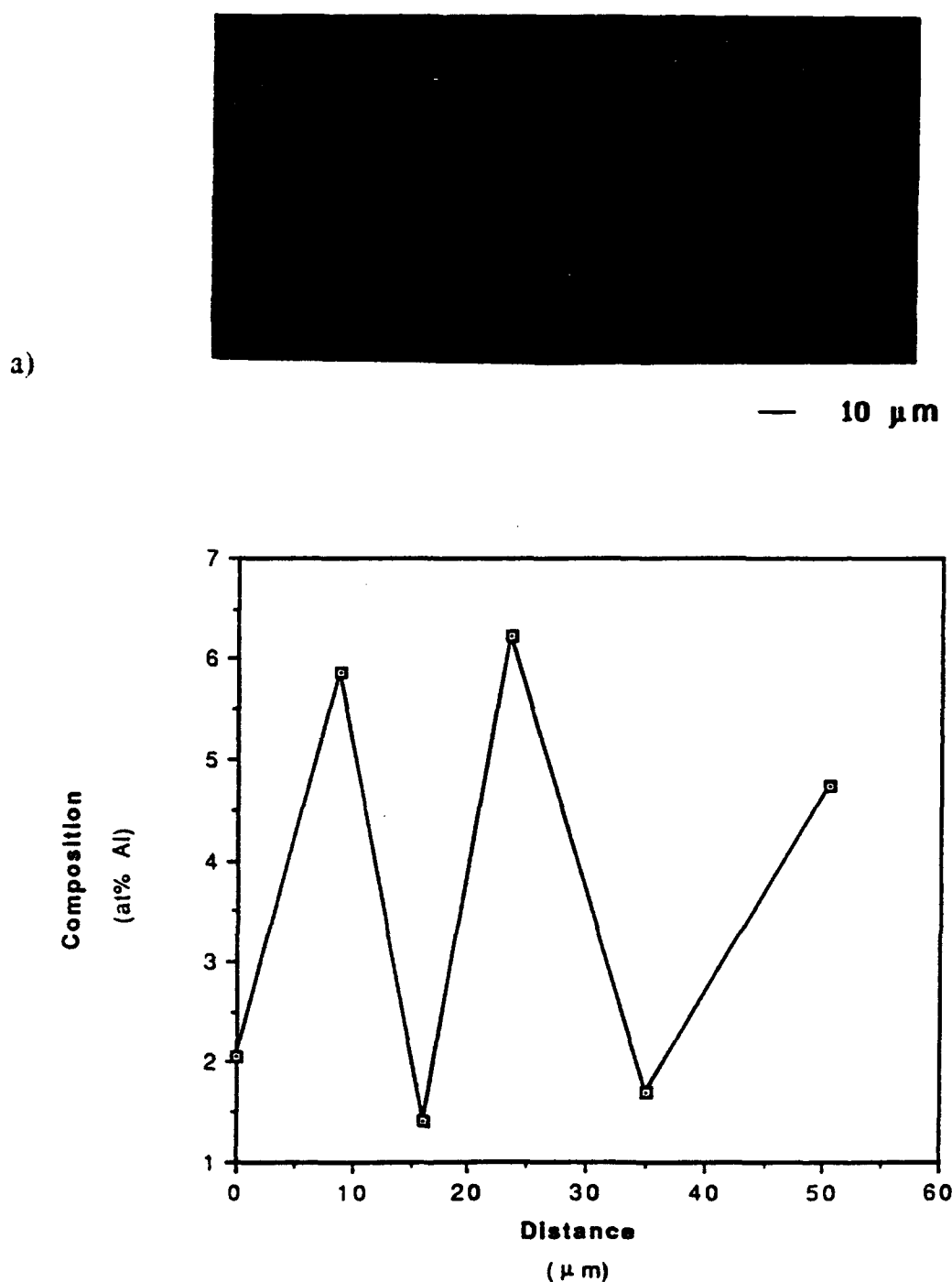


Figure 4.3

a) BSE micrograph, and b) a typical experimental composition profile for Al obtained by microprobe analysis showing microsegregation through a dendrite in an arc-melted Nb-4.5Al specimen.

gradient in the dendrite, arms in conjunction with the Al diffusion coefficient reported in Reference [6]. Assuming that the concentration dependence of Al on distance obeys a simple harmonic behavior [58], the homogenization time for the arc-melted Nb-4.5at%Al was calculated to be 8.5 hours at 1400 °C.

#### b. Homogenized Structure

In order to reduce the segregation observed in the as-cast structure, and therefore reduce the homogenization time, the arc-melted samples were deformed plastically in compression to a thickness of about 2 mm from an original thickness of 5 mm. The mechanical deformation applied broke down the dendritic structure, making it easier to homogenize the sample. In addition, the specimen size and shape factors were not a problem, since an adequate specimen for bonding was easily obtained by trimming the compressed sample after being annealed.

It should be mentioned that initially, based in the reported Nb-Al phase diagram [10] a composition of Nb-7at%Al was chosen for binary diffusion studies. This composition was close to the solubility limit of Al at low temperatures. After homogenization the segregation disappeared. However, a precipitate had formed at the grain boundaries (Figure 4.4). Microprobe analysis showed that this precipitate has a composition corresponding to Nb<sub>3</sub>Al (17.3 at%), whereas the matrix composition was 6.8 at%. In accordance with the Nb-rich part of the Nb-Al phase diagram (Figure 2.2), at 1400 °C the solubility of Al in Nb is about 11% and the second phase must have



— 5  $\mu\text{m}$

Figure 4.4 BSE micrograph of the levitated and copper-chilled quenched Nb-7.1Al alloy after homogenization at 1400°C for 2 hours and furnace cooling. Presence of particles Nb<sub>3</sub>Al in the matrix ( $\beta$  phase) is observed.

precipitated during cooling to room temperature. Therefore, a lesser amount of aluminum was added for the preparation of the arc-melting samples to ensure complete solubility of Al in the  $\beta$ -Nb matrix. The final Al content in alloy  $\beta_0$  used was 4.5 at%.

The plastically deformed samples with an Al content of 4.5 at% were homogenized at different temperatures and times. When the temperature and time of the heat treatment exceeded 1400 °C and 8 hours, respectively, extensive precipitation of a second phase in the  $\beta$ -Nb matrix was found. This new precipitate was observed not only at the grain boundaries, but also inside the grains of the  $\beta$  phase (Figure 4.5), and it had a different morphology than that exhibited by the Nb<sub>3</sub>Al. All these characteristics led us to think that the new second phase could be alumina Al<sub>2</sub>O<sub>3</sub>. In order to prove this, EDX and Auger analyses were conducted on a heat treated specimen.

EDX spectra from the matrix and precipitates, both at grain boundaries and inside grains, were obtained. Results are presented in Figures 4.6 and 4.7. The higher contents of aluminum and oxygen in the precipitates in comparison to the matrix content suggest the presence of aluminum oxide. The larger Nb peak in the spectrum of the precipitate inside the grain comparing to that at the grain boundary is probably due to the smaller thickness of the latter in this instance.

The results from the Auger analysis of these precipitates confirmed that they are alumina particles. Figure 4.8 shows the results obtained from a particle which was initially sputtered to remove the surface layer. The sputtering permitted to achieve a chemical analysis over a 'fresh' surface approximately 50 Å below



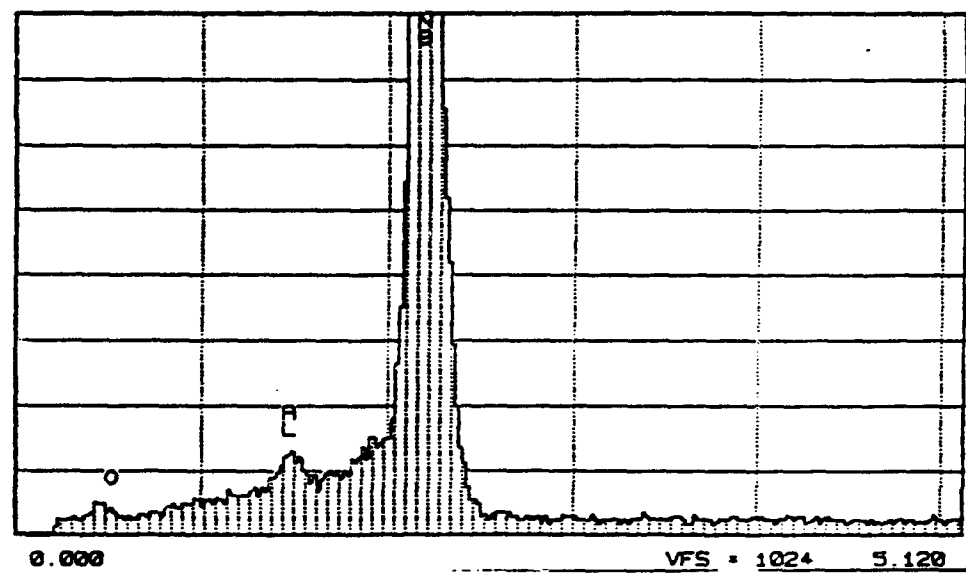
— 50  $\mu\text{m}$

Figure 4.5

BSE micrograph showing the two-phase structure obtained in a Nb-4.5Al alloy after annealing at 1400°C for 8.5 hrs.



Cursor: 0.000keV = 0

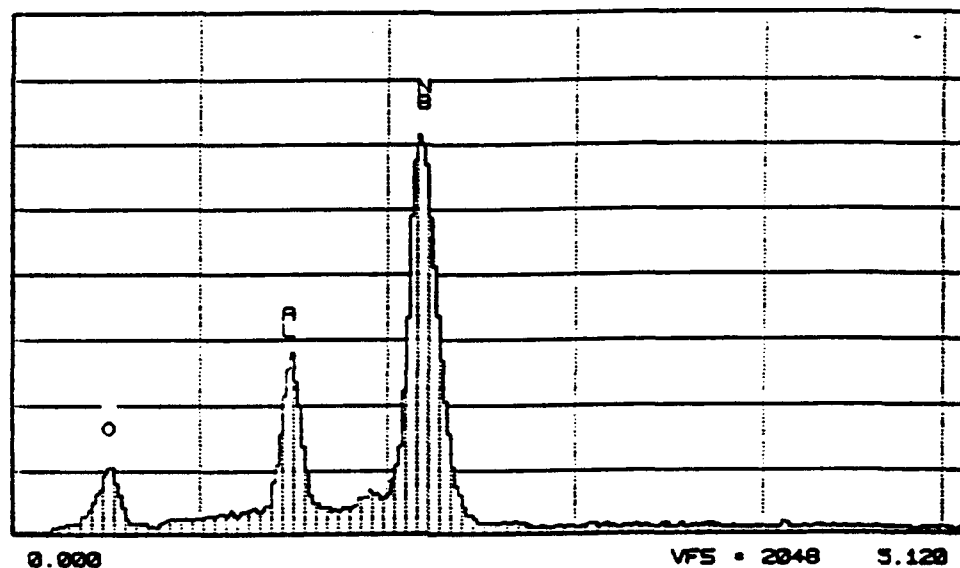


b)

Figure 4.6

a) Secondary Electron micrograph, and b) EDX spectrum obtained from the matrix ( $\beta$  phase) of a Nb-4.5Al alloy after annealing at 1400°C for 8.5 hours.

Cursor: 0.000KeV = 0



c)

Figure 4.6

(Continued) c) EDX spectrum obtained from a precipitate formed inside a grain of a Nb-4.5Al alloy after annealing at 1400°C for 8.5 hours.

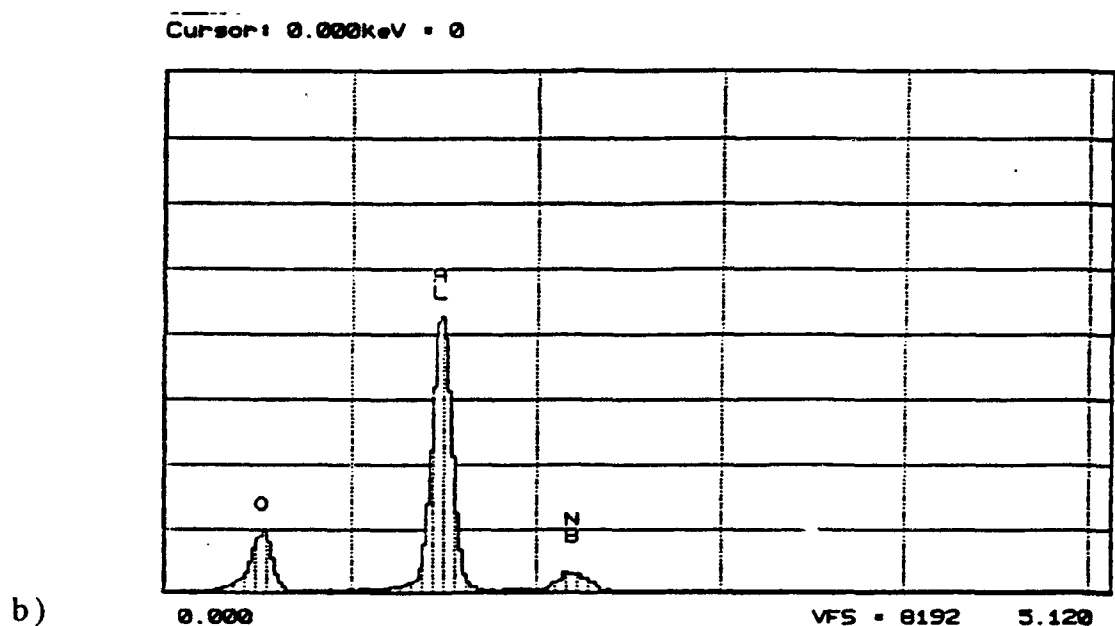
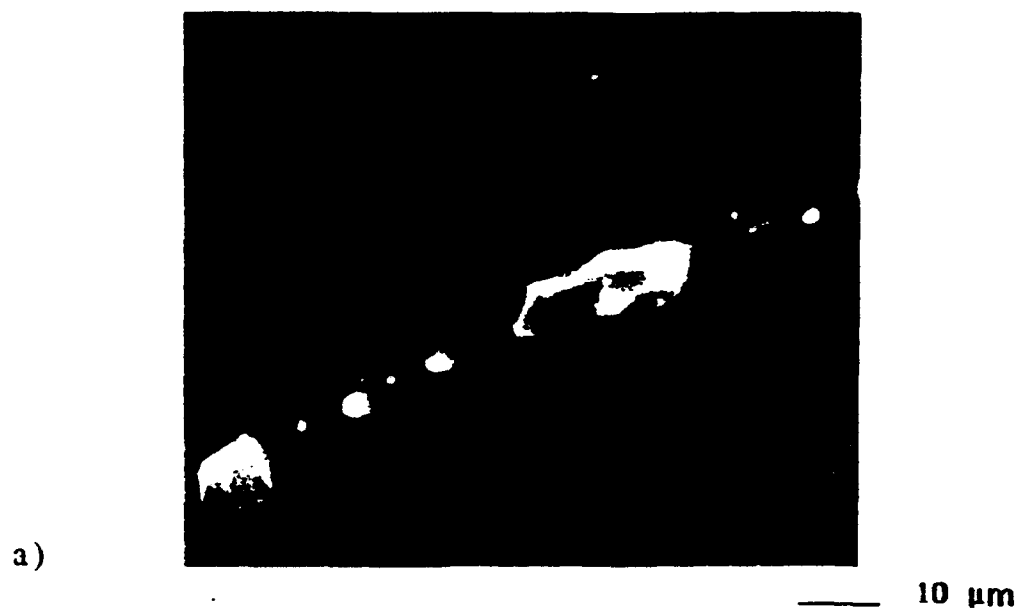


**Figure 4.7** a) Secondary Electron micrograph, and b) EDX spectrum obtained from a precipitate formed at the grain boundary of a Nb-4.5Al alloy after annealing at 1400°C for 8.5 hours.

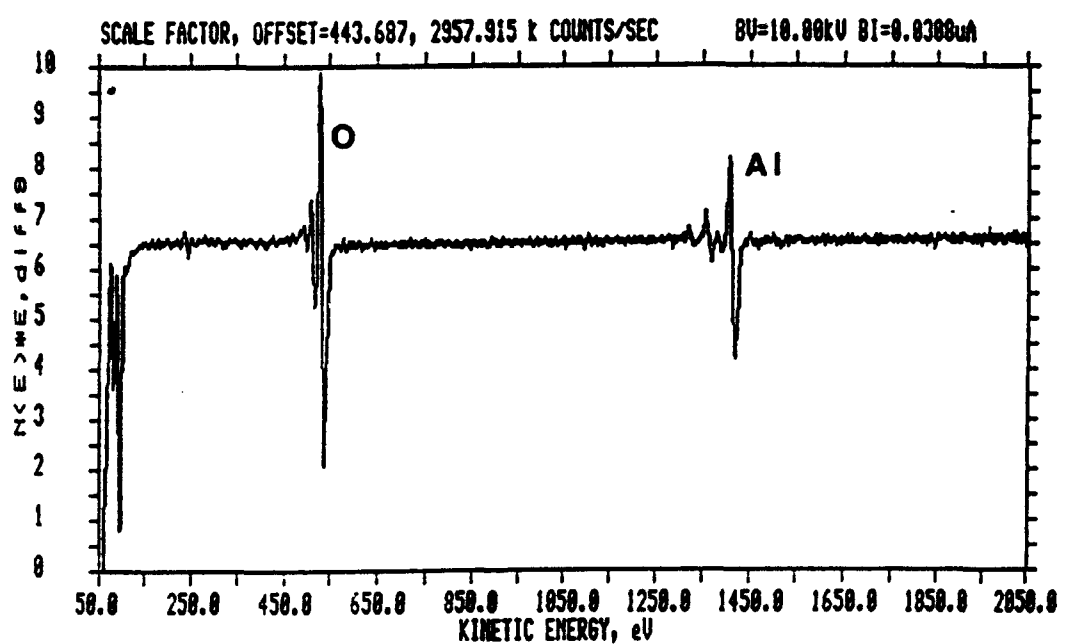
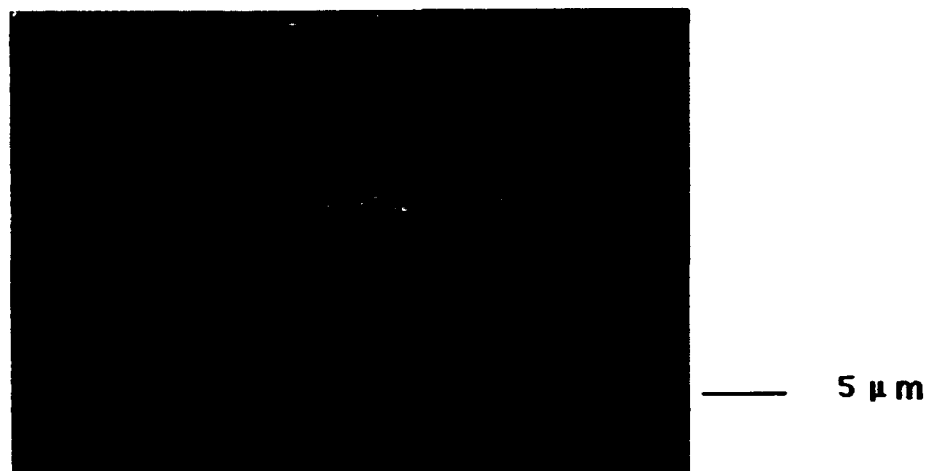


Figure 4.8      Auger analysis of a precipitate located inside a grain of Nb-4.5Al alloy annealed at 1400°C for 8.5 hours.

the original surface, where the particle is free of contamination from atmospheric compounds (i.e. O<sub>2</sub>, CO, CO<sub>2</sub>) that could influence the final result. When the Auger spectrum in Figure 4.8 is compared with that of standard Auger alumina sample (Figure 4.9) [73] an energy shift of 40 eV of both elements is detectable. The only difference between the two spectra is the excitation energy (3 and 10 keV, respectively) which only enhances the amplitude of the Auger signal, but does not produce a change in its kinetic energy. This displacement is due to the insulating properties of the alumina particles, which are embedded in the  $\beta$ -Nb matrix. These particles are charged by electron beam during analysis, causing the kinetic energies of the ejected Auger electrons to increase. As for the  $\beta$ -Nb matrix, Figure 4.10 shows the corresponding Auger spectrum. In this case, no displacement for any peak is observed. Therefore, it was concluded that the resultant precipitate after the homogenization treatment was due to the internal oxidation of aluminum at the annealing temperature.

The homogenization time and temperature was chosen based on a compromise between the process of internal oxidation and elimination of microsegregation. The annealing condition that produced the best result was that involving a temperature of 1400 °C for 6 hours. Figure 4.11 compares the microstructures obtained by annealing at 1400 °C for 8.5 and 6 hours. It was also observed that the presence of oxides is more pronounced near the surface than in the middle of the sample as shown in Figure 4.12. As mentioned earlier, the surface layers of the sample were trimmed off before the diffusion bonding treatment. The presence of alumina at the center

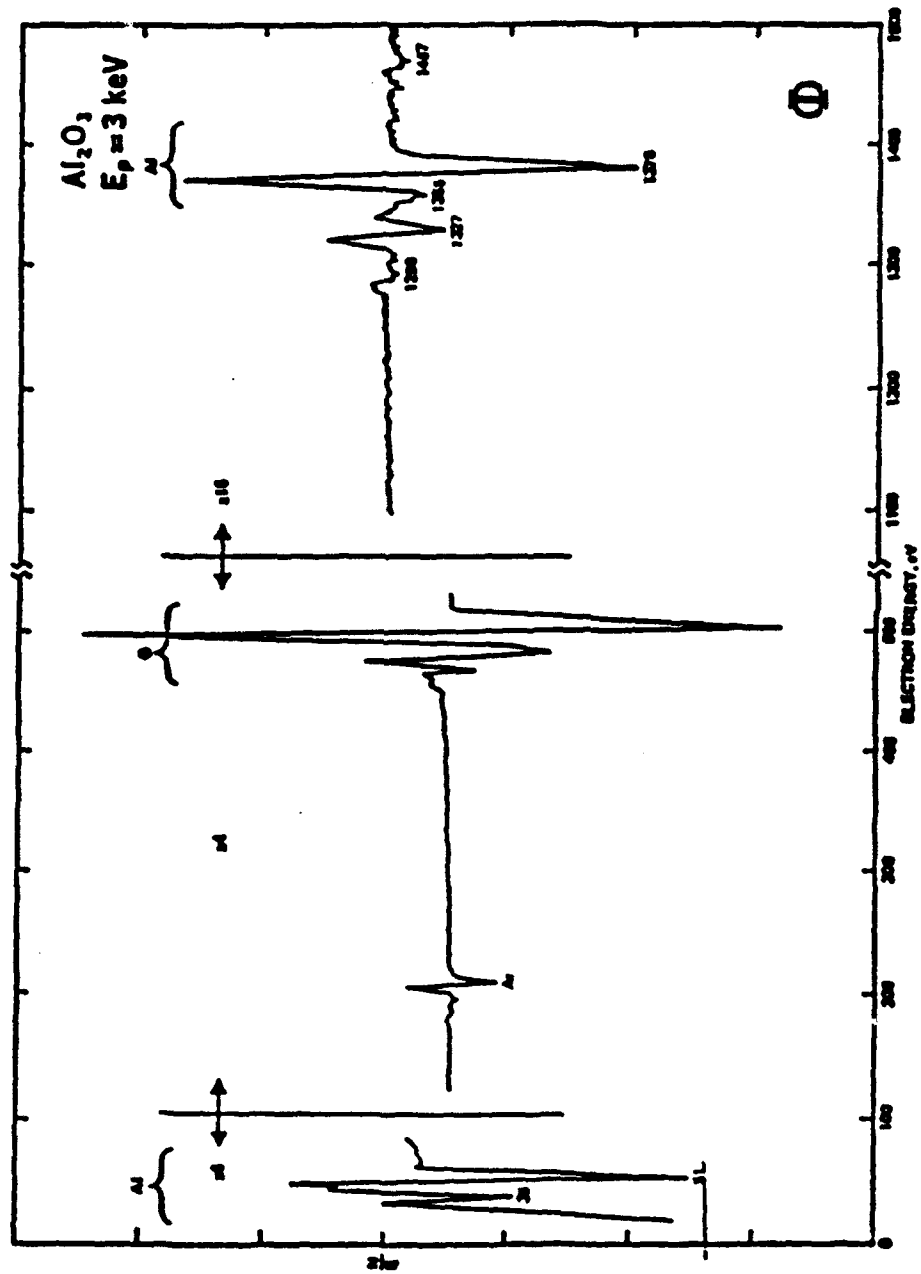


Figure 4.9 Standard Auger spectrum obtained from pure alumina [73].

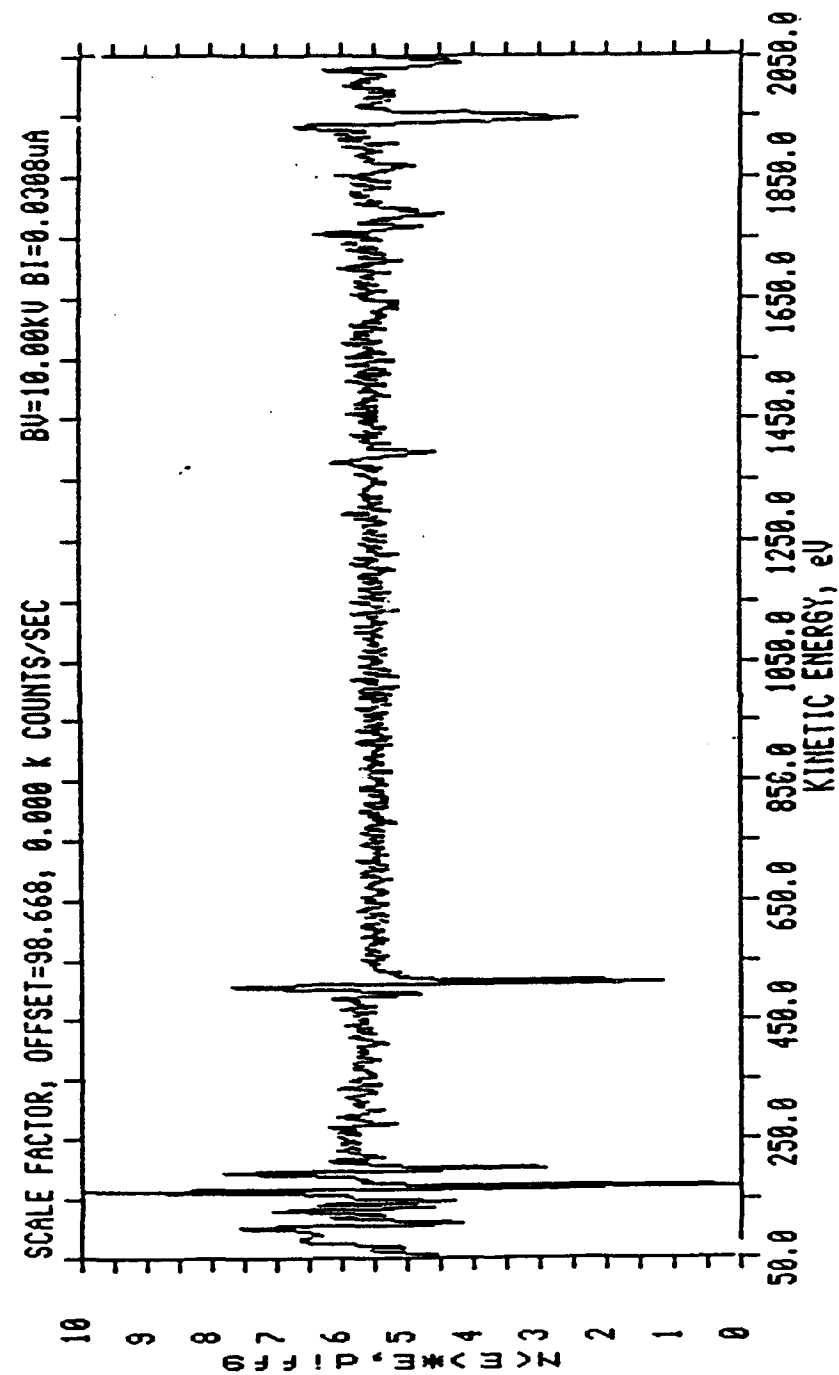


Figure 4.10 Auger spectrum obtained from the matrix ( $\beta$  phase) of a Nb-4.5Al alloy after annealing at 1400 °C for 8.5 hours.

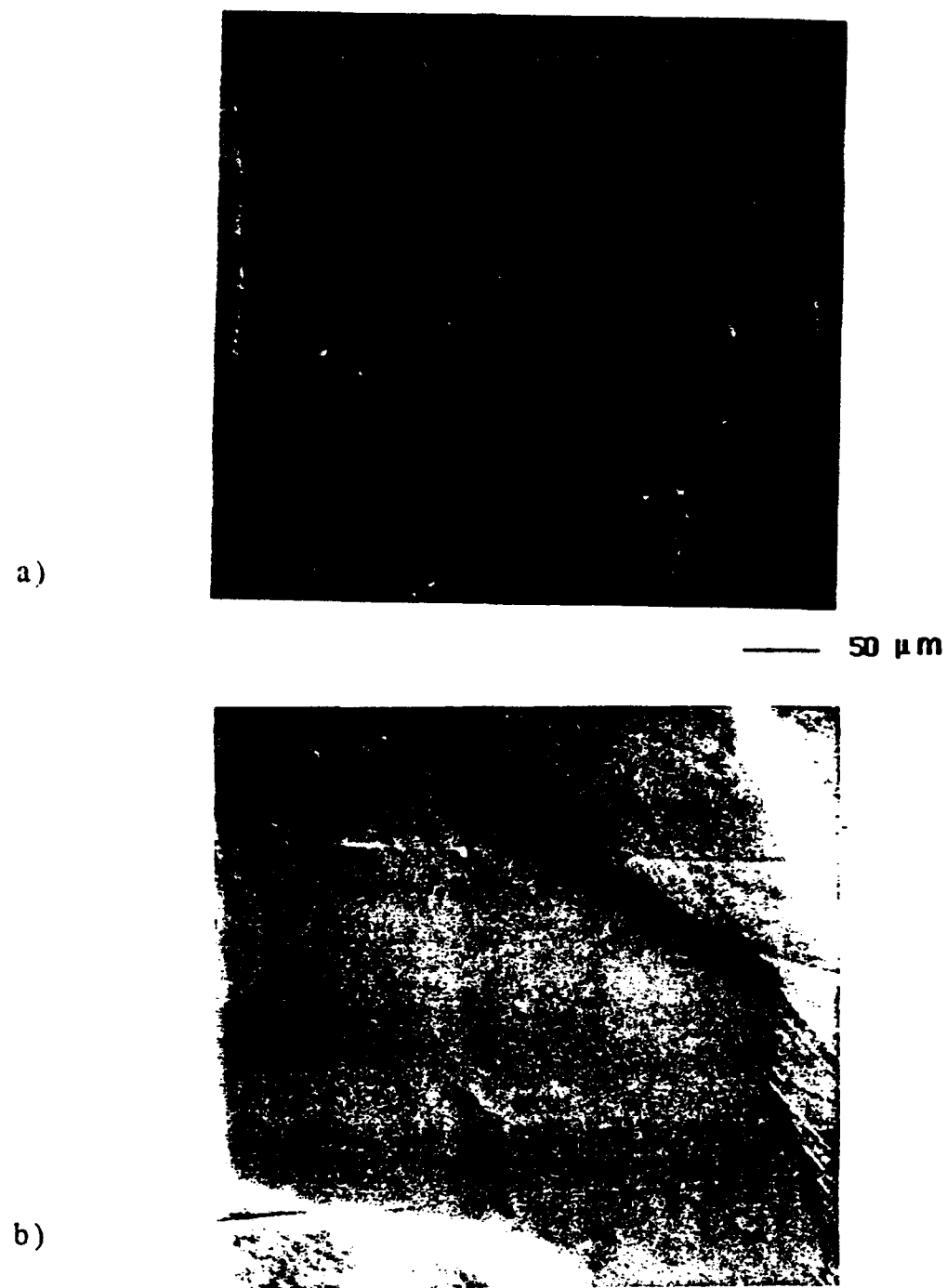


Figure 4.11      Optical micrographs showing the microstructure of a Nb-4.5Al alloy after two different homogenization treatments: a) 1400 °C for 8.5 hours. b) 1400 °C for 6 hours.



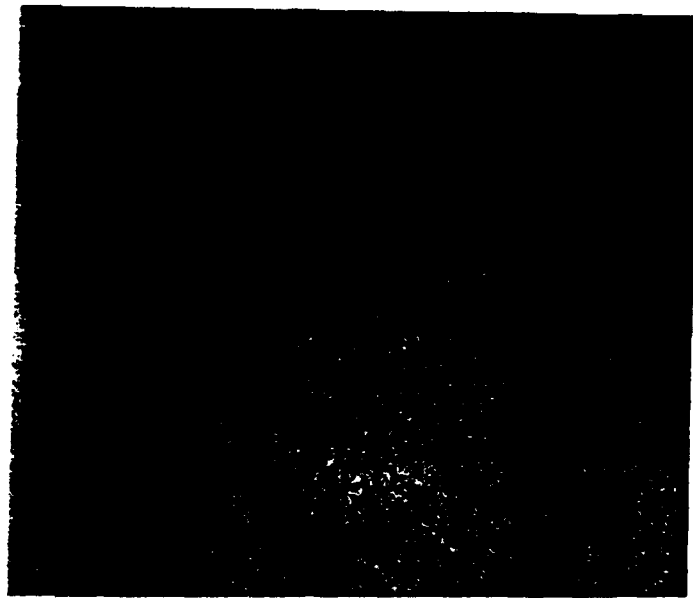
— 100  $\mu\text{m}$

Figure 4.12 A low magnification BSE micrograph of a Nb-4.5Al alloy after being heat treated at 1400°C for 6 hours. Note how the amount of alumina precipitation lessen from top (sample surface) to bottom (sample middle section).

of specimens was very scarce, with an average separation larger than 100 microns (Figure 4.13). As will be confirmed later, this separation between alumina particles is much larger than the penetration depth yielded by the diffusion treatments. Also the aluminum concentration gradient in the matrix close to the alumina particles was very small, as illustrated by the microprobe analysis shown in Figure 4.14. Therefore, even though we could not retard the internal oxidation of the Nb-Al alloy, the extent of it was reduced considerably to such a grade that was considered not to have any influence on the diffusivity measurements. The grain size achieved after the homogenization treatment was very large, approximately ASTM 2 size (Figure 4.11).

### c. Diffusion Bonding

After being homogenized and metallographically prepared, the  $\beta$ -alloy specimen as well as the pure Nb sample were bonded together in a hot-press furnace. Initially chopped zirconia ( $ZrO_2$ ) particles of less than 1  $\mu m$  in size were used as inner markers. Figure 4.15a shows the resultant bonded structure, which looks perfectly clean, free of any kind of precipitation. After the diffusion treatment, extensive precipitation of alumina appeared near the interface on the Nb-Al side as shown in Figure 4.15b. According to thermodynamic data given in Reference [74], zirconia and alumina have similar free energy of formation for equal moles of oxygen. Alumina is more stable at lower temperatures but  $ZrO_2$  becomes more stable at higher temperatures. According to the results found in this study



— 10  $\mu\text{m}$

Figure 4.13      BSE micrograph of a Nb-4.5Al sample as-homogenized condition. Alumina presence in the  $\beta$ -phase matrix is very scarce.

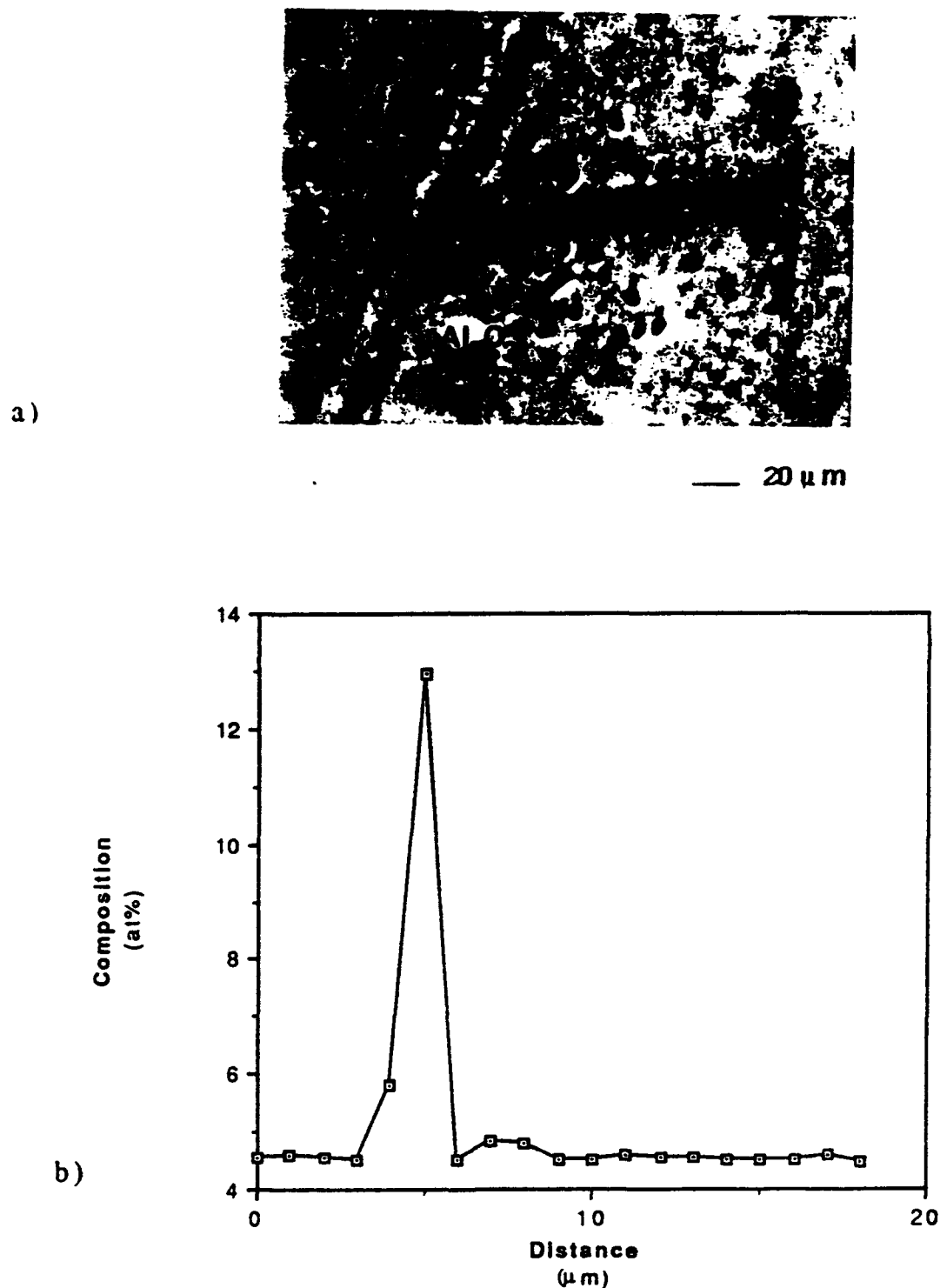


Figure 4.14 a) Secondary Electron micrograph, and b) Al composition profile of  $\beta$ -phase matrix close to an alumina particle.



a)

— 10  $\mu\text{m}$ 

b)

Figure 4.15

A low magnification BSE micrograph of a diffusion couple with zirconia markers: a) Before diffusion treatment, and b) after diffusion treatment at 1400 °C for 4 hours.

apparently a reaction between Al and ZrO<sub>2</sub> took place, and therefore the use of zirconia markers was discarded and yttria Y<sub>2</sub>O<sub>3</sub> markers were used instead. As in the previous case, a clean, precipitate-free bond was obtained under the same experimental conditions. Figure 4.16 shows the structure at the interface along with the composition profile obtained using microprobe analysis. The analytical result suggests that the boundary is sharp, indicating very limited diffusivity of aluminum in the Nb side, a highly desirable feature for the initial bonding of the diffusion couples.

#### 4.2 Diffusivity Analysis

The experimental concentration profile obtained by microprobe analysis from each of the treated diffusion couples were fitted to a smooth curve. Determination of the Matano plane position permitted to compute the interdiffusion flux, concentration gradient and interdiffusion coefficients at each diffusivity temperature. Under the assumption that  $D_{Al} \cdot N_{Nb} \gg D_{Nb} \cdot N_{Al}$ , the intrinsic diffusivity of Al in Nb as a function of composition was determined. Then, the temperature dependency of the coefficient of diffusion of Al in Nb, as well as the corresponding activation energy and frequency factor values were calculated.

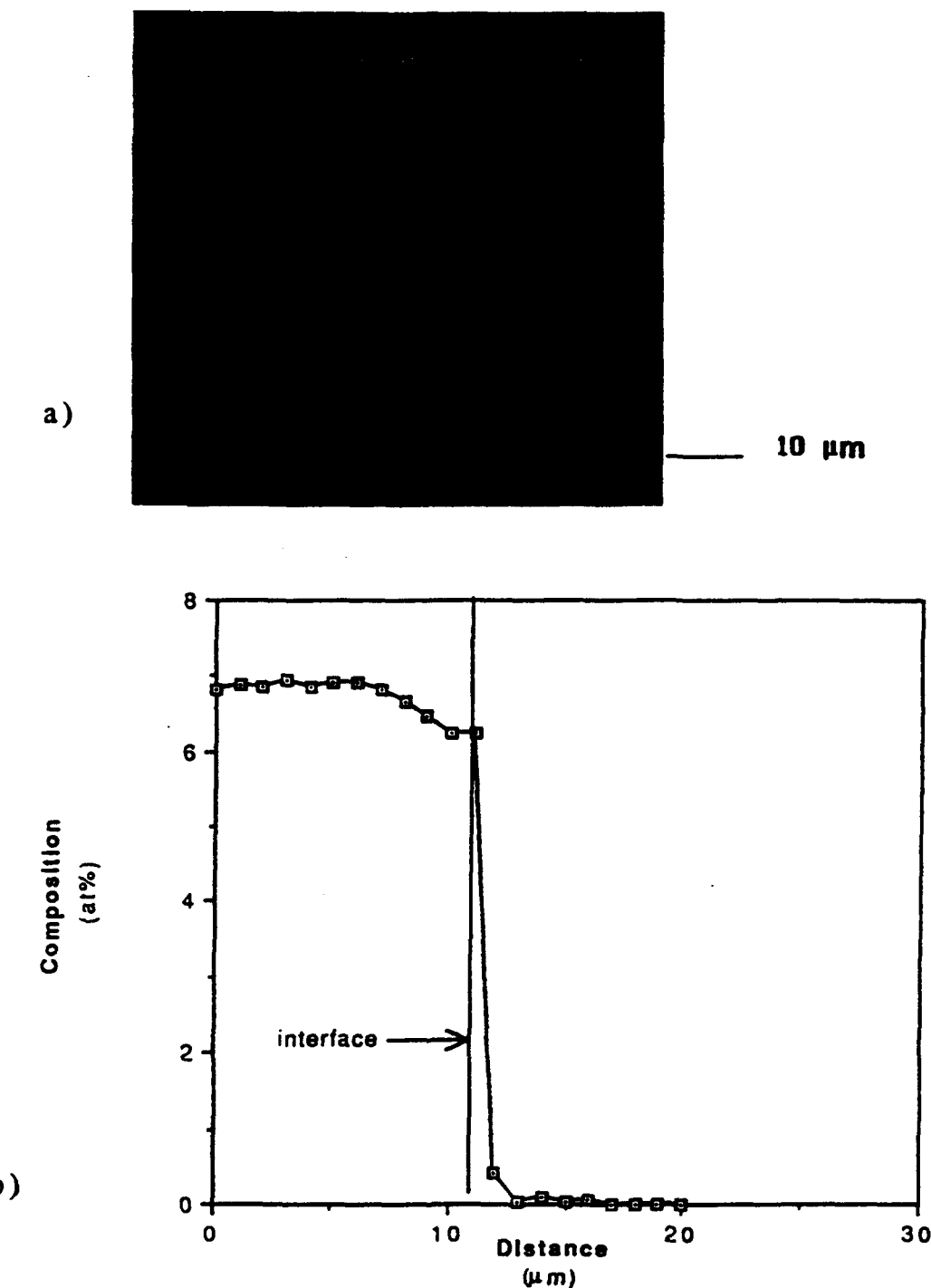


Figure 4.16 a) BSE micrograph of diffusion couple interface with Yttria markers before diffusion treatment, and b) the aluminum concentration profile across the boundary.

#### 4.2.1 Postdiffusion Microstructural Analysis of Binary Diffusion Couples

The use of yttria particles as markers in the diffusion couples inhibited the alumina precipitation along the bonded interface after the diffusion heat treatment. Figure 4.17 shows the resulting microstructure of a couple after interdiffusion treatment. The alumina in the structure of alloy  $\beta_0$  was present scarcely not only along the bonded interface of the couples, but also in the matrix. This fact helps to explain that zirconia particles were the source of oxygen for extensive formation of alumina near the bonded interface, but the material itself also had a propensity to internal oxidation of aluminum in the alloy. Chemical analysis of the interstitial content of the alloy  $\beta_0$  after diffusion treatment is reported in Table 4.1, together with that for the ternary alloys.

#### 4.2.2 Measurement of Concentration Profiles

The microprobe analysis performed used a beam size of approximately one micron. Therefore, the data for the composition profile were obtained from points one micron apart. A statistical resolution (standard deviation) of 0.1 at.% in the counting process was obtained by employing a beam intensity of 100 nanoamper and a dwell time of 200 seconds maximum at each point. When either a lower current or a shorter counting time was employed the tail of the aluminum concentration profile on the Nb side of the couple was missed (Figure 4.18). The compositional resolution obtained by the

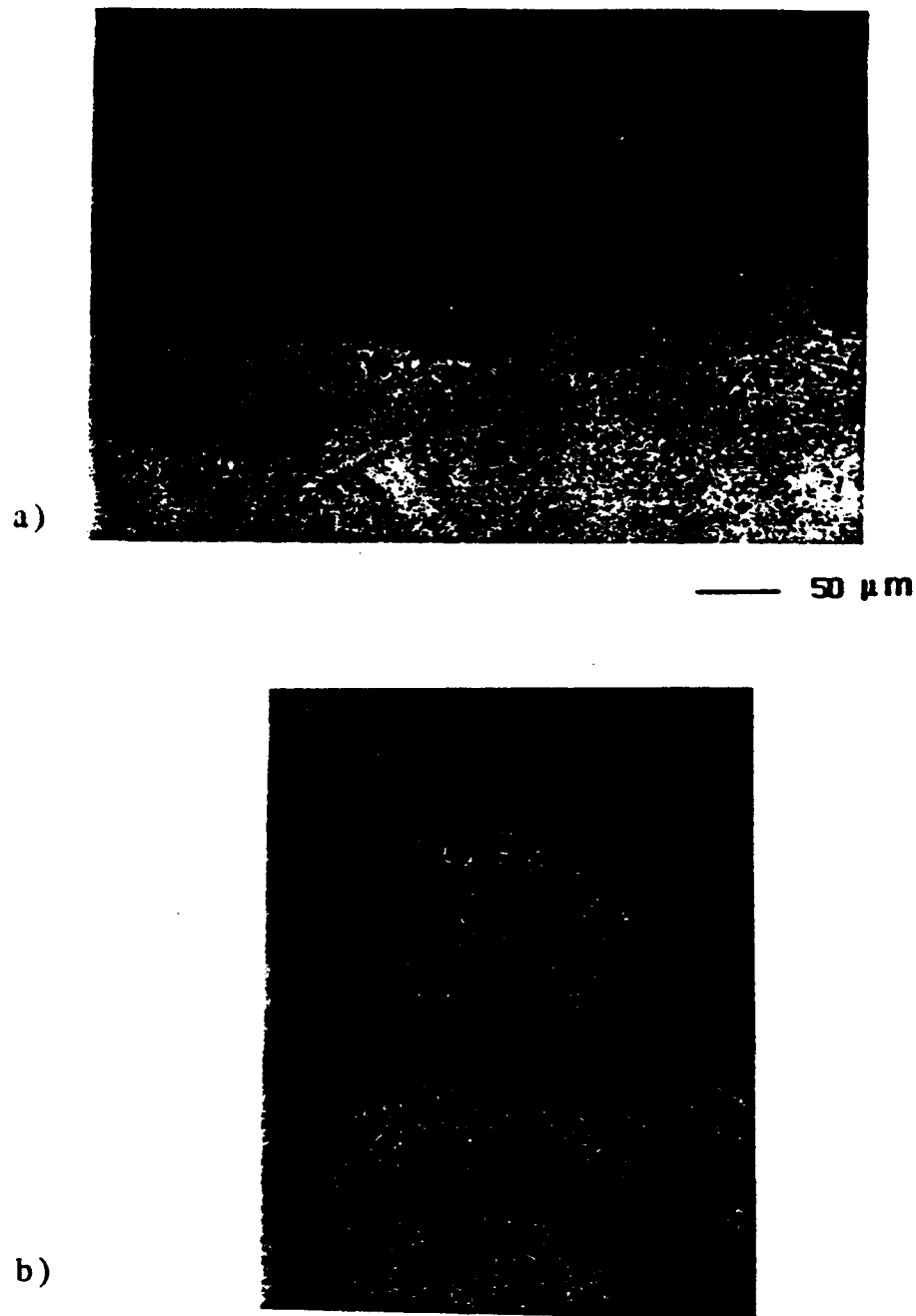


Figure 4.17 Backscattered electron micrographs showing the resultant microstructures of a Nb/Nb-4.5Al diffusion couple after diffusion treatment.  
a) Near interface. b) Away from interface.

Table 4.1 Interstitial content of alloys (\*)

Alloy	C	N	O	H
$\beta_0$	5.8	130	310	-
$\beta_2$	9.1	370	420	1.8
$\beta_3$	4.8	62	310	9.7

(\*) Chemical analysis made by Teledyne Wah Chang.

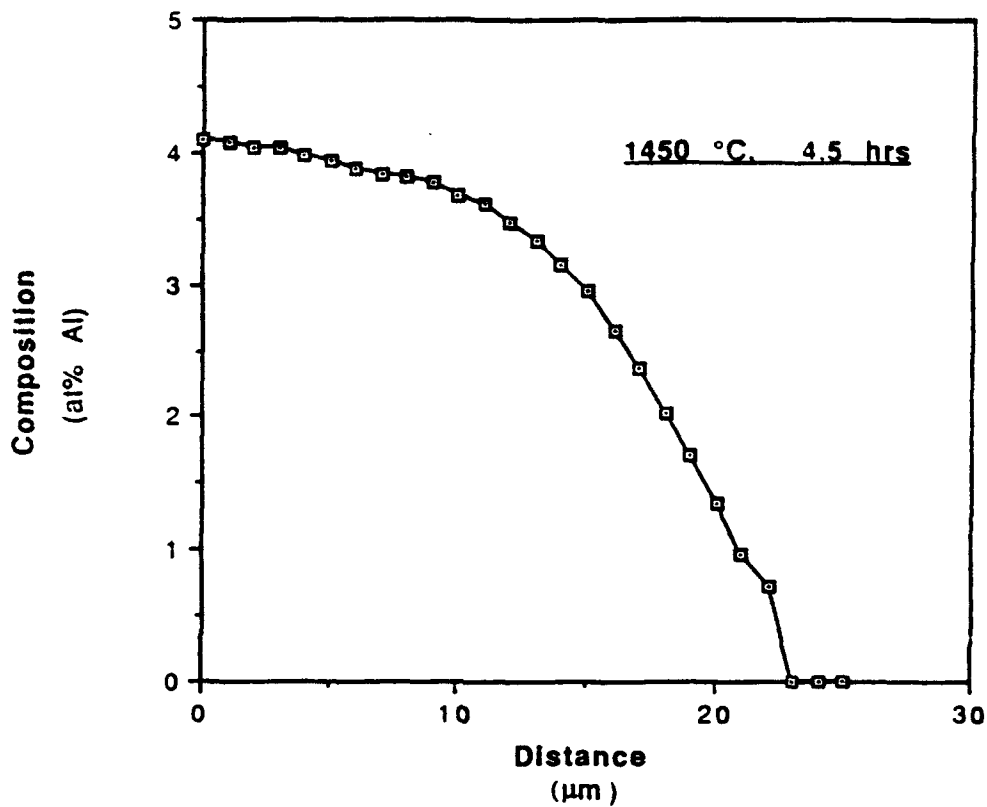


Figure 4.18

A typical experimental composition profile for aluminum obtained by microprobe analysis of a diffusion couple Nb/Nb-4.5Al after annealing at 1450 °C for 4.5 hours. Note the sudden drop in the Al composition profile in the Nb side of the couple.

microprobe analysis is governed by two factors: the background/peak intensity ratio, and the counting statistics. When a standard deviation larger than 0.1% is employed, e. g. 0.25%, the counting time for the analysis is shorter, and the number of events (x-ray counts) detected will be smaller. Consequently, in regions where the Al composition is low, the x-ray counts will be insufficient to be taken into account, and therefore the aluminum concentration at those points will be detected as zero%. The change to the condition mentioned above permitted to detect the missing part of the profile as more counts were detected at longer times. On the other hand, it was observed that employing longer analysis time results in a severe contamination of the surface of the sample, as observed in Figure 4.19. However, comparison of the experimental composition profiles obtained under the two conditions revealed no differences in the general result. The measurement of the Al concentration at each point took approximately 6-7 minutes. In average, to obtain an entire profile took 5 hours. A minimum of two profiles were measured for each diffusion couple. A typical composition profile is shown in Figure 4.19.

#### 4.2.3 Concentration Profile Analysis

The experimental raw data consisting of a set of positions along the diffusion direction and the corresponding concentrations of aluminum (atomic %) were fitted to a smooth curve using a modified spline cubic method [8]. To do so, generally, the set of  $n$  data points is divided into intervals separated by knots. These knots set imaginary regions along the composition profile in accordance to the general

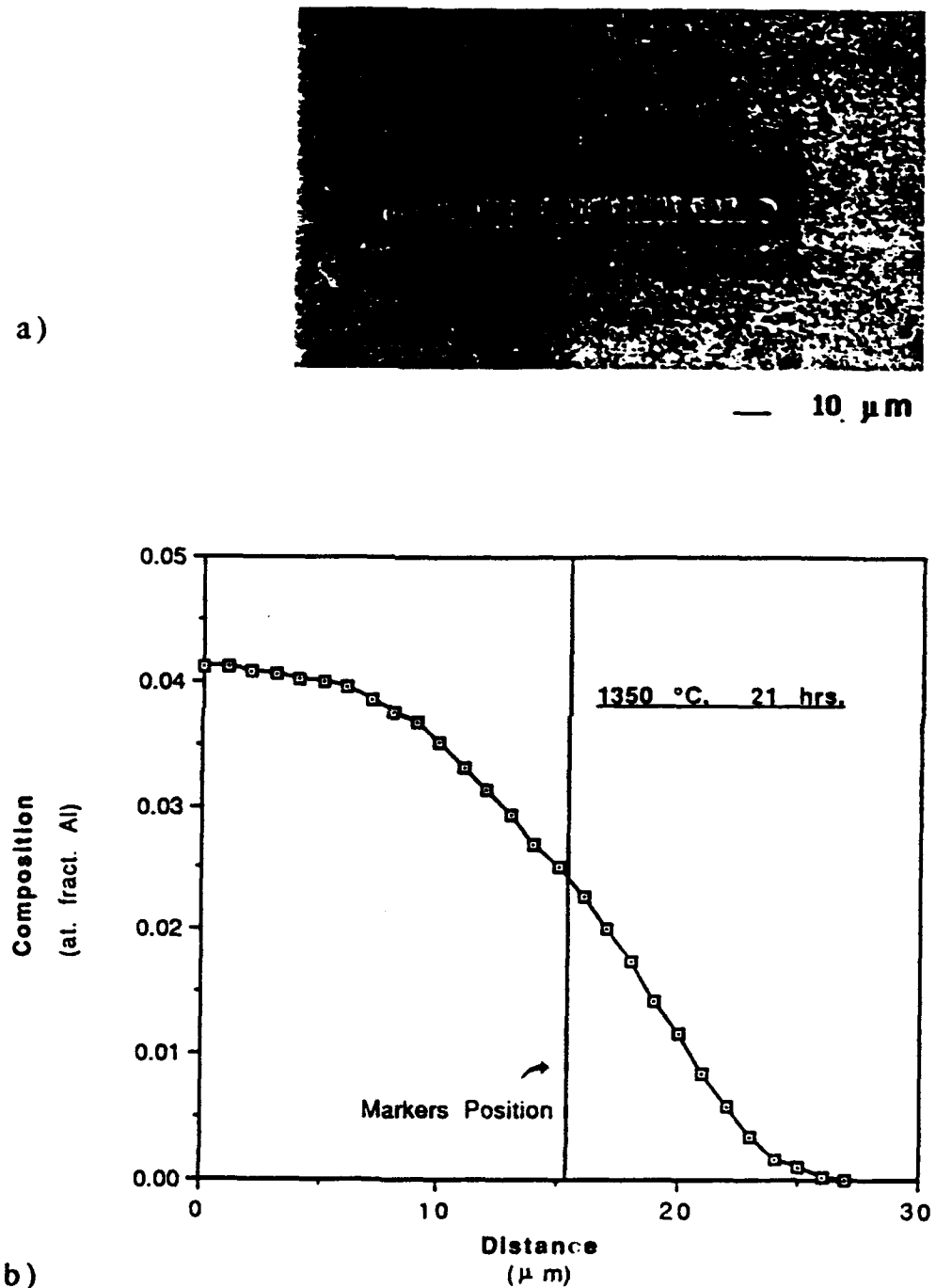


Figure 4.19

a) Secondary electron micrograph, and b) a typical experimental composition profile for Al obtained by microprobe analysis of a Nb/Nb-4.5Al diffusion couple after annealing at 1350 °C for 5.5 hours.

shape of the curve in that region (linear, parabolic, or spline cubic). The spline cubic zone is also subdivided in intervals separated by knots and then a cubic spline function fits a different cubic polynomial to the data in each interval of this zone. For example, the polynomial for the  $i^{th}$  interval will be:

$$C_{Ai}(x) = c_{i1} + c_{i2}(x-x_i) + c_{i3}(x-x_i)^2 + c_{i4}(x-x_i)^3 \quad (4.6)$$

where  $C_{Ai}(x)$  = Fitted concentration curve in the  $i^{th}$ . interval

$c_{ij}$  = Cubic coefficients for the  $i^{th}$ . interval

$x_i$  = position of the  $i^{th}$  data point

$x_j$  = position of the  $i^{th}$  knot

The coefficients  $c_{ij}$  and the final knot positions are determined by minimizing the least squared error of the fitted curve to the constraint that the function  $C_{Ai}(x)$  and its first two derivatives must be continuous at each knot. The number of knots used for the cubic spline fitting is important. The larger number of knots used tends to minimize the least square error, i. e., increase the goodness of the fit. In addition, five data points per interval must be set so that a third degree polynomial is adequately fitted. For the case of the modified spline cubic routine used in this research, the domain of data of the diffusion experiments are divided into five different regions, as shown in Figure 4.20. The central part of the data is fitted by a cubic spline approximation as mentioned above, and the points deemed to be outside of the diffusion zone are fitted with horizontal lines whose ordinates are the end concentrations of the alloys forming the diffusion couple. The reason for this horizontal line sections is that cubic spline fits do not easily yield flat sections typical of diffusion data outside the diffusion zone. Since neither the value of the spline

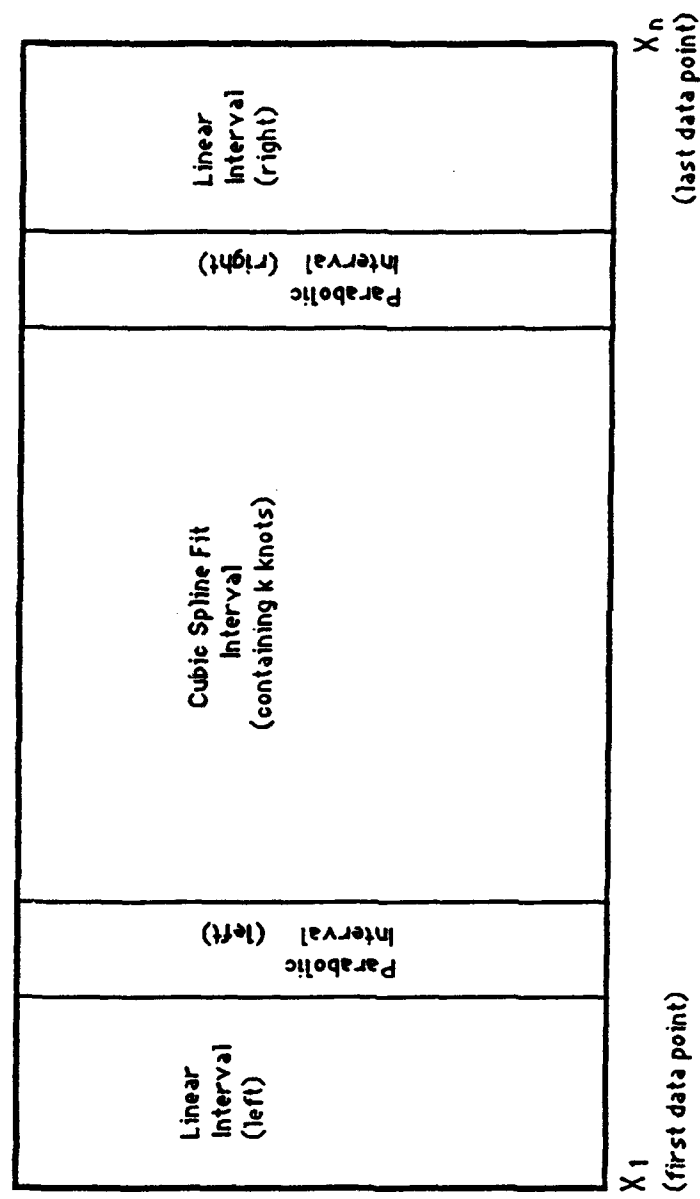


Figure 4.20 Schematic representation of the modified cubic spline intervals employed for curve fitting.

cubic nor its first derivative may be specified at the edges of the region fitted with cubic splines, small parabolic sections are used to smoothly join the cubic spline region with the linear zones. These parabolic sections are constrained to match ordinates and slopes with the horizontal line sections and ordinates with the cubic spline curves. When the limits for the parabolic section were not properly chosen, the fitted curve exhibited small discontinuities that do not belong to the data (Figure 4.21). To avoid this problem several intervals for the parabolic limits where tried. This matter is discussed in detail in a subsequent section.

The program used for curve fitting produced two output files. One file contained the polynomial equations employed for the other subroutines to calculate parameters such as the Matano interface, interdiffusion fluxes, concentration gradients, and coefficients of interdiffusion; the other output file contained 100 data points of the fitted curve, which were also computed by the polynomial equations in the previous file. Figure 4.22-4.26 contrast the experimental profiles with those after curve fitting for the different diffusion treatments performed in this investigation. It can be observed that there are not discontinuities along the entire profile and a smooth curve could be obtained.

#### 4.2.4 Calculation of the Interdiffusion Coefficient

##### a. Determination of the Matano Interface

The position of the Matano interface was calculated in order to evaluate the coefficient of interdiffusion in the binary alloy couple

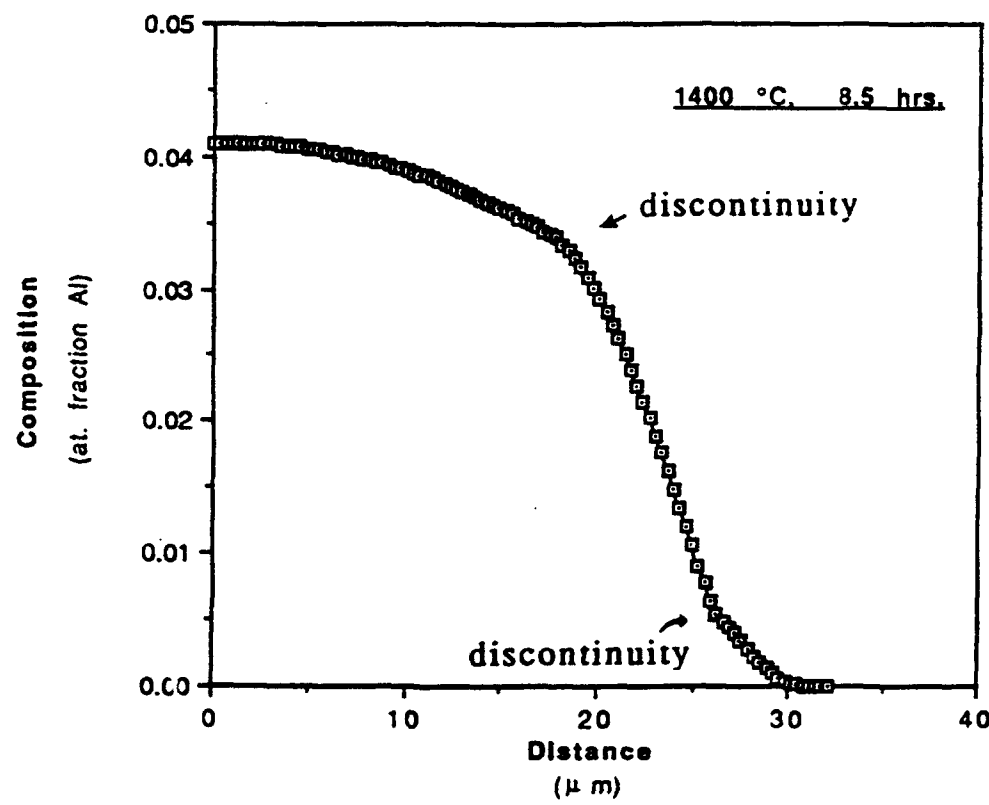
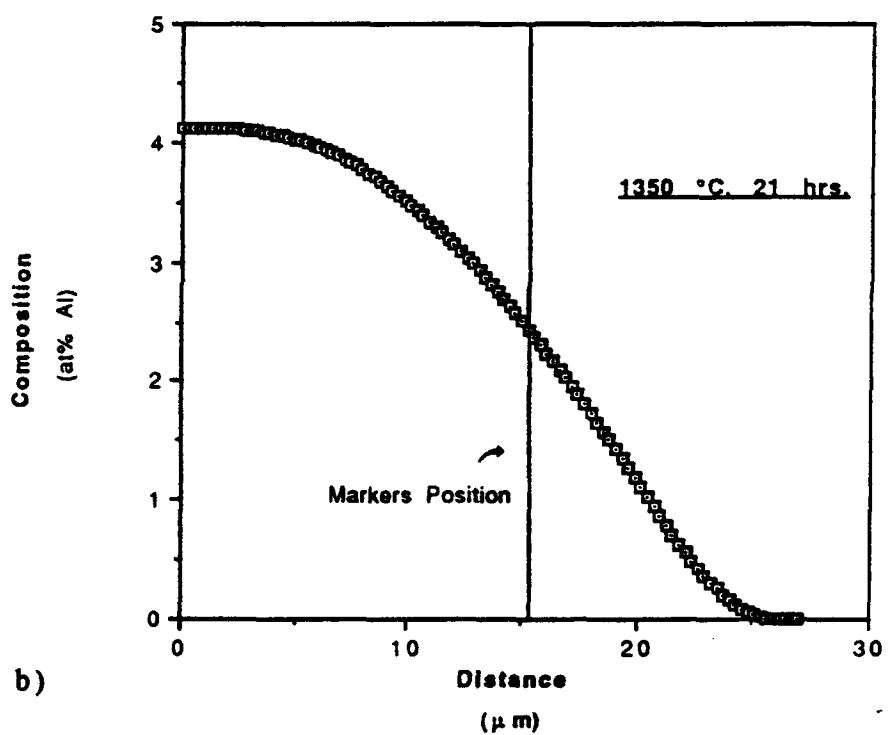
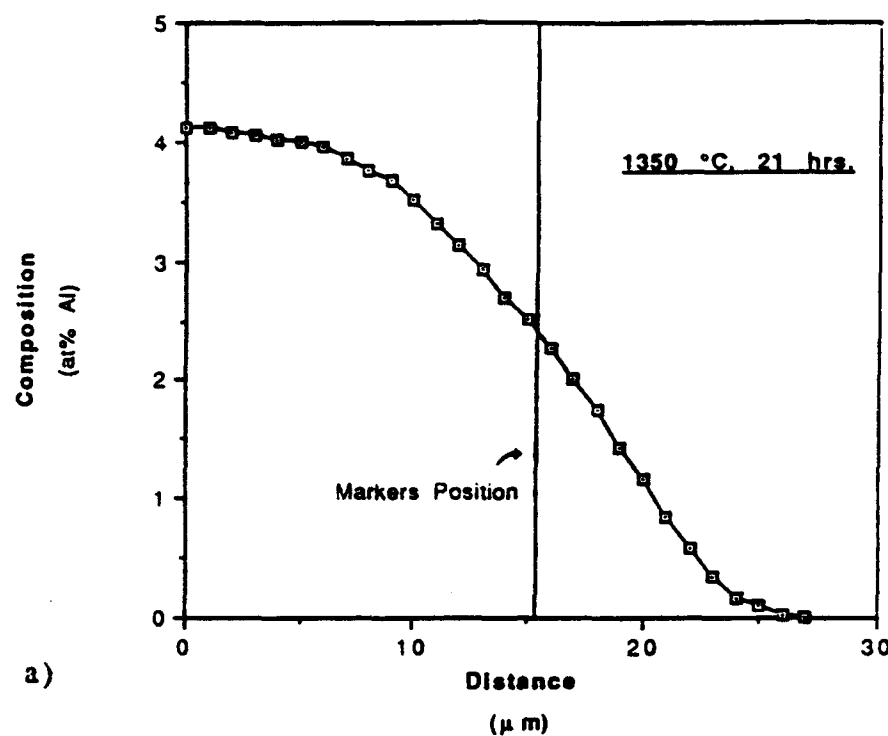


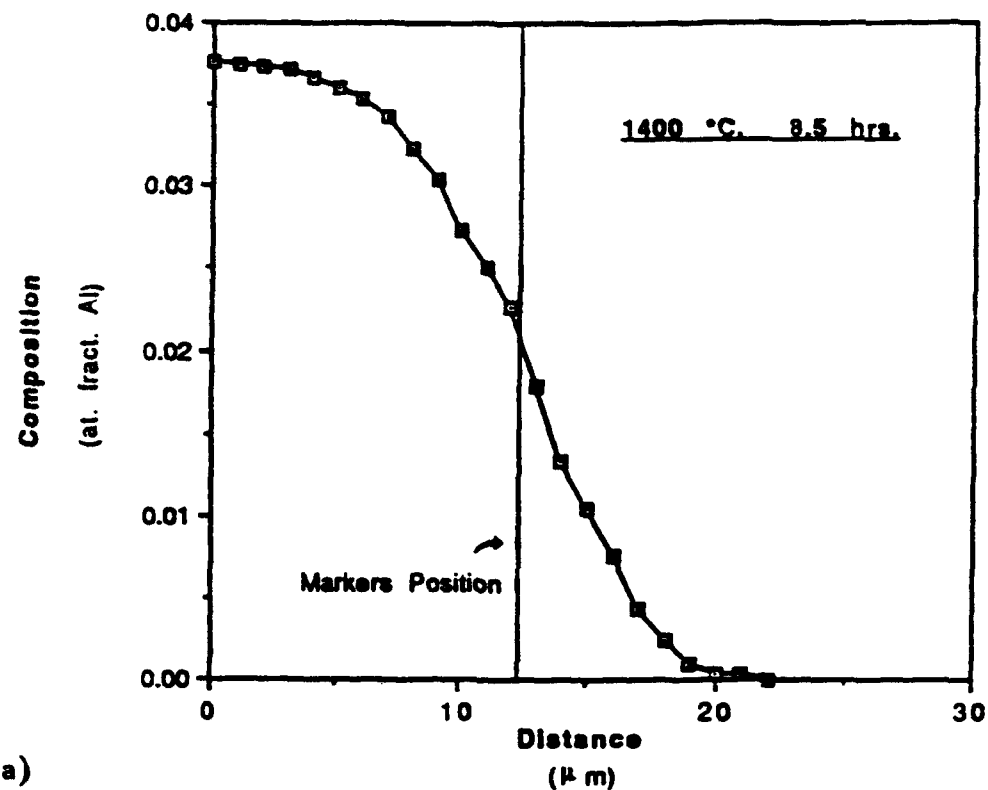
Figure 4.21

A typical composition profile for aluminum after incorrect spline cubic fitting. Note the discontinuities along the curve.

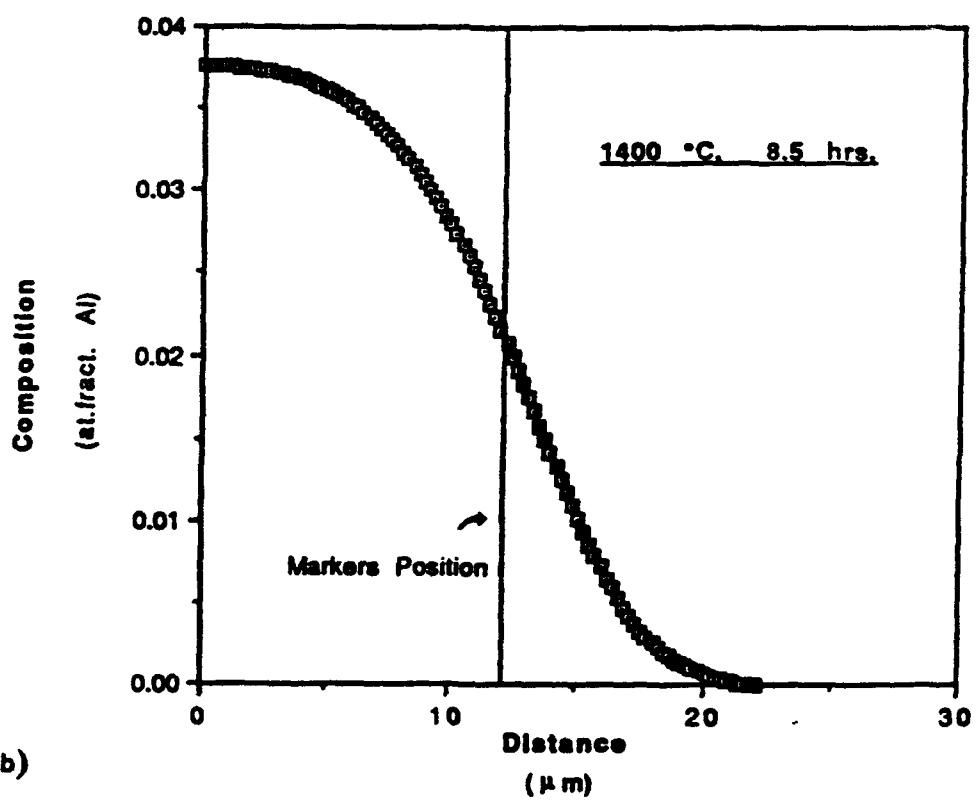
Figure 4.22 Fitting of experimental composition profiles by the spline cubic method for the Nb/Nb-4.5Al couple heat treated at 1350 °C:  
a) Experimental curve,  
b) Fitted profile.



**Figure 4.23** Fitting of experimental composition profiles by the spline cubic method for the Nb/Nb-4.5Al couple heat treated at 1400 °C:  
a) Experimental curve,  
b) Fitted profile.



a)



b)

**Figure 4.24** Fitting of experimental composition profiles by the spline cubic method for the Nb/Nb-4.5Al couple heat treated at 1450 °C:  
a) Experimental curve,  
b) Fitted profile.

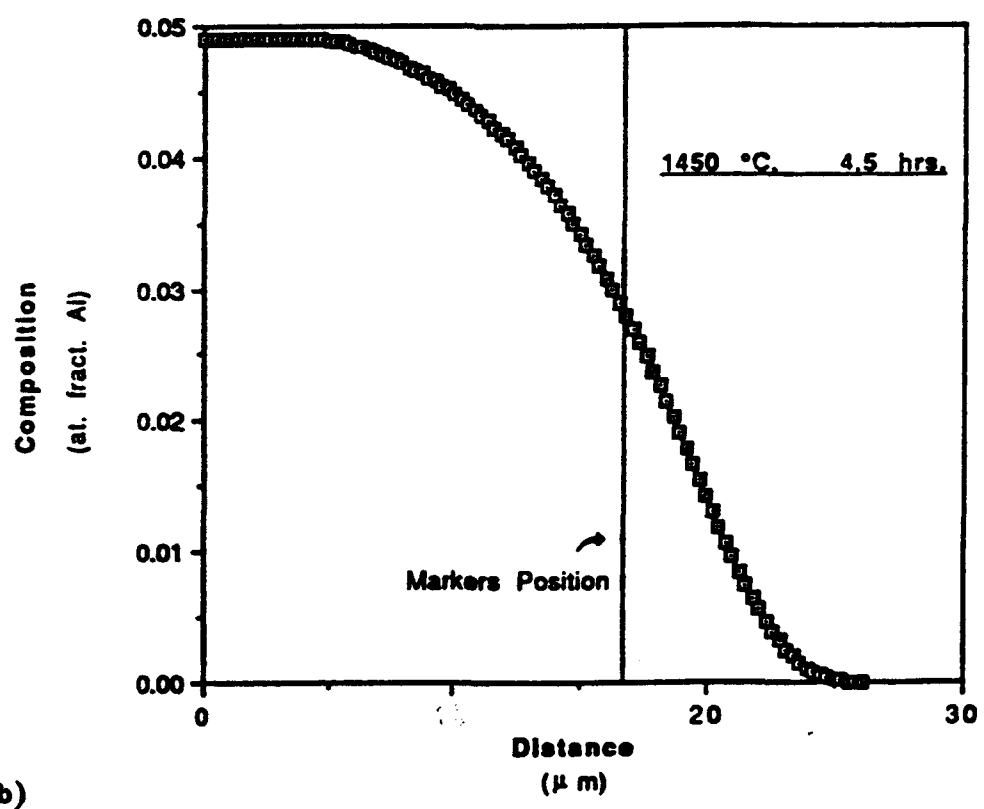
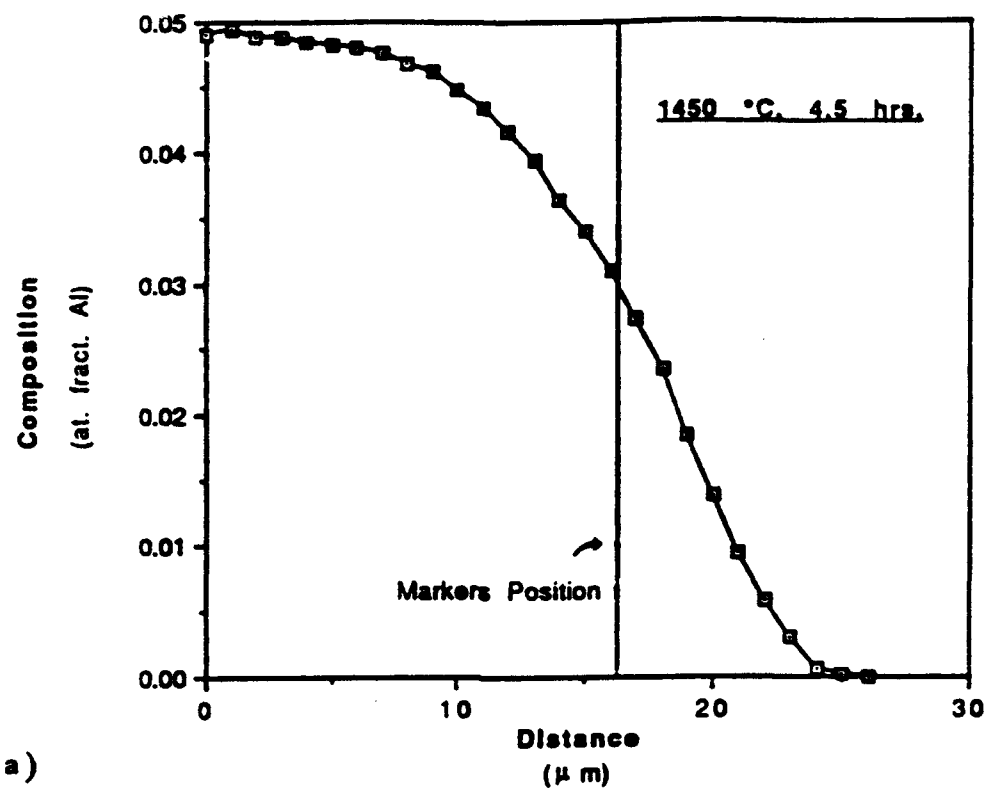


**Figure 4.25** Fitting of experimental composition profiles by the spline cubic method for the Nb/Nb-4.5Al couples heat treated at 1500 °C:  
a) Experimental curve,  
b) Fitted profile.

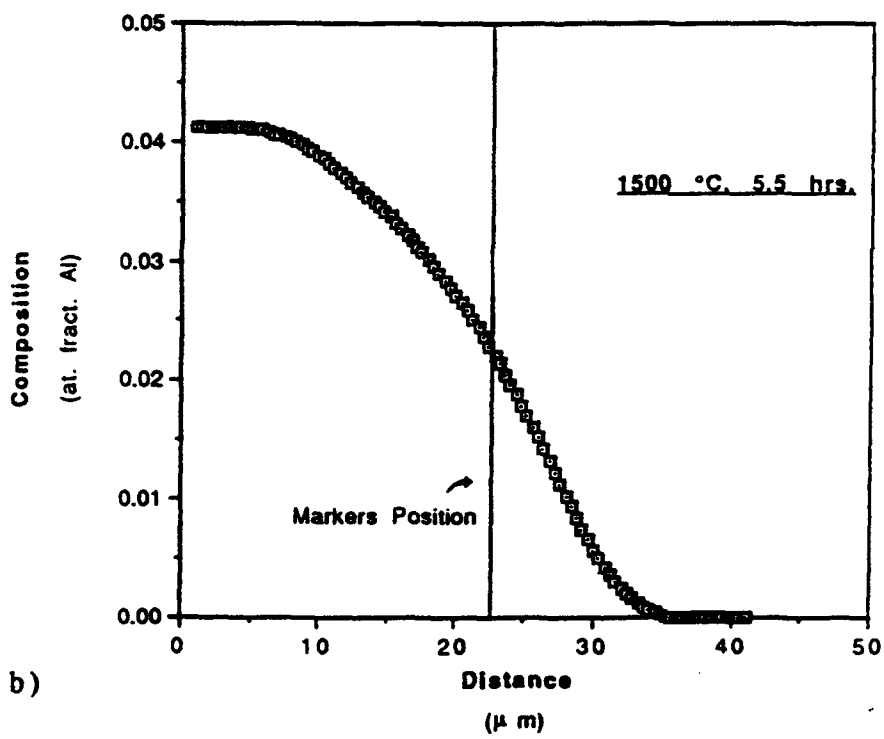
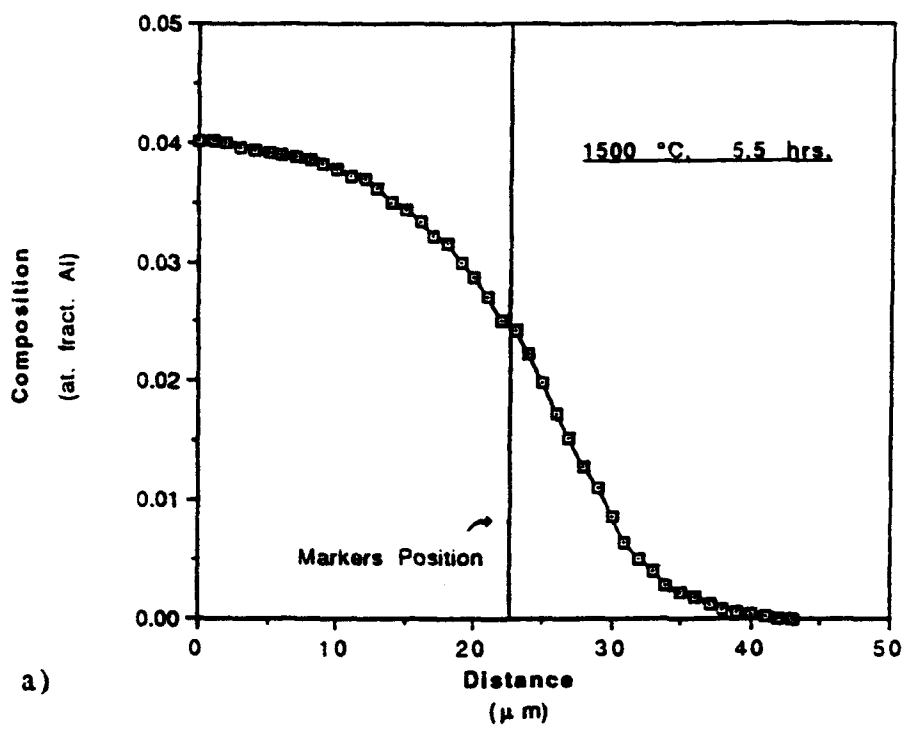
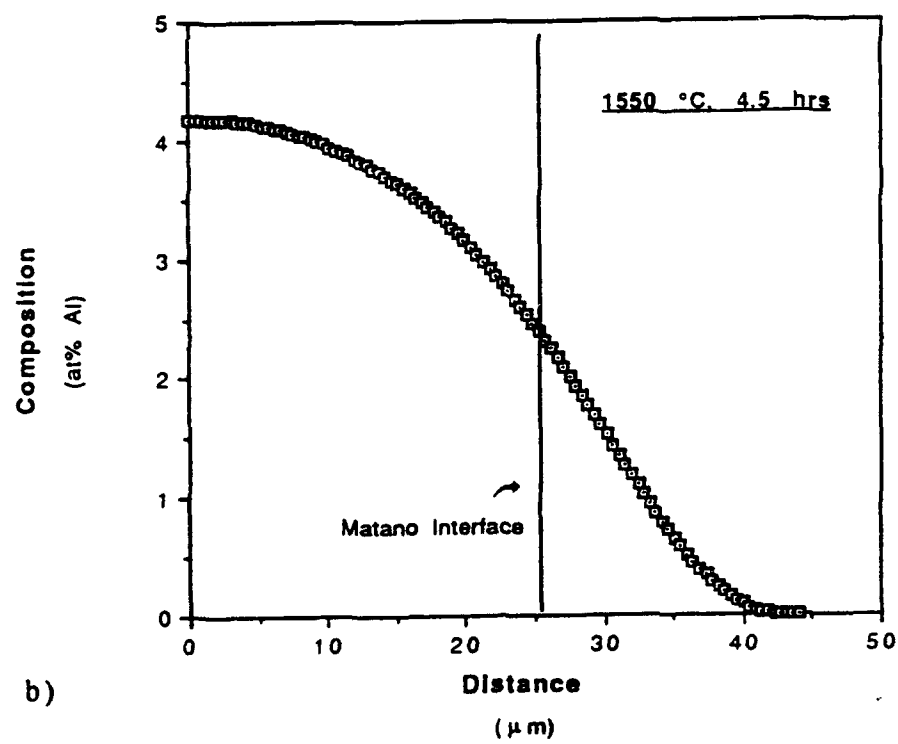
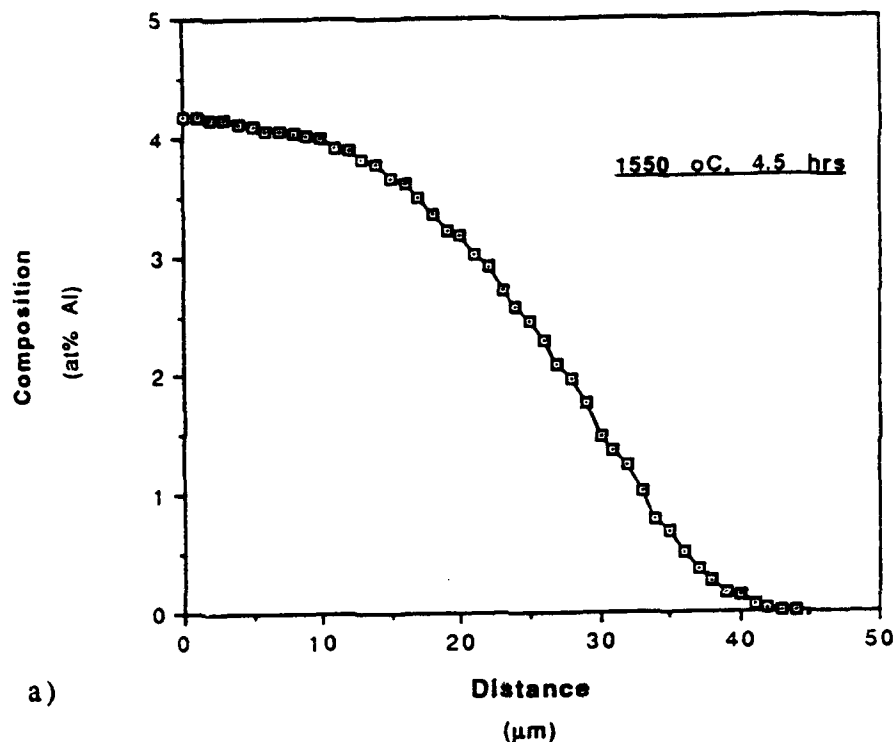


**Figure 4.26** Fitting of experimental composition profiles by the spline cubic method for Nb/Nb-4.5Al couple heat treated at 1550 °C:  
a) Experimental curve,  
b) Fitted profile

**Note:** Position of the marker plane was not determined accurately at 1550 °C; instead, position of the Matano Plane in the fitted profile is provided.



using the Matano-Boltzmann technique. The position of the Matano plane can be determined as a function of known quantities as:

$$x_m = (x_- C_{Al^-} - x_+ C_{Al^+} + \{A\}) / (C_{Al^-} - C_{Al^+}) \dots \dots \dots (4.13)$$

where  $\{A\}$  = entire area under the curve.

$x_-, x_+$  = terminal position values at the end of the diffusion zone.

$C_{Al^-}, C_{Al^+}$  = terminal composition values at the end of the diffusion zone.

Equation 4.13 was applied to the fitted composition profiles computed for Al concentration data from each diffusion couple as those shown in Figures 4.22-4.26.

### b. Evaluation of $J_i(x)$

The interdiffusion flux  $J_i$  was calculated as:

$$J_i(x) = 1/2t [ (x - x_m) C_i(x) - (x_+ - x_m) C_i^+ + \int_x^{x_+} C_i dx ] \dots \dots \dots (4.16)$$

Here  $t$  is the diffusion time and  $C_i^+$  is the terminal concentration of the  $i^{\text{th}}$  component at the right end of the diffusion zone. Once the Matano interface is evaluated, all the parameters in equation 4.16 are known, and the interdiffusion flux can be evaluated at each point on the concentration fitted curve. Figure 4.27 and 4.28 show examples of the computed interdiffusion flux profile. As expected, the maximum value of flux is obtained at the Matano plane location, and it is larger at higher temperatures.

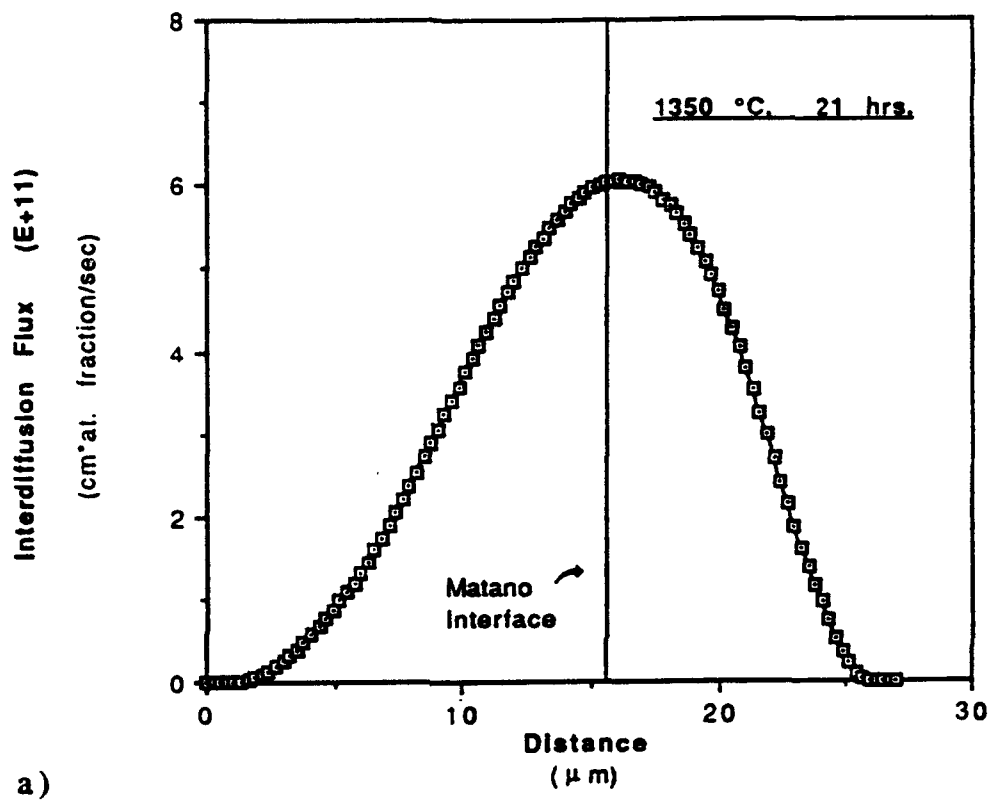


Figure 4.27 a) Typical calculated interdiffusion flux profiles for binary diffusion couples Nb/Nb-4.5Al interdiffused at 1350 °C.

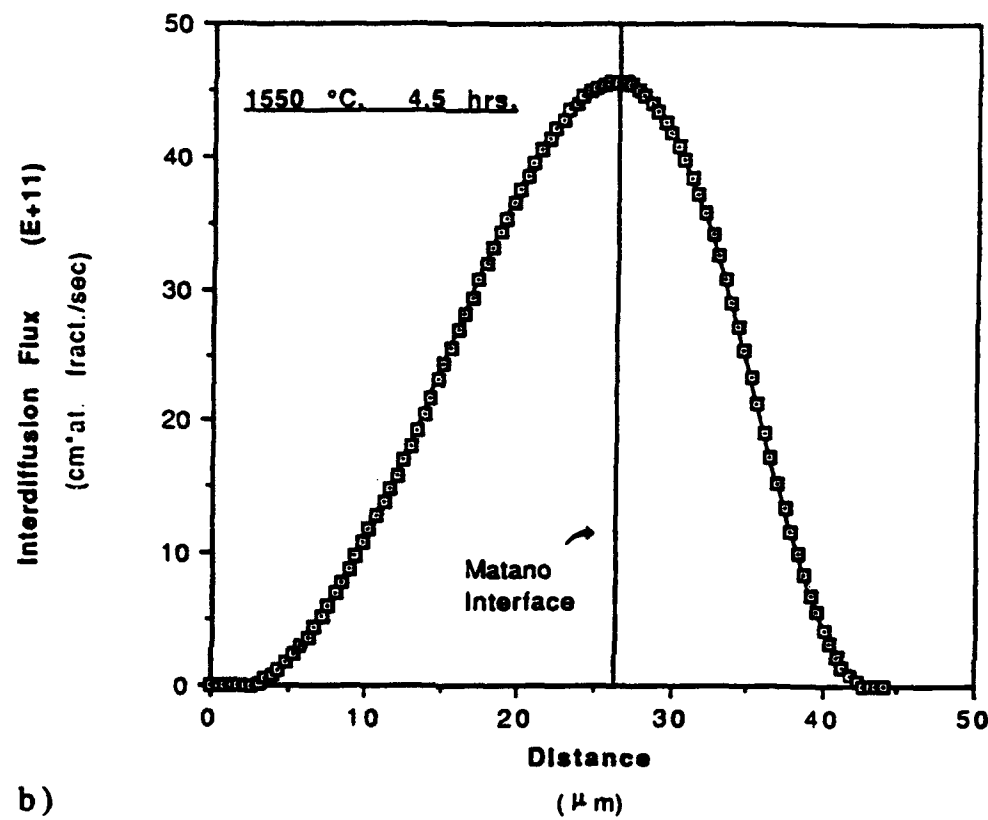


Figure 4.28 b) Typical calculated interdiffusion flux profiles for binary diffusion couples Nb/Nb-4.5Al interdiffused at 1550 °C.

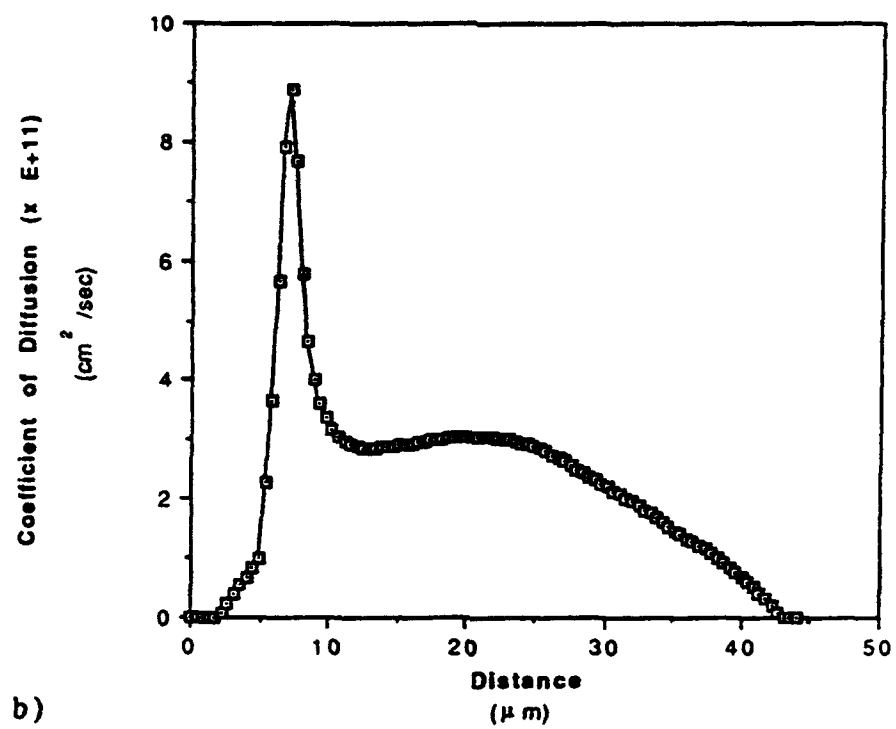
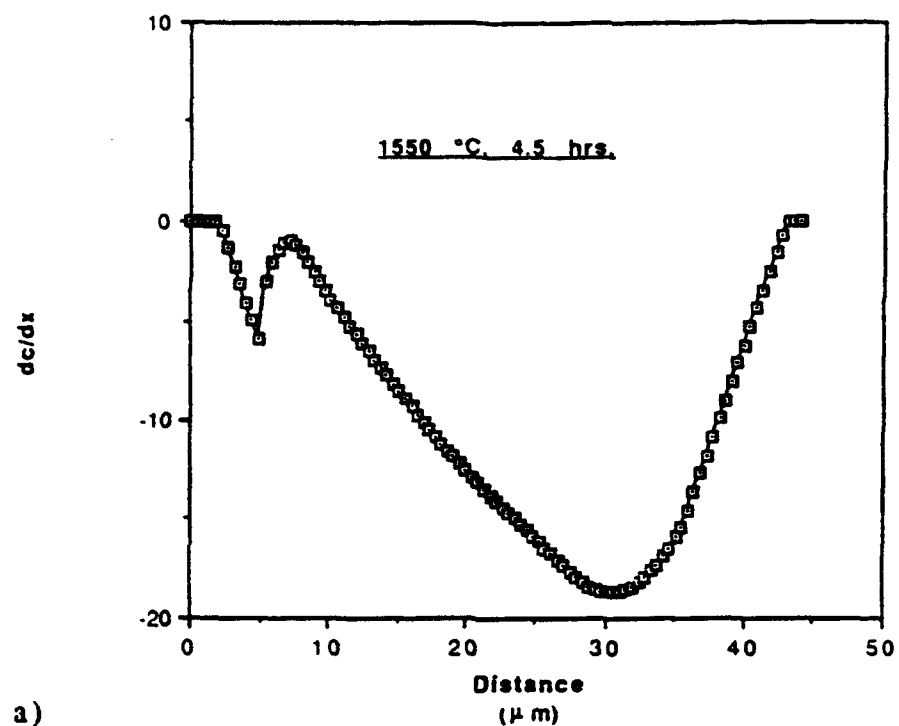
### c. Evaluation of Concentration Gradient

The composition gradient was calculated by finding the analytical derivatives of the fitted equations to the concentration profile. It was found that the calculated concentration gradient was very sensitive to the choice of the limits for connecting the parabolic zone to the linear and spline cubic regions during the curve fitting procedure. Even though the concentration fitted curve appeared to be smooth and continuous, the fitting method did not provide a continuous derivative, and discontinuities and/or jumps in both gradient concentration and diffusivity curves were observed (Figure 4.29). It was noted that the number of knots employed into the cubic spline region affected such profiles. By try and error suitable limiting positions of the different regions along with different number of knots, that resulted in a smooth curve for the concentration gradient as a function of position, were obtained. It was noted that the linear-parabolic connection was easier to fit than the parabolic-spline cubic one. The link of the three regions was easier to get in the pure Nb side of the couple as the concentration profile was steeper at very low Al concentrations, where the parabolic region extended for a few microns. The connection on the other side of the couple, on the other hand, was much more difficult as a larger penetration of the diffusion zone in the Nb-Al alloy ( $\beta\alpha$ ) was obtained, producing a less step concentration gradient. This asymmetry in the concentration profile, with a deeper penetration on the high aluminum side, reflects a difference in the intrinsic diffusivity of the two components, indicating that the aluminum may move faster than niobium.

**Figure 4.29**

Typical calculated composition gradient and interdiffusion coefficient profiles illustrating false peaks due to a bad designation of parabolic regions during the fitting procedure for binary diffusion couples Nb/Nb-4.5Al interdiffused at 1550 °C.

- a) Derivative
- b) Coefficient of Interdiffusion



d. Evaluation of Diffusivity, Activation energy, and Frequency Factor

When adequate links were set, smooth profiles of interdiffusion coefficient were obtained. Figures 4.30-4.34 present the calculated composition gradient and composition-dependent interdiffusion coefficient curves for the b.c.c. solid solution of the binary Nb-Al system in the temperature range of 1350 °C to 1550 °C. The interdiffusion coefficients are summarized in Table 4.2, where the variation of the interdiffusivity with the composition is evident as it drops at lower Al contents. The interdiffusion coefficient showed a linear dependency on the Al concentration as shown in Figure 4.35. The diffusivity coefficient doubles its value at a given temperature with an increase in concentration from 1 to 3 at% Al. This strong dependency suggests that the activity coefficient of Al depends considerably on the composition of Al.

The variation of the interdiffusion coefficient as a function of temperature was found to obey an Arrhenius type behavior. The activation energy and frequency factor values were computed according to:

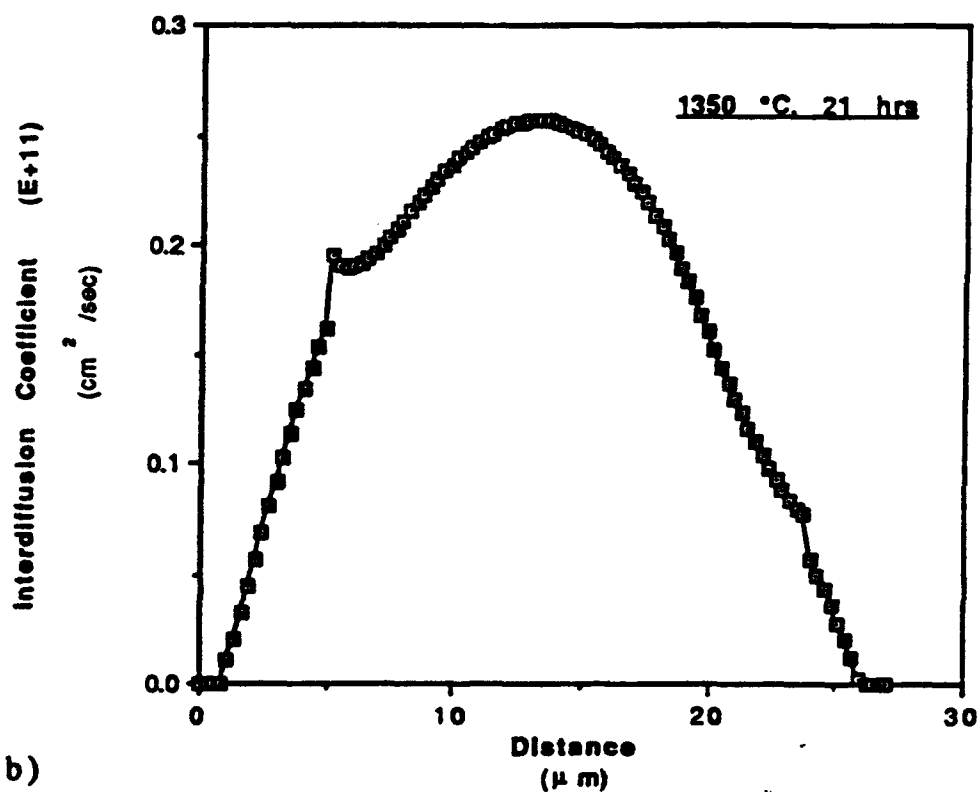
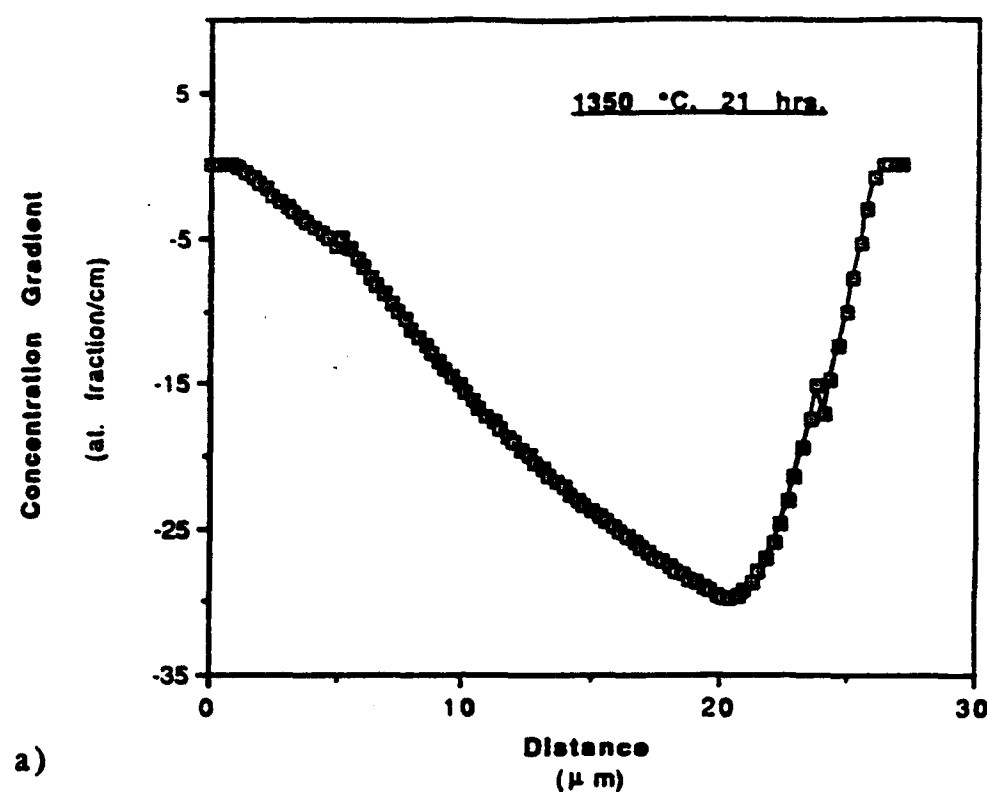
$$D = D_0 \exp(-Q/RT) \quad \dots\dots\dots (4.17)$$

Table 4.3 shows the resultant values of Q and  $D_0$  as a function of composition. The average values for the activation energy Q and frequency factor  $D_0$  in the temperature range from 1350° to 1550 °C were found to be:

$$Q = 80.165 \text{ Kcal}$$

$$D_0 = 0.1136 \text{ cm}^2/\text{sec}$$

**Figure 4.30** a) Composition gradient, and b) interdiffusion coefficient profiles for Nb/Nb-4.5Al diffusion couple heat treated at 1350 °C.



**Figure 4.31** a) Composition gradient, and b) interdiffusion coefficient profiles for Nb/Nb-4.5Al diffusion couple heat treated at 1400 °C.

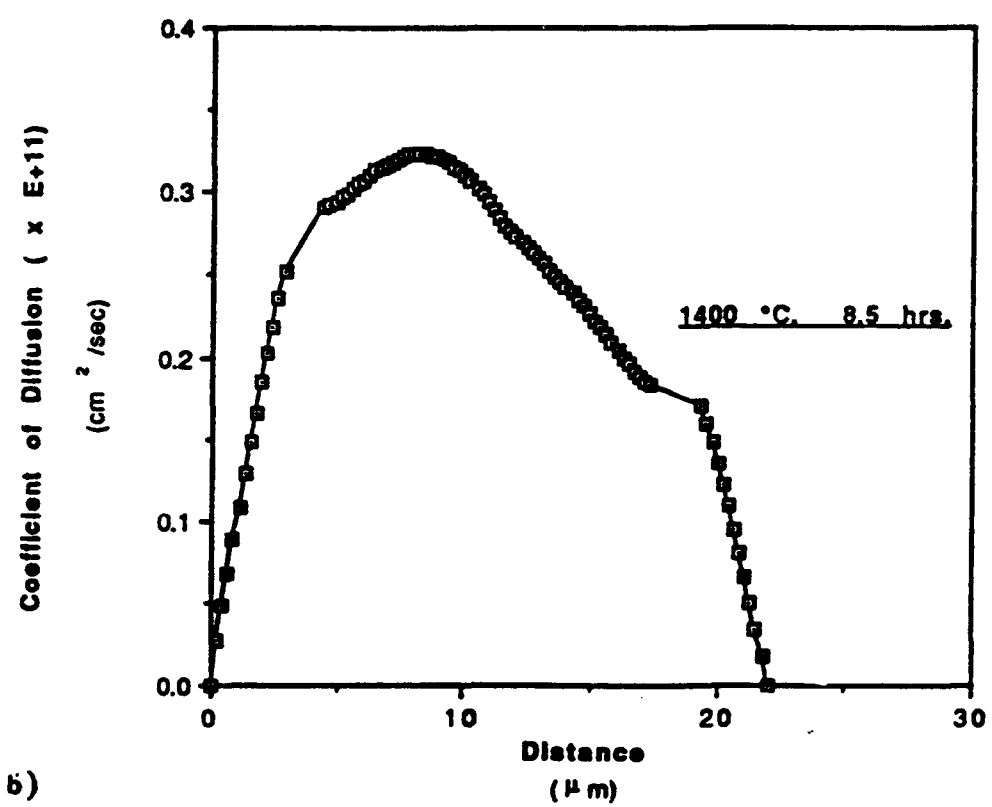
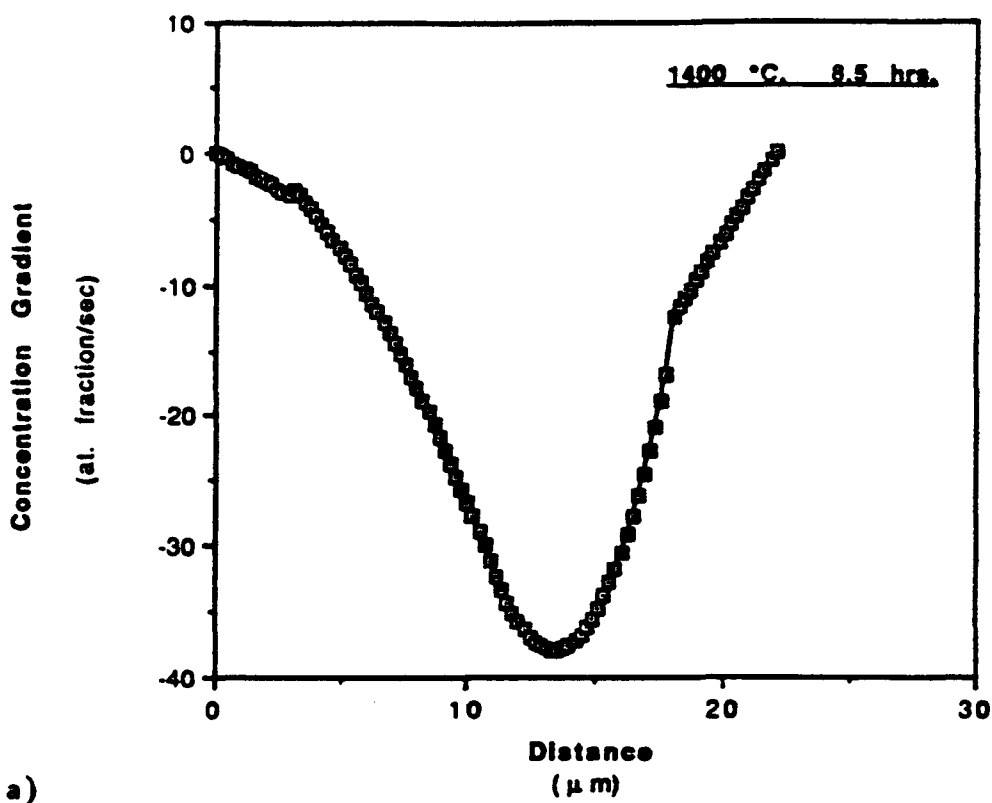


Figure 4.32      a) Composition gradient, and b) interdiffusion coefficient profiles for Nb/Nb-4.5Al diffusion couple heat treated at 1450 °C.

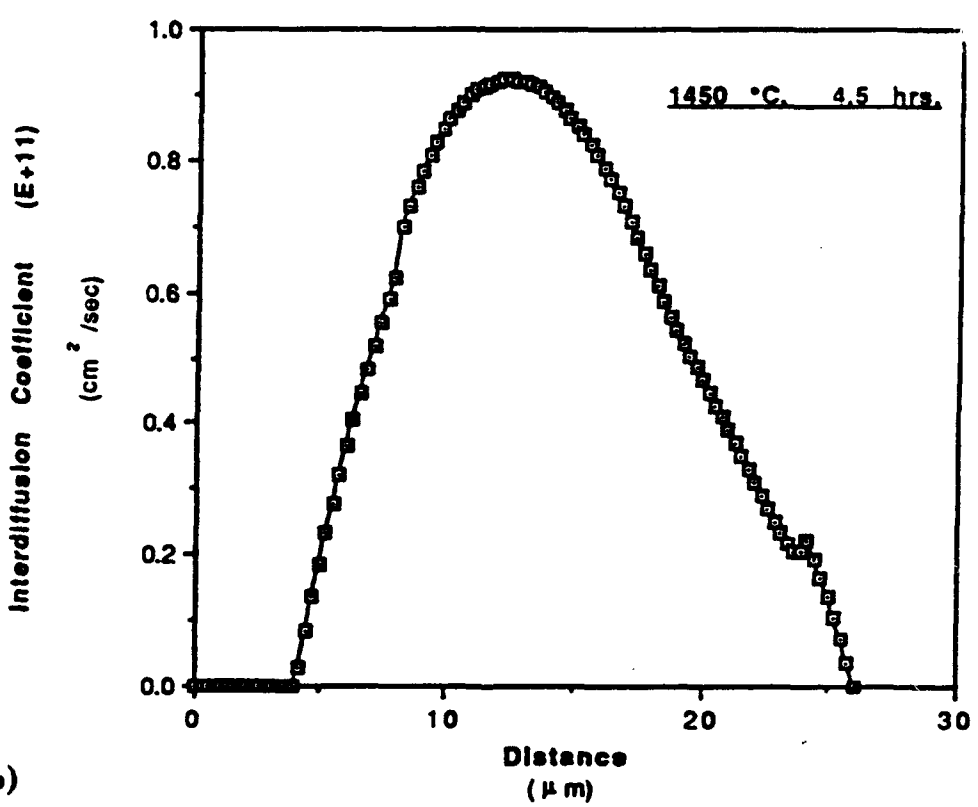
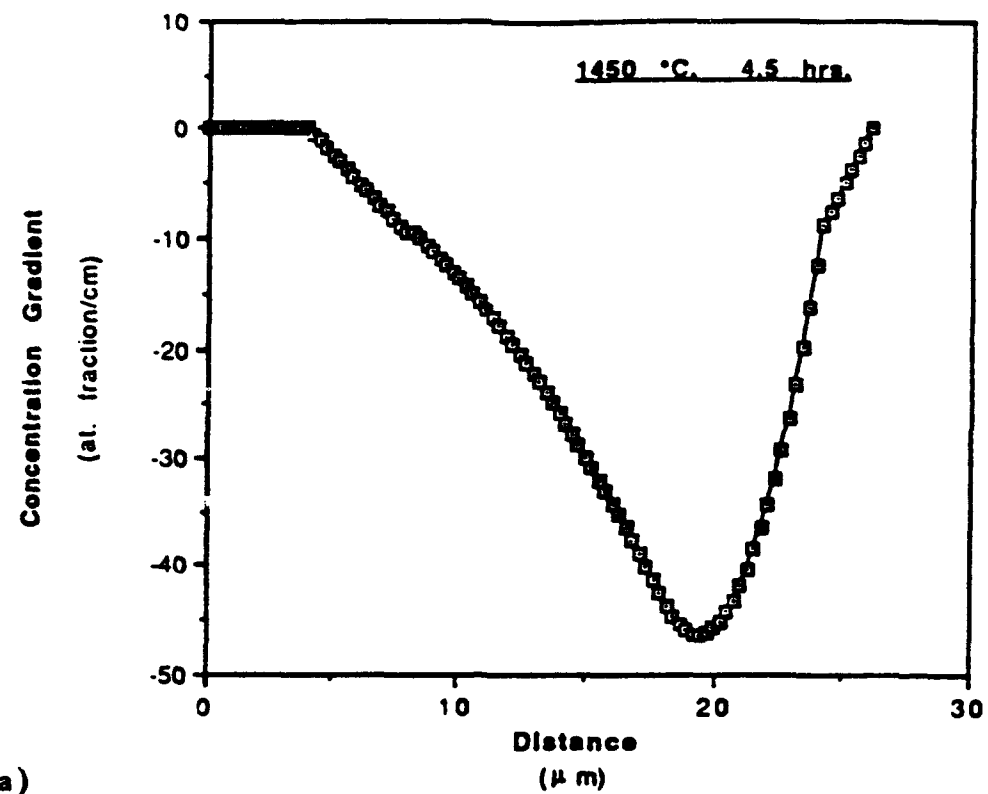


Figure 4.33      a) Composition gradient, and b) interdiffusion coefficient profiles for Nb/Nb-4.5Al diffusion couple heat treated at 1500 °C.

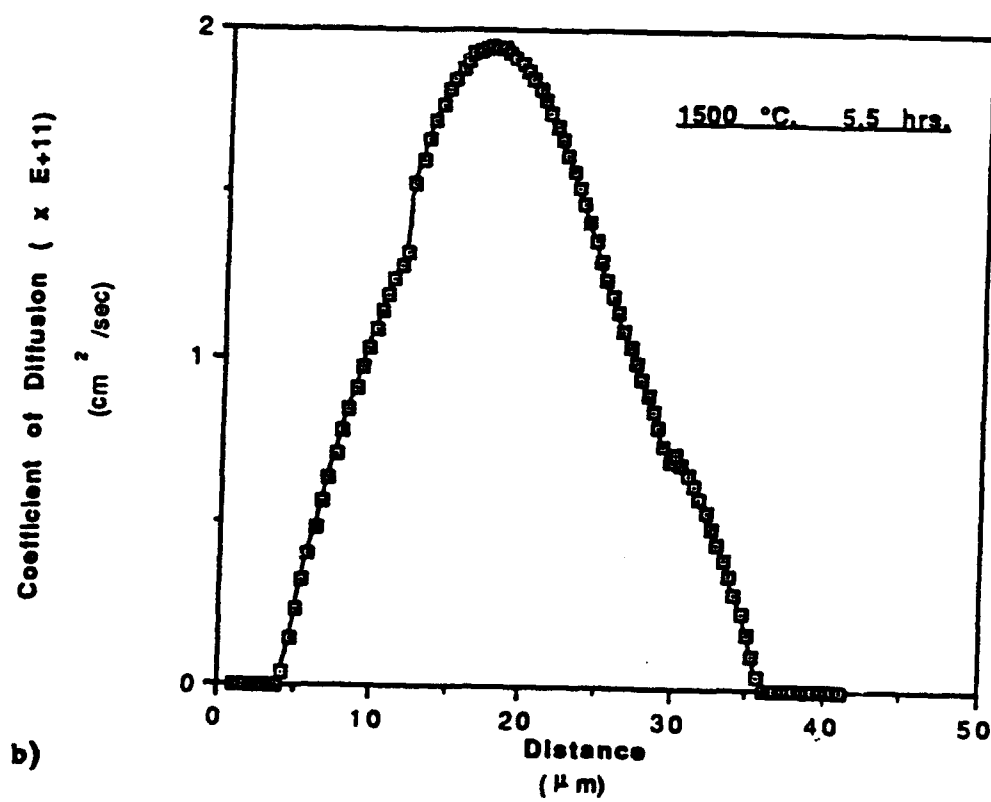
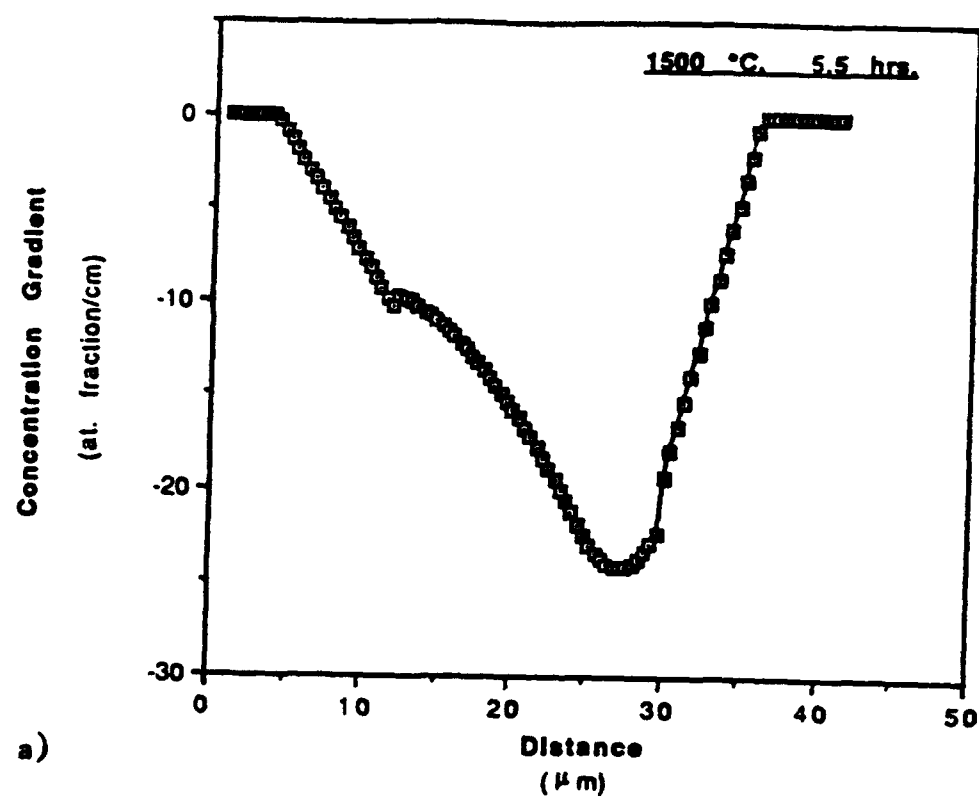


Figure 4.34      a) Composition gradient, and b) interdiffusion coefficient profiles for Nb/Nb-4.5Al diffusion couple heat treated at 1550 °C.

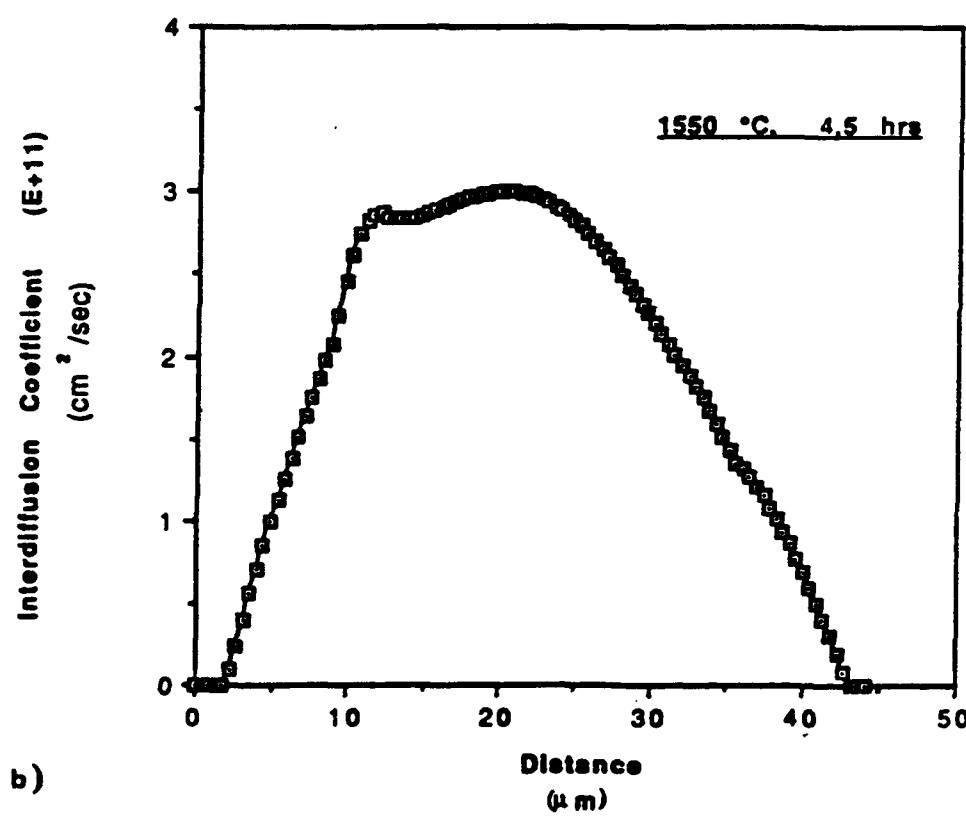
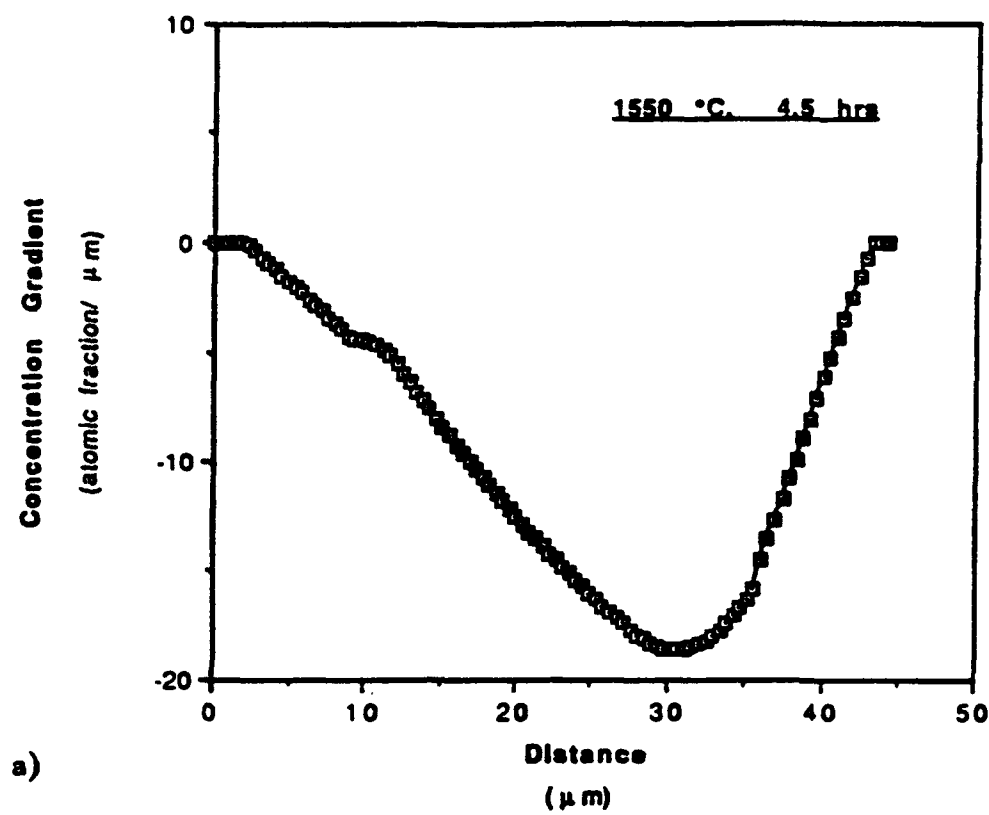


Table 4.2 Temperature and concentration dependencies of the interdiffusion coefficient in the Nb-Al system.

Temperature (°C)	Composition (at% Al)			
	3.0	2.5	2.0	1.5
1550	2.745	2.595	2.260	1.919
1500	2.028	1.755	1.430	1.180
1450	0.968	0.848	0.711	0.585
1400	0.424	0.332	0.290	0.261
1350	0.217	0.206	0.178	0.151

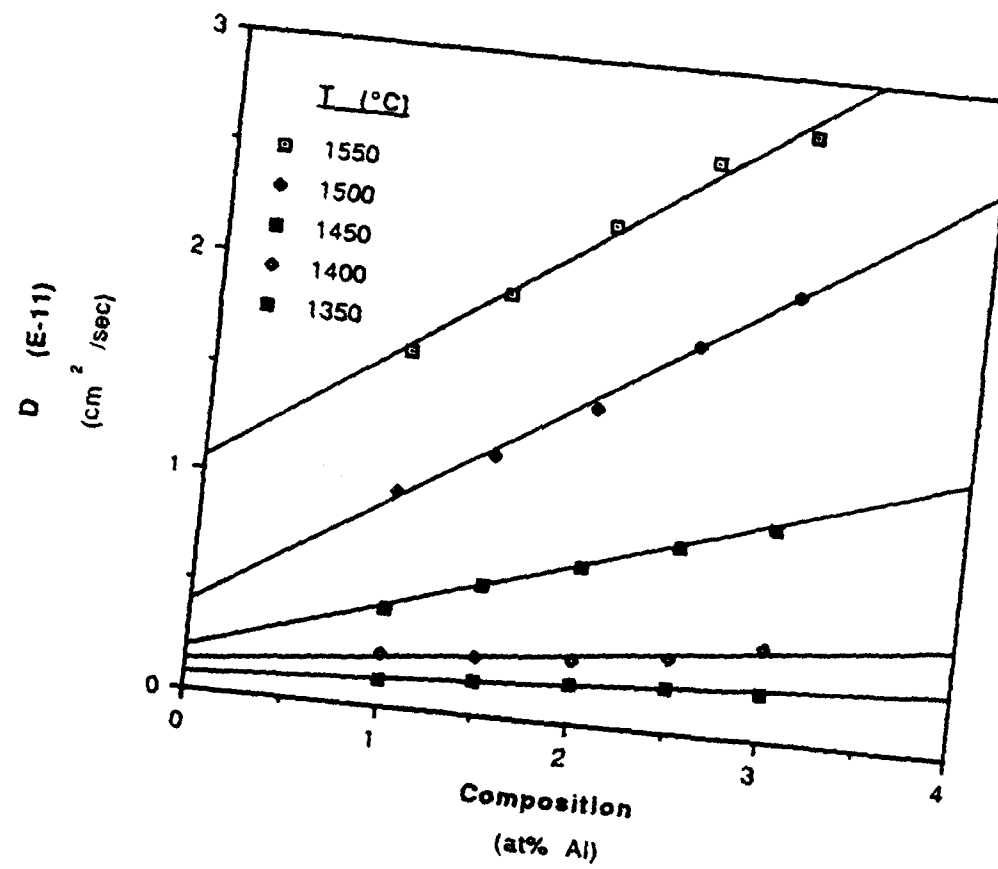


Figure 4.35

Dependency of the interdiffusion coefficient on the Al composition at several temperatures.

TABLE 4.3 Activation energy and frequency factor values for interdiffusion in b.c.c. Nb-Al alloy at different Al composition

Composition (at% Al)	$Q$ (cal/mol)	$D_0$ (cm <sup>2</sup> /sec)
3.0	78,697.7	0.0997
2.5	81,156.8	0.175
2.0	80,391.8	0.1168
1.5	80,446.4	0.0997
1.0	80,132.2	0.0768
average	80,165	0.1136

#### 4.2.5 Calculation of Intrinsic Diffusivities

In accordance with Darken's analysis (section 2.2.1.4), equations 2.38 and 2.39 permit to evaluate the intrinsic diffusion coefficients of binary system when the experimental parameters such as marker velocity and concentration gradient are known. The results of this research, however, indicated that the position of the Matano interface is very close to the markers position; the distance between the final marker position and the Matano interface for the largest depth of penetration (1550 °C, 5 hours) was less than a few micrometers, which is within the accuracy of the measurements. Therefore, the interface velocity could not be calculated accurately. The intrinsic diffusivity of Al was estimated (Table 4.4) by assuming that

$$D_{Al} N_{Nb} \gg D_{Nb} N_{Al}$$

$$D \approx D_{Al} N_{Nb}$$

This assumptions is justified by the fact that the self-diffusion coefficient of Nb in the temperature range of this study is in the order of  $10^{-13} \text{ cm}^2/\text{sec}$ . [22, 23]. It is acknowledge that alloying increases the diffusivity of Nb, however, it is expected to be orders of magnitude smaller than  $\sim 10^{-11} \text{ cm}^2/\text{sec}$ , which is the interdiffusion coefficient calculated for the Nb-Al binary system. Furthermore  $N_{Al} \ll N_{Nb}$  in the couples studied. Figures 4.36 to 4.40 present the Arrhenius plots for different aluminum concentrations (1% to 3%). The calculated activation energy and frequency factor values are given in Table 4.5. The diffusivity data for lower and higher Al contents were not considered since large errors are obtained in the

Table 4.4 Intrinsic diffusivity of Al in (bcc) Nb

Temperature (°C)	DAIx 10 <sup>11</sup> (cm <sup>2</sup> /sec)				Composition (at %)
	3.0	2.5	2.0	1.5	
1550	2.82990	2.6615	2.3061	1.94820	1.62630
1500	2.09120	1.8000	1.4592	1.19800	0.97980
1450	0.998450	0.8703	0.7255	0.59442	0.44949
1400	0.437630	0.3410	0.2959	0.26548	0.24697
1350	0.223710	0.2113	0.1821	0.15381	0.11818

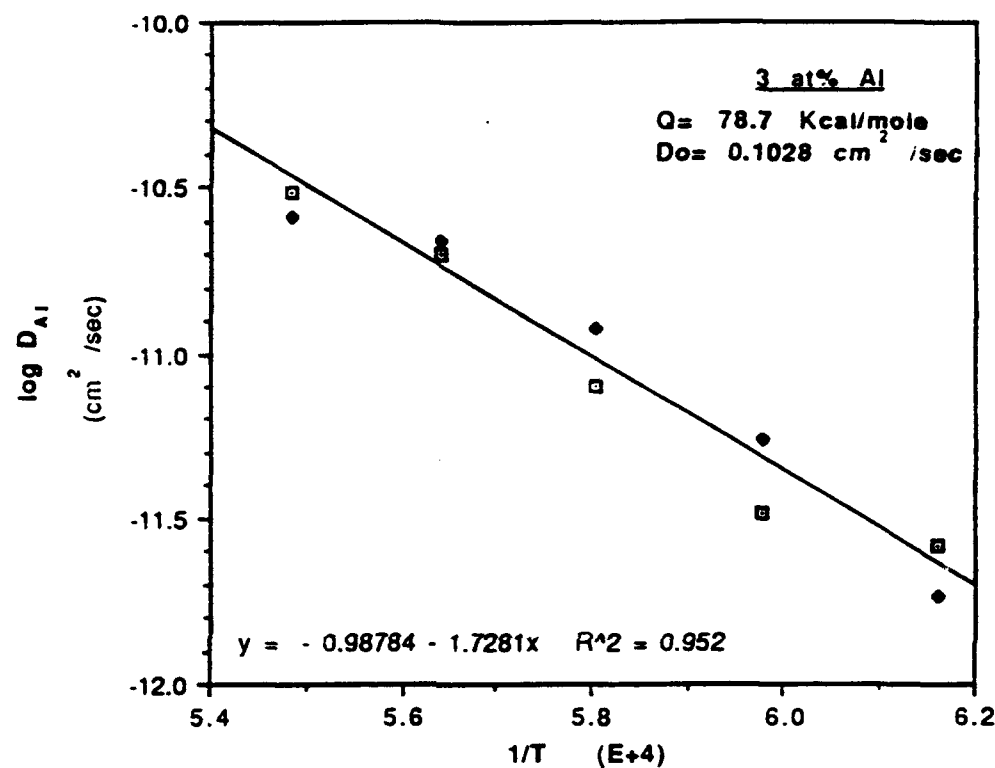


Figure 4.36 The temperature dependency of the intrinsic diffusion coefficient of Al in Nb at the aluminum concentration of 3.0 at%.

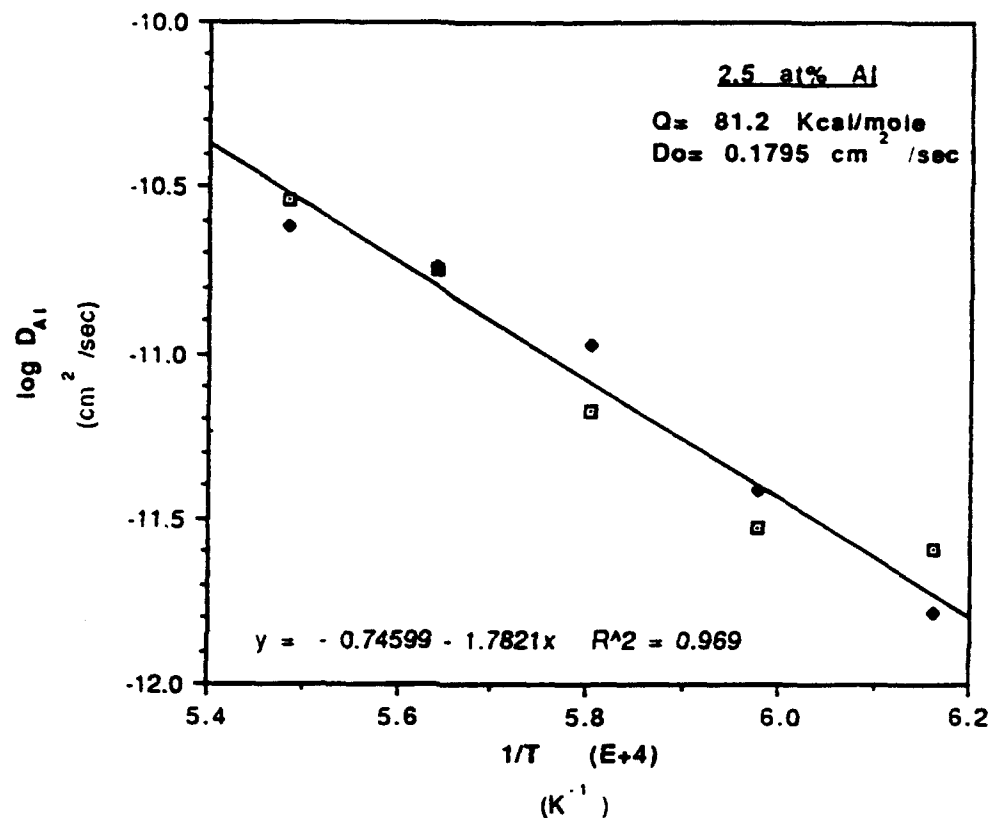


Figure 4.37      The temperature dependency of the intrinsic diffusion coefficient of Al in Nb at the aluminum concentration of 2.5 at%.

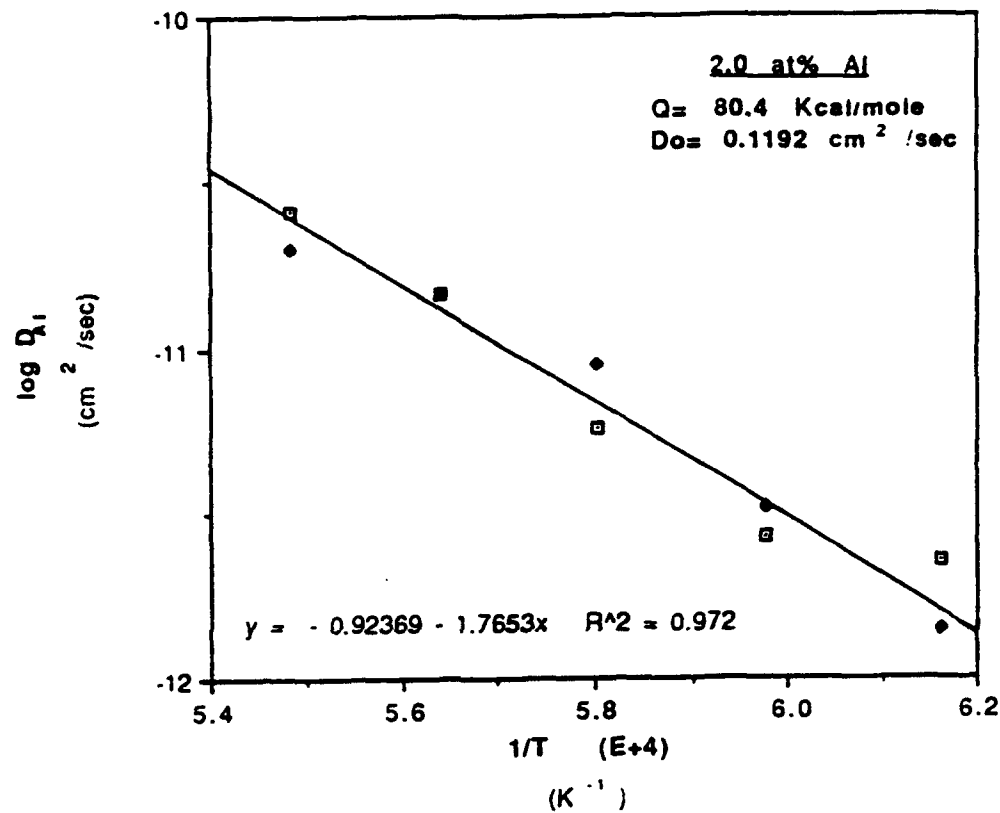


Figure 4.38      The temperature dependency of the intrinsic diffusion coefficient of Al in Nb at the aluminum concentration of 2.0 at%.

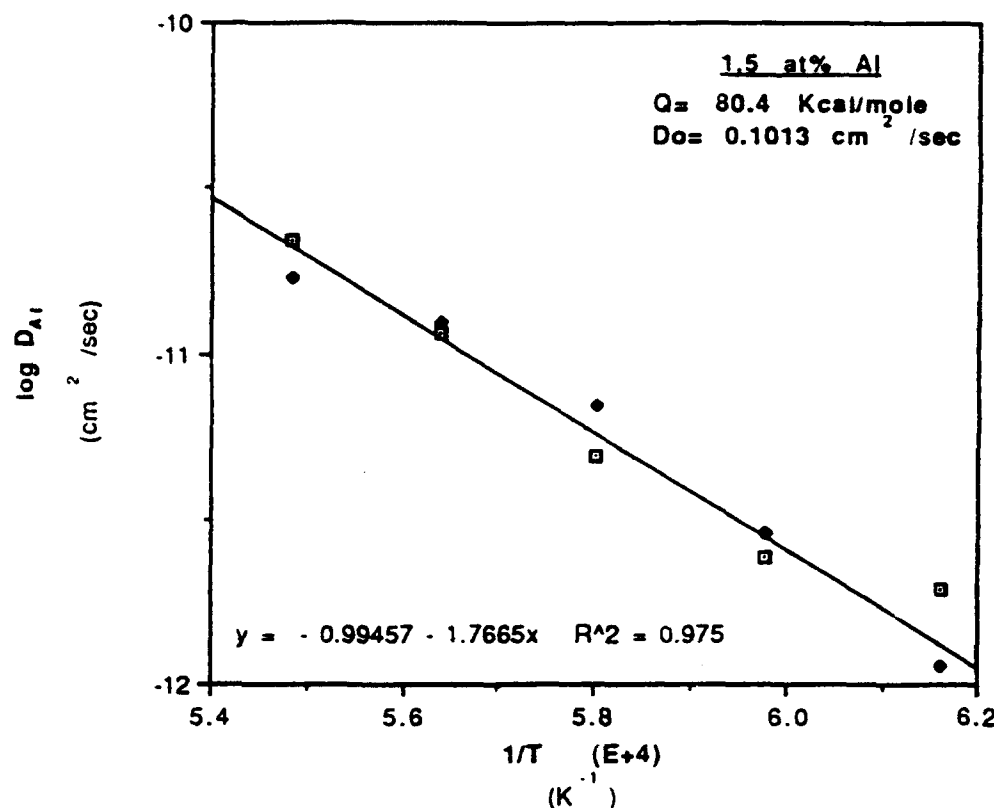


Figure 4.39

The temperature dependency of the intrinsic diffusion coefficient of Al in Nb at the aluminum concentration of 1.5 at%.

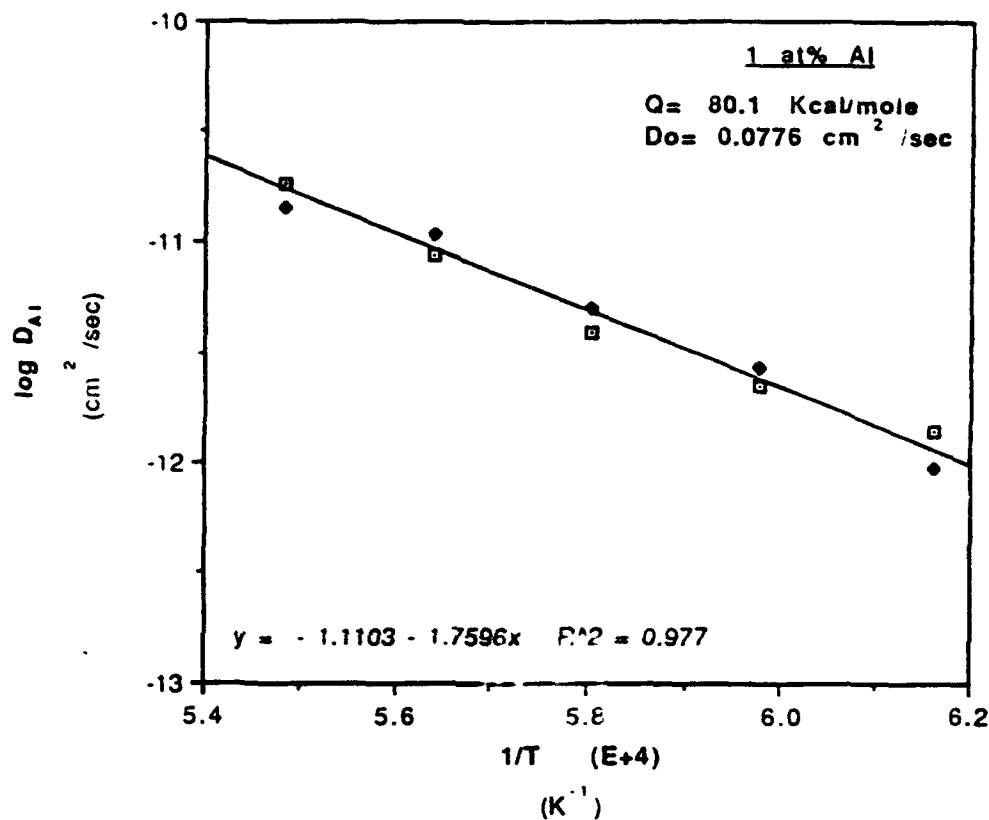


Figure 4.40 The temperature dependency of the intrinsic diffusion coefficient of Al in Nb at the aluminum concentration of 1.0 at%.

TABLE 4.5 Composition-dependent activation energy and frequency factor values for intrinsic diffusion of Al.

Composition (at% Al)	$Q$ (cal/mol)	$D_0$ (cm <sup>2</sup> /sec)
3.0	78,697.7	0.1028
2.5	81,156.8	0.1795
2.0	80,391.8	0.1192
1.5	80,446.4	0.1013
1.0	80,132.2	0.0776
average	80,165	0.1161

integration step when the composition is close to the terminal compositions. The linear curve fitting obtained is very good as shown by the values of the correlation coefficient  $R^2$  ( $>0.95$ ) in the worst case). The average values of the activation energy and frequency factor for the diffusivity of Al in Nb in the composition range of 1.0 to 3.0 atomic percent of Al are calculated to be

$$D_0 = 0.1161 \text{ cm}^2/\text{sec},$$

$$Q = 80.2 \text{ Kcal/mole}$$

#### 4.3 Discussion

There has been only one reported study on the diffusivity of Al in b.c.c. Nb [6]. As detailed in Chapter 2, Bodrov and Nikolaev [6] calculated the diffusion coefficient of Al in Nb at the temperature range of 1500° to 1950 °C by an analysis of the kinetics of evaporation of Al present as a dilute impurity in Nb in a concentration range of  $10^{-2}$ - $10^{-3}$  at% using atomic absorption spectroscopy. In order to compare the results of this study with theirs, the  $D_{Al}$  values were plotted as a function of Al concentration. The  $D_{Al}$  values for dilute solutions were estimated by the extrapolation of the Al intrinsic diffusivity to zero concentration. With the extrapolated results a new Arrhenius curve was obtained which is shown in Figure 4.41 together with their results. The  $D_{Al}$  values calculated in this study are an order of magnitude smaller. Furthermore the activation energy reported by Bodrov and Nikolaev

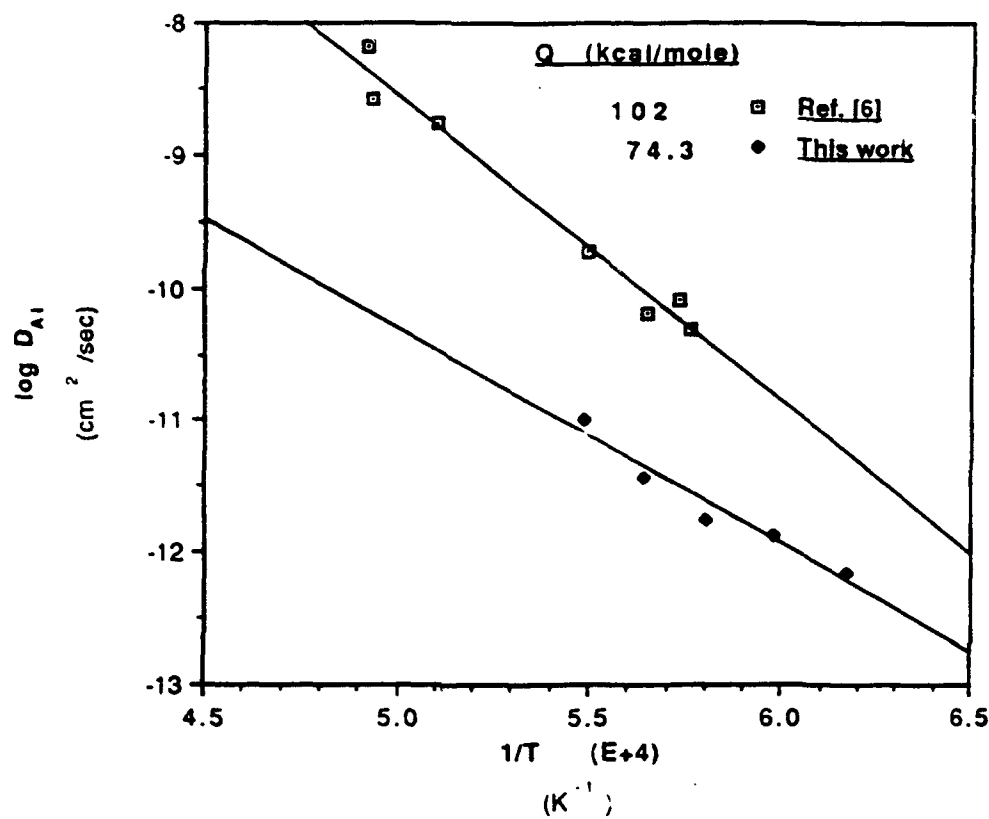


Figure 4.41 Comparison between this work and Ref. [6] for the temperature dependence of the diffusion coefficient of Al in Nb.

[6] is much larger (102 Kcal/mole) than the value obtained in this study (74.3 kcal/mole). These discrepancies can be discussed in terms of the differences between the two studies:

(i) Method: The indirect method of evaporation of Al employed by Bodrov and Nikolaev involves assumptions, which their validity is not justified (see section 2.1.2). The traditional method employed in this study is a direct method and is believed to yield more accurate results.

(ii) Temperature range: This study was conducted a lower temperature range 1350-1550 °C in comparison to 1500-2000°C, which was applied to their experiments. The self-diffusivity of Nb is reported to be very high close to its melting point [23]. This phenomenon has been attributed to the rapid motion of divacancies at high temperatures [52]. This section was explained in detail in section 2.1.2. The contribution of divacancies at high temperatures can explain a larger activation energy and higher diffusion coefficient at temperatures close to the solidus temperature of the alloy. However, since there is an overlap of test temperature between this study and that of Bodrov and Nikolaev the low diffusivity of Al measured in this study can not be explained solely by a divacancy mechanism.

(iii) Interstitial Content: The processes of bonding and diffusion treatment introduced a high concentration of nitrogen and oxygen in the alloys used in this study (see Table 4.1). Eizinger *et. al.* [23] have reported that oxygen content has no effect on the self-diffusion of Nb. Al is expected to bind with oxygen, however, such trapping would expect to increase the activation energy in comparison to a purer

system. Therefore, the observed inconsistency can not be attributed to the relatively high concentration of interstitials in the alloys used in this study.

Bodrov and Nikolaev also measured the intrinsic diffusivity of Al in Ta:

$$D_0 = 1.525 \text{ cm}^2/\text{sec}$$

$$Q = 73.14 \text{ kcal/mol}$$

$$D_{1500^\circ} = 1.3646 \times 10^{-9} \text{ cm}^2/\text{sec}$$

It is interesting to note that the Q value for Ta-Al is much smaller and closer to the Q value found in this study for the Nb-Al system. Furthermore a recent work by Maslov *et. al.* [75], who have investigated the diffusion of Al in V in the temperature range of 1000-1500 °C, gives:

$$D_0 = 0.084 \text{ cm}^2/\text{sec}$$

$$Q = 64.1 \text{ kcal/mole}$$

The activation energies for self-diffusion of Ta, Nb and V normalized for melting point ( $Q/T_m$ ) are very close [28, 76] (see Figure 2.10), and the phase diagram of these elements with Al are very similar. Therefore one would expect that the activation energy for diffusivity of Al in Nb to be in between that in Ta and V, consistent with the result obtained in this study.

Most of the existing interdiffusion studies including Nb as one of the components are those involving another transition metal as the second component in the diffusion couple. Table 4.6 [77] present the value of the activation energy for the binary system Nb-X (X= Ti, V, Zr, Mo, Ta, W, Al). In this Table the intrinsic diffusivities of the solutes are compared to the self-diffusion of Nb. All these elements form

Table 4.6 Solute diffusion in Nb-X system  
(from Ref. [77])

X	Q (kcal/mole)	D <sub>solute</sub> /D <sub>Nb</sub> (at 1545 °C)(*)
Ti	87, 88.5	0.85, 2.21
V	85, 90, 55.6	32.2, 1.71, 3.9
Zr	87	3.9
Mo	122	0.046
Ta	99.3	0.27
W	156	0.003
Al	80.1(**), 102	6.5, 48

(\*) D<sub>0Nb</sub> = 0.85 × 10<sup>-4</sup>, Q<sub>Nb</sub> = 94.1 kcal/mole

(\*\*) This study

extensive b.c.c. solid solution regions in the phase diagram when combined with Nb. Except for Mo and W, the other elements show relatively a similar activation energy for diffusion. Although Al is not a transition metal, the results of the ternary diffusivity obtained in this study (see Chapter 5) suggest that in the Nb corner of the ternary phase diagram Al and Ti have similar penetration tendencies at 1200 °C and 1400 °C annealing temperatures. Again, this observation suggests that in comparison to the Bodrov and Nikolaev study the lower diffusivity coefficients obtained in this study correlate better with the diffusivity of Ti in Nb.

The results of interdiffusivity for different phases in the Nb-Al system are summarized in Table 4.7 [78-80]. The activation energy for the interdiffusion in the  $\beta$  phase is somewhat smaller than Nb<sub>3</sub>Al. The activation energy seems to decrease with increasing the Al content and for NbAl<sub>3</sub> it reaches the activation energy for self-diffusion in pure Al (35 kcal/mole) [77].

#### 4.4 Summary

The binary diffusion in the  $\beta$  Nb-Al solid solution was evaluated by the Matano-Boltzmann method. The Nb-4.5Al alloy used for this research was susceptible to internal oxidation. The formation of Al<sub>2</sub>O<sub>3</sub> near the interface could be lessened substantially by using yttria markers instead of zirconia ones. Due to the oxidation restriction both temperature and time of interdiffusion treatment had to be shortened and therefore, the extent of composition profiles obtained was limited to a maximum of 45  $\mu\text{m}$ . As a result,

Table 4.7 Interdiffusivity data for the phases in the  
Nb-Al system.

Phase	$D_0$ (cm <sup>2</sup> /sec)	Q (kcal/mole)	Reference
$\beta$ -phase	0.049	78.4	This study
Nb <sub>3</sub> Al	2.5	87.5	[78]
Nb <sub>2</sub> Al	0.002	55.0	[79]
NbAl <sub>3</sub>	2.0	36.5	[80]

appreciable movement of markers after interdiffusivity was not detected either.

Spline cubic fitting of the experimental composition profiles worked successfully, even though difficulties arose during curve fitting, specially in the parabolic region of the profile in the  $\beta_0$  alloy side of the diffusion couple.

The results of this study indicate that the interdiffusion coefficient in  $\beta$  solid solution of Nb-Al system varies linearly with Al composition in the concentration range of 1-3 at% Al and it follows a linear Arrhenius behavior as function of temperature in the 1350 °C-1500 °C range. The activation energy for diffusivity of Al in Nb was found to be 80.2 kcal/mole, which is smaller than the previously reported value of 102 kcal/mole that has been obtained in the 1500 °C-1900 °C temperature range. It is suggested that this discrepancy is associated with the differences in the evaluation method and possibly the temperature range.

## CHAPTER 5 DIFFUSIVITY ANALYSIS IN THE TERNARY Nb-Ti-Al SYSTEM

The purpose of this part of the study was to investigate the diffusivity in B.C.C. solid solution of ternary Nb-Ti-Al system. The ternary diffusion couples prepared in this study are illustrated in Figure 5.1.

The Nb-42.5at%Ti-15at%Al ( $\beta_1$ ) alloy was chosen as the main alloy and it was coupled with pure Ti, pure Nb and the Nb-50at%Ti ( $\beta$ ) alloy. The composition of Al was chosen based on the information available on the  $\beta$ -transus temperature. An increase in the Al content in this part of the ternary phase diagram results in an increase in the  $\beta$ -transus temperature and order-disorder temperatures [81]. Therefore 15 at% was estimated to be the maximum Al content of an alloy that would have a  $\beta$ -transus and order-disorder temperatures below 1000 °C. Two additional couples consisting of the Nb-47.5at%Ti-5at%Al ( $\beta_2$ ) alloy coupled with the  $\beta_3$  and  $\beta_0$  alloys were also prepared to complement the binary diffusivity results.

In this chapter the results of the diffusivity experiments performed on the ternary Nb-Al-Ti system and their discussion are presented. The first part of the chapter deals with the microstructural details of the ternary couples before and after the diffusion treatment. Then, in order to have a better understanding of

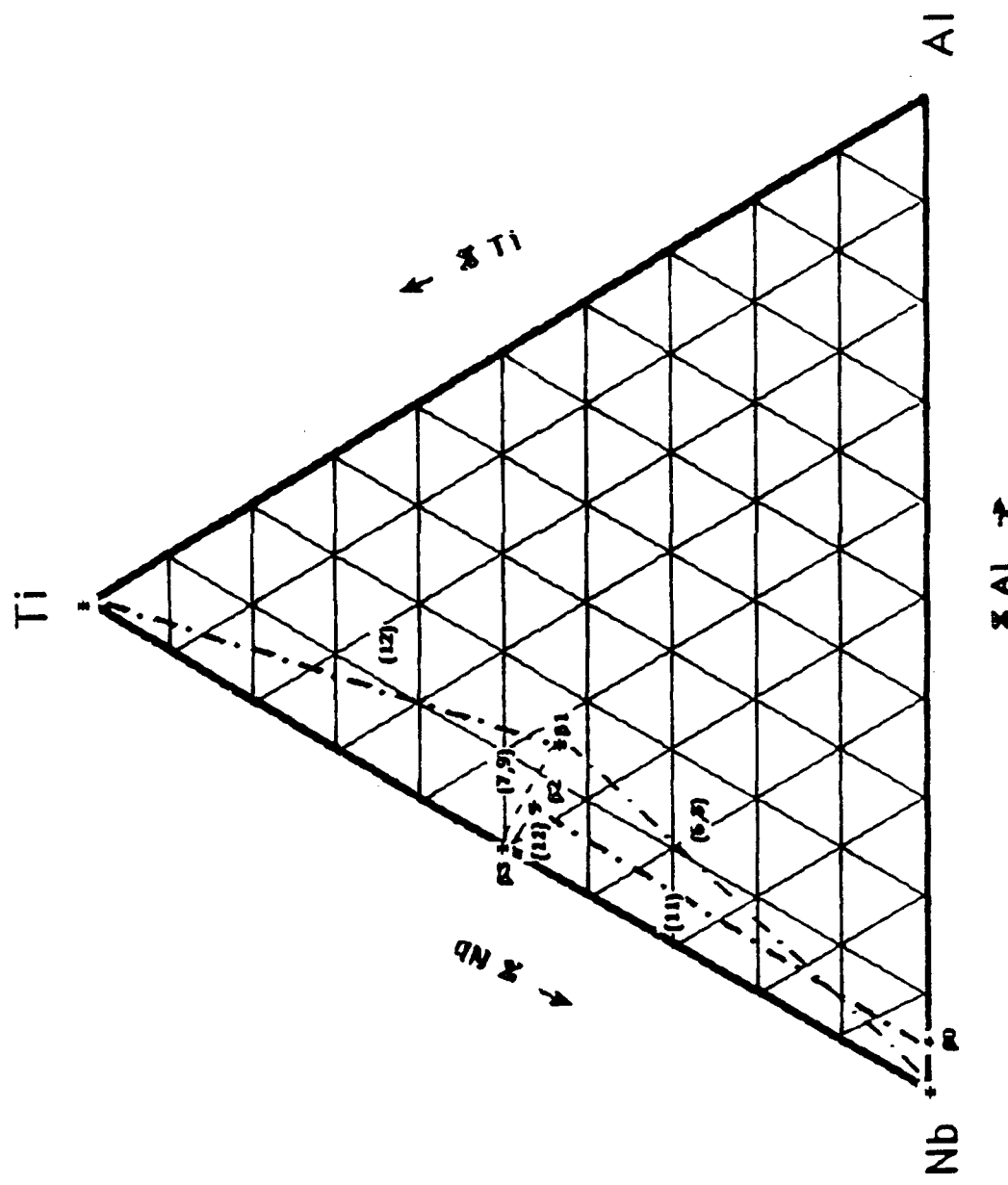


Figure 5.1 Schematic representation of the ternary diffusion couples employed in this research.

the diffusivity behavior of the system, the composition profiles obtained by microprobe analysis are given in different groups depending on the compositional characteristic of the couple. The information provided by these composition profiles is presented and analyzed with the help of concepts such as Penetration Tendencies, Composition Paths, Kirkendall Shifts, and Crossover Displacements. A summary of the findings is given at the end of the chapter.

### 5.1 Microstructural Analysis

The microstructure of the individual alloys and the diffusion couples after both the bonding and the diffusion treatments were investigated using optical and electron microscopy techniques.

Pure Ti undergoes an allotropical transformation at 882 °C, from a high temperature body-centered cubic ( $\beta$ ) phase to a hexagonal close-packed ( $\alpha$ ) structure (see Figures 2.1 and 2.3). The Ti alloy phase diagrams in the Ti-rich section are usually classified into three types. Elements that stabilize  $\alpha$ -phase and increase the  $\alpha/\beta$  transus. Aluminum and oxygen are the most important  $\alpha$  stabilizers. Elements that depress the  $\alpha/\beta$  transus and stabilize  $\beta$ -phase are classified in two groups: those which form binary systems of the  $\beta$ -isomorphous type, such as Nb (see Figure 2.1) and those which favour formation of a  $\beta$ -eutectoid such as hydrogen. In general the microstructure observed is sensitive to the cooling rate from the  $\beta$ -phase regime. A fast cooling rate can result in formation of martensitic  $\alpha'$  phase.

The as-received Ti used in this study had a duplex microstructure consisting of  $\alpha + \beta$  phases as shown in Figure 5.2. The small amounts of impurities (see Table 3.1) are sufficient to result in an  $(\alpha + \beta)$  microstructure rather than a single  $\alpha$ -phase at room temperature. On the other hand  $\beta_1$  (Nb-42.5Ti-15Al),  $\beta_2$  (Nb-47.5Ti-5Al) and  $\beta_3$  (Nb-50Ti) alloys displayed a single phase microstructure as shown in Figure 5.3, while the phase diagram suggests that these alloys should consist of  $\alpha$  and  $\beta$  phases at room temperature. This observation can be explained by the low mobility of Nb at the  $\alpha/\beta$  transition temperature for these alloys. TEM analysis of a 50Nb-40Ti-10Al alloy [82] has revealed that this alloy is composed of the disorder  $\beta$ -phase. Although the exact  $\beta$ -transus temperature for these alloys are not known, based on the binary Nb-Ti phase diagram, they can be estimated to be below 1000 °C.

As shown in Figure 5.4 the duplex microstructure of the pure Ti persisted after bonding with the  $\beta_1$  alloy at a bonding temperature of 700 °C, which is below the  $\beta$ -transus temperature of titanium. However, in the vicinity of the interface, where some interdiffusion had occurred, the microstructure consists of a single phase as shown in Figure 5.5a. The microprobe analysis showed slight penetration of both Al and Nb to the single phase region as given in Figure 5.5b. Since Al is a strong  $\alpha$ -stabilizer it may be speculated that this narrow zone of penetration consists of  $\alpha$ -phase. Figure 5.5 also shows that a thin darker band has developed in the ternary side of the couple. This is probably due to the slight interdiffusion of Ti into the  $\beta_1$  phase which is detected by the composition dependent BSE image. A

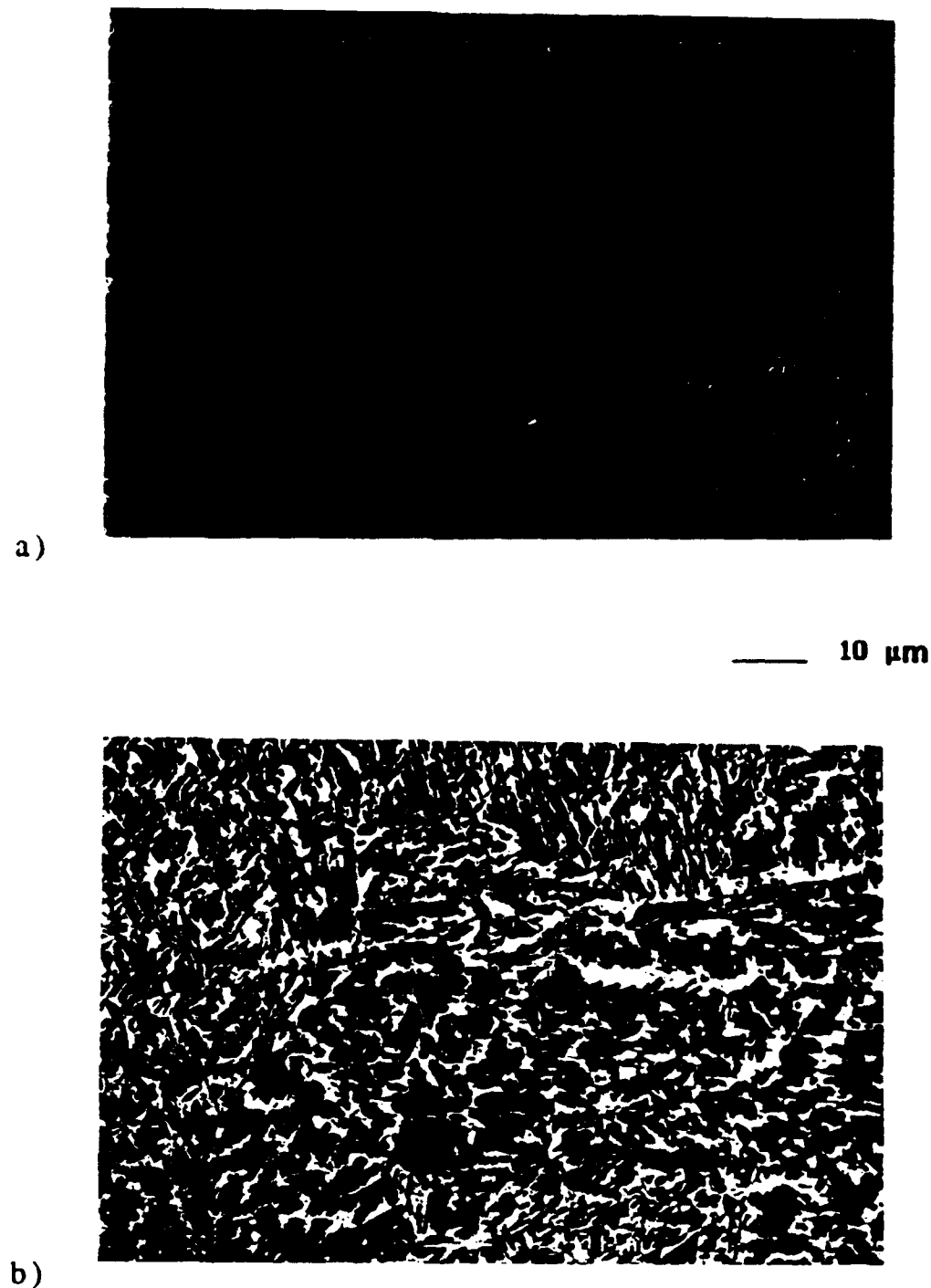
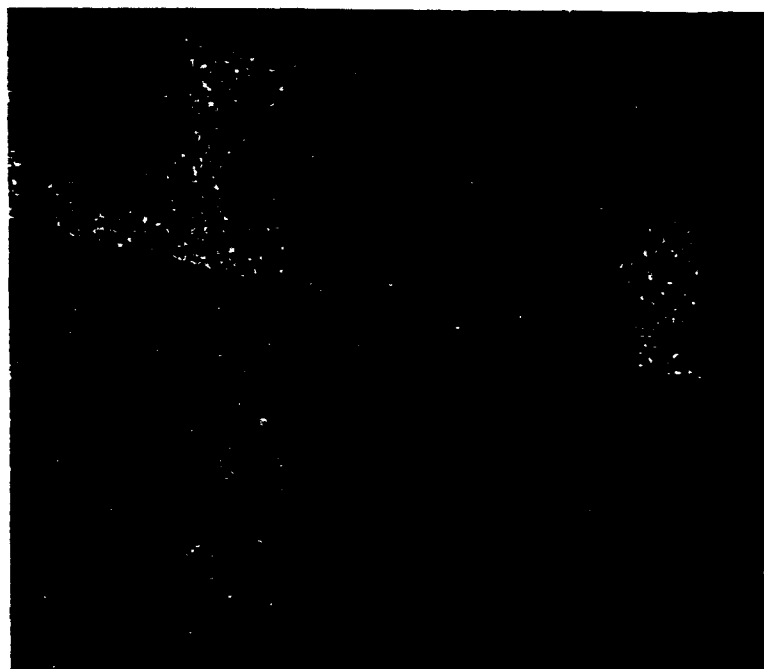


**Figure 5.2** Micrographs showing the duplex structure ( $\alpha+\beta$ ) of the as-received Ti: a) Optical micrograph, as-etched condition; b) BSE image.



— 10  $\mu\text{m}$

Figure 5.3      BSE micrograph of  $\beta 1$  alloy (Nb-42.5Ti-15Al) after homogenization at 1400  $^{\circ}\text{C}$  for 6 hours.

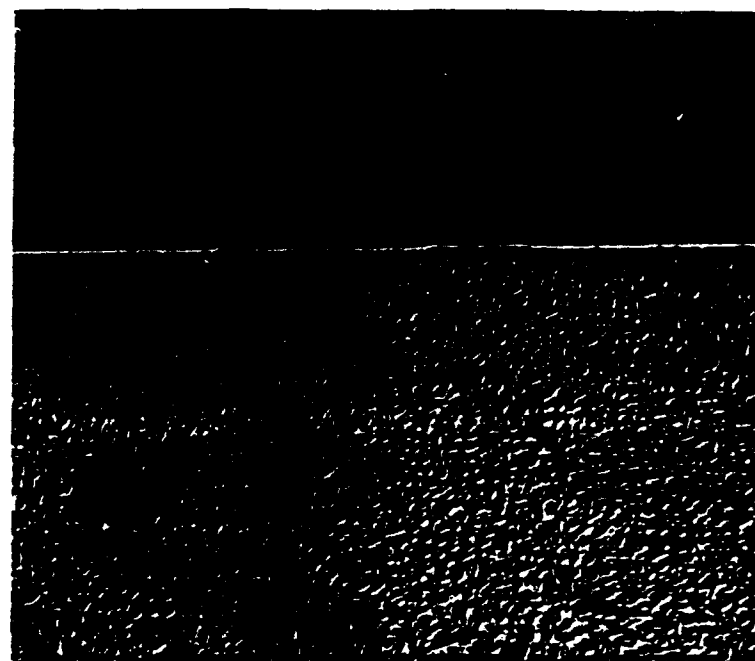


Figure 5.4

Optical micrograph of the bonded interface in diffusion couple #12 ( $\beta$ 1/Ti) after bonding at 700 °C for 2 hours showing the duplex structure  $\alpha+\beta$  of the Ti side of the couple.

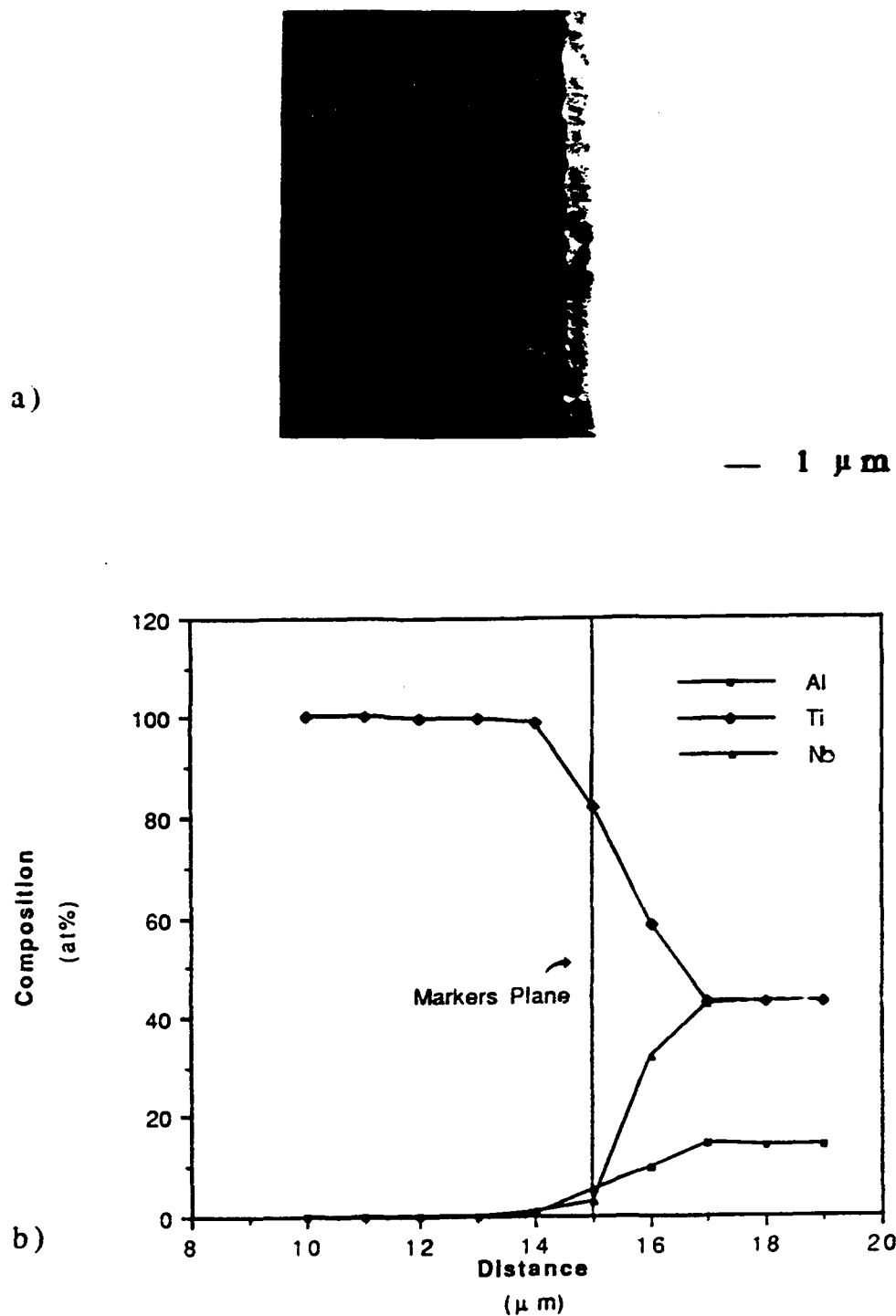


Figure 5.5      a) BSE micrograph of interface in diffusion couple #12 ( $\beta\text{I}/\text{Ti}$ ) before diffusion treatment;  
b) the three composition profiles across the boundary

diffusion treatment at 1200 °C resulted in a two-phase region adjacent to the interface (Figure 5.6). The microstructure resembles the typical Widmanstatten ( $\alpha + \beta$ ) structure that develops in Ti alloys. The development of a two-phase region adjacent to the interface in the 1200 °C treated couple can be attributed to the facts that (i) at 1200 °C the microstructure consists of single  $\beta$  phase, (ii) the higher temperature allows the diffusion of Nb into the Ti side, and (iii) the cooling rate achieved in the vacuum furnace is faster than that obtained in the hot press, which was used for the bonding treatment. The acicular morphology of this two-phase region in comparison to the equiaxed morphology of Ti can be explained by the higher alloying content of it.

Similarly the other ternary couples that were bonded at 900 °C showed the formation of alpha phase, which precipitated along grain boundaries and at the bonded interface as shown in Figure 5.7. These areas have a higher surface energy, which induced the formation of  $\alpha$  phase. Figure 5.8 shows BSE micrographs where this precipitate looks dark indicating its high Al content. The effect of the aluminum content on the presence of this second phase is corroborated by the following observation. No precipitation was observed in the binary Ti-Nb side of any couple (#7, #9). However, when a small amount of Al (0.5 at%) was present in the Nb-Ti side ( $\beta_3$ ) of couple # 10, precipitation was observed on both sides of the couple as shown in Figure 5.9. After interdiffusion treatment at either 1200° or 1400 °C, no  $\alpha$  phase was detected anywhere (Figure 5.10), which means that due to the higher temperature the structure transformed completely to  $\beta$  phase and because of the redistribution of Al and Nb around the

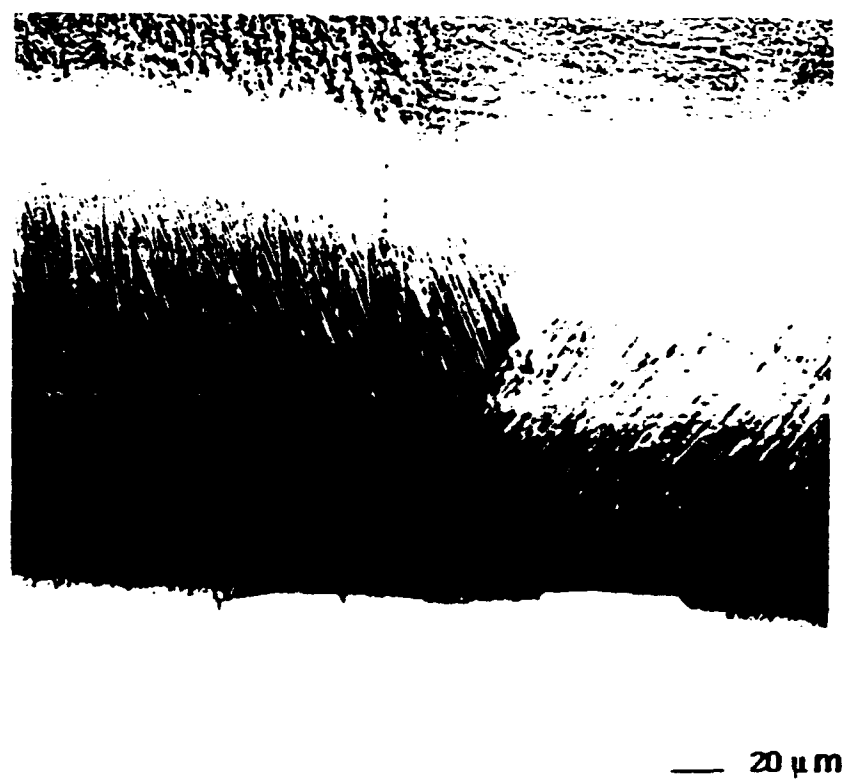


Figure 5.6

Optical micrograph of the Ti side next to the bonded interface in diffusion couple #12 ( $\beta_1/\text{Ti}$ ) after diffusion treatment at 1200 °C for 6 hours. Note the duplex ( $\alpha+\beta$ ) zone with the acicular morphology next to the interface.

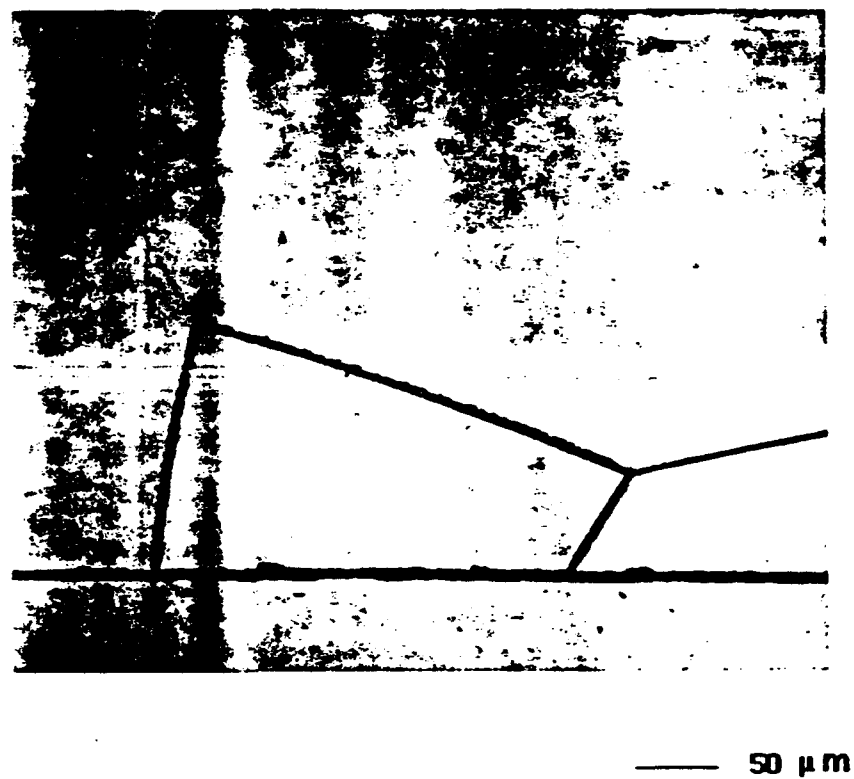


Figure 5.7

Optical micrograph showing precipitation of  $\alpha$  phase at the interface and grain boundaries of the ternary  $\beta_1$  (Nb-42.5Ti-15Al) side of the couple after bonding at 900 °C for 2 hours.

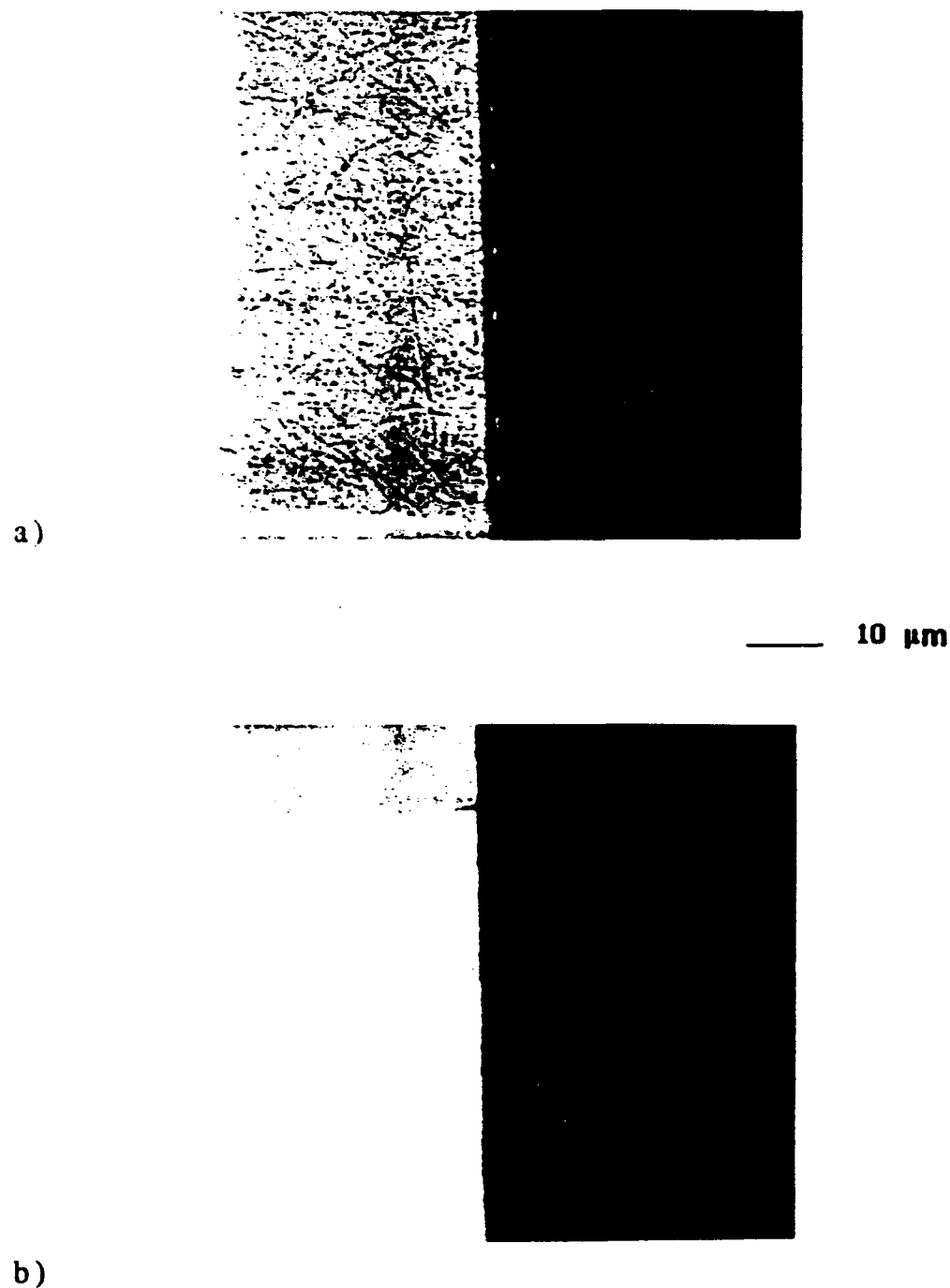


Figure 5.8

BSE micrographs showing precipitation of  $\alpha$  phase in the ternary side of the couples along the interface: a) diffusion couple #9 ( $\beta_1/\beta_3$ ); and b) diffusion couple #11 ( $\beta_2/\beta_0$ ).

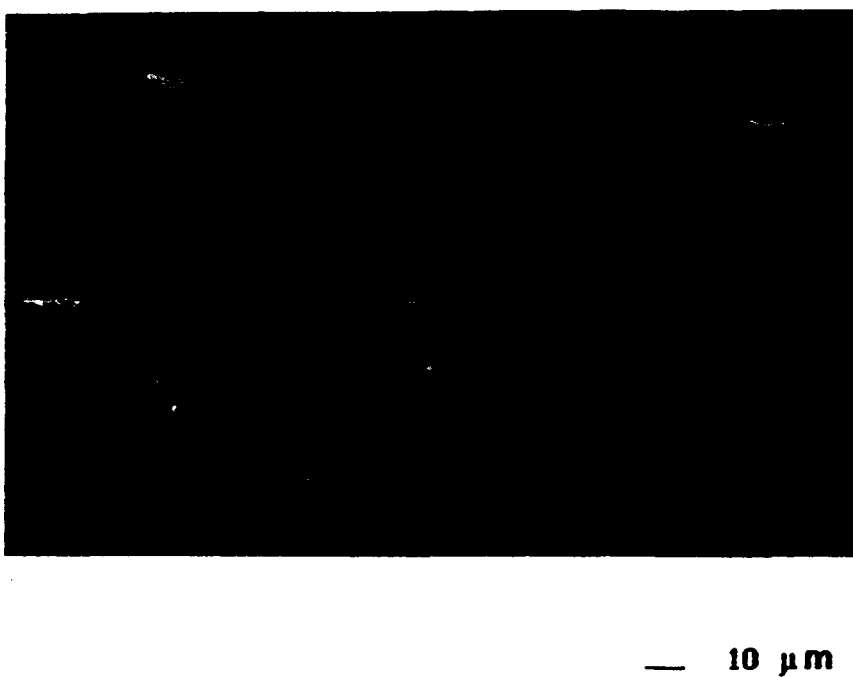
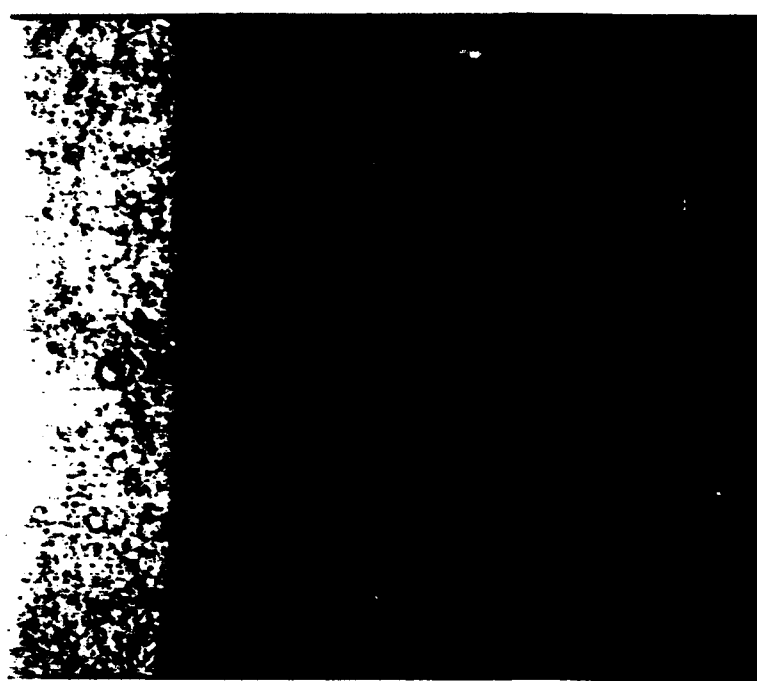


Figure 5.9

BSE micrograph of bonded interface in diffusion couple #10 ( $\beta_2/\beta_3$ ) after bonding at 900 °C for 2 hours showing the presence of second phase ( $\alpha$ ) on both sides of the interface.



— 10  $\mu\text{m}$

Figure 5.10      BSE micrograph of the interface in diffusion couple #6 ( $\beta\text{I}/\text{Nb}$ ) after diffusion treatment at 1400 °C for 6 hours. Microprobe analysis contamination over the precipitation-free structure is detailed.

interface and the relatively faster cooling rate, in the vacuum furnace the precipitation of  $\alpha$  phase from  $\beta$  was inhibited. After the diffusion treatment, the couples were reheated at 920 °C in the vacuum furnace in order to study the stability of the microstructure. Again precipitation occurred at the grain boundaries, interfaces, and on the dislocations substructure, but there was a denuded zone near the interface (Figure 5.11), which matched the diffusion zone after the heat treatment at 1200 °C. These observations, in addition to the fact that the structure of ternary alloys after homogenization at 1400 °C consists of the single  $\beta$  phase, lead to the conclusion that at the interdiffusion temperature of 1200 °C and above the microstructure was composed of single b.c.c.  $\beta$  solid solution.

## 5.2 Composition Profiles

The composition profiles for the different ternary diffusion couples after interdiffusion at 1200° and 1400 °C for 6 hours, as obtained by microprobe analysis are shown in Figures 5.12 to 5.18. Note that the profiles are presented in different scales. At least two composition profiles were obtained for each couple, as it has been discussed in Appendix A. Next, the composition profiles for two different cases are discussed, and the presence of critical points and the effect of temperature are presented.

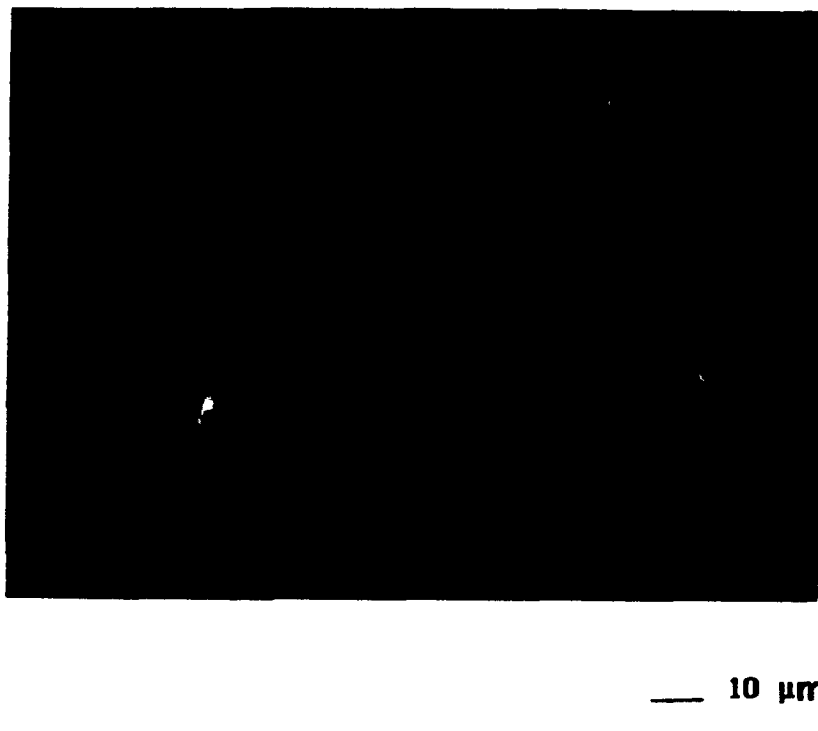


Figure 5.11 BSE micrograph of the  $\beta_2$  side away of the interface of diffusion couple #10 ( $\beta_2/\beta_3$ ) after diffusion treatment at 1200 °C for 6 hours, and subsequent treatment at 920 °C for 2 hours. Reprecipitation of the second phase is observed.

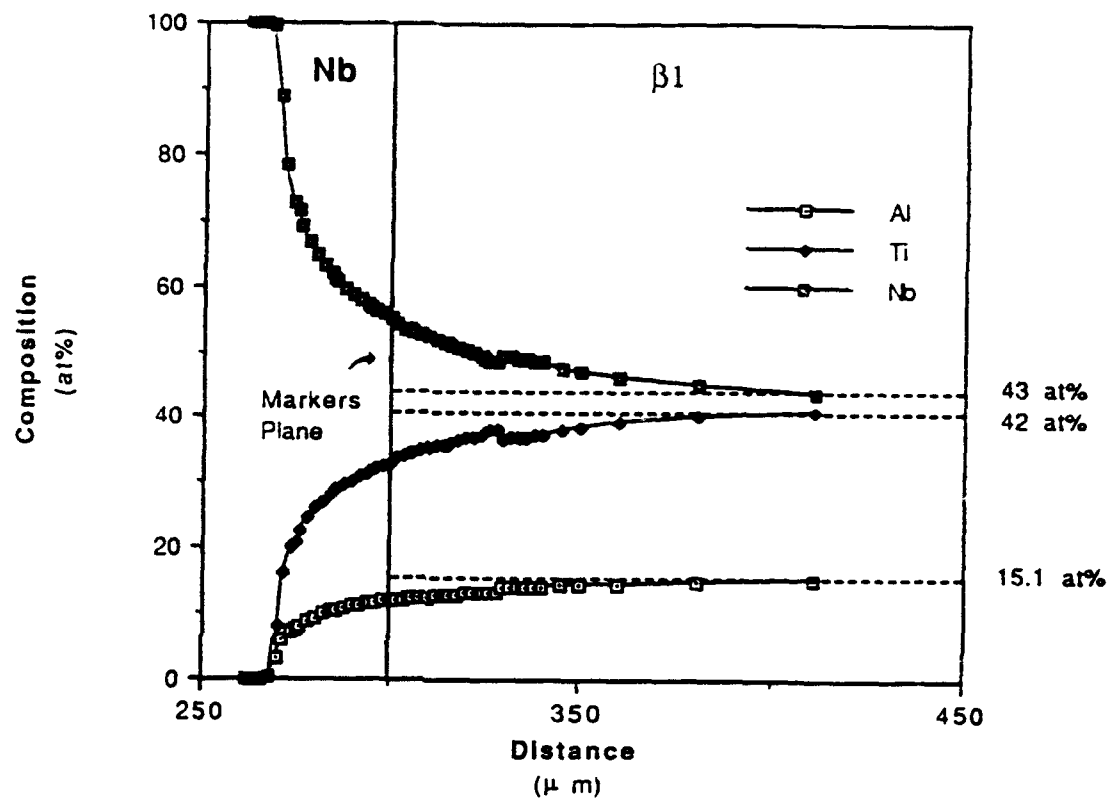


Figure 5.12 Penetration curves of the 3 components in the couple #6 ( $\beta_1/\text{Nb}$ ), heat treated at 1400 °C for 6 hours.

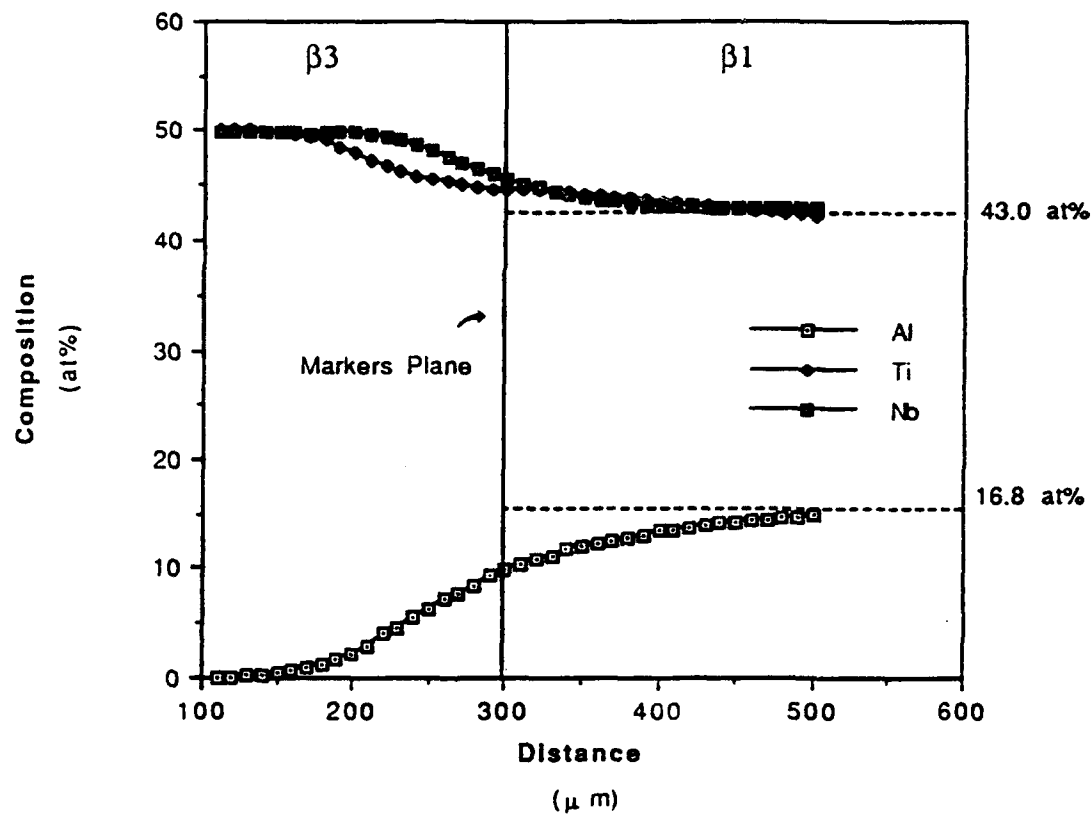


Figure 5.13 Penetration curves of the 3 components in the couple #7 ( $\beta_1/\beta_3$ ), heat treated at 1400 °C for 6 hours.

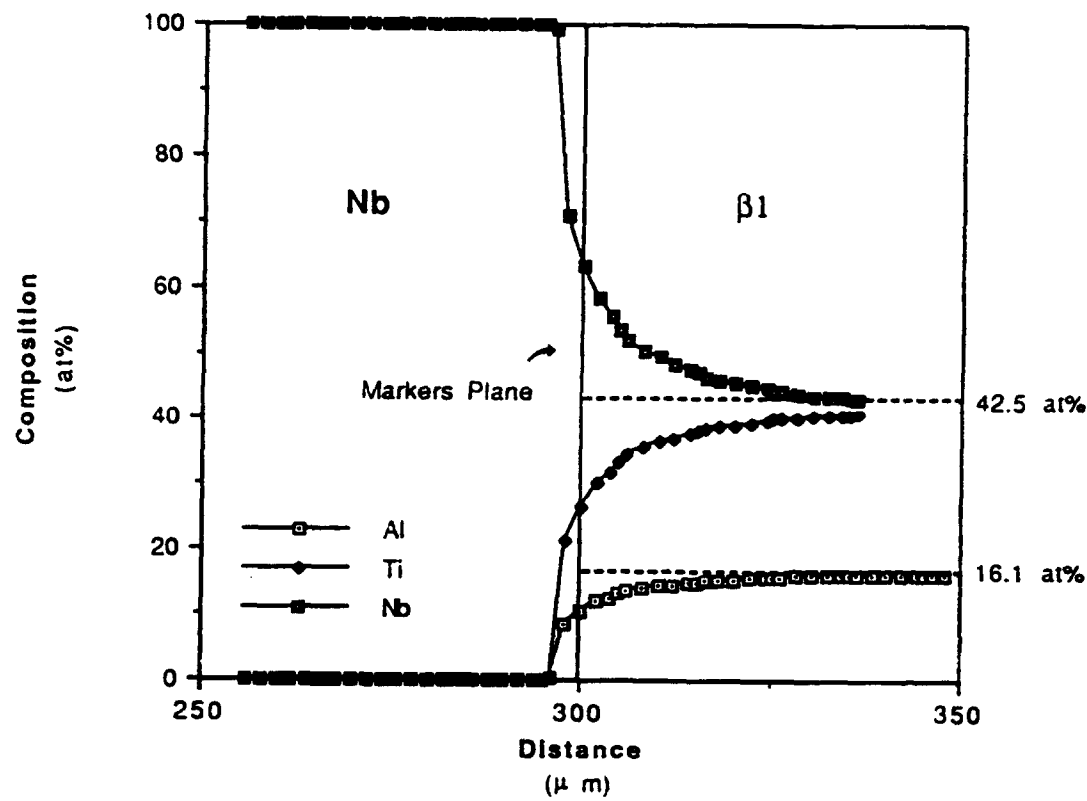


Figure 5.14 Penetration curves of the 3 components in the couple #8 ( $\beta_1/\text{Nb}$ ) heat treated at 1200 °C for 6 hours.

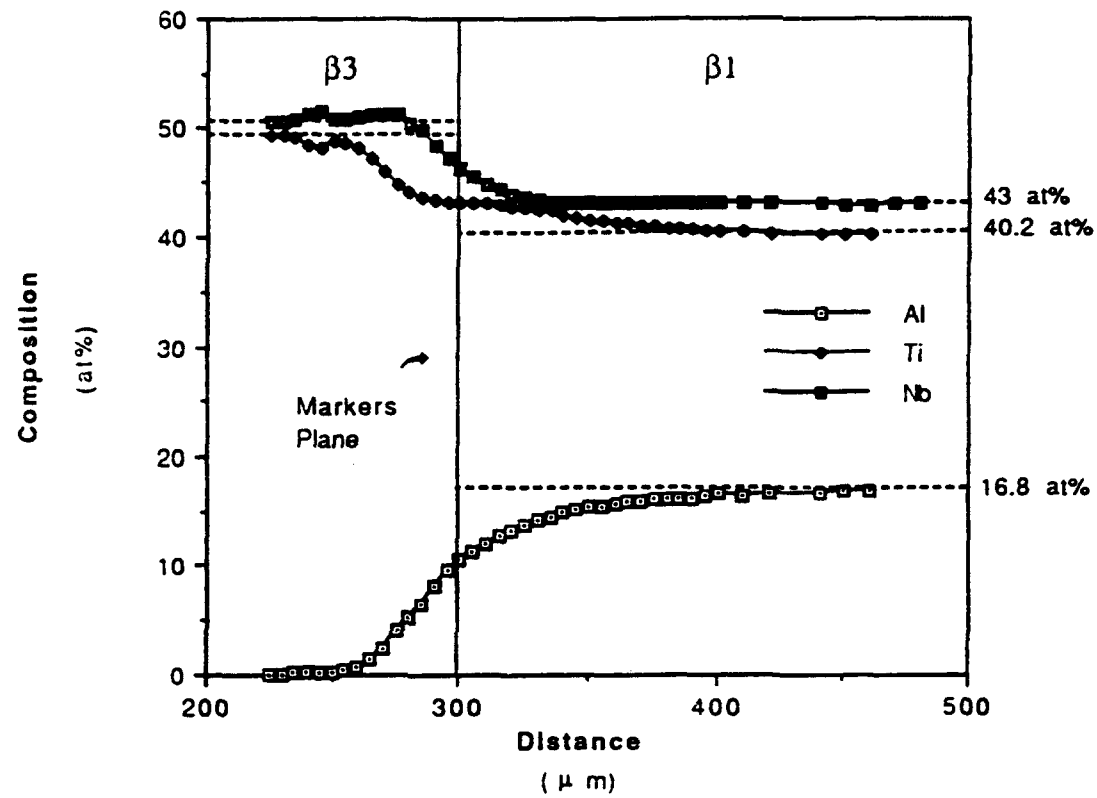


Figure 5.15 Penetration curves of the 3 components in the couple #9 ( $\beta_1/\beta_3$ ), heat treated at  $1200\text{ }^{\circ}\text{C}$  for 6 hours.

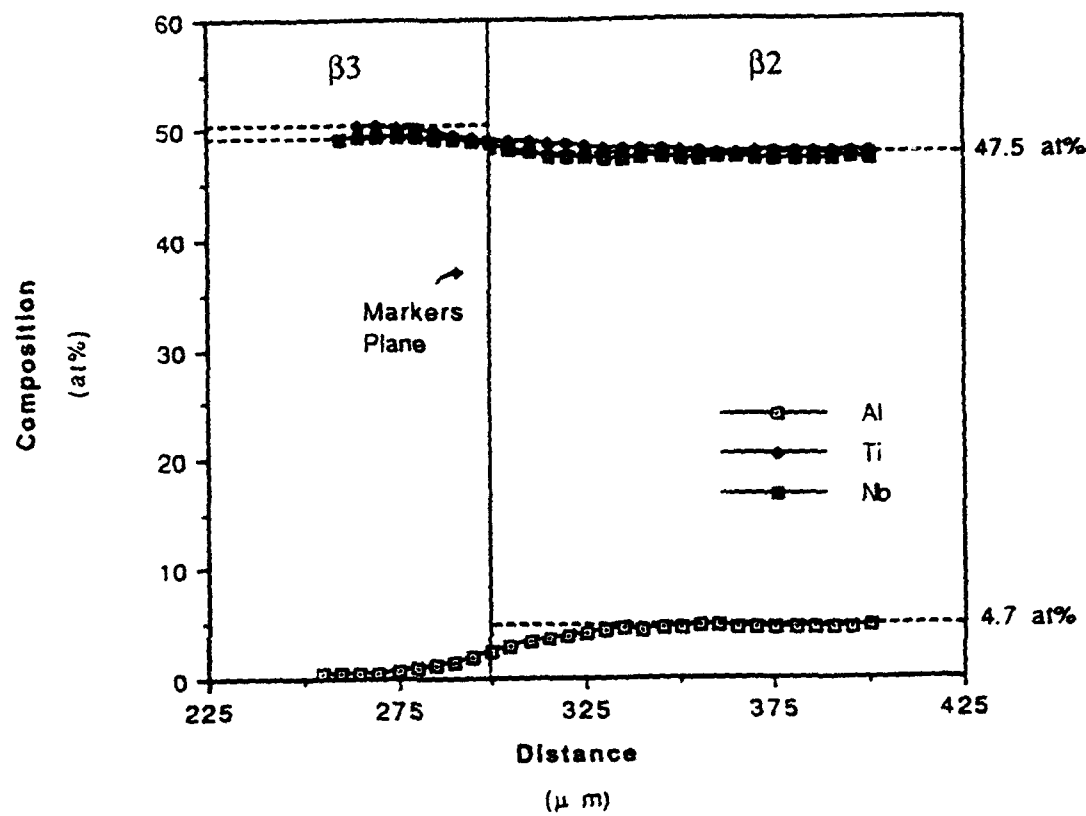


Figure 5.16 Penetration curves of the 3 components in the couple #10 ( $\beta_2/\beta_3$ ), heat treated at 1200 °C for 6 hours.

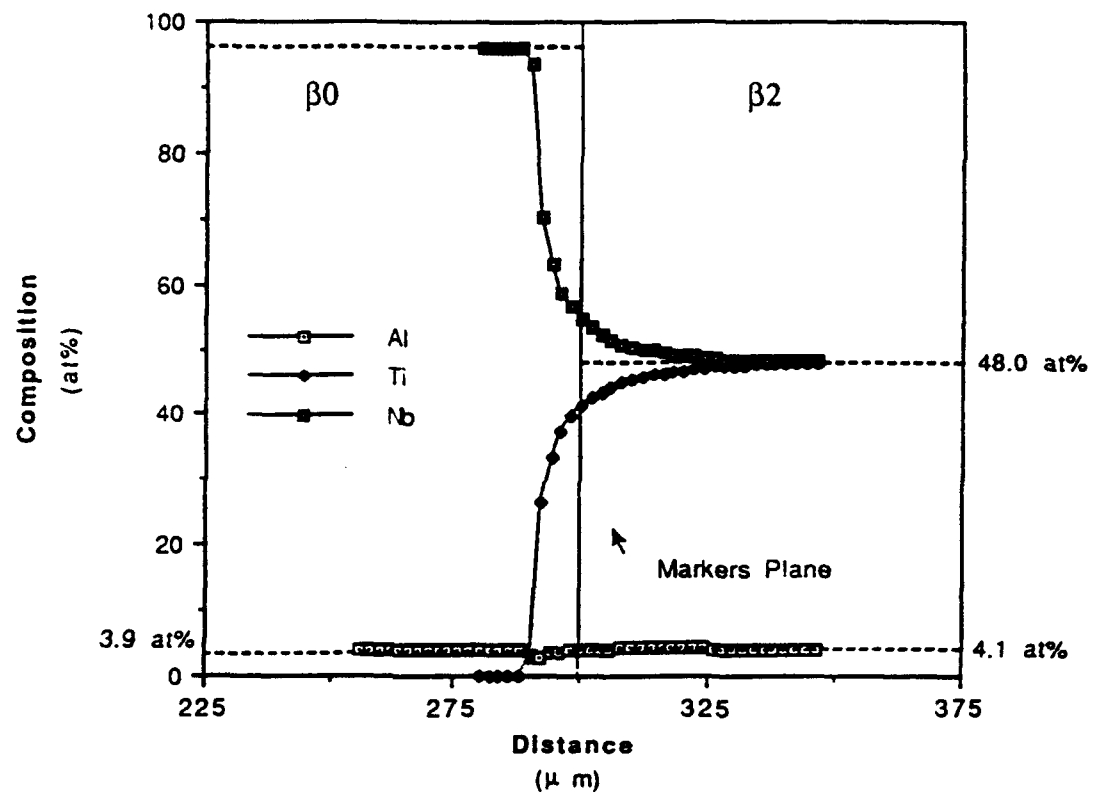


Figure 5.17 Penetration curves of the 3 components in the couple #11 ( $\beta_2/\beta_0$ ), heat treated at 1200 °C for 6 hours.

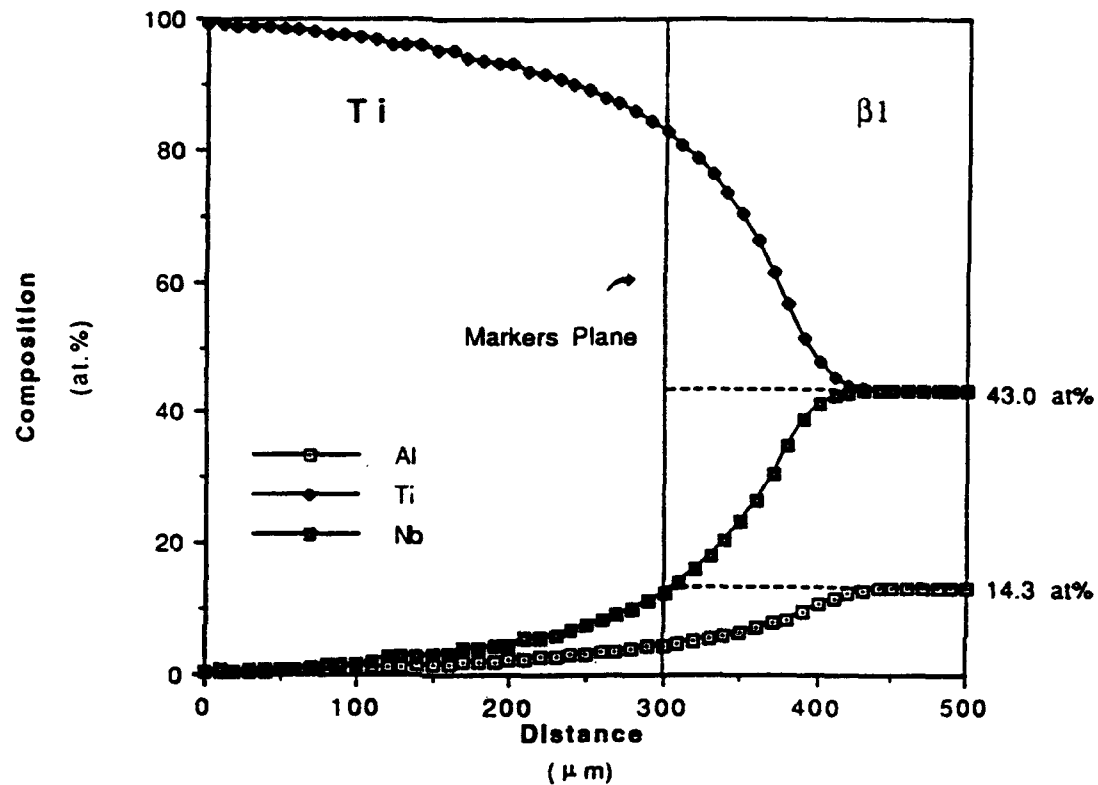


Figure 5.18 Penetration curves of the 3 components in the couple #12 ( $\beta_1/\text{Ti}$ ) heat treated at 1200 °C for 6 hours.

### 5.2.1 The $\beta_1/X$ couples: Effect of Ti content

The penetration curves of the three couples containing  $\beta_1$  alloy are compared for individual elements in Figures 5.19 to 5.21. It is observed that the depth of penetration in the counterpart side of  $\beta_1$  is in general larger as its Ti content increases. For example, penetration curve for couple #8 shows only a shallow penetration of the three elements (less than 5  $\mu\text{m}$ ) into the Nb side, whereas couples #9 and #12 show much deeper penetration into the  $\beta_3$  and Ti, respectively. As to the penetration in the ternary alloy side  $\beta_1$ , the depth of penetration for each element is also larger as the Ti content of the counterpart side increases.

### 5.2.2 Effect of Concentration Gradient

Figures 5.22 to 5.24 compare the composition profiles of each element for two cases with a constant Nb:Ti ratio and different Al composition gradient (couples #9 and #10). As expected, larger composition gradient results in a larger penetration depth of Al. When the Al concentration on both sides of the couple is the same the composition profile is given in Figure 5.25. A larger diffusion zone on the ternary side of the couple than that of the binary Nb-4.5Al side is observed. However, when the concentration profiles for diffusion couples #11 ( $\beta_0/\beta_2$ ) and #10 ( $\beta_3/\beta_2$ ) are compared to each other some interesting observations are made (see Figures 5.26-5.28). It is observed that although the concentration gradients of Ti and Nb are smaller in couple #10, it has a larger diffusion zone than

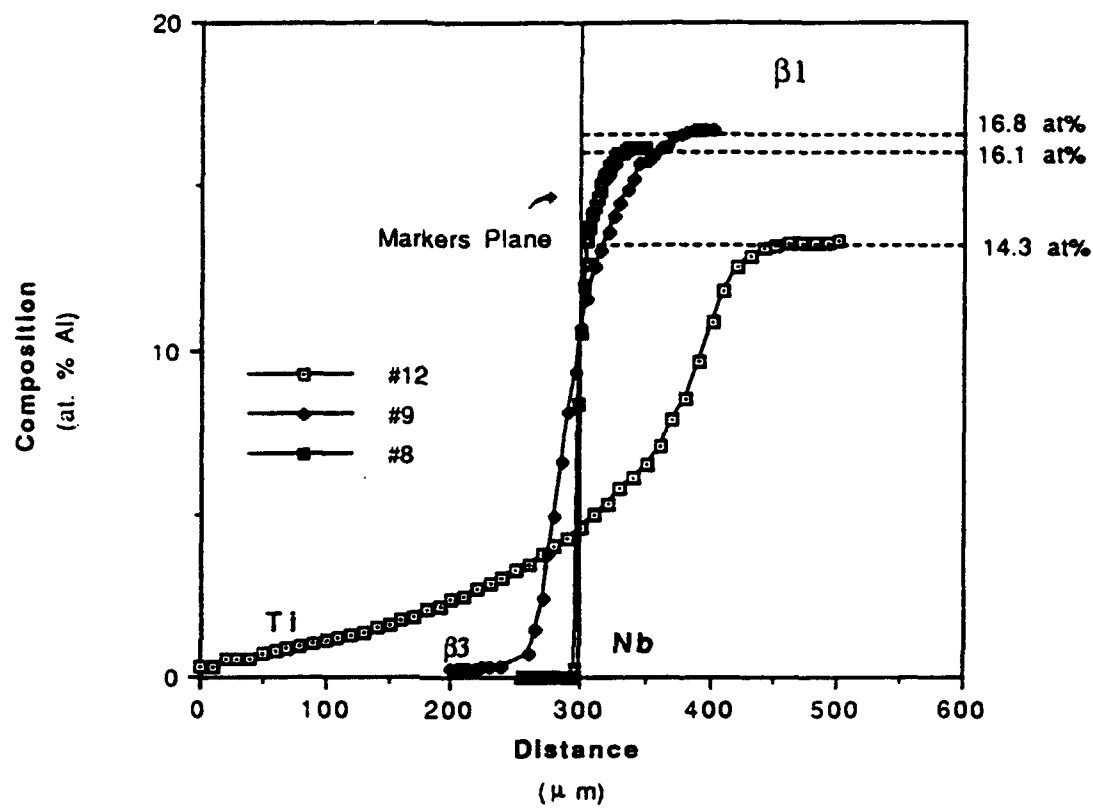


Figure 5.19 Penetration curves of Al in three different diffusion couples heat treated at 1200 °C for 6 hours.

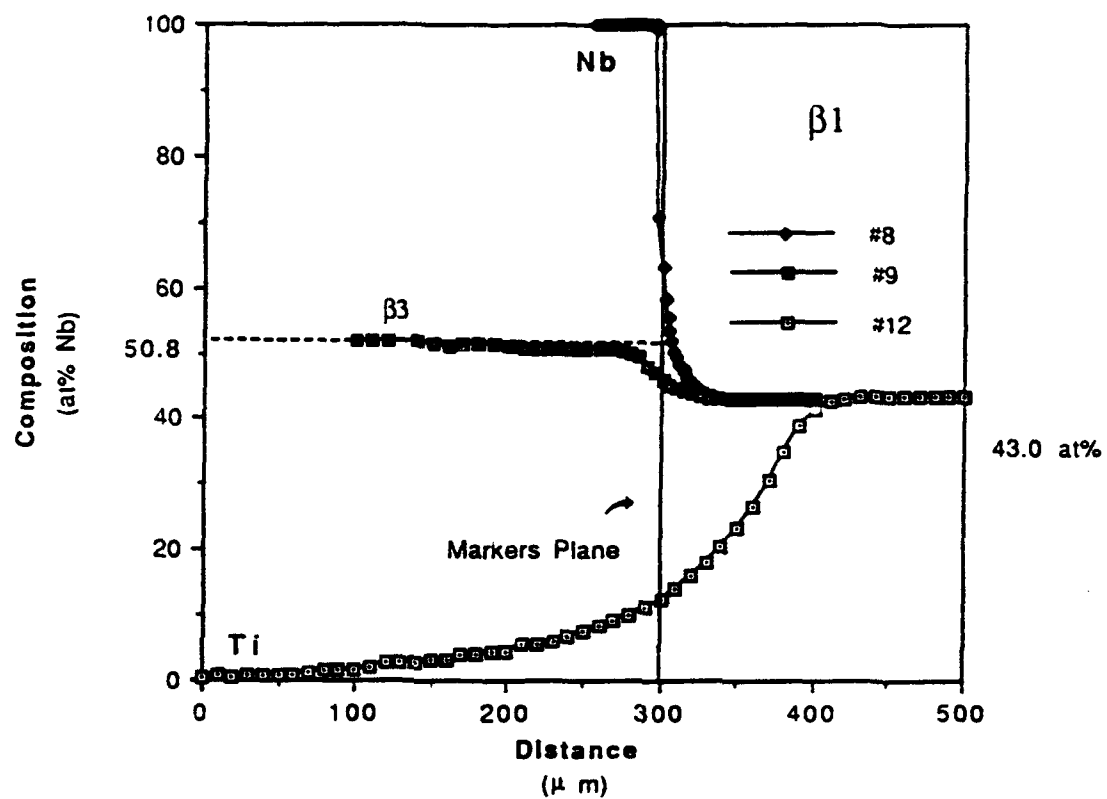


Figure 5.20 Penetration curves of Nb in three different diffusion couples heat treated at 1200 °C for 6 hours.

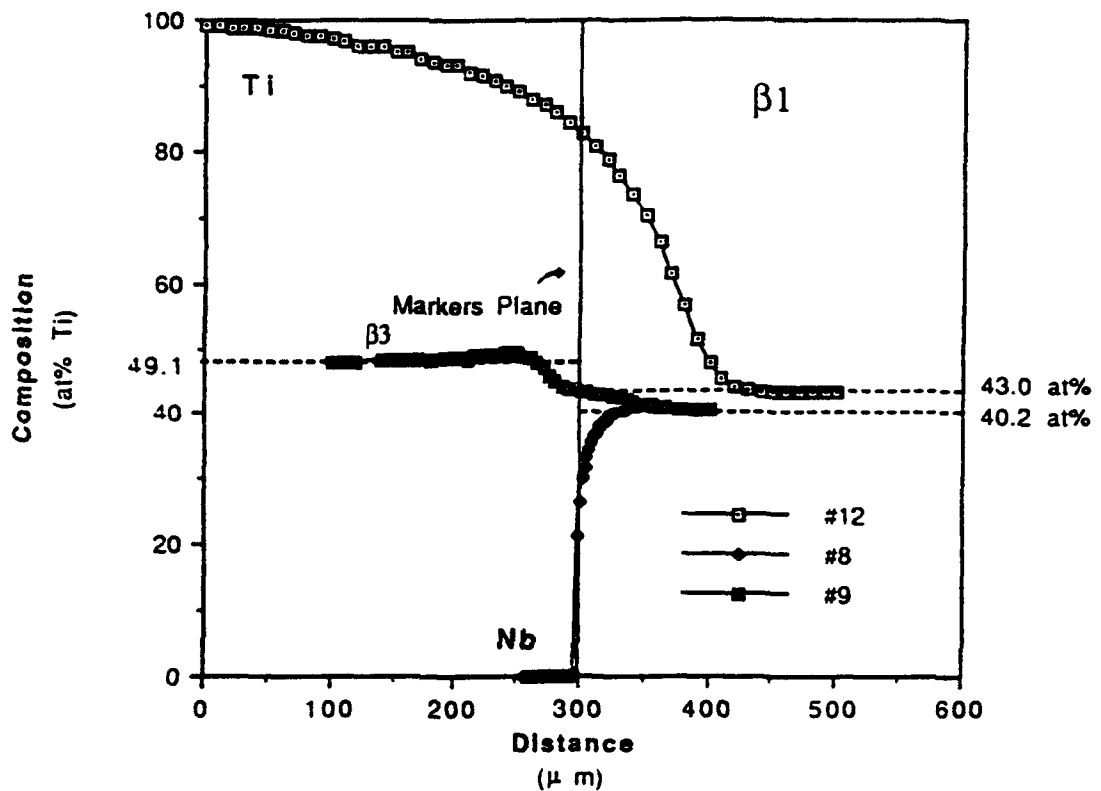


Figure 5.21 Penetration curves of Ti in three different diffusion couples heat treated at 1200 °C for 6 hours.

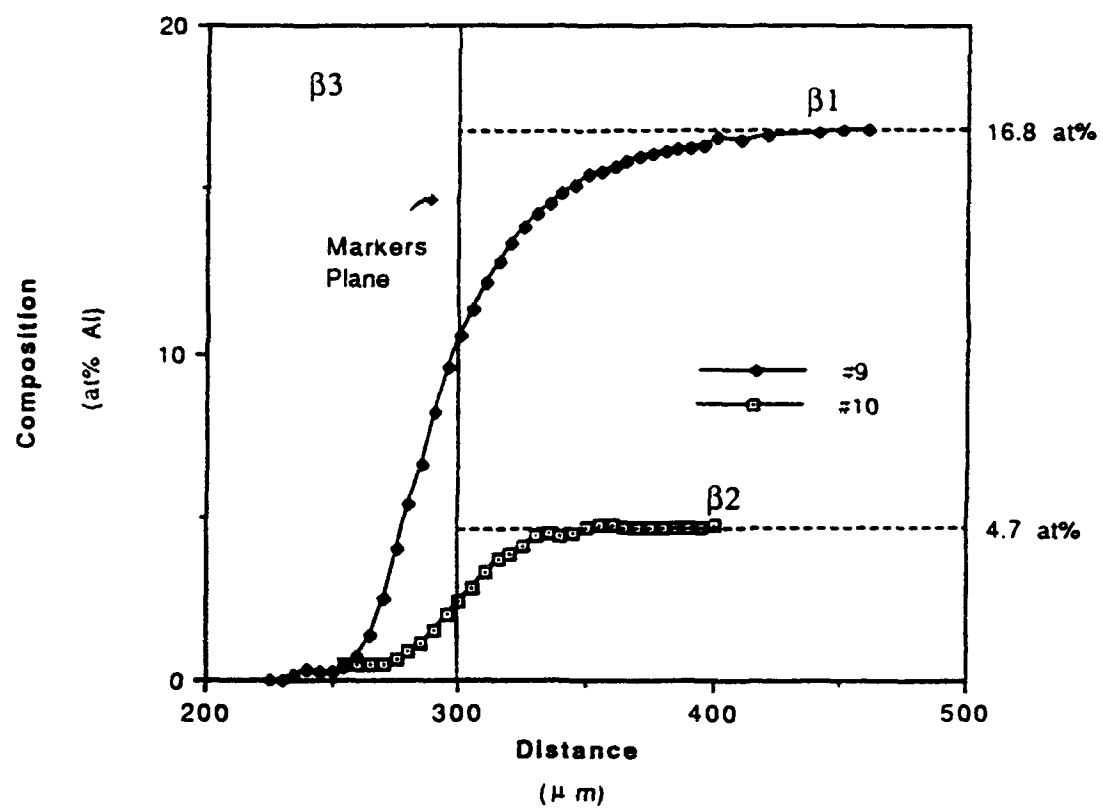


Figure 5.22 Composition profiles of Al in diffusion couples #9 and #10 after heat treatment at 1200 °C for 6 hours.

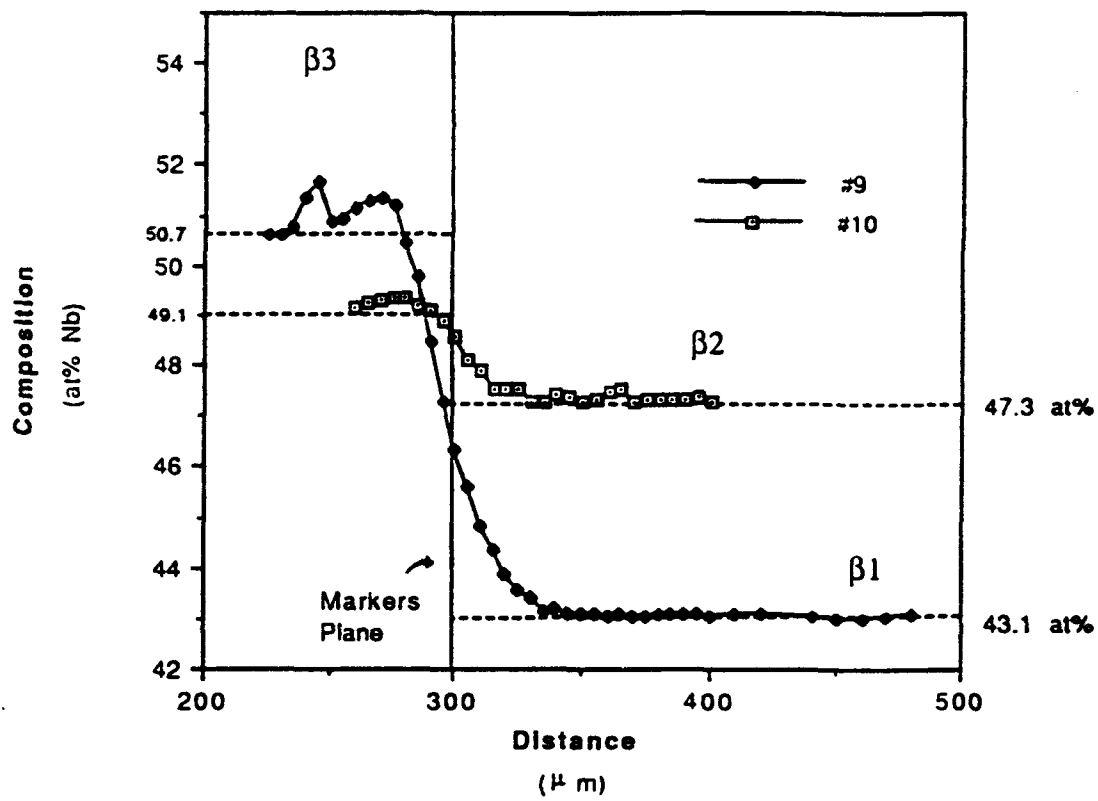


Figure 5.23 Composition profiles of Nb in diffusion couples #9 and #10 after heat treatment at 1200 °C for 6 hours.

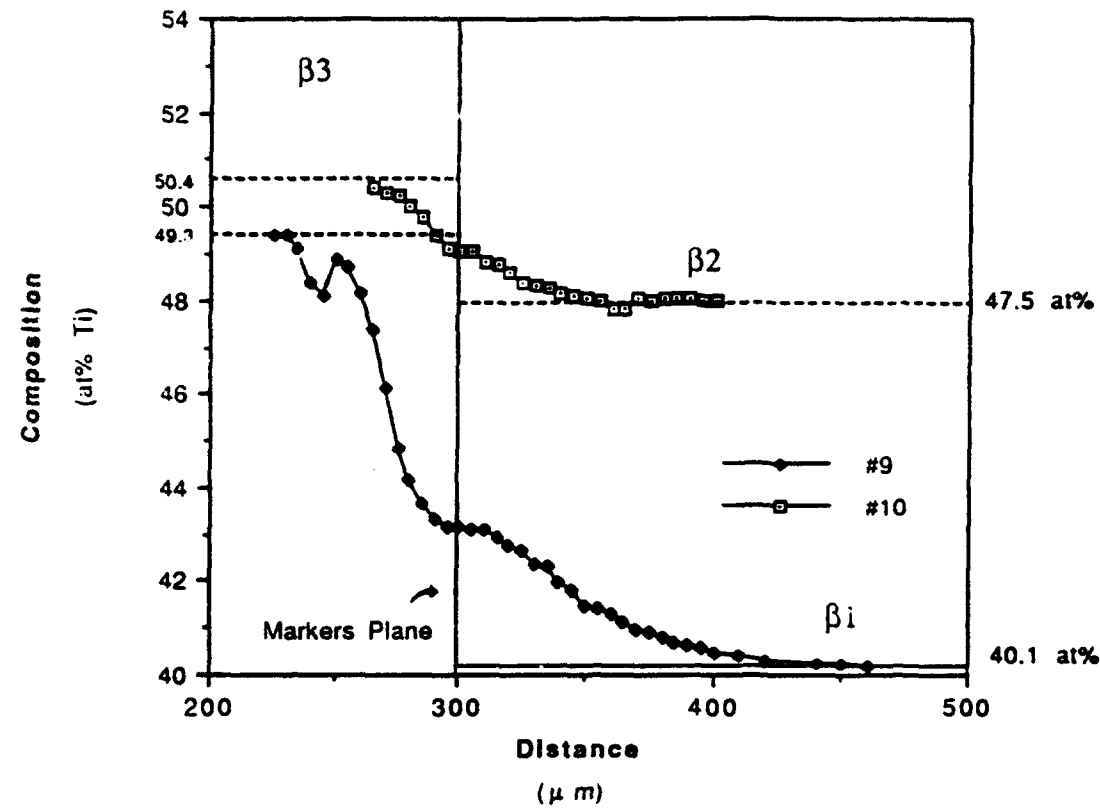


Figure 5.24 Composition profiles of Ti in diffusion couples #9 and #10 after heat treatment at 1200 °C for 6 hours.

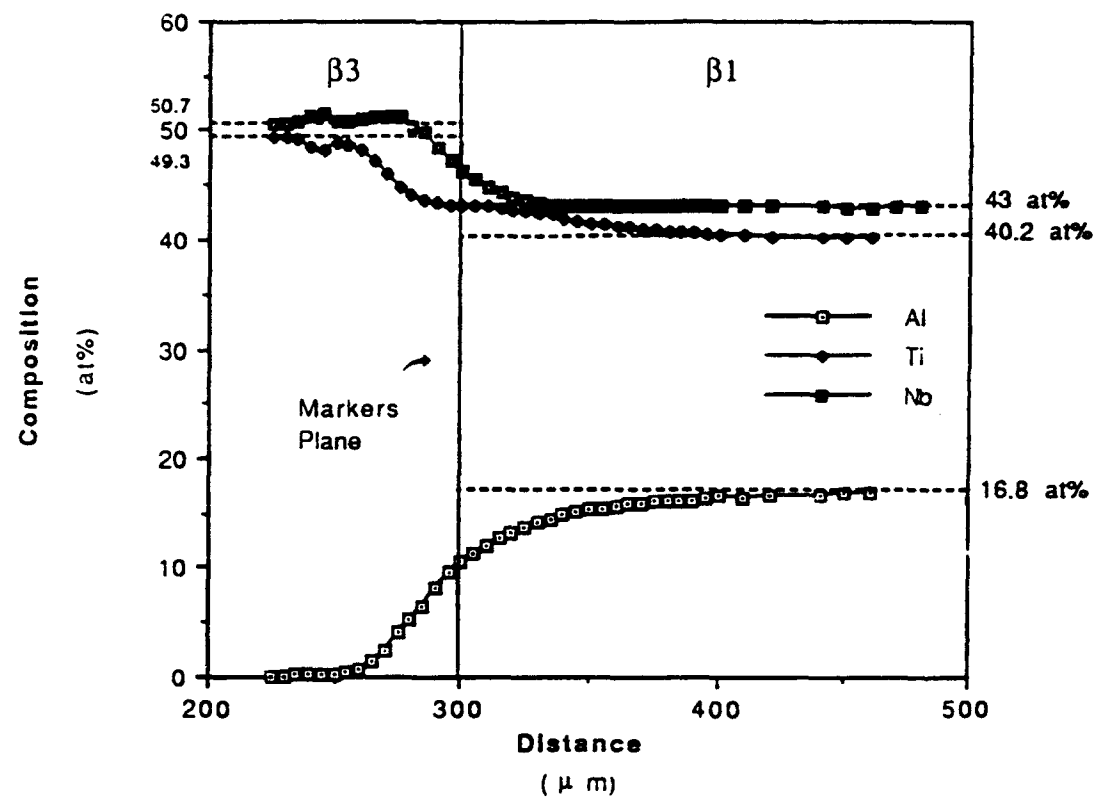


Figure 5.25

Composition profiles of the 3 components at constant Al concentration (couple #9  $\beta_1/\beta_3$ ) after heat treatment at 1200 °C for 6 hours.

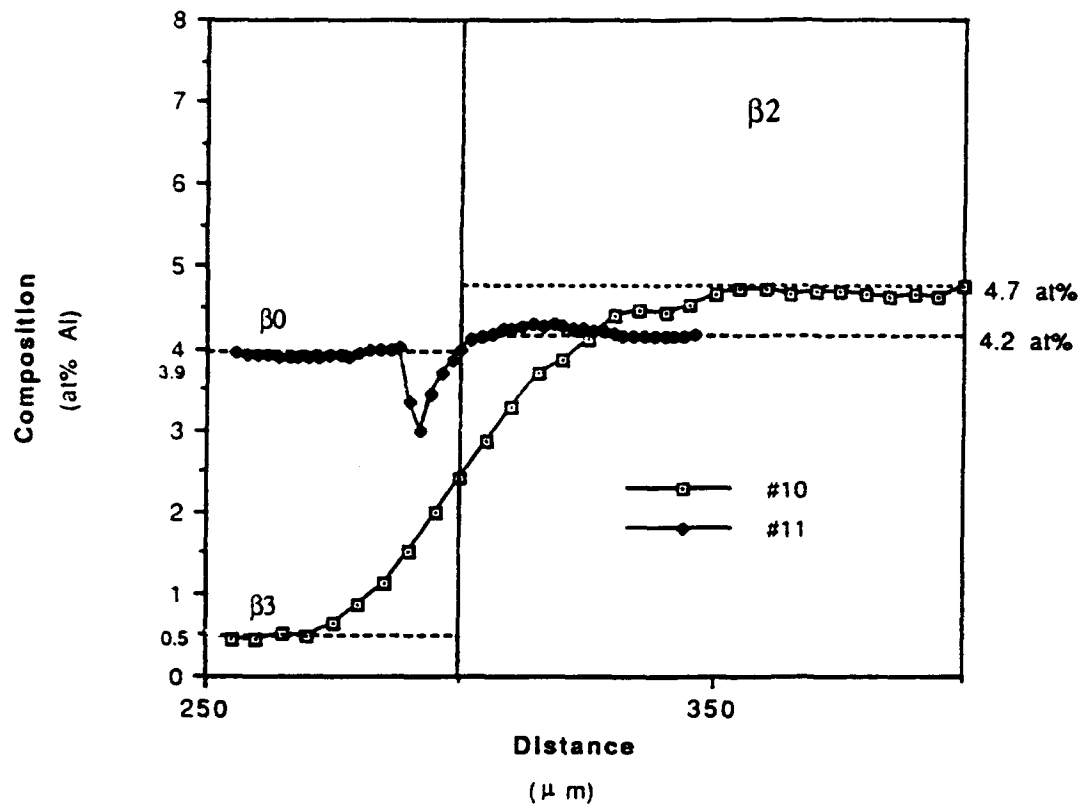


Figure 5.26 Comparison of penetration depth of Al in couples involving alloy  $\beta_2$  (#10 ( $\beta_3/\beta_2$ ) and #11 ( $\beta_0/\beta_2$ ))

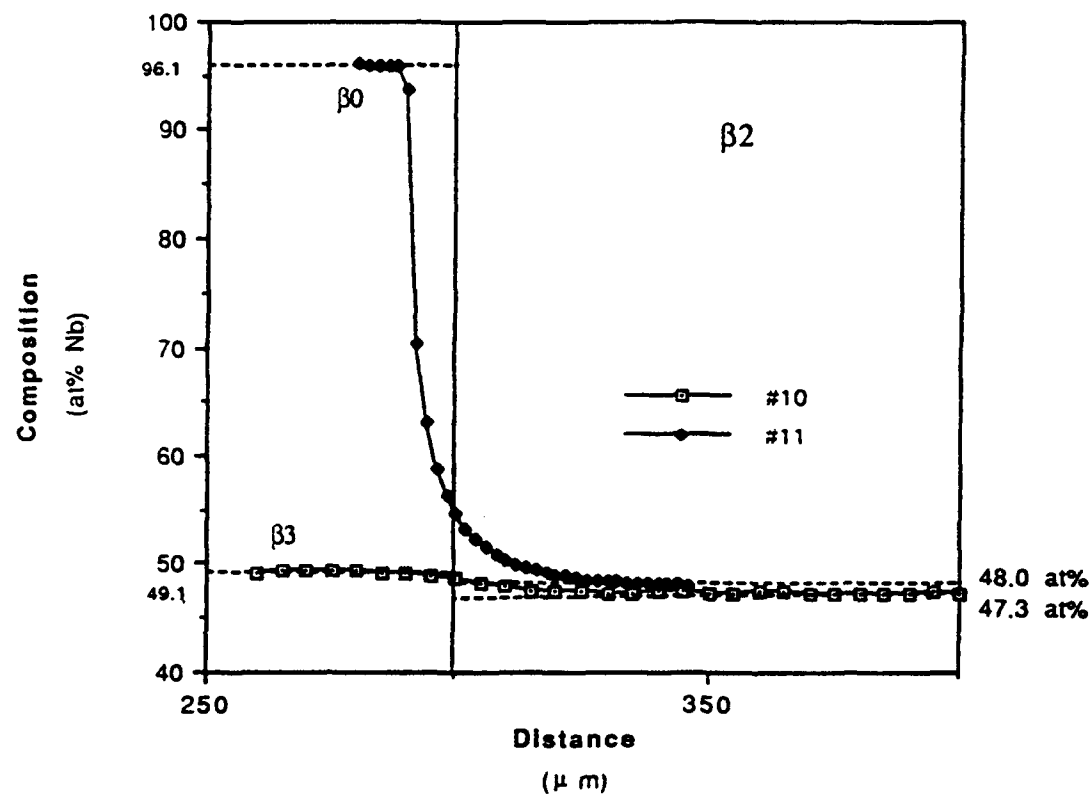


Figure 5.27

Comparison of penetration depth of Nb in couples involving alloy β<sub>2</sub> (#10 (β<sub>3</sub>/β<sub>2</sub>) and #11 (β<sub>0</sub>/β<sub>2</sub>))

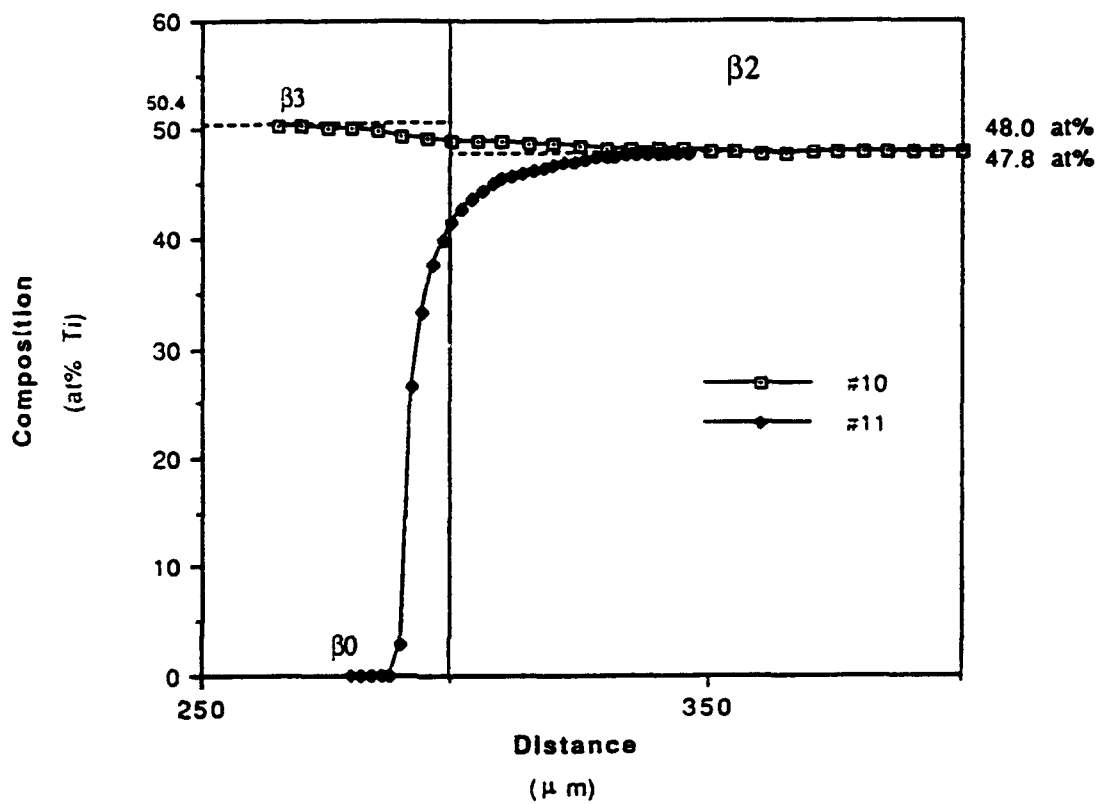


Figure 5.28 Comparison of penetration depth of Ti in couples involving alloy  $\beta_2$  (#10 ( $\beta_3/\beta_2$ ) and #11 ( $\beta_0/\beta_2$ ))

the couple #11 does. This could be explained readily by comparing the solidus temperatures of the alloys involved in the respective couples; the  $\beta_0$  alloy has a much higher solidus temperature than the  $\beta_3$  alloy does.

### 5.2.3 Critical Points

Except in a few cases, all composition profiles of the couples studied did not exhibit critical points and their shape was smooth and similar to that obtained in the binary diffusion studies. Figures 5.29 to 5.31 shows the compcsition profiles for those cases, in which inaxima and minima where observed. An interesting observation is that these critical points appeared always when the concentration gradient of the element was small, i. e. for Al in couple #11 (Figure 5.29), for Nb in couples #7, #9, and #10 (Figure 5.30), and for Ti in couple #9 (5.31). When the diffusion temperature is increased for the couple  $\beta_3/\beta_1$  from 1200 °C (#9) to 1400 °C (#7) the maxima in the composition profiles of the Ti is completely removed, and for the Nb at 1400 °C the profile shows a small tendency for maximum. These observations suggest that limited physical movement of atoms due to a low interdiffusion temperature, low concentration gradient or high melting point of the element such as Nb results in the occurrence of maxima and minima in the concentration curves as obtained by microprobe analysis. As suggested by DeHoff *et. al.* [69] the apparent diffusion zone measured by the microprobe analysis does not represent the actual physical distance over which the atoms have moved. When the movement of one element is limited due to the

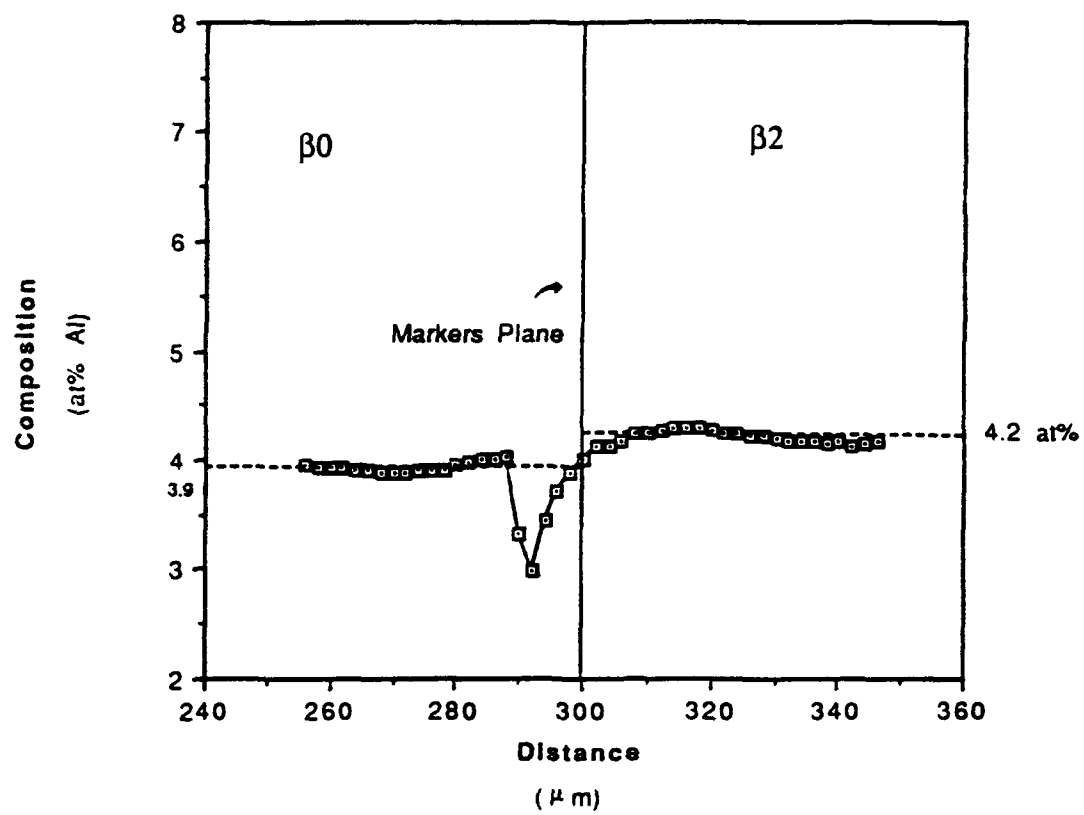
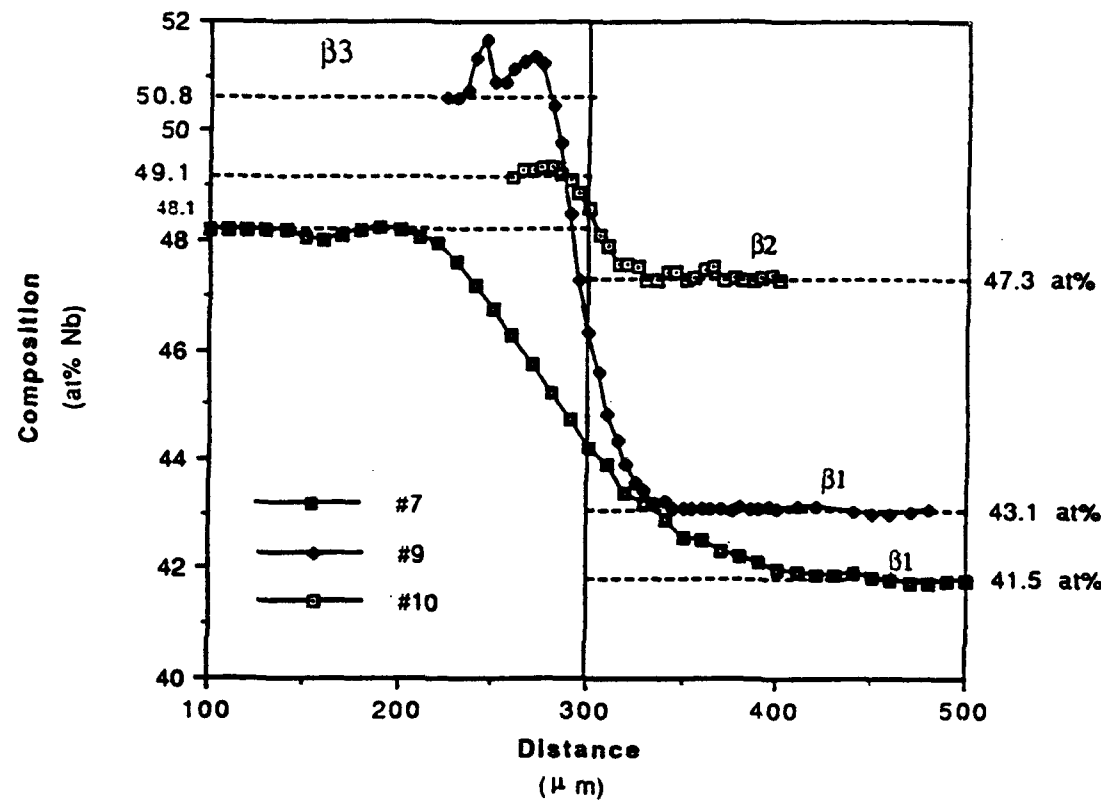


Figure 5.29 Critical point observed in the Al composition profile after diffusion treatment of couple #11 ( $\beta_0/\beta_2$ ) at 1200 °C for 6 hours.



**Figure 5.30** Critical point observed in the Nb composition profile after diffusion treatment of couples #7 ( $\beta_0/\beta_2$ ), #9 ( $\beta_3/\beta_1$ ) and #10 ( $\beta_3/\beta_2$ ) at 1200 °C for 6 hours.

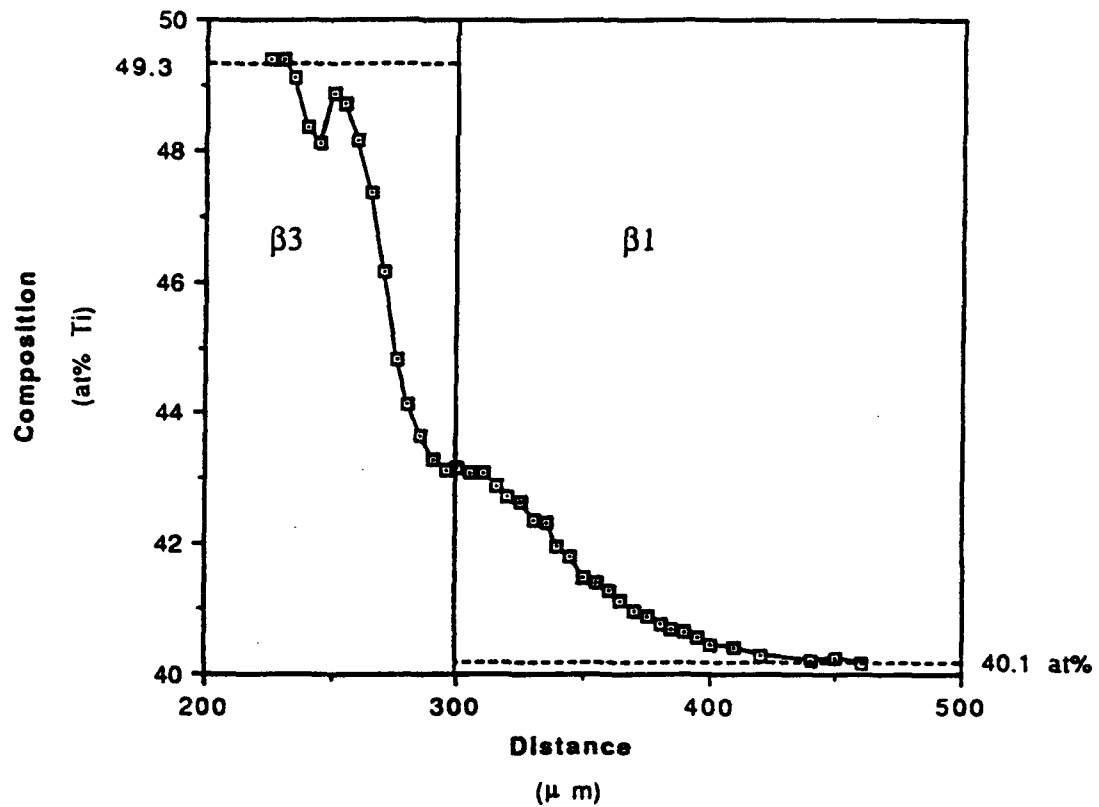


Figure 5.31 Critical point observed in the Ti composition profile after diffusion treatment of couple #9  $\beta_3/\beta_1$  at 1200 °C for 6 hours.

above mentioned reasons, such as Nb in the Nb-Ti-Al system the atomic fraction profile of this element represent the unequal mobility of the other constituent elements.

#### 5.2.4 Temperature Effect

The composition profiles for each element of the systems consisting of Nb/ $\beta_1$ /Nb (#6, #8), and  $\beta_3/\beta_1/\beta_3$  (#7, #9) interdiffused at 1400 °C and 1200 °C are compared in Figures 5.32 to 5.34 for the former case and Figure 5.35 to 5.37 for the latter one. At 1400 °C the general behavior observed in the diffusion couples treated at 1200 °C is maintained. That is, the penetration depth is larger in the ternary side of the couples. As expected, the depth of penetration of each component becomes deeper as the temperature is raised.

### 5.3 Penetration Depth

As was shown in Figures 5.12 to 5.18 the depth of the penetration of the composition profiles is not symmetrical in both sides of a given couple. Table 5.1 shows the depth of penetration for the different couples as measured by microprobe analysis. Next, each case is analyzed individually.

a)  $\beta_1/\text{Nb}$  (1200 °C): In this case the three components show an equal penetration depth on each side of the couple; however, their penetration curves are not symmetrical. A much larger penetration is observed on the  $\beta_1$  side, i. e. the side with the lower solidus temperature.

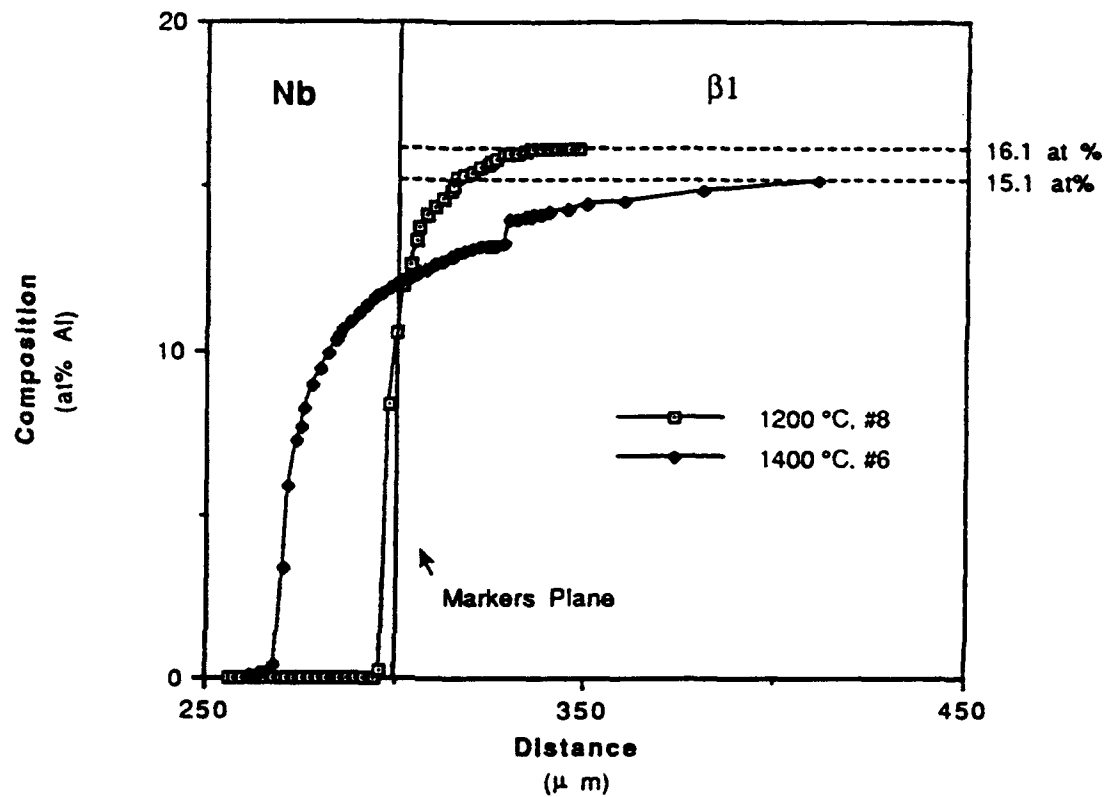


Figure 5.32 Composition profile for Al after interdiffusion treatment at  $1200^{\circ}C$  (#8) and  $1400^{\circ}C$  (#6) for 6 hours.

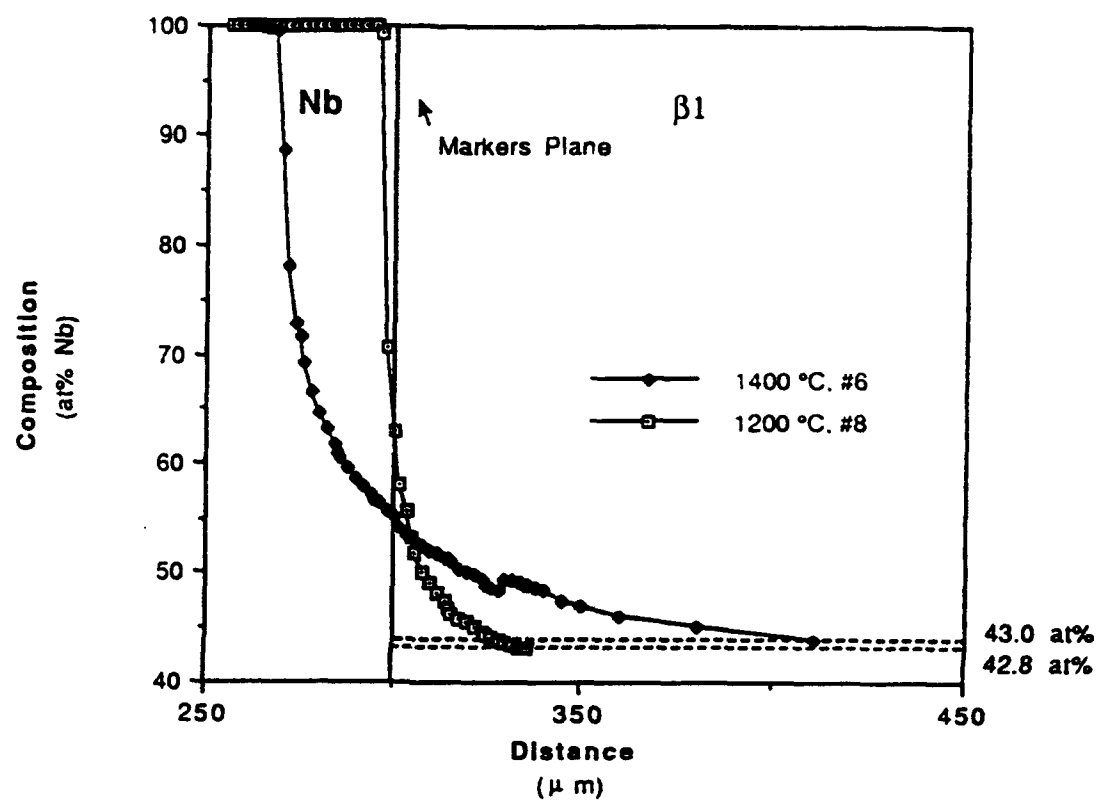


Figure 5.33 Composition profile for Nb after interdiffusion treatment at 1200 °C (#8) and 1400 °C (#6) for 6 hours.

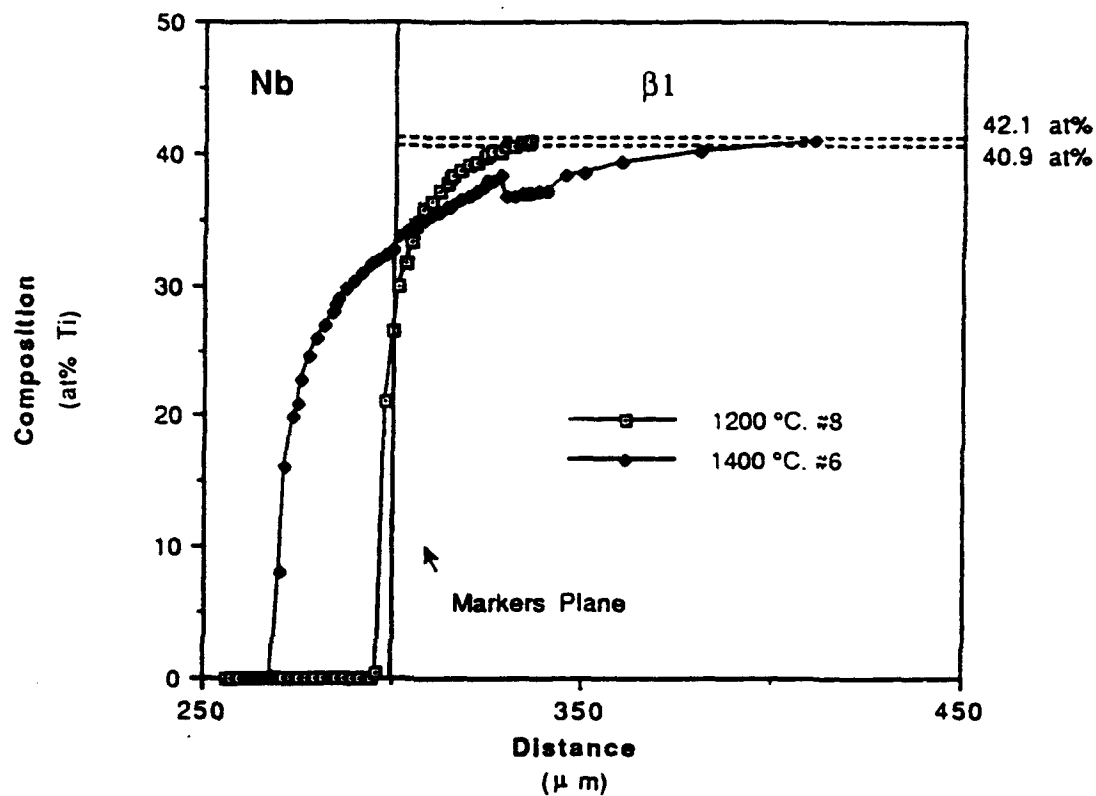


Figure 5.34

Composition profile for Ti after interdiffusion treatment at 1200 °C (#8) and 1400 °C (#6) for 6 hours.

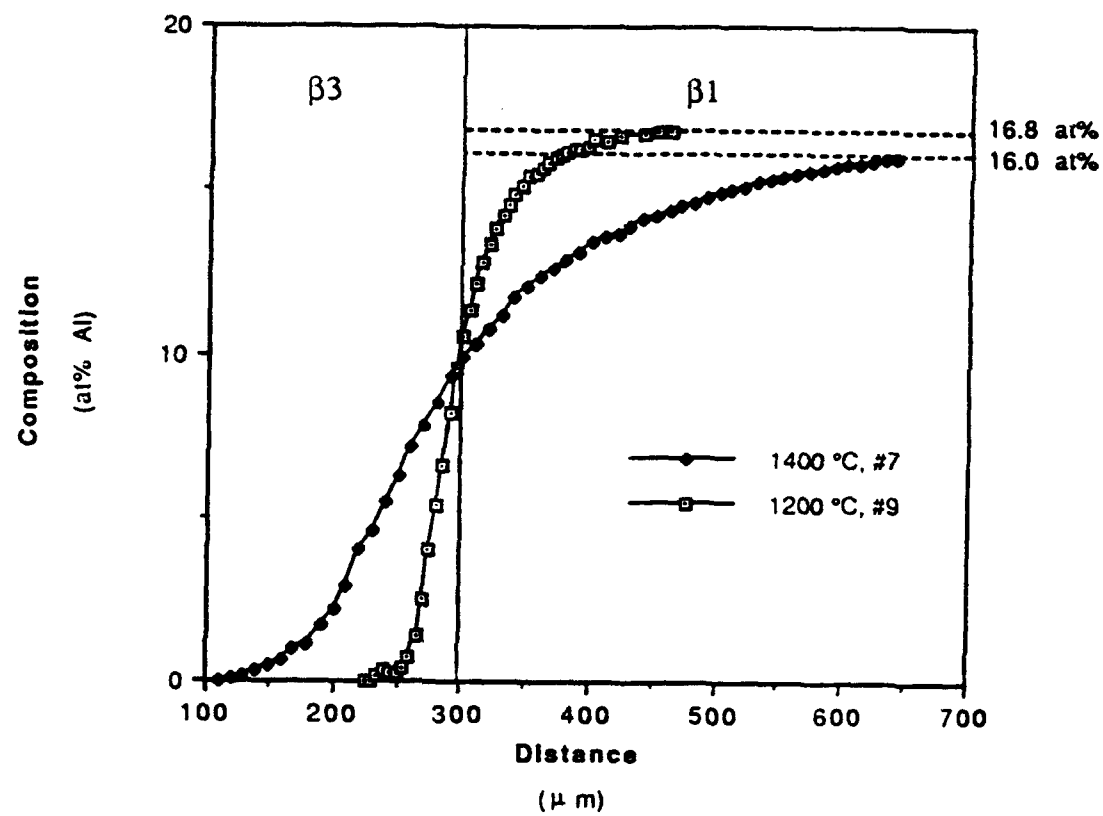


Figure 5.35 Composition profile for Al after interdiffusion treatment at 1200 °C (#7) and 1400 °C (#9) for 6 hours.

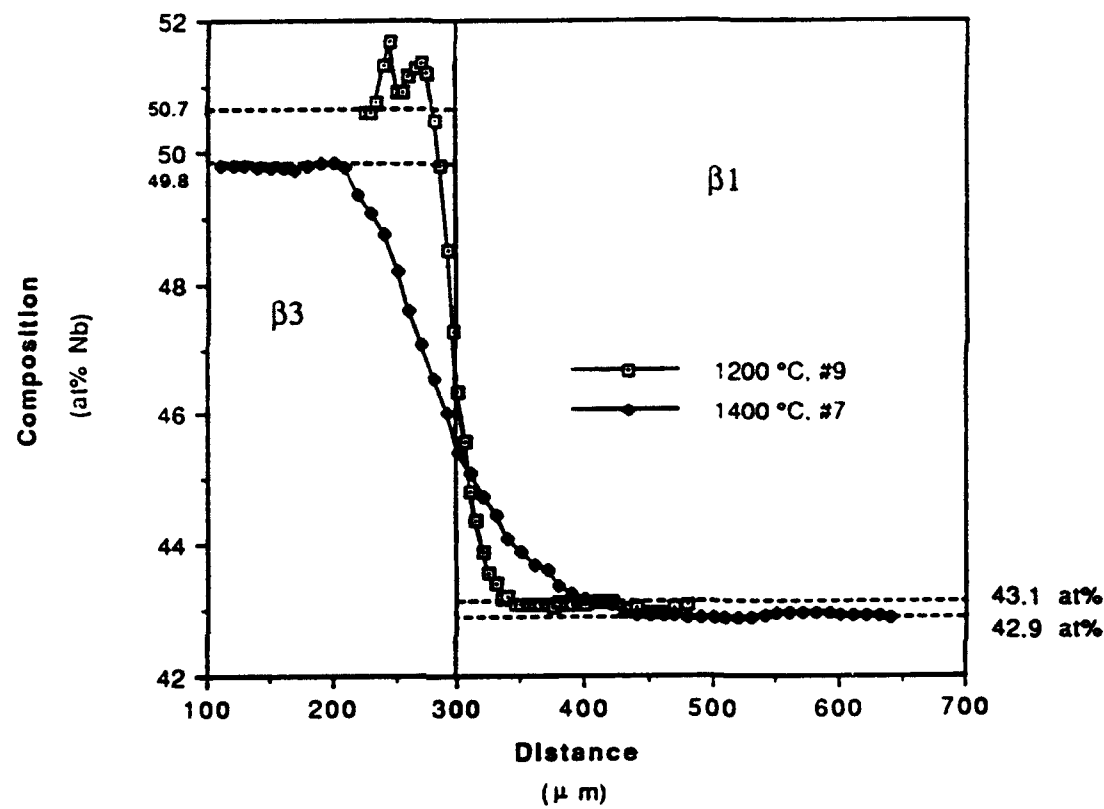


Figure 5.36 Composition profile for Nb after interdiffusion treatment at 1200 °C (#7) and 1400 °C (#9) for 6 hours.

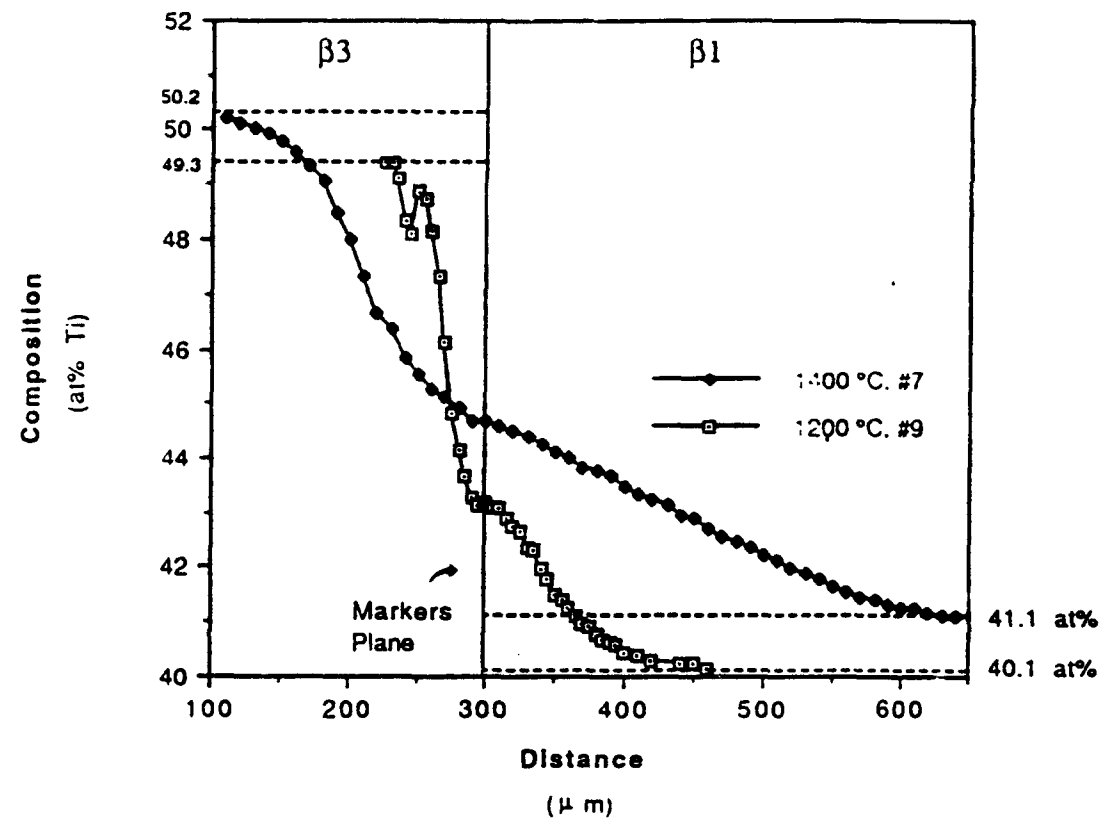


Figure 5.37 Composition profile for Ti after interdiffusion treatment at 1200 °C (#7) and 1400 °C (#9) for 6 hours.

Table 5.1 Depth of penetration in ternary diffusion couples of system  
(B.C.C.) Nb-Ti-Al  
( $\mu\text{m}$ )

Couple #	Side	Component			Side	T ( $^{\circ}\text{C}$ )
8	$\beta_1$	Nb	Ti	Al	Nb	Al
		3.4	3.6	3.5	3	3
9	$\beta_1$	4.3	8.3	8.3	a	197
					197	72
12	$\beta_1$	10.2	12.7	12.7	t	293
					323	313
10	$\beta_2$	3.6	5.5	5.5	a	30
					3.5	31
11	$\beta_2$	3.9	4.6	4.3	n	5
					6	7
6	$\beta_1$	13.4	13.4	13.4	o	1
					1	1
7	$\beta_1$	17.7	20.2	20.2		
					12.3	19.8
					18.8	$\beta_3$
						1400

b)  $\beta_1/\beta_3$  (1200 °C): In this case the solidus temperatures of the two sides are not expected to be very different, and therefore the concentration gradients of the components play an important role in the final shape of the penetration curve. Aluminum is the element with the largest composition gradient and penetrates from the  $\beta_1$  to the  $\beta_3$  side producing an approximately similar penetration depth on both sides of the couple. The flux opposite to the Al motion is mainly due to Ti, as indicated by the small penetration of Nb in the  $\beta_1$  side. It is interesting that Al penetration depth in the  $\beta_3$  side is much smaller than the draw depth of Nb and Ti. A comparison of the diffusion zone size with that at 1400 °C for the same couple reveals that the apparent draw depth of Nb on the  $\beta_3$  side decreases with increasing temperature. This observation suggests that indeed the apparent draw depth of Nb at 1200 °C does not represent the actual physical motion of Nb. However, since Al does not penetrate to the same depth, unless the crystal can tolerate very large fractions of vacancies there should be an actual uphill diffusion of Nb. Another possibility that can contribute to this observation is a large composition dependency of the molar value in this system. Unfortunately no precise lattice parameter data for these compositions are known. Here, the Ti comes from a large distance within the  $\beta_3$  side. The apparent large penetration depth of Nb on the  $\beta_3$  side is due to the readjustment of the atomic fraction due to the loss of Ti. It should be noted that the penetration depths evaluated by microprobe analysis may not represent the physical distance that atoms have moved, since a variation in their atomic fraction may be

a result of the diffusivity of any of the other species in that part of the couple [69].

c)  $\beta_1/\text{Ti}$  (1200°C): The relative penetrations of Al and Ti are equal on each side of this couple and larger than that of Nb. It is observed again that the side with the lower solidus temperature (Ti-side) exhibits the larger penetration depths. The depths of penetration in this case are in general much larger as compared to those in the  $\beta_1/\text{Nb}$  couple. In the latter the kinetics are limited by the motion of atoms and vacancies in the Nb side, however, in the former couple it is the motion in the  $\beta_1$  side that controls the penetration.

d)  $\beta_2/\beta_3$  (1200 °C): In this case the penetration depth of Al is smaller than the  $\beta_1/\beta_3$  couple due to a smaller Al concentration gradient. It is interesting to note that in this couple, contrary to the  $\beta_1/\beta_3$  couple the Nb and Ti draw depths are much smaller and equal to the penetration depth of the Al on the  $\beta_3$  side. This behavior may be related to the lower concentration gradient of Ti in the  $\beta_2/\beta_3$  couple than in the  $\beta_1/\beta_3$  couple.

e)  $\beta_1/\beta_0$  (1200 °C): This couple exhibits similar behavior to the  $\beta_1/\text{Nb}$  couple analyzed previously. Here, basically the penetration depth of the elements is controlled by the motion of Nb in the Nb-rich side, which has the higher solidus temperature.

f)  $\beta_1/\text{Nb}$  (1400 °C): The behavior of this couple is similar to that observed in the same system at 1200 °C, except that, as expected, larger penetration depths for each component are obtained.

g)  $\beta_1/\beta_3$  (1400 °C): At 1400 °C the mobility of Al is higher, and consequently the penetration depth of it is larger. At this temperature Ti penetrates deeper into  $\beta_1$  side, however, its draw

depth from the  $\beta_3$  side is the same as that at 1200 °C. As mentioned previously the draw depth of Nb from the  $\beta_3$  side indeed decreases with increasing temperature. This observation and the absence of maxima and minima in the composition profile of Ti at 1400 °C and its almost equal depth of draw with that of Al penetration on the  $\beta_3$  side, contrary to the pattern at 1200 °C, suggest that at the latter diffusion diffusion temperature, uphill diffusion of Nb have occurred. Further investigation is required to understand the composition patterns in this system.

#### 5.4 Composition Paths

The composition paths for the different diffusion couples are presented in 3 parts depending on their position over the Gibbs triangle:

- a) Nb-rich corner
- b) Constant Nb:Ti ratio zone
- c) Ti-rich corner

##### 5.4.1 The Nb-Rich Corner

The composition paths of the diffusion couples involving a pure Nb side (couples #8 and #6) show an interesting similarity to the line joining the end compositions of the couple as shown in Figures 5.38 and 5.39 for interdiffusion temperatures of 1200 °C and 1400°C, respectively. This composition path behavior indicates [69] equal mobility of the elements in this corner, consistent with the results

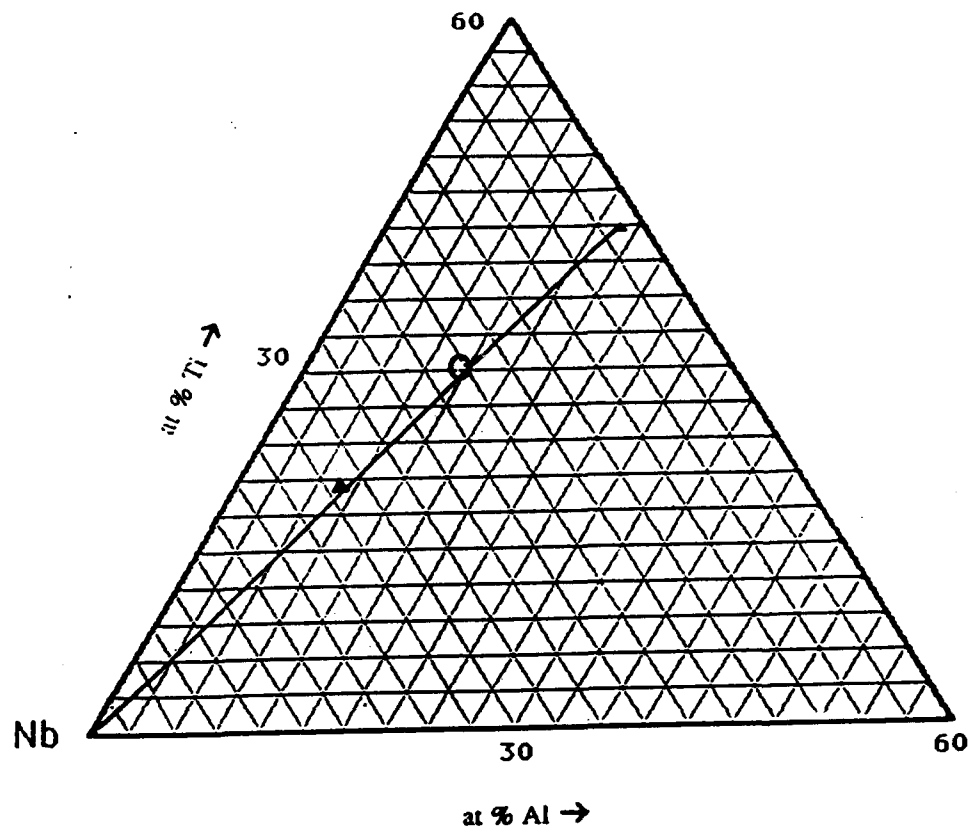
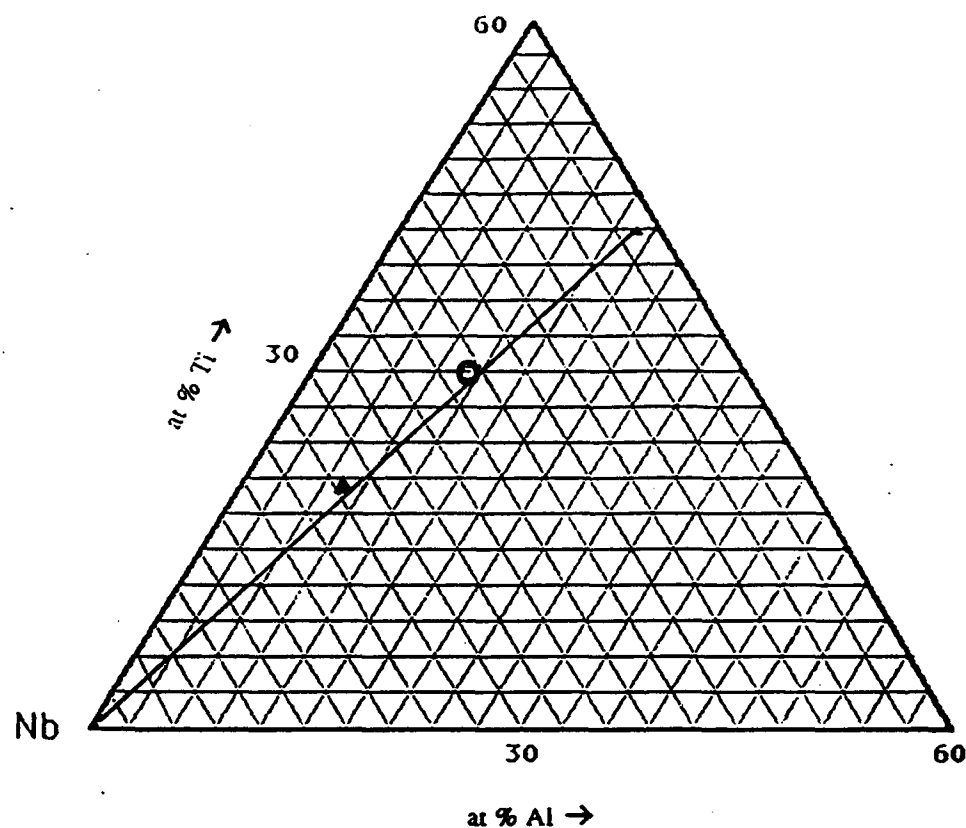


Figure 5.38 Composition path for diffusion couple #8 ( $\beta_1/\text{Nb}$ ), and schematic representation of the crossover displacement.  $\blacktriangle$  Middle point composition.  
 $\circ$  Matano plane composition.



**Figure 5.39** Composition path for diffusion couple #6 ( $\beta_1/\text{Nb}$ ), and schematic representation of the crossover displacement.  $\blacktriangle$  Middle point composition.  $\circ$  Matano plane composition.

shown in Table 5.1. The composition path for the other couple in this corner, #11 (Figure 5.40), shows a visible bending of the path with a crossover point close to the  $\beta_2$  composition. In this couple the Al concentration gradient is almost zero, however, as shown in Figure 5.29 there is an apparent redistribution of Al possibly due to unequal mobility of Ti and Nb in this couple.

#### 5.4.2 The Constant Nb:Ti Ratio Zone

For this section the composition paths for diffusion couples #10, #9 and #7, which are given in Figures 5.41, 5.42 and 5.43 respectively, are considered. The similarity of the composition paths for these 3 couples is evident. Both ends of the composition paths are directed toward the Ti corner and the midsection at the crossover seems to follow a path parallel to a constant Ti composition.

#### 5.4.3 The Ti-Rich Corner

There is only one composition path for the discussion of the diffusivity behavior in this corner (couple #12). The pattern followed by this path is somehow similar to that obtained for couple # 11, but with a more pronounced tendency to deviate from the line connecting the composition ends and it bends toward the Nb-Ti side of the couple as shown in Figure 5.44. A high magnification of the path near the Ti corner is shown in Figure 5.45. It is observed from these Figures that the end of the paths at both ends point toward the Al corner of the Gibbs triangle, which implies that Al moves faster

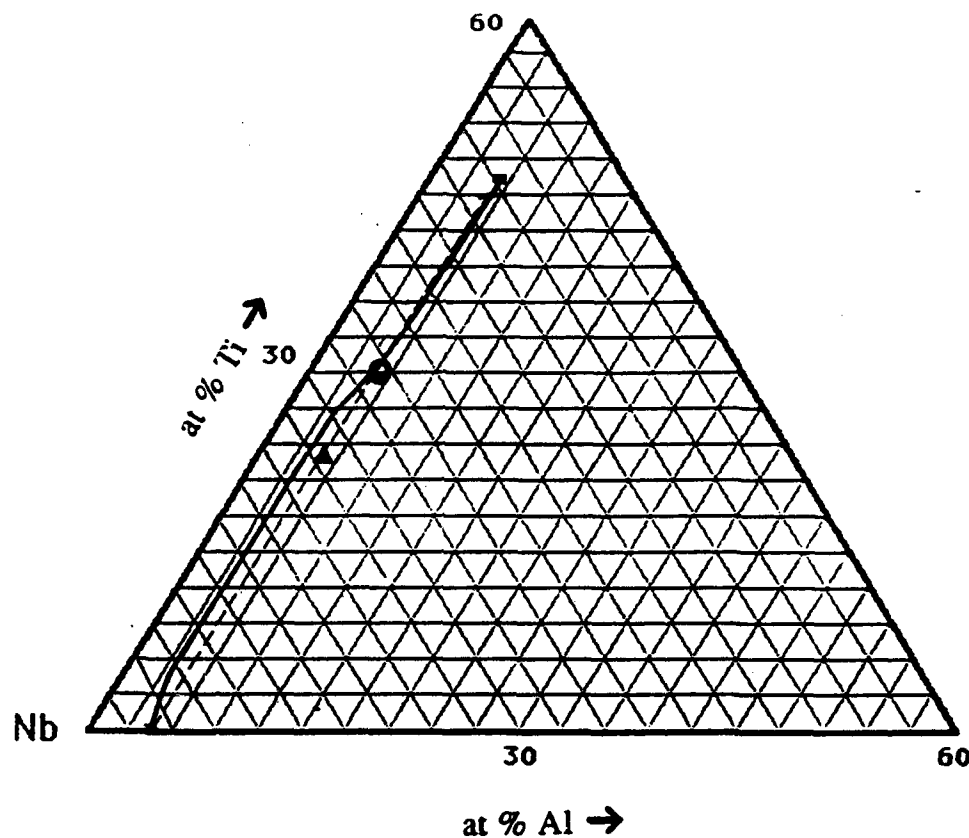


Figure 5.40

Composition path for diffusion couple #11 ( $\beta_0/\beta_2$ ) and schematic representation of the crossover displacement. ▲ Middle point composition. ○ Matano plane composition.

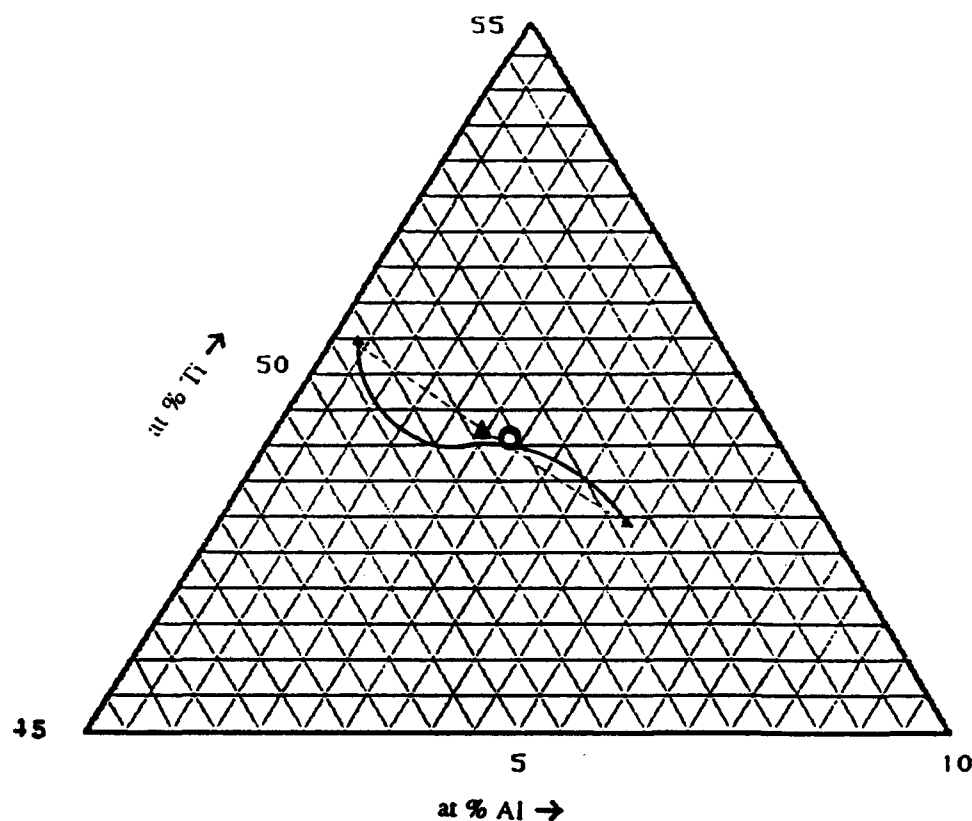


Figure 5.41

Composition path for diffusion couple #10 ( $\beta_3/\beta_2$ ), and schematic representation of the crossover displacement. ▲ Middle point composition. ○ Matano plane composition.

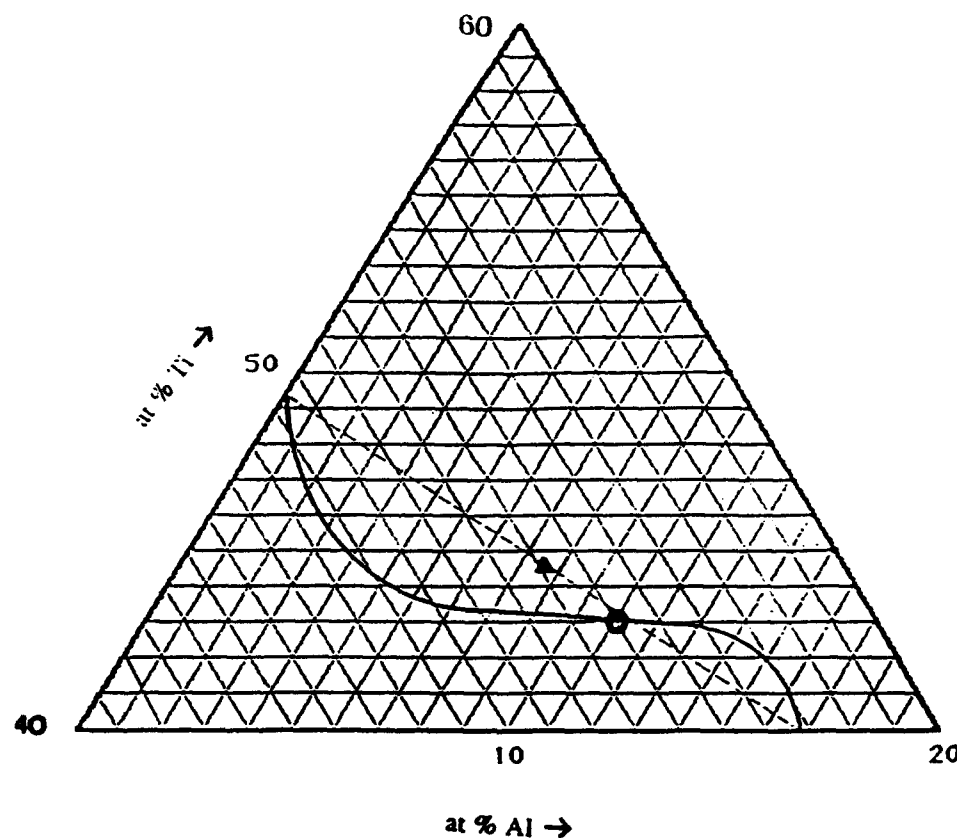


Figure 5.42 Composition path for diffusion couple #9 ( $\beta_3/\beta_1$ ), and schematic representation of the crossover displacement. ▲ Middle point composition. ○ Matano plane composition.

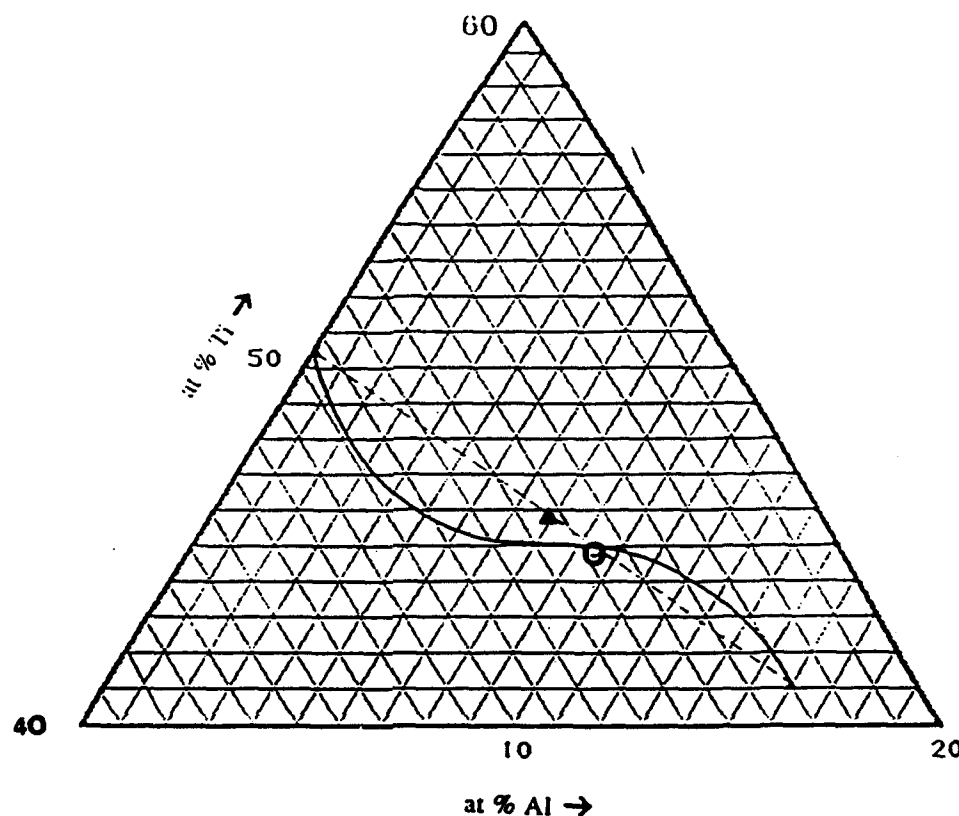


Figure 5.43 Composition path for diffusion couple #7 ( $\beta_3/\beta_1$ , 1400 °C), and schematic representation of the crossover displacement. ▲ Middle point composition. ○ Matano plane composition.

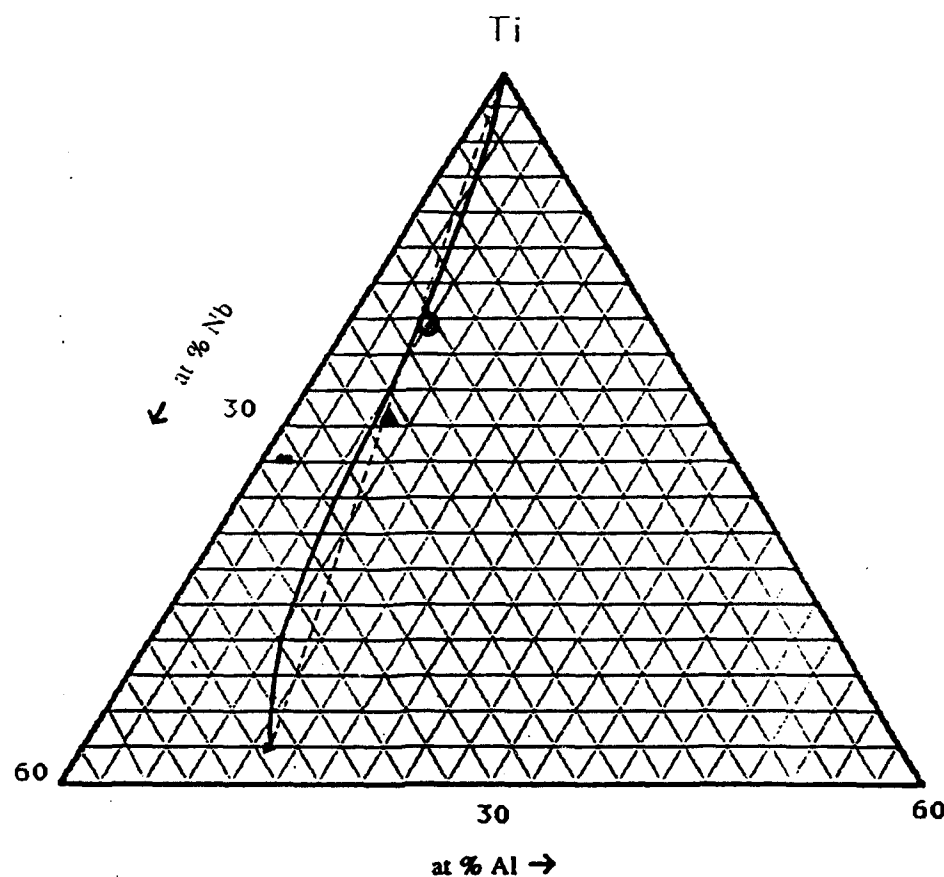


Figure 5.44 Composition path for diffusion couple #12 ( $\beta_1/\text{Ti}$ , 1400 °C), and schematic representation of the crossover displacement. ▲ Middle point composition. ○ Matano plane composition.

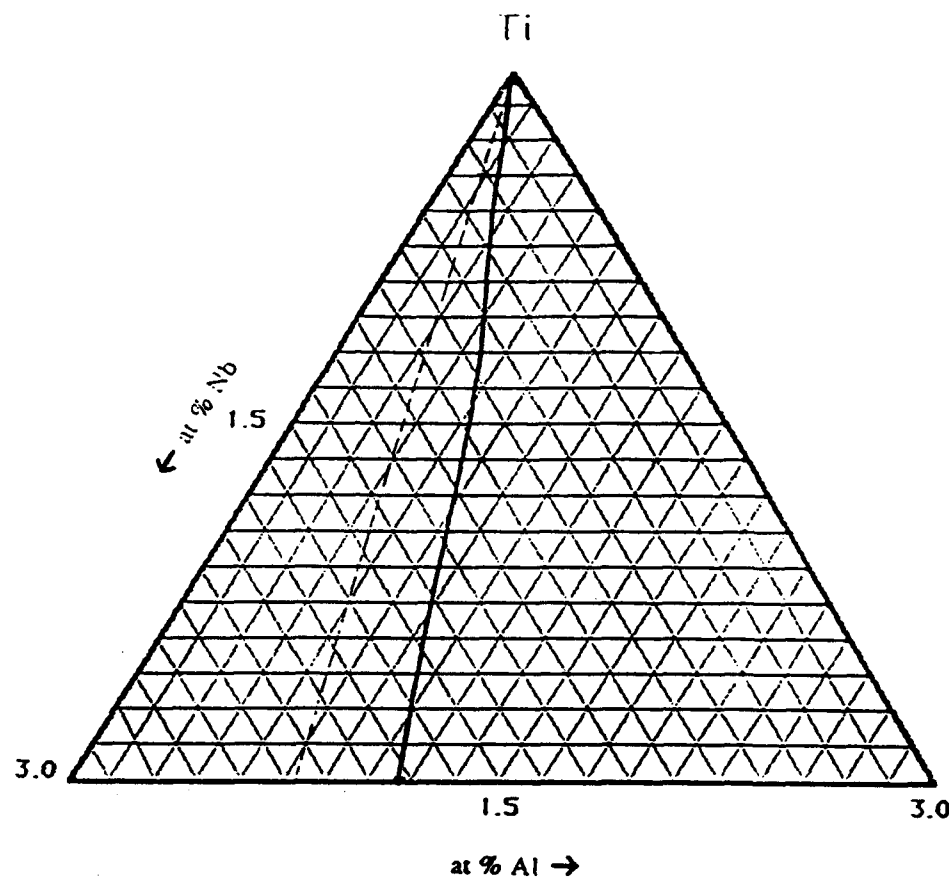


Figure 5.45      Ti-rich side of the composition path for diffusion couple #12 ( $\beta_1$ /Ti).

than Nb. The relative mobility of Ti and Al may be deduced by the displacement of the crossover point toward the Ti corner suggesting a relative higher mobility of Ti. This matter will be discussed later in detail (section 5.6).

### 5.5 Kirkendall Shifts

Two different methods were employed to measure the Kirkendall shift in the systems under study. The first of them was done experimentally by measuring the distance between the two interfaces present in the sandwich-like couples before and after the diffusion treatment. The resultant difference was then divided by 2 to get the net displacement of the markers. The second method employed the same computer program used for the evaluation of the Matano Interface in the binary system. In this case, the Matano plane determination was conducted over the profiles of the 3 components for each diffusion couple. In general, the calculated Matano interface position was approximately the same for the three elements. Table 5.2 shows the Kirkendall shift as calculated by the above mentioned methods. There is an excellent agreement between the two methods, except for the couple #11 ( $\beta_2/\beta_0$ ), for which both methods show similar displacements but in opposite directions. It was observed that the agreement between results of both methods is better when the computer program was applied to the experimental Al composition profiles. The reason for this could be the absence of critical points in the Al profiles in most cases. One problem associated with the experimental method was the lack of statistical

Table 5.2. Kirkendall shift measurements

Diffusion Couple Number	Marker Displacement Magnitude ( $\mu\text{m}$ )	Direction	Matano Plane Displacement ( $\mu\text{m}$ )	Direction
6 Nb/ $\beta_1$ 1400 °C	4.0	Nb $\pm$ $\beta_1$ $\rightarrow$	2.4	Nb $\pm$ $\beta_1$ $\rightarrow$
7 $\beta_3/\beta_1$ 1400 °C	1	$\beta_3 \pm \beta_1$ $\rightarrow$	2	$\beta_3 \pm \beta_1$ $\rightarrow$
8 Nb/ $\beta_1$ 1200 °C	8	Nb $\pm$ $\beta_1$ $\rightarrow$	2	Nb $\pm$ $\beta_1$ $\rightarrow$
9 $\beta_3/\beta_1$ 1200 °C	3	$\beta_3 \pm \beta_1$ $\rightarrow$	3	$\beta_3 \pm \beta_1$ $\rightarrow$
10 $\beta_3/\beta_2$ 1200 °C	4	$\beta_3 \pm \beta_2$ $\rightarrow$	3	$\beta_3 \pm \beta_2$ $\rightarrow$
11 $\beta_0/\beta_2$ 1200 °C	4	$\beta_0 \pm \beta_2$ $\leftarrow$	6	$\beta_0 \pm \beta_2$ $\rightarrow$
12 Ti/ $\beta_1$ 1200 °C	3.2	Ti $\pm$ $\beta_1$ $\leftarrow$	2.3	Ti $\pm$ $\beta_1$ $\leftarrow$

measurements as only a few number of yttria markers were available. For the case of couple #12, they were not even found as they were probably dissolved in the Ti matrix. Instead, in this case the measurements were made using oxide markers developed in the bonded interface during the hot-pressing operation.

At 1200 °C, the diffusion couple with pure Ti (#12) shows the largest displacement observed with a Kirkendall shift toward the Ti side of the couple. Regarding the two 1400 °C treated couples, a significant marker displacement (Kirkendall shift) was observed for couple #6 pointing toward the ternary side of the couple (rich Ti, poor Nb). As to the other couple treated at 1400 °C (#7) and those interdiffused at 1200 °C, the Kirkendall shift is small and in some cases negligible. For example, the  $\beta_1/\beta_3$  couples with constant Nb:Ti ratio and 15 at% Al (couples #7 and #9) exhibited a negligible displacement of the markers at either temperature, 1400 °C or 1200 °C. Assuming only the Al composition gradient, then one would expect a larger shift in the  $\beta_1/\beta_3$  couple than in the  $\beta_3/\beta_2$  couple (5at% Al). However, the consideration of the increase in Nb and Ti gradients suggests that more Nb and Ti flow into the ternary side in the  $\beta_3/\beta_1$  couple than they do in the  $\beta_3/\beta_2$  couple.

### 5.6 Crossover Displacements

As mentioned in Chapter 2, the crossover point of a composition path in the Gibbs triangle is displaced from the mid point of the line connecting the end compositions when the penetration tendencies of the components are concentration-

dependent. The composition of the crossover point should correspond to the composition of the original weld interface, which is given by the composition of the Matano interface. In Figures 5.38 to 5.44 the Matano interface compositions are marked on the composition paths. There is a good correlation between the calculated and crossover compositions, mainly in the couples involving  $\beta_1$ ,  $\beta_2$ , and  $\beta_3$  alloys.

### 5.6 Discussion

The discussion of the diffusivity in the ternary Nb-Ti-Al  $\beta$ -solid solution is based on the results obtained for penetration tendencies (see Table 5.1), composition paths (see Figures 5.38-5.45), and Kirkendall shifts (see Table 5.2). An analysis of the composition profiles permitted to evaluate the approximate penetration ratios of the components in the different couples. These ratios are given in Table 5.3, and it can be observed that they depend strongly on the composition of the alloys. The discussion of these results will be focused on three different regions and emphasis will be placed on the diffusion composition patterns following DeHoff *et. al.* [69].

#### a) Nb/Ti Constant Ratio

The composition paths of the 3 couples in this region (#10, #9, #7) as shown in Figures 5.41 to 5.43 are similar in behavior. It is observed that the end segments are directed toward the Ti corner, therefore, indicating that Ti is the fast diffuser. The midsection of these paths are parallel to the Nb-Al side suggesting that Al and Nb have similar penetration tendencies. When the midsections of the  $\beta_3/\beta_1$  couples annealed at two temperatures are compared in more

Table 5.3 Penetration ratios observed in the ternary couples of this study

Couple (#)	Ti	Al	Nb
$\beta_1/Nb$ (8)	1	1	1
$\beta_1/\beta_3$ (9)	1.8	1	1.5
$\beta_1/Ti$ (12)	1.14	1.11	1.0
$\beta_2/\beta_3$ (10)	1.36	1.30	1.0
$\beta_2/\beta_0$ (11)	1.2	1.2	1.0
$\beta_1/Nb$ (6)	1	1	1
$\beta_1/\beta_3$ (7)	1.33	1.30	1.0

detail (#7 and #9), it is observed that the midsection of couple #7 (1400 °C) presents a slight rotation toward the Al corner, suggesting that the mobility of Nb increases as the temperature increases. It is also observed that deviation of the composition path from the straight line behavior in couples #7 and #9 decreases with increasing the annealing temperature, which suggests that the mobility of Al and Nb is closer to that of Ti at higher temperatures.

As far as the penetration tendency ratios are concerned (Table 5.3), the three couples show the highest penetration ratio for the element Ti, consistent with the observations regarding the composition paths. However, when the ratios for Nb and Al are compared, an artificially large penetration of Nb is found for the  $\beta_1/\beta_3$  couple (#9) annealed at 1200 °C. As demonstrated by DeHoff *et al.* [69], the penetration depths calculated from the microprobe analysis, particularly for elements that are not indeed mobile, do not represent the physical distance over which the elements have moved. In this case the imbalance in distribution of Al and Ti alters the percentage of Nb. This is supported by the facts that Nb shows a larger depth at 1200 °C than it does at 1400 °C in the  $\beta_3$  side, and that the reaction depth of Ti at 1200 °C is much larger than that of Al.

A comparison of the penetration depths for  $\beta_1/\beta_3$  and  $\beta_2/\beta_3$  couples (Table 5.1) reveals that in general the depths are much larger for the  $\beta_1/\beta_3$  couple, which had a larger concentration gradient of the elements. The penetration depth of Al on the  $\beta_3$  side (Nb-50Ti) decreases from 72  $\mu\text{m}$  to 31  $\mu\text{m}$  with a decrease in concentration gradient. It is interesting to note that the Nb and Ti are apparently

drawn from much deeper in the  $\beta_1/\beta_3$  couple, however, in the  $\beta_2/\beta_3$  couple their depth of draw is similar to the penetration depth of Al. The larger depth of draw of Ti in the  $\beta_1/\beta_3$  couple can be attributed to the larger concentration gradient of this element in comparison to the  $\beta_2/\beta_3$  couple. Consistently, in both couples Nb penetrates to a shorter depth into the counterpart side of the  $\beta_3$  than does Ti.

As far as Kirkendall shift for these couples are concerned, the displacements were measured to be very small but always toward the ternary side, indicating that physically more Al atoms were transferred to the  $\beta_3$  side. This observation is consistent with the larger concentration gradient of Al than those of Ti and Nb for these couples.

b) Ti Corner

In consistency with the assumption that Ti moves much faster than Al and Nb the composition path of  $\beta_3/Ti$  couple (couple #12) showed the tendency toward a straight line behavior (see Figure 5.44). The end segment at the  $\beta_3$  composition is directed toward the Al corner indicating that in this corner Al moves faster than Nb. Consequently the composition path deviates slightly from the straight line behavior, but due to a much faster diffusivity of Ti it crosses over very close to the Ti corner.

The system, in general, shows the highest penetration depths in this corner consistent with the fact that Ti has the lowest melting point among all constituent alloys used in this study. As shown in Table 5.1 all elements show a larger depth of diffusivity in the Ti side than in the  $\beta_1$  side consistent with the high solidus temperature

of the latter alloy. Nb tends to show shorter draw and penetration depths than Ti and Al do.

The Kirkendall Shift measured in this couple is also one of the largest observed in all couples, and accordingly, it predicts a larger flux of Ti into the  $\beta_1$  side of the couple.

c) Nb Corner

The penetration ratio values (1:1:1) given in Table 5.3 for couples #6 and #8 are in complete agreement with the matching of composition paths to the straight line connecting the end compositions observed for these couples. This behavior can be interpreted as a result of the low jump frequencies of all three components in this region of the diagram, which again can be correlated to the solidus temperature of the alloys involved and is supported by the depth of penetration measured on the two sides of the couples. These penetrations consistently show a very small penetration into the Nb side and it is the same for the three elements. The penetration depth in the  $\beta_1$  side, on the other hand shows a deeper diffusion region due to the lower solidus temperature of this alloy. The low value of the Kirkendall shift observed at 1200 °C also shows that the mobility of the three elements is similar. However, when the temperature is increased to 1400 °C, the Kirkendall shift measured is very large (see Table 5.2), which is difficult to interpret since it indicates that a large displacement of Ti and Al atoms toward the Nb had occurred. Such observations do not agree with the composition path and the penetration depth results. Further investigation is required to resolve these inconsistencies.

The results of this study suggest that the diffusivity of the components in general is larger when the amount of titanium present in a couple increases. The Kirkendall shift and crossover point displacement results also indicate that the mobility of the system increases as the titanium content increases, but they also suggest that the aluminum owns a larger mobility than niobium as both the Kirkendall shift and crossover displacement point opposite to the niobium corner. In accordance with these results, titanium owns the largest jump frequency followed by aluminum and the niobium.

Another observation of this study is that the Kirkendall and crossover shifts are in agreement as to the direction of the displacement, and the composition at the Matano interface correlates well with the crossover composition. The mobility of all components is larger close to the Ti corner of the diagram. The jump frequency of the system changes more drastically as going from the Nb corner side of the system toward the Ti corner. This behavior causes, therefore, a similar crossover shift in the couples involving end compositions in the Ti-rich section of the ternary system, and a larger crossover shift in the couples involving Nb-rich end compositions.

### 5.7 Summary

Contrary to the behavior of Nb-4.5 at% Al solid solution, no propensity to internal oxidation was detected in the ternary alloy. This observation suggests that the addition of Ti reduces the susceptibility of the alloys to internal formation of  $\text{Al}_2\text{O}_3$ . Despite the observation of two-phase microstructures at room temperature, it

## CHAPTER 6 CONCLUSIONS

The diffusion behavior in the binary Nb-Al and the ternary Nb-Ti-Al systems were studied employing Matano-Boltzmann diffusion couple method. The results obtained have led to the following conclusions:

- 1- The binary Nb-4.5at% Al alloy was very susceptible to internal oxidation. However, the addition of Ti to the b.c.c. solid solution completely retarded the internal oxidation.
- 2- The zirconia particles used as markers, were unstable in the Nb-Al  $\beta$  solid solution and decomposed at high temperatures. The substitution of the markers with yttria proved that this oxide is completely inert in the binary Nb-Al  $\beta$ -solid solution, however, in the presence of Ti some reactivity was observed.
- 3- The interdiffusion coefficient of the binary Nb-Al system varied linearly with composition in the range of 1-3 at% Al and it showed a linear Arrhenius behavior as a function of temperature. The average interdiffusion coefficient in the temperature range of 1350 °C to 1550 °C can be expressed through the following equation:

$$D = 0.1136 \exp(-80,105 \text{ (cal/mole)/RT}) \text{ cm}^2/\text{sec}$$

The activation energy was independent of the composition in the 1-3 at% range. The average intrinsic diffusivity of Al in the same

temperature range, calculated based on a dilute solution assumption is given by:

$$D_{Al} = 0.1161 \cdot \exp(-80,165 \text{ (cal/mole)/RT}) \text{ cm}^2/\text{sec}$$

4- Kirkendall shift measurements correlate well with the calculated crossover displacements in the ternary Nb-Ti-Al system. The direction and magnitude of displacements in conjunction with an analysis of the composition paths suggest that Ti is the fastest component of the system at all compositions, with a very small difference in the relative mobilities of Al and Nb. The addition of Ti increases the general diffusivity of the system partially due to a reduction in the solidus temperature of alloys.

5- The occurrence of maxima and minima in the composition profiles obtained by microprobe analysis correlates with the existence of small composition gradients or very low relative mobilities.

6- Results of this study show that the 3 elements Nb, Ti and Al, have similar but very low jump frequencies in the Nb-rich corner of the Gibbs triangle. In the Ti-rich corner the jump frequencies of these elements are unequal but much higher than the Nb jump corner. Ti has the highest jump frequency in this corner.

**APPENDIX A**  
**PROBLEMS ASSOCIATED WITH THE MEASUREMENT OF COMPOSITION  
PROFILES BY MICROPROBE ANALYSIS**

## APPENDIX A

PROBLEMS ASSOCIATED WITH THE MEASUREMENT OF COMPOSITION  
PROFILES BY MICROPROBE ANALYSIS

The evolution of electronic analysis techniques such as the Electron Microprobe for the study of diffusivity process have provided the capability to measure gradient concentrations at very low spatial resolutions ( $1\mu\text{m}$ ) that traditional techniques would have never been able to reach. This has permitted to study diffusion at very short scales, such as low temperature and/or short time treatments. However, the success of the application of this technique relies on the accuracy of the data obtained. In order to report reliable results, several composition profiles were measured in each of the diffusion couples studied in this research. At least two matching profiles were obtained for each couple (Figures A.1), and the one with the smoother curve was chosen for calculating of the Matano plane position.

The inconsistency in composition profiles obtained for an element in the same couple was found to occur in two ways. Sometimes a constant shift in the composition profile was detected. Due to a change in parameters associated with the calibration of the instrument, the entire profile was shifted with respect to the initial profile. Since this displacement was equal for all compositions, no effect on the calculated depth of penetration was detected. The

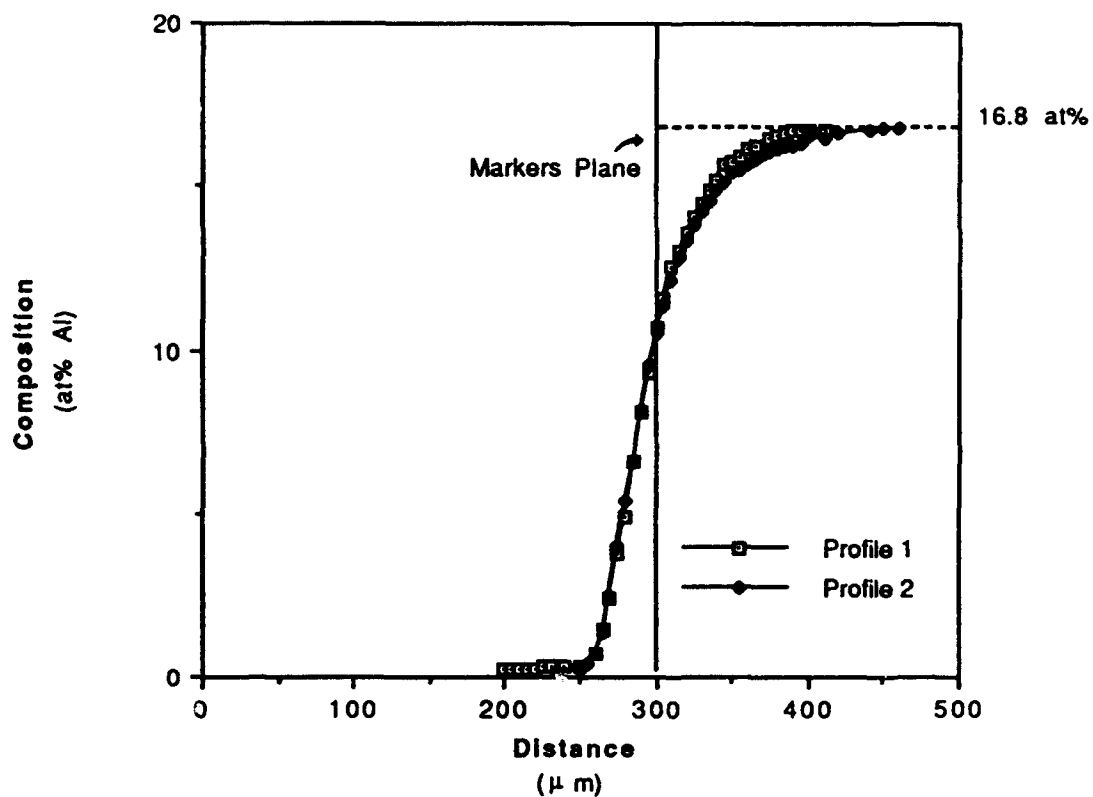


Figure A4

Composition profiles of Al after interdiffusion treatment of couple #9 at 1200 °C for 6 hours.

computation of the Matano interface was not affected either, since the end compositions employed in such calculations were those obtained while measuring the resulting composition profiles. Figure A2 shows this behavior for the Nb composition profiles in couple #9. The other effect on the measurement of the composition profiles was that due to the existence of markers close to the point from which the profile was obtained. Figure A3 shows the BSE micrograph of a diffusion profile measured in diffusion couple #10 and the presence of yttria markers. When the microprobe analysis of the couple was performed, the closeness of the markers produced compositions profiles as that shown in Figure A4.a. When the analysis was performed in zones far enough from the markers, normal profiles as that shown for the same couple in Figure A4.b was obtained.

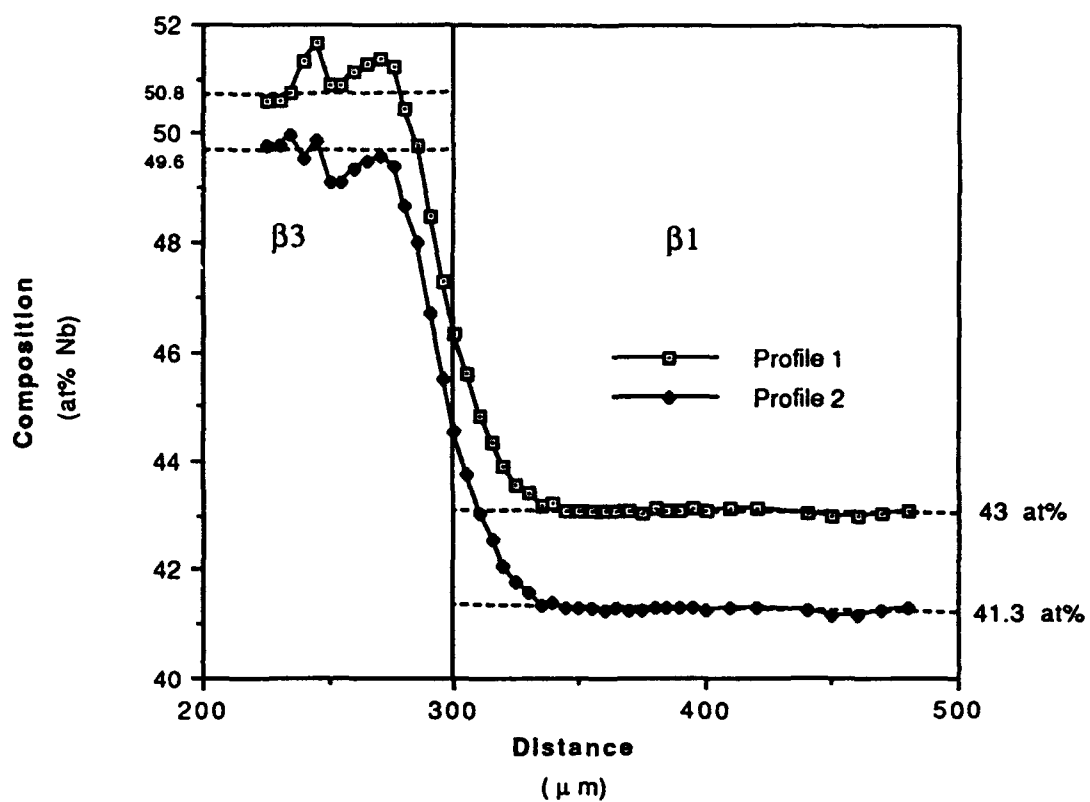
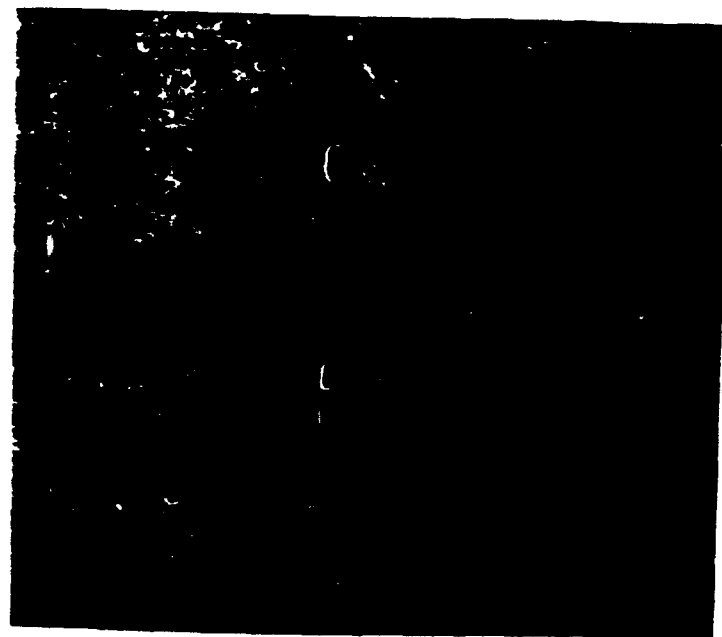


Figure A2

Composition profile of Nb after interdiffusion treatment of couple #9 at 1200 °C for 6 hours.



— 10  $\mu\text{m}$

Figure A3

BSE micrograph showing microprobe analysis contamination close to yttria markers in couple #10 ( $\beta_3/\beta_2$ ).

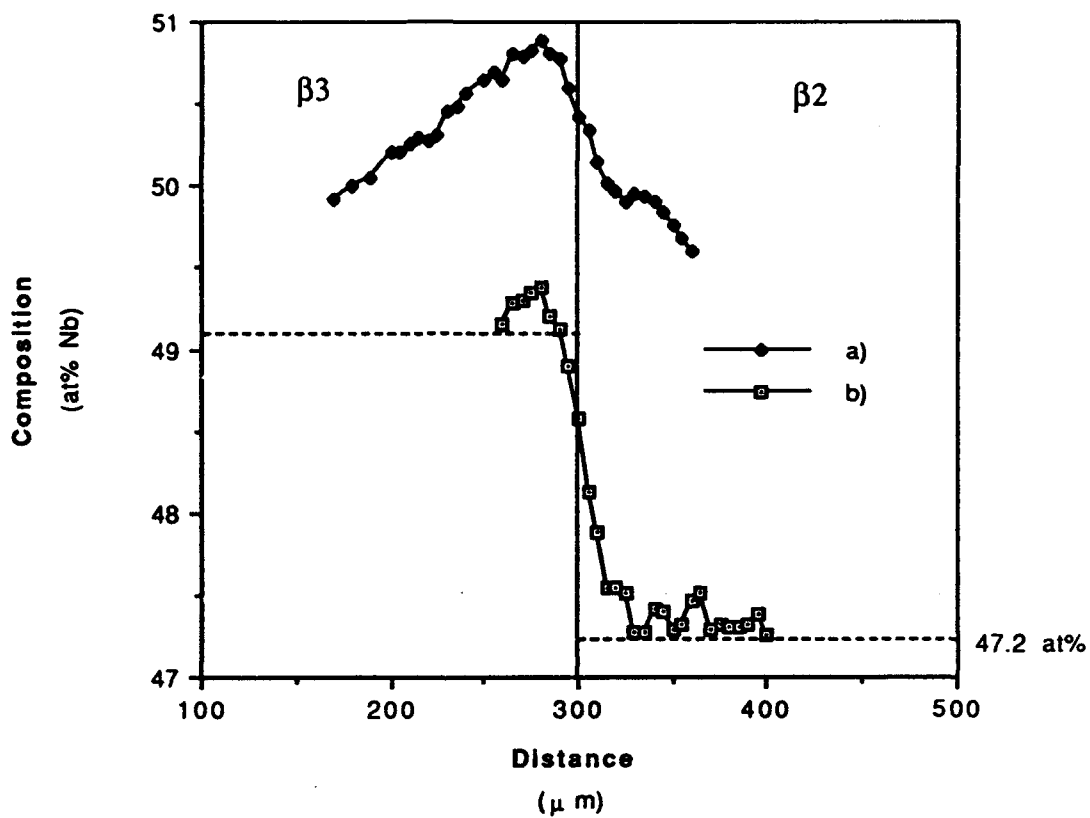


Figure A4

Composition profiles of Nb after interdiffusion treatment of couple #10 at 1200 °C for 6 hours.

- a) Measured close to yttria markers
- b) Measured away from markers.

## REFERENCES

- [1] P. Kofstad, and S. Espevik, *J. Electrochem. Soc.*, **112** (2) (1965), pp.153-160.
- [2] J. F. Brady, J. N. Ong, Jr. "Oxidation Rate of Nb as a Function of Temperature and Pressure", Columbium Metallurgy, 10, Ed. Interscience, NY, (1960), p. 719.
- [3] H. Inouye, "Nb in High Temperature Applications", Proceedings of the International Symposium Niobium '81, Ed. H. Stuart, AIME, Warrendale, Pa.
- [4] R. A. Perkins, G. H. Meier, K. T. Chiang, "Effect of Alloying, Rapid Solidification, and Surface Kinetics on High Temperature Environmental Resistance of Nb", LMSC-F195926 Report for Air Force Office of Scientific Research under contract F49620-86-C-0018, (June 15, 1987).
- [5] R. C. Svedberg, "Oxides Associated with the Improved Air Oxidation Performance of some Nb and Intermetallics and Alloys", Properties of High Temperature Alloys, Z. A. Foroulis and F. S. Pettit eds., Electrochemistry Society 1976, p. 331.
- [6] G. I. Nikolaev, N. V. Bodrov, *Zh. Fiz. Khim.*, **52** (1978), p. 1430.
- [7] E. O. Kirkendall, and A. D. Smigelskas, *Trans. AIME*, **171** (1947), p. 130.
- [8] P. G. Happoldt, *Master of Sc. Thesis*, University of Purdue, 1988.
- [9] J. L. Murray, "Phase Diagrams of Binary Ti Alloys", Ed. J. L. Murray, ASM Intern., Metals Park, OH, (1987), p. 188.
- [10] C. E. Lundin, A. S. Yamamoto, *Trans. AIME*, **236**, (1966), p. 863.
- [11] J. L. Murray, "Phase Diagrams of Binary Ti Alloys", ed. J. L. Murray, ASM Intern., Metals Park, OH, (1987), p. 173.

- [12] J. H. Perepezko, Y. A. Chang, L. E. Seitzman, J. C. Lin, N. R. Bonda, T. J. Jewet, J. C. Mishurda, "High Temperature Phase Stability in the Ti-Al-Nb System", High Temperature Aluminides and Intermetallics Proc. Symp. Indianapolis, Ind., Oct. 1989 ASM/TMS-AIME.
- [13] K. Kaltenbach, S. Gama, D. Pinatti, K. Schulze, E. Henig, *Z. Metallkde.*, 80, (1989), p. 535.
- [14] L. Bendersky, W. Boettinger, "Investigation of B2 and Related Phases in the Ti-Al-Nb Ternary System", Mat. Res. Soc. Symp. Proc., 133, (1989), p. 45.
- [15] T. J. Jewett, J. C. Lin, N. R. Bonda, L. E. Seitzman, K. C. Hsieh, Y. A. Chan, "Experimental Determination of the Ti-Al-Nb Phase Diagram at 1200 °C", Mat. Res. Soc. Symp. Proc. 133, (1989), p. 69.
- [16] A. D. LeClaire, "Diffusion in B.C.C. Metals", A.S.M., Cleveland Ohio, (1965).
- [17] G. Newmann, V. Tolle, *Phil. Mag. A*, 54, (1986), p. 619.
- [18] J. F. Murdock, T. S. Lundy, E. E. Stanbury, *Acta Metall.*, 12, (1964), p. 1033.
- [19] G. Kidson, *Canad. J. Phys.*, 41, (1963), p. 1563.
- [20] W. Petry, T. Flottmann, A. Heiming, J. Trampenau, M. Alba, G. Vogl, *Phys. Rev. Lett.*, 61, (6), (1988), p. 722.
- [21] C. Herzig, U. Kohler, *Mater. Sci. Forum*, 15/18, (1987), p. 301.
- [22] W. Bussmann, C. Herzig, H. A. Hoff, J. N. Mundy, *Phys. Rev. B*, 23 (12) (1981), p. 6216.
- [23] R. E. Eizinger, J. N. Mundy, H. A. Hoff, *J. Nucl. Matl.*, 69/70, (1978), p. 523.
- [24] A. E. Pontau, D. Lazarus, *Phys. Rev. B*, 19, (8), (1979), p. 4027.
- [25] S. L. Sass, *J. Less-Common Met.*, 28, (1972), p. 157.

- [42] R. J. Lauf, Report 1978, COO-1198-1216, 104pp. Avail. NTIS. From Energy Res. Abstr., 4, (6), (1979), Abstr. # 14004.
- [43] G. Canelli, R. Cantelli, Hydrogen Met., Proc. Int. Congr., 2nd, 1977, 1, Paper 1B2, 5 pp., Pergamon Press: Oxford, England.
- [44] W. S. Gorsky, *Phys. Z. Sowjetunion*, 8, (1935), p. 457.
- [45] J. F. Stringer, "High Temperature Corrosion of Aerospace Alloys", AGARD-AG 200, Advisory Group for Aerospace Research and Development, NATO, August 1975.
- [46] N. Birks, G .H. Meier, "Introduction to the High Temperature Oxidation of Metals", Edward Arnold, Ltd; London, 1958.
- [47] F. Gesmundo, F. Viani, *Oxid. Metalls.* 25, (1986), p. 269.
- [48] C. Wagner, *Z. Elektrochem.*, 63 (1959) p. 772.
- [49] K. Kirano, Y. Ijima, "Inter- and Reaction Diffusion between Alloys of very Different Diffusional Properties", Diffusion in Solids: Recent Developments, M. A. Dayananda & G. E. Murch eds., AIME, 1985, p.141.
- [50] J. E. Morral, M. S. Thompson, O. J. Devereux, *Scripta Met.*, 32 (1986), p. 1562.
- [51] R. C. Frank, R. J. Lauf, C. J. Alstetter, *Met. Trans. A*, 13A, (4), (1982), p. 539.
- [52] B. D. Bastow, G. C. Wood, D. P. Whittle, *Corros. Sci.*, 25, (1985), p. 253.
- [53] J. A. Nesbit, R. W. Heckel, "High Temperature Protective Coatings", ed. S. C. Singhal, AIME, (1984), p. 75.
- [54] A. Fick, "Uber Diffusion", *Poggendorff's Annalen*, 94 (1855), p. 59.
- [55] L. Boltzmann, *Ann. Phys., Leipzig*, 53 (1894), p. 959.
- [56] C. Matano, *Japan Journal Phys.*, 8 (1933), p. 109

## BIOGRAPHICAL SKETCH

Jose Guadalupe Luis Ruiz Aparicio was born on February 28, 1960, in Mexico City, D.F., Mexico. He received his elementary and secondary school there, graduating from C.C.H. High School in 1977. In 1985 Mr. Ruiz graduated with honors from Universidad Nacional Autonoma de Mexico (National University of Mexico), Mexico City, Mexico, with a degree in Chemical Metallurgical Engineer.

In 1982 he joined the faculty of the Universidad Nacional Autonoma de Mexico as Assistant Professor in the Department of Chemical Metallurgical Engineering. From 1982 to 1987 he worked there in the area of Physical Metallurgy.

He joined the mechanical metallurgy group in the Department of Material Science and Engineering, University of Florida in 1988. Since then he has pursued work toward the degree of Master of Science and Engineering. After graduation, he will pursue work toward the degree of Doctor of Philosophy in Materials Science and Engineering at the University of Pittsburgh. He plans to reincorporate to the National University of Mexico afterwards.

The author is married to former Laura G. Barquera Lopez from Mexico city, Mexico. He is member of the TMS and ASM.